HIGH VOLTAGE AND LONG CYCLING CATHODE MATERIALS BASED ON $LiCoO_2$

LIN ZEZHOU

PhD

The Hong Kong Polytechnic University

2025

The Hong Kong Polytechnic University

Department of Applied Physics

High Voltage and Long Cycling Cathode Materials Based on $LiCoO_2$

LIN Zezhou

A thesis submitted in partial fulfillment of the requirements for the degree of Doctor of Philosophy

Aug 2024

CERTIFICATE OF ORIGINALITY

I hereby declare that this thesis is my own work and that, to the best of my knowledge and belief, it reproduces no material previously published or written, nor material that has been accepted for the award of any other degree or diploma, except where due acknowledgement has been made in the text.

_____(Signed)

_____LIN Zezhou_____ (Name of student)

Abstract

To meet the ever-increasing demands of portable smart devices, electric vehicles, and grid storage, the pursuit of high energy density remains a longstanding objective in rechargeable battery development. $LiCoO_2$ (LCO) has emerged as the predominant commercial cathode material due to its stable charge/discharge voltage plateaus, high tap density, high volumetric energy density, and excellent electrochemical cycling durability. However, to achieve even higher capacity, it is necessary to explore methods that can enhance the performance of the existing cathodes. One such approach involves raising the cut-off voltage to extract more Li^+ ions during the charging process. Unfortunately, exceeding a cut-off charge voltage higher than 4.5 V (vs. Li/Li^+) leads to rapid capacity decay that limits its cycle life. It is urgent to find an appropriate modification strategy as the primary tool in improving Li-ion batteries (LIBs).

Firstly, considering the significantly different diffusivities of dopant ions (as confirmed by density functional theory calculations), we propose a proof-of-concept strategy to forming core-shell structured $LiCoO_2$ (CS-LCO) via a simple two-step co-doping method. In this process, high diffusivity Al^{3+}/Mg^{2+} ions occupy the core matrix while low diffusivity Ti^{4+} ions enrich the shell layer. The presence of Al^{3+}/Mg^{2+} in the core matrix helps optimize physical properties, such as electrical

conductivity and Li^+ ion diffusivity. On the other hand, the Ti^{4+}-enriched shell layer, with Ti substitution and stronger Ti-O bond, leads to the reduction in the number of oxygen ligand holes and an enhancement of the oxygen stability. Furthermore, CS-LCO exhibits mitigated phase transition from O3 to H1-3, resulting in reduced contraction of *c*-axis and structural distortion.

Secondly, among different surface coating modifications, we find that the utilization of triethylamine template promotes the phase transformation from traditional amorphous $AlPO_4$ to crystalline $AlPO_4$-5 zeolite on the surface of LCO and provides several advantages. (1) The electrochemically and mechanically stable $AlPO_4$-5 zeolite coating acts as a protective layer to reduce the lattice oxygen loss and the side reactions on the LCO surface. (2) The crystalline $AlPO_4$-5 zeolite establishes a stable diffusion pathway for Li^+ ion transport, which accelerates the Li^+-desolvation process and improves the Li^+ kinetics. (3) The full coverage of the elastic $AlPO_4$-5 zeolite coating layer effectively provides mechanical reinforcements to suppress the phase transition from O3 to H1-3. Consequently, a multifunctional $AlPO_4$-5 zeolite coating layer enables stable 4.6 V high voltage operation of LCO cathode.

The third work proposes a novel cathode called CeO_2 interspersed massage-ball-like LCO (LCO@CeO_2). In addition to their role in surface protection and insulation from electrolyte, CeO_2 nanoparticles also play a crucial role in facilitating Li^+ conduction by establishing easier pathways for Li^+ de/intercalation. Moreover, the interspersed

CeO_2 nanoparticles contribute to maintaining the reversibility of the lattice oxygen. As a result of these design considerations, the optimized LCO@CeO_2 cathode, prepared at 850℃, exhibits outstanding electrochemical performance and effectively mitigates the generation of undesirable gases.

Overall, this thesis focuses on the coating and doping strategies to achieve high voltage and long cycling cathodes based on LCO. Satisfactory results are obtained, which will provide guidance in the design and development of future generation of LCO.

List of publications

1. **Zezhou Lin**, Ke Fan, Tiancheng Liu, Zhihang Xu, Gao Chen, Honglei Zhang, Hao Li, Xuyun Guo, Xi Zhang, Ye Zhu, Peiyu Hou* and **Haitao Huang***, Mitigating lattice distortion of high-voltage $LiCoO_2$ *via* core-shell structure induced by cationic heterogeneous co-doping, ***Nano-Mirco Letters***, 2024, 16, 48.

2. **Zezhou Lin**, Yiran Ying, Zhihang Xu, Gao Chen, Xi Gong, Zehua Wang, Daqin Guan, Leqi Zhao, Mingyang Yang, Ke Fan, Tiancheng Liu, Hao Li, Honglei Zhang, Huangxu Li, Xi Zhang, Ye Zhu, Zhouguang Lu, Zongping Shao*, Peiyu Hou* and **Haitao Huang***, Multifunctional zeolite film enables stable high-voltage operation of $LiCoO_2$ cathode, ***Energy Environ Sci***, 2024, Accepted.

3. **Zezhou Lin**, Zhihang Xu, Yiran Ying, Gao Chen, Xi Gong, Daqin Guan, Leqi Zhao, Tiancheng Liu, Hao Li, Huangxu Li, Xiao Sun, Ting-Shan Chan, Yu-Cheng Huang, Xi Zhang, Ye Zhu, Peiyu Hou, Zongping Shao*, and **Haitao Huang***, Multifunctional surface modification for stable high-voltage lithium-ion batteries, To be submitted.

4. **Zezhou Lin**, Yiran Ying, Tiancheng Liu, Gao Chen, Xi Zhang, Peiyu Hou* and **Haitao Huang***, Progress on high-voltage $LiCoO_2$ cathode for high-energy Li-ion battery, To be submitted.

Acknowledgements

The past three years of my Ph. D journey have been both brief and enduring, constituting a profoundly significant chapter in my life. The free and open learning environment in The Hong Kong Polytechnic University has enriched me in ways immeasurably. During this period, I embarked on the journey of acquiring knowledge in battery-related fields from scratch and learned how to scientifically analyze and solve problems. These skills have greatly impacted my future personal and professional development.

I would like to express my deepest gratitude to Prof. Huang Haitao for granting me the precious opportunity to join his research group. I am grateful to Prof. Huang for guiding me into the fascinating world of scientific research. I am thankful for his provision of a complete experimental environment and access to advanced characterization techniques, enabling me to conduct targeted scientific explorations. I appreciate his rigorous guidance and careful revisions, which provided me with the correct research direction and facilitated the successful publication of research papers. I am also grateful for the valuable opportunities he provided me to engage in Research Student Attachment Programme (RSAP) of Hong Kong Polytechnic University. I was funded to go to Curtin University for short-term research activities as a Visiting

Research Associate from 01/12/2023 to 31/05/2024. Overall, the guidance and support of Prof. Huang have been immeasurable, and words cannot fully express my gratitude.

Additionally, I would like to express my appreciation to Prof. Zhang Xi for her guidance during my master's studies, which paved the way for me to pursue my Ph. D studies at The Hong Kong Polytechnic University. I extend my gratitude to Dr. Hou Peiyu, Dr. Guan Daqin and Dr. Chen Gao for their collaboration in research, as well as to Prof. Shao Zongping for his research guidance. I am thankful for the assistance provided by my fellow students at The Hong Kong Polytechnic University and those at Curtin University. Finally, I would like to thank my family and girlfriend (Ms. Xu Zewen), for their unwavering support and companionship. With your support and mutual learning, my Ph. D journey has not been a solitary one.

I am profoundly grateful to all those who have assisted and supported me throughout this journey.

Thank you all sincerely!

Table of contents

Lists of figures

Lists of tables

Chapter 1 Introduction

1.1 Background

The Earth's environment is under severe threat from energy waste and the worsening greenhouse effect, jeopardizing human survival[1-3]. To counter environmental degradation, the global trend now focuses on sustainable energy utilization. Urgent attention is required for the study of sustainable energy, with efficient and cost-effective energy collection, conversion, and storage being vital for modern sustainable energy systems[4, 5]. Furthermore, the development of clean and efficient advanced energy storage systems is crucial for the continuous transportation, networking and urban energy supply required in modern intelligent societies. While portable electronic devices have witnessed explosive growth and constant hardware and software updates over the past decade, progress in portable energy storage systems has been comparatively slow[6-8].

Figure 1.1 The modern sustainable energy system, including **a** energy harvest, **b** electricity storage, and **c** LIBs application and main crucial parts of energy consumption in modern society.

The Industrial Revolution played a pivotal role in driving societal development and introduced more efficient energy utilization and storage systems. The pursuit of green, sustainable energy and advanced energy storage systems has become an inevitable trend in modern society's development. As shown in **Fig. 1.1**, modern sustainable energy system mainly consists of three components: (1) The harvest and conversion of sustainable green energy, including wind energy, waste heat energy, hydroelectricity,

and solar energy, etc. (2) Rechargeable batteries are now the predominant energy storage devices in modern society. They have high efficiency of energy conversion and high reversibility between charging and discharging. Through redox reactions of transition metal (TM) ion, energy is converted between electrical energy and chemical energy, with captured electrical energy stored as chemical energy in the electrodes. (3) The efficient utilization of energy has permeated various aspects of human life, particularly with the rapid expansion of portable electronic equipment, which greatly leverage the advantages of rechargeable batteries, especially in the form of portable power banks. Nowadays, rechargeable batteries are extensively employed in areas such as smartphones, laptops, power tools, and electric vehicles[9-12].

Among the electricity storage device, Li-ion battery (LIBs) have long been regarded as the optimal choice for powering portable electronic products due to their portability and high energy density[12, 13]. Since the 21st century, LIBs have experienced rapid development, characterized by reduced volume, increased energy density, and extended stability, aligning perfectly with the lightweight trend of modern smart electronic devices[14, 15]. These advancements owe much to the development of layered structural cathode materials, which exhibit excellent reversible charge-discharge performance. Since the emergence of LIBs, they have been widely applied in daily human life, becoming indispensable advanced energy storage devices. LIBs achieve the conversion of electrochemical potential energy by reversibly extracting/inserting Li^+ ions into the cathode lattice. The energy density of a battery is equal to the

multiplication of reversible capacity and voltage, so that higher charge cut-off voltage significantly enhances the battery's energy density[16-18].

As sustainable energy storage devices, LIBs play a greater role in future application scenarios beyond portable electronic devices. LIBs have potential to accelerate the process of sustainable development and modernization in smart societies. To meet the demand for green sustainable energy, in-depth research on the working principles, failure mechanisms, and optimization of battery configurations becomes crucial. Through fundamental research, the environmental and efficient new cathode materials can be explored to achieve higher capacity and better stability while saving costs and simplifying the manufacturing process.

1.2 Research motivation and scope

LIBs consist of several components, including the cathode, anode, separator, and electrolyte. This structural composition has been used since the emergence of LIBs and remains in use today. The cathode (such as $LiCoO_2$ and $LiFePO_4$) and anode (such as graphite) in the battery employ electrochemical intercalation reactions that exhibit good reversibility[8, 19]. Interlayer reactions require the electrode material to be layered, capable of accommodating Li^+ ions and facilitating their easy extraction and insertion. Transition metal oxides (Li_xTMO_2) are common cathode materials that offer a variety of choices for battery applications, making modified cathode materials a subject of considerable research interest[20]. Several factors are involved in determining the specific capacity and cycling durability: (1) the redox ability of TM ions in the cathode to undergo valence state changes, (2) the available space for Li^+ ion intercalation in layered materials, and (3) the structural reversibility during Li^+ ion intercalation reactions. Generally, higher charge cut-off voltage leads to higher specific capacity, but it also brings structural degradation of the cathode material[18, 21]. Excessive Li^+ ion extraction can gradually limit the release of Li^+ ions due to irreversible structural phase transitions, thereby affecting specific capacity and cycling durability. These challenges associated with high voltage limit the advancement of high-energy density batteries. Overall, these high-voltage challenges must be summarized and addressed in the future to modern advanced batteries system.

To achieve higher energy density, we must confront the challenges posed by high

voltage[22]. Before that, it is crucial to acquire a comprehensive of the working principles and failure mechanisms of cathodes in LIBs, as well as commonly used modification strategies[23]. Investigating modification strategies for cathode materials under high voltage is crucial for the development of LIBs. By optimizing the lattice structure and surface coatings of cathode materials, it is possible to enhance the specific capacity, reliability, and cycling lifespan of LIBs. This is important for the progress of lightweight portable equipment and advanced energy storage research, providing strong support for the efficient application of sustainable energy and driving the clean energy revolution.

This thesis focusses on layered LCO cathode material, which thoroughly investigate the working and failure mechanisms of LCO under high voltage. Moreover, possible targeted modification strategies are provided for each issue so that scientists can solve these issues and work toward modern advanced batteries. In this thesis, three appropriate modification strategies (co-doping, surface coating and multifunctional modification) are employed to develop LCO cathode materials with high cycling durability under high voltage of 4.6 V.

1.3 Synopsis of thesis

As a layered metal oxide cathode, LCO exhibits stable charge/discharge voltage plateaus, high tap density, high energy density, and exceptional electrochemical cycling durability, establishing it as the leading commercial cathode material currently available. However, research on high-voltage LCO is limited. To achieve stable operation of LCO batteries at 4.6 V, further efforts and research are necessary. This thesis focuses on the study of high-voltage LCO cathode, and the objectives are listed:

(i) Optimization of bulk and surface doping: Enhancing the stability of the internal and external crystal structures by combining multi-element doping, bulk doping, and surface doping to mitigate structural phase transitions under high-voltage. This approach ensures stability in both bulk and surface crystal structures.

(ii) Development of efficient protective coatings: Developing and implementing effective protective coatings to minimize the interaction between the cathode surface and organic electrolyte. This action helps stabilize the lattice oxygen and cobalt dissolution on the surface while reducing the involvement of unstable lattice oxygen in the oxidative decomposition of the organic electrolyte. Consequently, this enhances the stability of the cathode structure and hinders the formation of detrimental gases.

(iii) Development of functional surface structural design: Functional surface structural design provide multiple effects, including physical isolation and enhancement of interfacial charge transfer, stabilization of Li^+ ion transport pathways, and collection

of surface-unstable lattice oxygen. These structural designs offer new modification directions for high voltage LIBs.

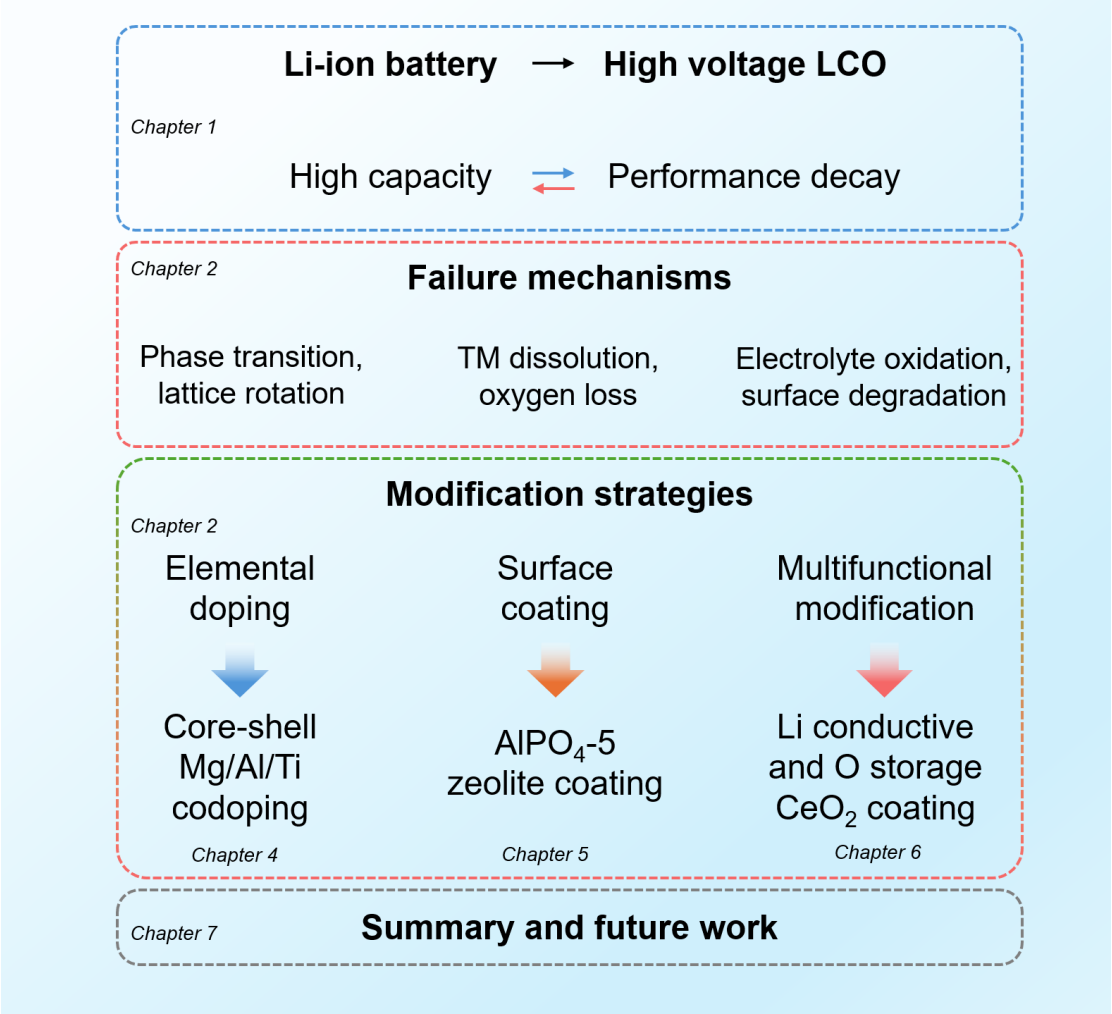

Figure 1.2 Synopsis of thesis.

As shown in **Fig. 1.2**, through understanding their working mechanisms, failure mechanisms, modified strategies, and enhanced performance. The high voltage LCO modified by three different methods have been discussed. The followings are the contents of this thesis:

Chapter 1: This chapter provides a brief overview of high-voltage LIBs, outlining the

research motivation and scope, and summarizing the thesis synopsis.

Chapter 2: This chapter provides a concise introduction to the evolution of LIBs, summarizes the failure mechanisms, and outlines common strategies. The urgent need and challenges for modifying the high voltage LCO cathode have been discussed.

Chapter 3: The experimental methods employed in this thesis are outlined.

Chapter 4: This section presents a simple two-step multi-element co-doping strategy to fabricate core-shell structured LCO. By considering for the varying diffusivities of different dopant ions, core-shell structured LCO can effectively alleviate lattice distortion under high-voltage.

Chapter 5: This section presents a multifunctional $AlPO_4$-5 zeolite coating with unique porous structure for developing high voltage LCO cathode. The $AlPO_4$-5 zeolite serves as a protecting layer over LCO, enabling fast Li^+ diffusion and accelerating the Li^+-desolvation.

Chapter 6: This section presents a novel cathode called CeO_2 interspersed massage-ball-like LCO. CeO_2 nanoparticles play a crucial role in facilitating Li^+ conduction and contribute to maintaining the reversibility of the lattice oxygen.

Chapter 7: This section summarizes the series work about high voltage LCO cathode. Proposed future work includes further exploration of modified strategies for high voltage and durable LIBs.

Chapter 2 Literature review of high voltage LCO cathode for Li-ion batteries

2.1 Overview of Li-ion batteries

Global carbon neutrality is a crucial issue that must be considered in human development. Against this backdrop, reducing greenhouse gas emissions and exploring sustainable energy storage devices have become hot topics. The advent of the Internet of Things (IoT) has further propelled in-depth research on rechargeable batteries, particularly in the context of portable equipment like mobile phones, laptops, and power tools, as well as the popularity of electric vehicles. Rechargeable LIBs have become indispensable components in portable electronic products and the most reliable energy storage method in current new energy electric vehicles. They have greatly facilitated the development of the 21st century, meeting the ever-growing demand for "mobile intelligent lifestyles". Rechargeable LIBs are pivotal in realizing a more sustainable future and are integral as the next generation of green energy. To enhance the battery life of portable devices, the most effective strategy is to increase the battery's charge cut-off voltage without increasing costs. Therefore, urgent research on high-voltage cathode materials is imperative.

2.1.1 Development of modern Li-ion batteries

The commercialization of rechargeable batteries is a necessary condition for the social development of modernization. In 1991, Sony commercialized LIBs, introducing them to the public, and $LiCoO_2$ (LCO) has since become widely used as the mainstream cathode material[12]. Significant efforts have been directed towards the creation of novel cathode materials[24, 25]. Diverse varieties of cathode materials have been engineered, like $LiFePO_4$[26], $LiMn_2O_4$[27], $LiNi_{1-x-y}Co_xMn_yO_2$ (NCM)[28, 29], $LiNi_{0.5}Mn_{1.5}O_4$[30] and $LiNi_{0.80}Co_{0.15}Al_{0.05}O_2$ (NCA)[31]. These cathode materials have found extensive application in different fields of modern society based on their respective characteristics. Among these, $LiMn_2O_4$, $LiFePO_4$, NCM, and NCA have found extensive application in new energy electric vehicles (EVs) and smart energy storage systems. As shown in **Fig. 2.1**, $LiMeO_2$ composition represents a broad system where the cathode material exhibits different crystal structures and charge/discharge properties by substituting transition metal (Me) ions[20]. Among various cathode materials, LCO possesses several unique performance benefits, such as high Li^+ ion/electron conductivity, high density, exceptional cycle life, and notable safety and reliability. It is these remarkable attributes that have solidified LCO as the primary cathode material in the portable electronics market[19].

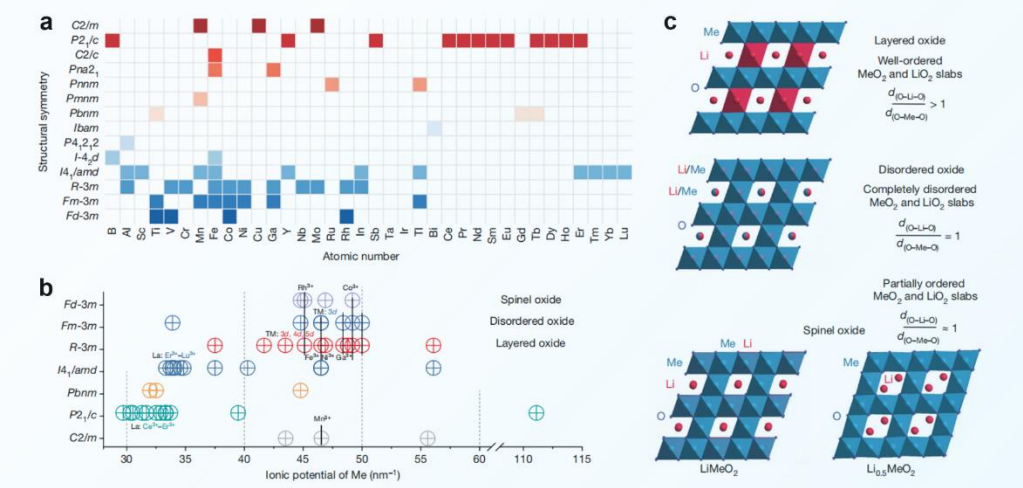

Figure 2.1 Structural symmetry of $LiMeO_2$ compositions. **b** Ionic potential of Me ions. **c** Structure transformation in layered, disordered and spinel oxides[20].

Despite the cost advantage of ternary NMC cathode in the market, LCO still dominates the current mainstream portable devices such as smartphones, laptops, wearable smartwatches, and drones. This is because LCO possesses a single-crystal structure, which yields a higher volumetric energy density in comparison to other commercial cathode materials, and compact size is a decisive advantage for portable devices. The daily lives of people are closely intertwined with LIBs, making battery lifespan and available capacity major areas of research and development focus. To achieve lightweight LIBs, further improvement of the reversible capacity of LCO cathodes is crucial. Taking LCO as an example, it can only deliver approximately 140 mAh g^{-1} capacity under the currently mainstream charging cut-off voltage of 4.2 V. This means that half of the Li^+ ions remain unutilized and are still stored in the CoO_2 lattice. Researchers have found that by elevating the upper cut-off voltage during charging, LCO exhibits significant potential for further enhancing energy density[32].

Considering the ultra-high tap density of LCO single crystals, LIBs employing LCO exhibit superior volumetric energy density, which is a crucial benefit for portable device power sources. Therefore, LCO has tremendous potential to become the cathode material for future lightweight mobile power sources.

Single-crystal LCO, with its low specific surface area and high mechanical strength, can effectively minimize surface side reactions and enhance battery energy density. Large-particle single-crystal LCO with inert element doping stands out as a pivotal technological strategy for amplifying the volumetric energy density and electrochemical performance. Inert element doping can effectively suppress the phase transition under high-voltage, thereby increasing the material's reversible capacity. Surface coating can reduce surface side reactions and structural transformations during charge and discharge processes, maintaining the layered structural stability. In addition, large-particle single crystals can markedly enhance the packing density.

As sustainable energy storage devices, LIBs play a greater role in future application scenarios beyond portable electronic devices. LIBs have potential to accelerate the process of sustainable development and modernization in smart societies. To meet the demand for green sustainable energy, in-depth research on the working principles, failure mechanisms, and optimization of battery configurations becomes crucial. Through fundamental research, scientists are dedicated to exploring green and efficient new materials to achieve higher capacity and better stability while saving costs and simplifying the manufacturing process.

2.1.2 Composition of Li-ion batteries

LIBs, which have reached a mature stage, consist of several fundamental components, and their configuration has remained largely unchanged over the past few decades. A typical battery comprises a cathode material, anode material, separator, and electrolyte (**Fig. 2.2**). Layered metal oxide cathodes are commonly used as the cathode material, while graphite is employed as the anode material. These electrodes are segregated by a porous separator.

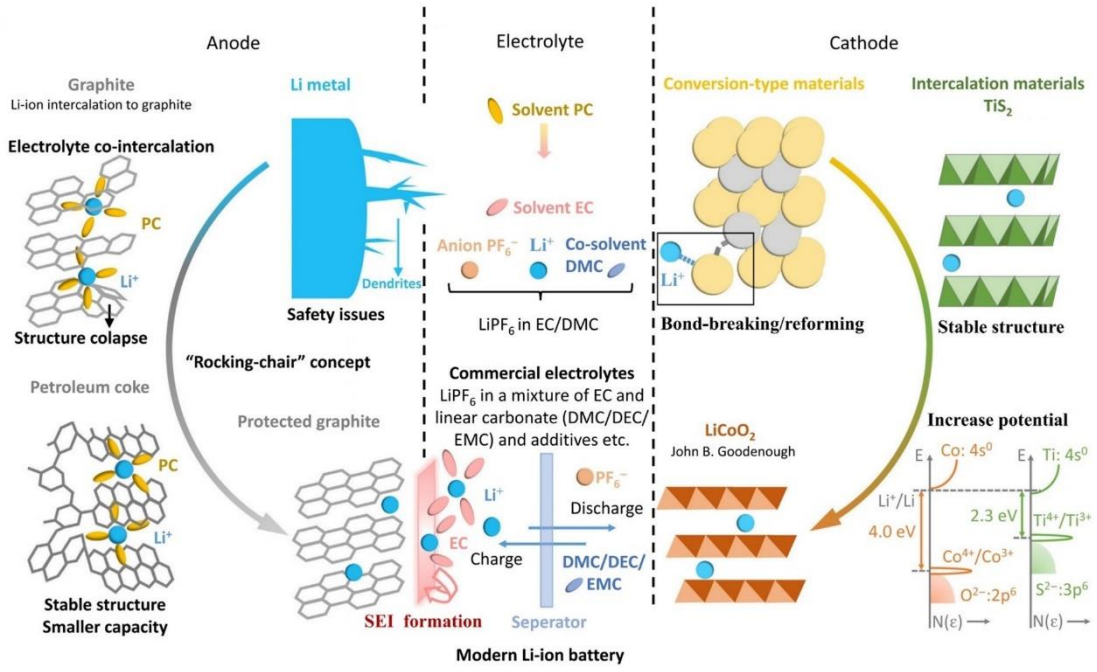

Figure 2.2 Composition of the modern LIBs[8].

While charging, Li^+ ions shift from the cathode and intercalate within the graphite layers, forming Li compounds (typically denoted as LiC_6). Conversely, while discharging, Li^+ ions detach from the graphite layers and shift back to the cathode material. This insertion/extraction of Li^+ ions are reversible processes within an

appropriate working voltage range. However, operating the cathode under higher voltage often leads to more profound insertion/extraction of Li^+ ions, potentially causing irreversible impacts on the electrochemical performance of LIBs.

Anode

Compared to other metals, Li can store more charge in the same volume. Additionally, the lower electrode potential of Li has made it possible to develop rechargeable batteries that surpass high voltage limitations. Nonetheless, the advancement of high voltage LIBs encounters challenges due to the behavior of Li metal under high-voltage. Li metal is highly reactive and susceptible to surface reconstruction during cycling, culminating in the creation of Li dendrites. Excessive Li dendrites can penetrate the separator, causing short circuits between the positive and anode materials, significantly impacting the cycle life, safety, and reliability of LIBs.

To address the high cost and surface reconstruction issues associated with pure Li metal electrodes, researchers initially introduced graphite as the anode. Research outcomes underscored the efficacy of graphite as anode, owing to its layered structure facilitating the easy insertion/extraction of Li^+ ions. Furthermore, the interaction between the orbitals of graphite and Li reduces volume expansion upon Li^+ insertion and hinders the proliferation of surface Li dendrites during cycling. Therefore, graphite, known for its high safety profile and cost-effectiveness, emerged as the classical anode material and has been widely used to this day. However, graphite anode materials also face some challenges. During the initial cycles, some Li^+ ions

may remain trapped within the graphite electrode, resulting in lower coulombic efficiency of the battery. To maintain high coulombic efficiency, commercial graphite electrodes often require prelithiation. Additionally, the electrolyte oxidative decomposition and the Co dissolution from cathode under high-voltage lead to the creation of a solid electrolyte interphase (SEI) on the anode material surface, ultimately precipitating the collapse and failure of the graphite structure. Therefore, to achieve high voltage LIBs, further research on the failure mechanisms of anode materials and the implementation of modification strategies are necessary.

Cathode

Cathode materials are pivotal components in LIBs. Traditional cathode materials include metal fluorides, sulfides, and others, enabling the extraction and insertion of Li^+ ion. However, their unstable lattice structure limits the long-term cycling durability of LIBs. During cycling, bond breakage and reformation lead to rapid structural deterioration and capacity decay. Materials with layered structures hold great potential as cathode materials due to their lower Li^+ ion migration barriers. In 1974, Whittingham developed TiS_2/Li batteries, significantly improving the cycling durability of LIBs. However, their operating voltage was limited to 2.5V, greatly restricting the battery's energy density. To achieve higher energy density, researchers have continuously explored cathode materials capable of supporting high voltage operation. Inspired by layered structure materials, Goodenough invented LCO, also known as LCO, in 1980. LCO exhibits excellent compatibility with Li metal under

voltage above 4V and maintains good cycling durability. The invention of LCO marked the beginning of a new era for LIBs and r continues to be among the most utilized cathode materials in portable electronic equipment. Building upon LCO, researchers have formulated a range of layered transition metal oxides for LIBs. These layered oxides possess high capacity and volumetric energy density, making them one of the most popular cathode materials to date. LCO electrodes are now widely applied in portable energy storage, within many portable electronic devices.

Electrolyte

Electrolytes are integral to LIBs as their electrochemical window is defined by the energy band positions of the highest occupied molecular orbital (HOMO) and the lowest unoccupied molecular orbital (LUMO). The voltage should fall within the range between the HOMO and LUMO to prevent oxidation reactions in cathode and reduction reactions in anode. Currently, the mainstream electrolyte for LIBs involves dissolving $LiPF_6$ in a solvent such as EC and a combination of DMC, DEC, or EMC. Different solvent ratios are suitable for different application scenarios. Experimental evidence demonstrates that the use of EC significantly improves the stability of graphite electrodes, making it an indispensable solvent in electrolytes of LIBs, often used in combination with different ratios of DMC/DEC/EMC and other solvents. During cycling, the electrolyte forms a SEI on the graphite surface, which contains a high fluorine content. This SEI product facilitates the expansion of the electrochemical window of the electrolyte and further suppresses electrolyte

degradation between the cathode and anode.

As the ongoing evolution of LIBs, there is a constant drive to achieve higher specific capacity, resulting in an increase in charge cut-off voltage. However, the electrolyte undergoes oxidative decomposition reactions on the surface of cathode under high-voltage. With increasing cut-off voltage, the organic components EC and $LiPF_6$ in the electrolyte experience more severe oxidative decomposition reactions, resulting in the creation of a thicker SEI film and gas generation. Additionally, a significant amount of Co dissolves and permeates through the separator, depositing on the anode surface and disrupting the original SEI at the anode, further promoting continuous electrolyte decomposition reactions. Therefore, the preparation of stable and thin SEI is an area of focus for researchers. Designing these thin, inherent protective layers and studying their protective mechanisms are pivotal for the advancement of high-voltage LIBs.

2.1.3 Urgent need for high energy density

The daily lives of people are closely intertwined with LIBs, making battery lifespan and available capacity major areas of research and development focus[14]. Due to the higher tap density brought by the single crystal structure, LCO still dominates the current mainstream portable devices such as smartphones, laptops, wearable smartwatches, and drones. In contrast to other commercial cathode materials, the single-crystal structure of LCO results in higher volumetric energy density and smaller cathode volume.

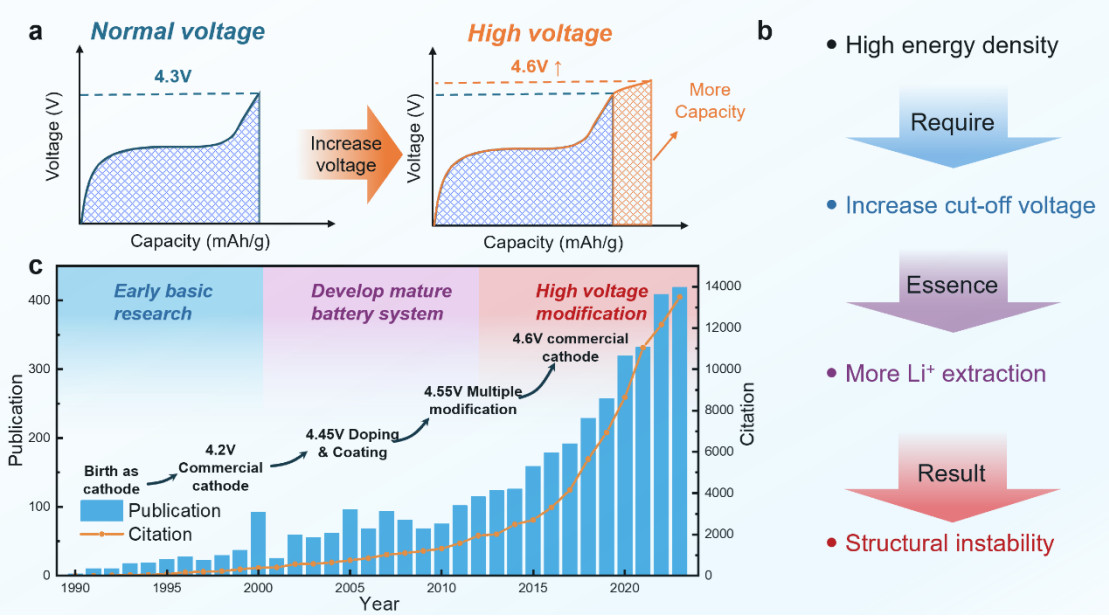

Figure 2.3 a The high-voltage bring more capacity. **b** High-voltage result in structural instability. **c** Distribution of citation and publication of LCO study from 1990 to 2023. The data is from Web of Science, the search topic include “battery” and “LCO”.

As shown in **Fig. 2.3**, research on LCO as a cathode material for LIBs has undergone exponential growth since its birth. It has evolved from early basic research to the development of mature battery systems and, more recently, high-voltage modifications. To achieve lightweight LIBs, further improvement of the reversible capacity of LCO cathodes is crucial. Taking LCO as an example, it can only deliver approximately 140 mAh g^{-1} capacity under the currently mainstream charging cut-off voltage of 4.2 V, which means that half of the Li^+ ions remain unutilized and are still stored in the Li_xCoO_2 lattice[18]. Given the current infrastructure, elevating the charge cut-off voltage stands out as the most efficient method to enhance capacity, which means the cathode material will undergo deeper Li^+ ion insertion and extraction

processes. The charging cut-off voltage continues to increase over time. While elevating the upper charging cut-off voltage, LCO exhibits significant potential for further enhancing energy density[32]. Therefore, LCO has tremendous potential to become the cathode material for future lightweight mobile power sources.

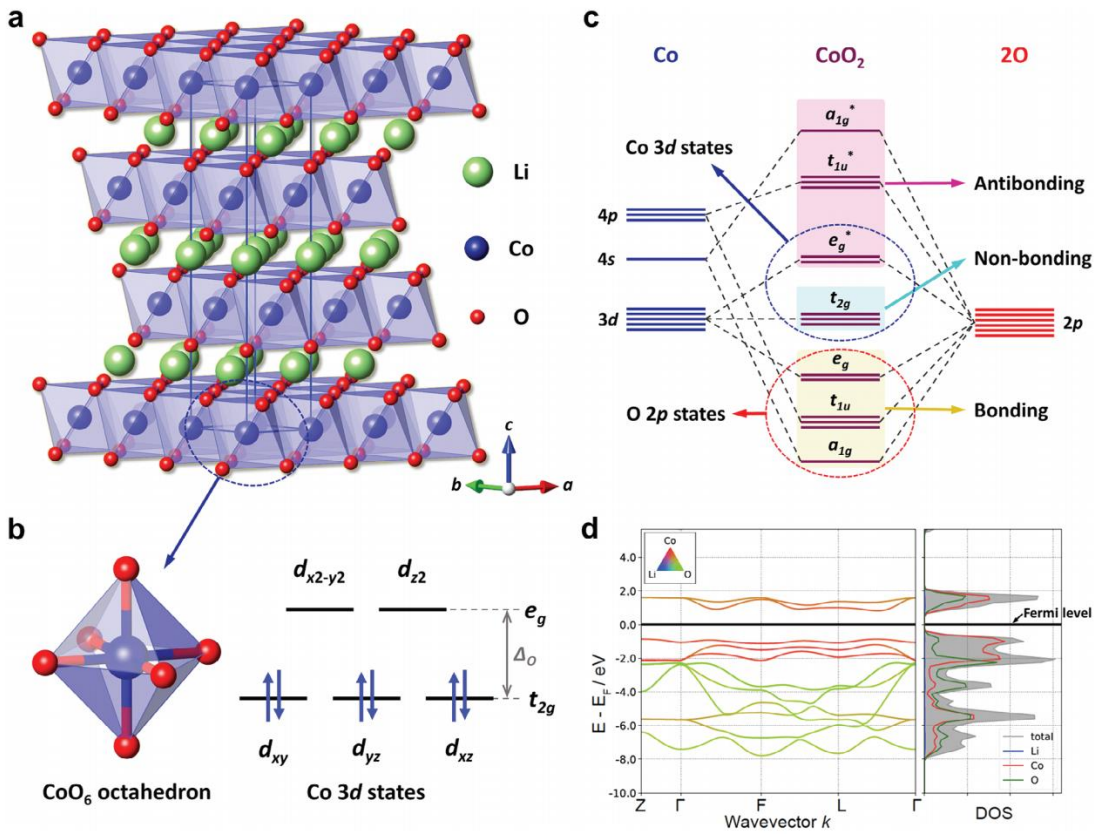

Figure 2.4 a Layered lattice structure of LCO. **b** CoO_6 octahedron structure and Co^{3+} 3d states. **c** Molecular orbital diagram for CoO_2. **d** Electronic structure and density of states (DOS) of LCO[33].

For LIBs, the LCO cathode material undergoes Li deintercalation and intercalation processes during long-term charge and discharge cycles. As shown in **Fig. 2.4**, LCO possesses an α-$NaFeO_2$-type layered structure. During the charging process, as the

working voltage gradually increases, Li^+ ions are continuously extracted from the LCO. LCO experiences five phase transitions state from the O3 (H1, H2, M1, H3) to H1-3 and O1 phases[18]. Within the low voltage charging range, transitions occur between the H1, H2, M1, and H3 phases, and although the unit cell parameters change between these different phases, there is good reversibility between adjacent phases. During this multiphase transition, LCO maintains its O3 structure without interlayer sliding. However, with further increase in charging voltage, phase transitions from H3/H1-3 (4.55V) to H1-3/O1 (4.64V) occur, exhibiting poorer reversibility due to significant anisotropy. Particularly, throughout the phase transition from the H3 to H1-3/O1, the rate of contraction along the c-axis intensifies, resulting in a notable reduction in the lattice volume. The sliding of CoO_2 layers and drastic lattice changes further increase stress accumulation. Moreover, during high-voltage cycling, harmful phenomena contribute to the further degradation of the stability of LCO. These detrimental processes interact and accelerate surface fractures in LCO. Enhancing the performance and longevity of LIBs necessitates additional research and enhancements in the design and preparation techniques of LCO cathode materials. These efforts aim to enhance their structural stability and cyclic performance while reducing stress accumulation and side effects of electrochemical reactions.

With the popularity of electric vehicles and the development of portable electronic equipment like laptops, smartphones, and wearable electronics, the demand for high-performance energy storage devices become urgent. Particularly with the advent of

the 5G era, mobile phones require faster processing and transmission speeds, posing challenges for energy storage batteries in terms of small capacity, short battery life, and slow charging. To address these issues, there is a need to develop new high-performance LIBs with high energy density, high power density, and long cycle life characteristics[22]. Currently, the development of LIBs for 3C applications mainly focuses on improving their volumetric energy density and rate capability while ensuring safe operation. Enhancing the battery's capacity is the primary task to meet the increasing demand for portable electronic devices[34].

2.2 Failure mechanisms of LCO cathode

Operating LIBs under high-voltage conditions enables higher reversible capacity and energy density. Nonetheless, it is also accompanied by accelerated performance degradation. Researchers have been exploring the failure mechanisms under high-voltage in recent years[23, 35]. As shown in **Fig. 2.5**, from a viewpoint of LCO cathode, the failure mechanism of LIBs under high voltage mainly involves three main aspects: (1) Phase transition and lattice rotation, (2) TM ion dissolution and lattice oxygen loss, (3) Electrolyte oxidation and surface degradation.

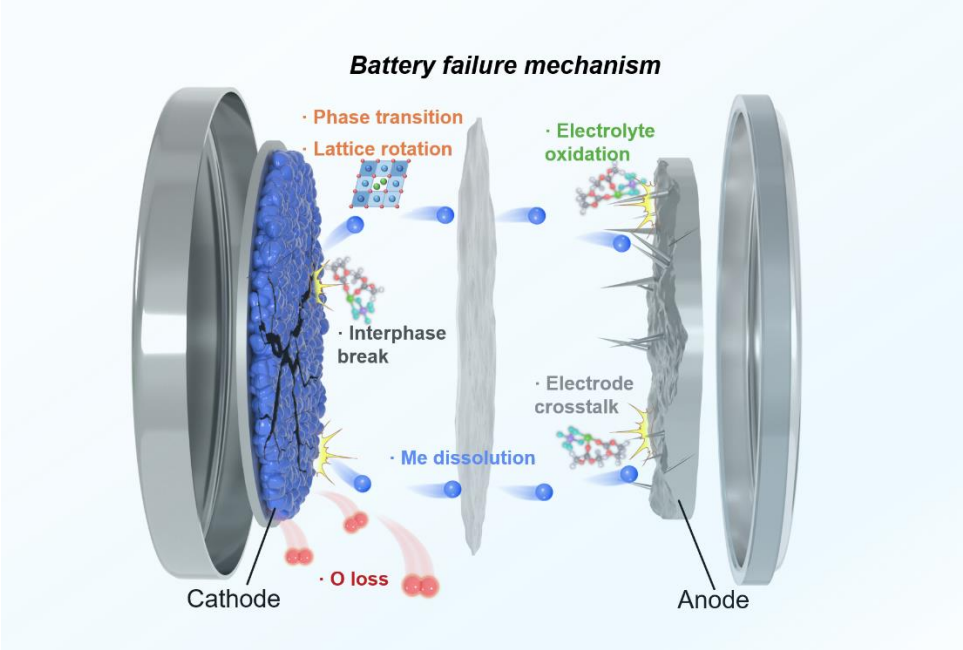

Figure 2.5 Schematic diagram of the failure process of LIBs as LCO cathode under high-voltage.

Firstly, the failure mechanisms of phase transition and lattice rotation are addressed. During the Li^+ ion de-intercalation process, LCO undergoes complex structural phase transitions accompanied by significantvolume changes, leading to particle cracking

and rapid decay of reversible capacity[36]. Secondly, the failure mechanisms of TM ion dissolution and lattice oxygen loss are discussed. High-voltage result in the instability of the LCO, causing Co^{2+} ions dissolution. Additionally, unstable O atoms on the surface undergo continuous oxidation under high-voltage, resulting in the O_2 release and structural degradation[37]. Thirdly, the issue of interfacial side reactions and surface degradation is addressed. Under high voltage, the oxidation reactions ocuur between the organic electrolyte and the LCO surface. The detrimental side reactions lead to the electrolyte oxidation, surface degradation, and deposition of cathode-electrolyte interphase (CEI). Simultaneously, a continuously growing CEI forms at the interfaces, resulting in irreversible surface structural deterioration. The impedance growth in LCO cathode under high-voltage conditions is intricately linked to surface degradation and the buildup of the CEI layer[38]. Understanding these failure mechanisms can provide guidance for improving cathode material design and enhancing battery performance.

2.2.1 Phase transition and lattice rotation

As shown in **Fig. 2.6a**, the structural evolution of LCO during the charging process can be segmented into two distinct regions[18]. In the low-voltage region ($0.45 \leq x \leq 1$), LCO undergoes solid solution reactions and three weak first-order phase transitions[39]. The first phase transition occurs within the range of x = 0.93−0.75 and is typically ascribed to the electronic delocalization. As Li^+ ions are further deintercalated, the electronic characteristics of LCO transform from semiconductor to metal. The other

two-phase transitions occur near x = 0.5, and as Li^+ ions are deintercalated, the structure undergoes a transformation from hexagonal to monoclinic and then back to hexagonal phase. The monoclinic phase transition is typically associated with structural damage, which is also a contributing factor to capacity loss when the voltage exceeds 4.2 V[40].

In the high-voltage region (x < 0.45), with further deintercalation of Li^+ ions from LCO in a highly delithiated state, a phase transition occurs from the O3 phase to the H1-3/O1 phases[41]. The H1-3 structure is considered a mixed structure of O1 and O3. Throughout the transition from O3 to H1-3, Li rearrangement leads to sliding of the O-Co-O layers, triggering internal stress and structural breakdown. Jiang et al. have conducted in-depth studies on the failure mechanism induced by phase transition of LCO by increasing the voltage above 4.7 V[16]. They found that irreversible bulk structural changes are the main cause of capacity loss. They observed the formation of stripe-like distribution of the O1 phase along grain boundaries in LCO during cycling under high-voltage, further triggering irreversible bulk structural transformations. Additionally, throughout the charge-discharge cycles, the drastic changes in the *a* and *c* dimensions of the unit cell led to interlayer sliding, mechanical fracture of the bulk structure, and the formation of microcracks[36]. These phase transitions accompanied by structural evolutions, have a pivotal influence on the capacity decline and performance deterioration of LCO. A profound comprehension of these failure mechanisms holds immense importance in enhancing the design and efficacy of LIBs.

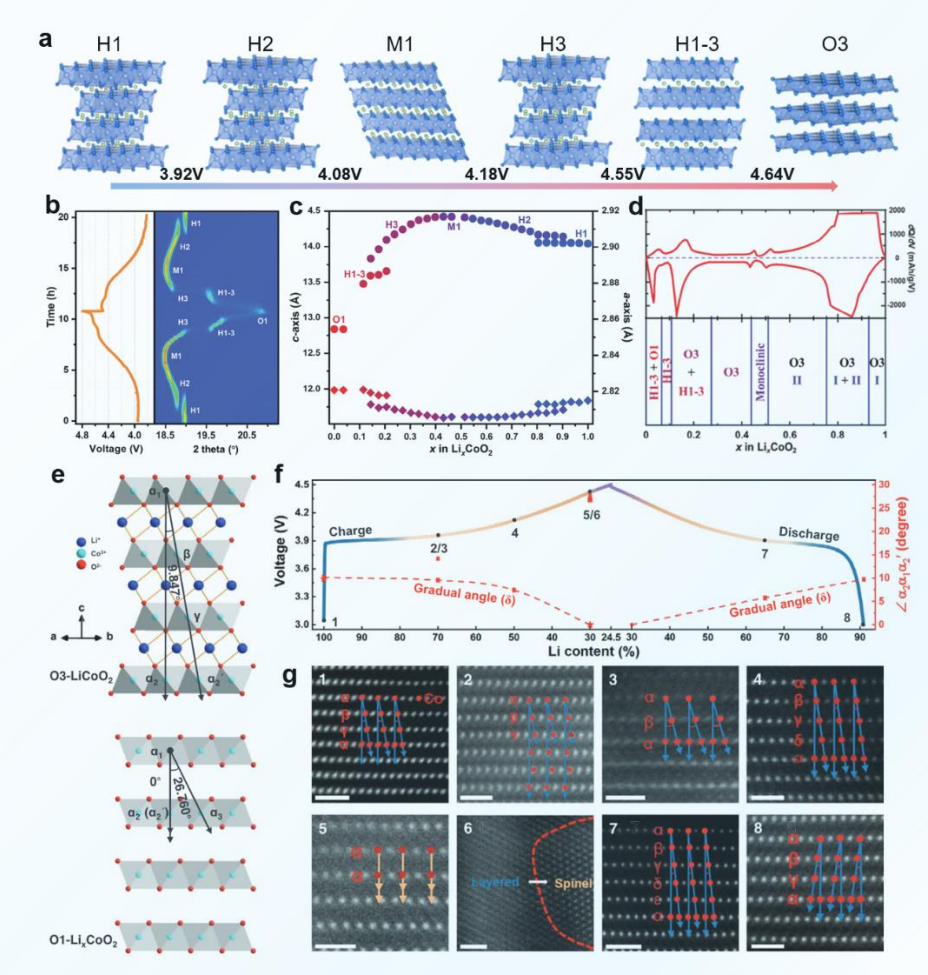

Figure 2.6 a The structure changes of LCO with varying degrees of Li^+ extraction. **b** *In-situ* X-ray diffraction (XRD) analysis of (003) peak[42]. **c** Variation of *c*- and *a*-axis dimensions, and **d** corresponding structure[18]. **e** Structural illustration of O3 and O1 phase. **f** Electrochemical profiles showing O3, O1, and rock-salt structure regions. **g** Corresponding states of transmission electron microscope (TEM) images in **f**[21].

The LCO thin film was used to investigate the failure mechanisms resulting from phase transitions, while eliminating the interference of conductive carbon and binders on the cathode material[43]. The relationship between the electrochemical behavior and structural phase transitions was analyzed above 4.2 V. The LCO thin films exhibited

good cycling durability when the charging cut-off voltage was set at 4.5 V. Nevertheless, the cycling durability witnessed a rapid decline once the charging cut-off voltage exceeded 4.6 V. These experiments demonstrated that the phase transition range below 4.5 V is reversible and has almost no impact on the reversible capacity[44]. When the degree of Li^+ ion deintercalation x is less than 0.4, further delithiation causes a rapid decrease in the Li^+ ion diffusion coefficient of LCO. This is because the lower lattice spacing in the H1-3 and O3 phases (**Fig. 2.6b-d**) requires Li^+ ions to overcome higher activation barriers for diffusion. Therefore, the Li^+ ion diffusion capacity of LCO is limited when $x < 0.4$. Additionally, long-term cycling under high-voltage results in irreversible structural damage on the surface of LCO thin films. This could be attributed to phase transitions and stress under high-voltage. This structural damage further impacts the cycling durability of LCO.

As shown in **Fig. 2.6e-g**, based on the experimental findings, it is evident that the bulk phase structure of LCO undergoes notable alterations when the charging cut-off voltage exceeds 4.5 V. Although there is no immediate drastic capacity degradation after extensive delithiation, long-term volume variations and stress accumulation can lead to structural damage, particularly in the structural changes occurring at 4.2 V in the monoclinic phase and 4.55 V in the H1-3 phase, resulting in collapse and formation of cracks in the bulk phase structure, thereby reducing cycling durability. Several studies have confirmed that when LCO exceeds 4.55 V, an O3 to H1-3 phase transition occurs, causing severe volumetric contraction and greatly increasing the

possibility of bulk phase structure deterioration. Additionally, surface phase transitions serve as another mechanism for interface degradation. Upon deep delithiation of LCO, an irreversible phase transition (disordered spinel structure). The thickness of the irreversible phase domain expands with both cycling voltage and the number of cycles. For instance, the thickness of the irreversible phase domain doubles with a charging cut-off voltage of 4.55 V, in contrast with that of the cut-off of 4.4 V. Li et al. have discovered that under high-voltage, as soon as LCO contact with the electrolyte, the Co^{3+} on the surface undergoes immediate reduction to Co^{2+}. Charging to high-voltage exacerbates local distortions on the surface structure, which subsequently propagates to the interior[45]. Therefore, inhibiting the detrimental phase transition at 4.55 V is crucial, as it profoundly enhances the cycling durability of LIBs functioning under elevated voltage.

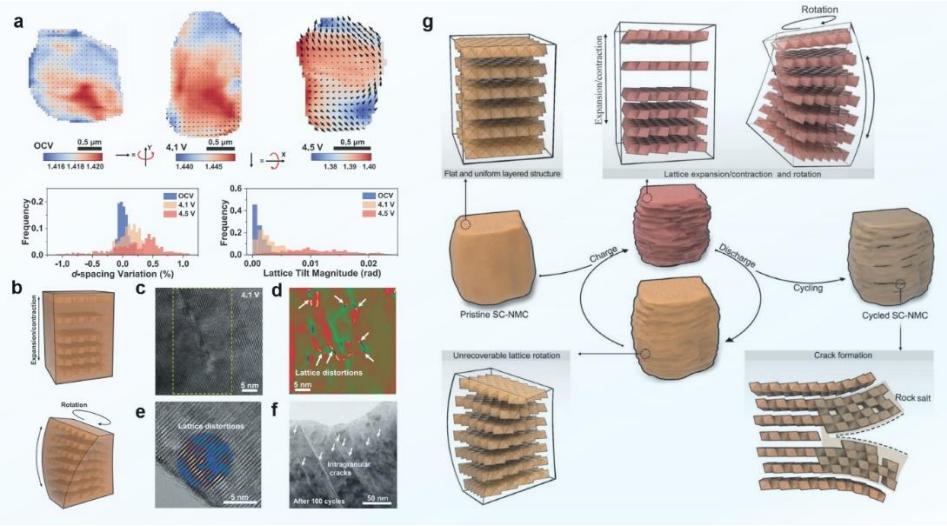

Figure 2.7 a Scanning diffraction x-ray microscopy (SDXM) scans capturing the (003) peak at open-circuit voltage, 4.1 V, and 4.5 V. **b** Diagram depicting lattice expansion

and contraction and lattice rotation. **c** TEM image at 4.1 V. **d** Strain state. **e** TEM images at 4.3 V. **f** TEM images after 100 cycles. **g** Diagram depicting the structural degradation of cathodes[46].

In addition to phase transition, Huang et al. observed that rotational lattice distortion in single-crystal cathodes is a key factor contributing to electrode failure[46]. As show in **Fig. 2.7**, the lattice rotation is associated with defect formation. The buildup of unrecovered lattice rotations throughout charge-discharge cycles culminates in morphological and structural deterioration of single-crystal grains, ultimately leading to irreversible mechanical breakdown. Uncovered lattice rotation triggers irreversible structural degradation, including microcracks, irreversible phase transitions, and surface structure deterioration, culminating in a profound decline in electrochemical performance. The existence of lattice rotation and lattice strain in charge-discharge electrochemical reactions is inevitable, highlighting the importance of mitigating lattice rotation to improve the stability of single-crystal cathode and prevent rapid capacity degradation.

2.2.2 TM ion dissolution and oxygen loss

Throughout the charging and discharging process, LCO undergoes continuous Li^+ insertion and extraction, as well as repeated structural phase transitions. The surface structure of the cathode is relatively unstable in comparison to the bulk structure, with a significant number of dangling bonds. Notably, under high-voltage conditions, the cathode surface is prone to TM ion dissolution and oxygen loss, which is often the direct cause of surface structure degradation[42]. The surface structure and chemical alterations of the cathode wield a pivotal influence on the cycling durability of LCO. The Co dissolution and the oxygen loss have the potential to induce compositional changes, thereby affecting its electrochemical performance and structural stability[45]. These chemical evolutions can result in capacity decay, structural damage, interface failure, and ultimately a decline in battery performance. Therefore, investigating the mechanisms underlying surface structure and chemical alteration in cathode is significant for understanding the failure mechanisms of LCO during long-term cycling.

Tarascon et al. demonstrated in their study that no Co dissolution or capacity decay was observed during cycling at 4.2 V[47]. However, a significant amount of Co elements was observed under 4.5 V, highlighting a direct association among high-voltage, Co dissolution, and capacity diminution, as shown in **Fig. 2.8a, b**. The researchers hypothesized that cycling under high-voltage leads to corrosion on the surface, consequently initiating the dissolution reaction of TM ions, thereby affecting

the interfacial reactions between the cathode and anode[45, 48]. The chemical shuttle reaction of TM cations from cathode to anode lead to the accumulation of TM ions at the anode, which affects the normal insertion and extraction of Li^+ ions, resulting in slower Li^+ ion kinetics[49].

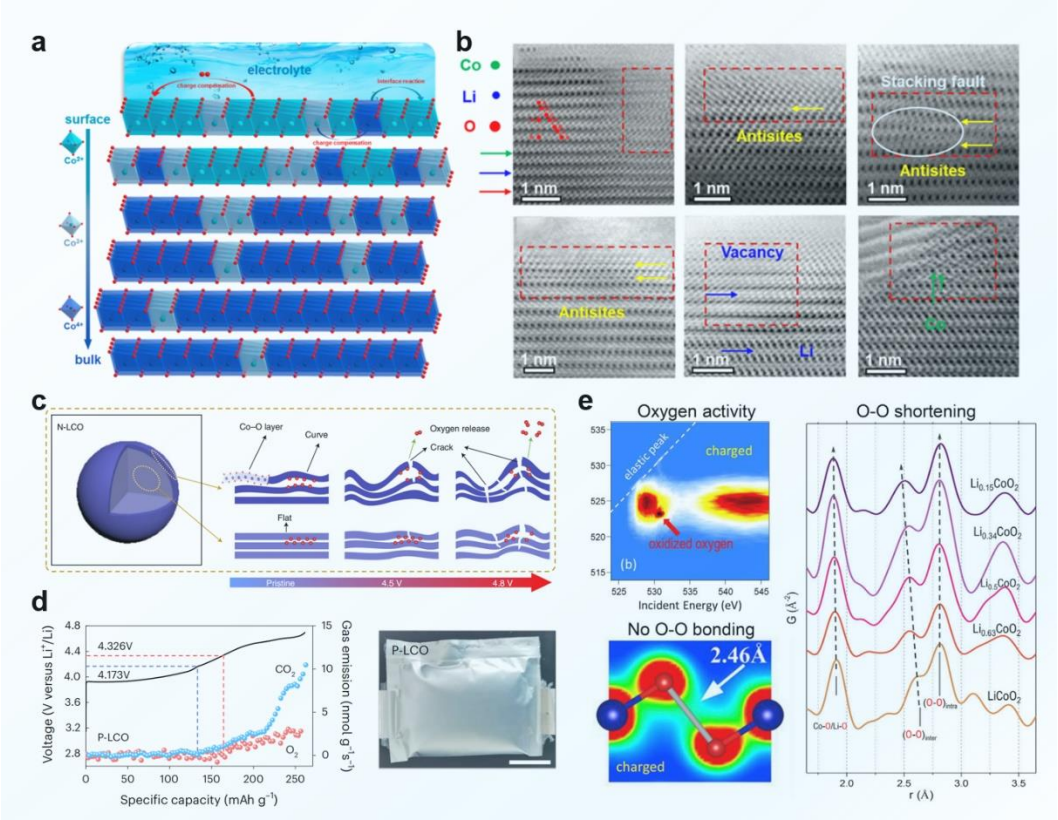

Figure 2.8 a Diagram depicting the surface Co distribution near surface under high-voltage. **b** Scanning transmission electron microscopy (SEM) bright-field images of cycled LCO at different state of charge (SOC)[45]. **c** Schematic illustration of the LCO structural evolutions during charge[42]. **d** *In-situ* differential electrochemical mass spectrometry (DEMS) profiles of LCO and photos of LCO pouch cells after 100 cycles[50]. **e** Mapping of resonant inelastic X-ray scattering of LCO at highly charged state[51].

During extended cycling, Co dissolution results in the creation of a CEI layer, surface structural corrosion chambers, and surface resistance layers. The direct Co dissolution contributes to the loss of active materials in LCO, which is a primary cause of rapid capacity decay. Additionally, a series of surface byproducts hinders Li^+ ion diffusion kinetics. Under high-voltage conditions, as Li^+ ions deintercalate, a partial conversion of Co^{3+} to Co^{4+} occurs to maintain charge balance. The highly active Co^{4+} interacts with the surface peroxide products, further exacerbating the chemical evolution of the cathode. The direct contact between the electrolyte and the cathode under high-voltage leads to Co dissolution and oxygen loss, typically observed as rapid capacity decay in the initial cycles under high-voltage. Therefore, the advancement of high-voltage cathode and the minimization of the contact area between the electrolyte and cathode material become imperative. This approach contributes to enhancing the stability of the surface structure and reducing the formation of additional byproducts.

Oxygen loss is a direct manifestation of surface structure degradation in LCO and one of the main causes of thermal runaway in cathode materials[52]. Above a certain voltage, such as 4.3 V, triggering the oxygen evolution reaction requires a certain overpotential. For LIB cathode, when the voltage exceeds 4.5 V, the surface layered structure becomes unstable as Li^+ ions are deeply extracted, and the lattice oxygen tends to further oxidize and release gaseous oxygen. Previous researches confirmed that the oxygen evolution in layered oxides arises from the overlap of oxygen 2p orbitals and TM 3d orbitals under high-voltage[53]. 4.5 V is the threshold voltage for oxygen release,

and exceeding this voltage renders the lattice oxygen of the cathode material highly unstable. As show in **Fig. 2.8c**, the bent surface structure further promotes the generation of oxygen gas[42]. Oxygen release not only leads to rapid cathode failure but also increases the production of a substantial volume of gas, thereby elevating the safety risks of the battery (**Fig. 2.8d**). Hu et al. explores the oxygen-redox reactions in LCO cathodes without O–O bonding during charge-discharge cycles, aiming to understand the reaction mechanism under high-voltage, including: the active involvement of oxygen in highly charged LCO, the absence of O–O bonding in significantly delithiated LCO, and the promise of achieving reversible deep delithiation for LCO-based electrodes (**Fig. 2.8e**)[51].

During long cycling, Zhou et al. also observed the formation of physical voids due to the local vacancy formation of O, indicating the formation of surface peroxides and the lattice oxygen release. Although the evolution process of lattice oxygen and the charge transfer mechanism of oxygen in the redox reaction are not fully understood[54], it is widely believed that the formation of peroxides and the release of oxygen gas caused by high-voltage disrupt the surface structure of LCO, leading to irreversible alterations in the surface structure and even the creation of spinel/rock-salt phases[55]. This results in increased interfacial transfer impedance and rapid capacity decay. Continuous oxidation of the unstable lattice oxygen in the high-valence state weakens the covalence between Co and O, further promoting the generation of undercoordinated oxygen. Therefore, preserving the lattice oxygen stability of the

surface structure is crucial for the development of high-voltage LIBs and high-temperature applications.

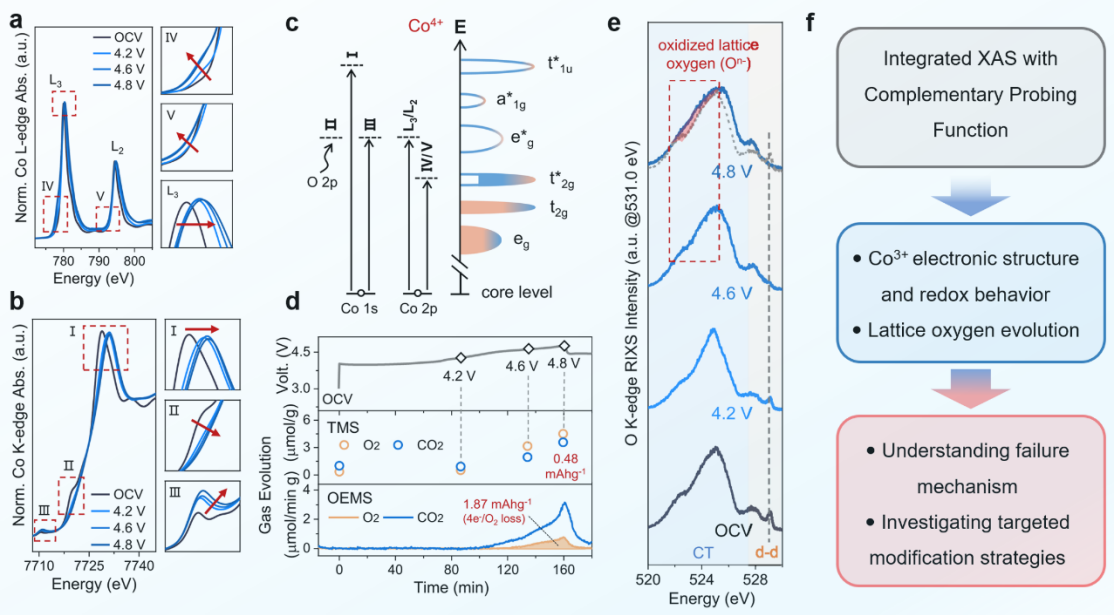

Figure 2.9 a *Co-L*$_3$ and **b** *O-K* edge XAS spectra. **c** *Co-K* edge/*L*$_3$ edge XAS result and corresponding electronic configurations of Co^{4+}. **d** Gas generation results for LCO. **e** Resonant inelastic X-ray scattering of *O-K* edge. **f** The workflow diagram of integrated XAS with complementary probing function[56].

Additionally, under high-voltage, the Co dissolution^{2+} and the release of O_2 further promote localized damage to the LCO structure, even forming isolated corrosion chambers near the surface. X-ray absorption spectroscopy (XAS) stands out as a potent tool for exploring the working mechanisms of rechargeable batteries, providing crucial insights into high-voltage failure mechanisms, electrode/electrolyte interfaces, and enhancement for surface modification[57-59]. As show in **Fig. 2.9**, XAS has been employed to monitor alterations in the electronic structure and redox behavior of the

cathode during cycling. Using XAS method to analyze the *O-K* edge with XAS enables a direct study of the evolution of lattice oxygen, while investigating the *Co-K* edge provides insights into the local coordination environment of Co. Those results show that the existence of a Li-deficient phase on the high delithiated LCO surface results in higher activation energy and ordered arrangement of vacancies, leading to sluggish Li kinetics. To observe the structural changes in LCO during the charging process more directly, Oh et al. employed TEM to examine LCO samples at different states of delithiation. During deep charging, Co partially migrates to Li sites, resulting in the creation of spinel/rock-salt phases. Inhomogeneous distribution of Li/Co and the emergence of an irreversible Co_3O_4 phase were observed on the surface structure of LCO[60]. The researchers concluded that under high-voltage, the fast capacity deterioration of LCO is linked to the irreversible spinel phase formation on the surface. When it comes to the redox reactions involving O^{2-}, the irreversible migration of Co leads to voltage hysteresis between charge and discharge, consistent with the electrochemical observation of hysteresis phenomena. Therefore, to reduce the impact of voltage hysteresis on disordered rock salt cathodes, it is important to suppress the irreversible migration of TM ions.

2.2.3 Electrolyte oxidation and surface degradation

The electrolyte serves as the transport medium between the anode and cathode in LIBs, facilitating the free movement of Li^+ ions through the separator. A comprehensive comprehension of the working and degradation mechanisms of the electrolyte is crucial for improving the cycling durability of LIBs.

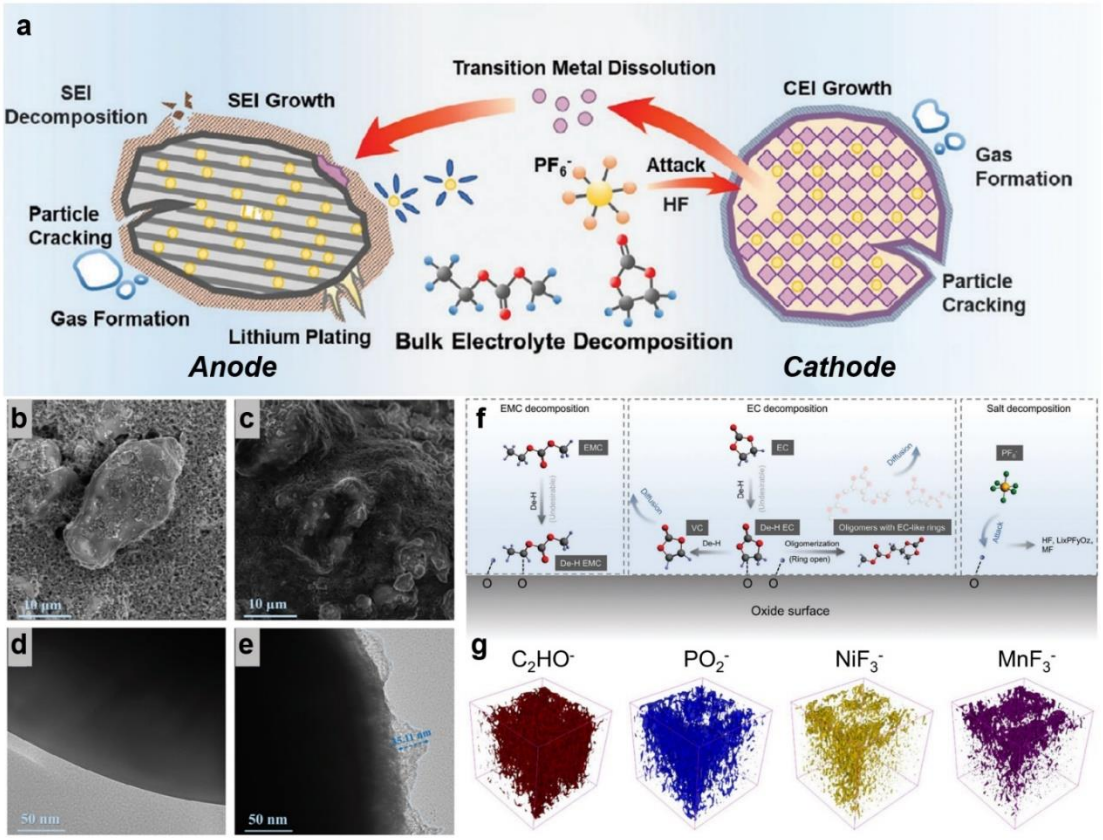

Figure 2.10 a Schematics illustrating the process of electrolyte degradation and the harmful effects of electrolyte degradation[61]. Morphology characterization of the **b**, **d** pristine LCO cathode and **c**, **e** after cycled under high-voltage[62]. **f** Proposed mechanism[38]. **g** 3D rendering TOF-SIMS fragments[63].

Fig. 2.10a summarizes the specific failure mechanisms of electrolyte oxidation and

decomposition within the anode and cathode. The oxidation process and failure mechanisms of the electrolyte can be categorized into three aspects: (1) the creation of fresh interfacial layers between the electrolyte and electrode surfaces, (2) the oxidative decomposition reactions of the electrolyte under high-voltage conditions, and (3) the detrimental effects of the degraded electrolyte on battery performance. The oxidation and decomposition reactions of the electrolyte directly impact the performance and lifespan of LIBs[64]. Therefore, it is important to understand the root causes and working mechanisms of electrolyte oxidation and decomposition.

As show in **Fig. 2.10b-e**, over the long-term cycling of LIBs, the electrolyte undergoes oxidation and reduction processes at the interfaces, leading to the creation of electrode/electrolyte interface layers. In traditional working environments, commercial electrolytes generally exhibit stable operation. However, with an increase in the charging cut-off voltage, traditional commercial electrolytes also encounter instability issues. The stability of electrolytes not only depends on the redox potential of the solvent but also on the interactions with other solvent molecules, electrolyte salts, and even electrode material surfaces. The failure process of electrolytes is a complex phenomenon influenced by multiple factors. Among these factors, the dissolution of TM ions and their catalytic reactions with the electrolyte play significant roles in electrolyte failure[65]. As show in **Fig. 2.10f**, with increasing voltage, the organic components (such as EMC and EC solvents) in the electrolyte undergo more severe oxidative decomposition reactions with salt ($LiPF_6$), resulting in the

creation of a thicker SEI film accompanied by gas generation[66, 67]. As the cathode operates over long-term cycling, the oxidative decomposition reactions continuously expose fresh LCO surface to the electrolyte, leading to ongoing cathode degradation. In this process, Co dissolves extensively, and Co ions under high-voltage exhibit certain catalytic activity, accelerating the continuous decomposition of the electrolyte[68]. The intense oxidative decomposition reactions of the electrolyte generate a significant amount of decomposition byproducts on the cathode surface. Additionally, because of the extensive Co dissolution, Co ions migrate across the separator and accumulate on the anode surface, disrupting the originally formed SEI and further promoting the continuous decomposition of the electrolyte[69, 70]. Therefore, these complex reaction processes collectively contribute to the failure of the electrolyte. Addressing this concern necessitates the development of more stable electrolyte systems and new electrolyte additives that suppress the dissolution and catalytic effects of TM ions, thereby reducing the decomposition reactions of the electrolyte and improving the battery's cycle life.

When designing a new LIBs system, it is crucial to consider not only the stable voltage of the cathode material and current collector, but also the electrolyte's stable operating voltage range. The working voltage range of the electrolyte is defined by the energy band positions of its LUMO and HOMO[71]. An excessive high or low potential can lead to electrolyte decomposition reactions. For the anode, if the electrochemical potential exceeds the LUMO energy of the electrolyte, a reduction

reaction occurs between the electrolyte and the anode. Similarly, for the cathode, if the electrochemical potential is lower than the HOMO energy of the electrolyte, an oxidation reaction takes place. In general, the SEI film on the anode and the CEI film can alleviate certain side reactions induced by the electrolyte. Therefore, the preparation of stable and thin SEI and CEI films is an area of focus for researchers. Designing these thin, intrinsic protective layers and studying their protective mechanisms are pivotal for the advancement of high-voltage batteries.

Directly observing the formation process and functioning mechanism of CEI films is challenging due to their instability in air. Dai et al. have conducted comprehensive studies on CEI films by investigating the electrochemical performance and surface chemical composition of cathode. As show in **Fig. 2.10g**, the time-of-flight secondary ion mass spectrometry (TOF-SIMS) results indicate that the capacity decay of cathode materials under high-voltage is mainly attributed to surface oxidation and decomposition reactions. When using traditional commercial electrolytes under high-voltage, the elevated voltage promotes oxidation and decomposition reactions of electrolyte. These reactions generate byproducts such as lithium fluoride and poly carbonate on the cathode surface, resulting in elevated interfacial impedance. This phenomenon becomes more severe with increasing cycle numbers and temperature. Numerous experiments have demonstrated that electrolyte oxidation and the creation of the CEI layer under high-voltage result in slower Li^+ ion diffusion kinetics, while the sustained surface oxidation state and exposure of fresh interfaces further

contribute to electrode degradation and more severe capacity loss[72, 73]. Although the CEI film significantly increases interfacial impedance, impeding the transport of Li^+ ions, the *in-situ* creation of CEI layer serves as a physical protective layer, limiting the interaction between the electrolyte and the cathode surface, thereby diminishing additional oxidation and decomposition reactions. Additionally, the oxidative decomposition reactions of the organic electrolyte itself are inevitable under high-voltage. Therefore, it is crucial to develop a CEI protective layer that safeguards the cathode surface, reduce impedance, and enhance Li^+ ion diffusion. For instance, electrolyte additives can be used during battery cycling. These additives facilitate the formation of a more durable and uniform CEI film. This high-quality CEI film can provide surface protection and enhance Li^+/electron kinetics, thereby improving the cycling durability of cathode materials under high-voltage. These investigations are critical for the advancement of high-voltage LIBs, as they help us better understand the interactions between cathode materials and electrolytes, optimize electrolyte systems, and interface engineering strategies to prolong the cycle life.

2.3 Modification strategies of high-voltage LCO

While increasing the charging cut-off voltage can enhance the battery's capacity, it also introduces numerous challenges associated with high-voltage. To address these failure issues, improving the cycling durability of LCO cathodes under high-voltage has become a focal point of research. Researchers have developed various modification strategies to enhance the performance of LCO cathode and have achieved significant progress under high-voltage. Recently employed modification strategies mainly include foreign-ion doping, surface modification, structural design, electrolyte additives, among others. In this section, our objective is to offer a comprehensive discourse on these strategies, highlighting their advantages and current research progress.

2.3.1 Foreign-ion doping

Foreign-ion doping is one of the most effective strategies for modifying crystal and electronic structures of layered cathode materials, and it has made significant research progress in recent years. By incorporating elements, the physical properties of the cathode material can be effectively controlled, including electronic structure, bandgap, charge distribution, and lattice parameters. Element doping has been utilized to occupy TM sites, thereby enhancing the material's conductivity and electrochemical potential. Additionally, by doping elements into Li sites, the pillar effect and stable transport of Li^+ ions in the material can be achieved, thereby enhancing the structural stability and electrochemical performance. Several factors need to be considered

during the doping process, including the type of dopant, doping concentration, doping sites, and doping methods.

As shown in **Fig. 2.11a**, appropriate doping contributes to the improvement of the cathode material's cycling durability under high-voltage, primarily manifested in the following aspects: (1) Nanomorphology[74]: controlling the doping distribution to optimize the nanomorphology for expected modification structure. (2) Crystal lattice[75]: enhancing the covalency between the dopant elements and oxygen, stabilizing lattice oxygen, and suppressing oxygen-related redox reactions, and tuning the interplanar spacing to enhance Li^+ ion transport; (3) Electronic structure[76]: adjusting electronic structure and charge distribution to increase the overall conductivity of the material and enhance Li^+ ion kinetics; (4) Surface stability[63]: suppressing high-voltage irreversible phase transitions, reducing volume changes and internal stress accumulation;

One of the earliest doping strategies for LCO is the doping of TM elements, as the $LiTMO_2$ family includes many classical cathode materials such as $LiNiO_2$, $LiMnO_2$, $LiAlO_2$, and $LiFeO_2$[77-80]. Partial substitution of Ni into Li sites provides interlayer support but inevitably sacrifices a portion of the active capacity. Additionally, Ni-doped LCO can further reduce the charge transfer impedance of the battery, enhance Li^+ ion kinetics, and demonstrate improved cycling durability. A minor incorporation of Ni through doping can reduce the ordering of the monoclinic phase. The disorder introduced by Ni can bolster the stability of the lattice structure and suppress lattice

distortion in LCO under high-voltage. However, for portable electronic devices where smaller battery size is desired to achieve higher energy density, the original LCO with high energy density remains the most ideal choice.

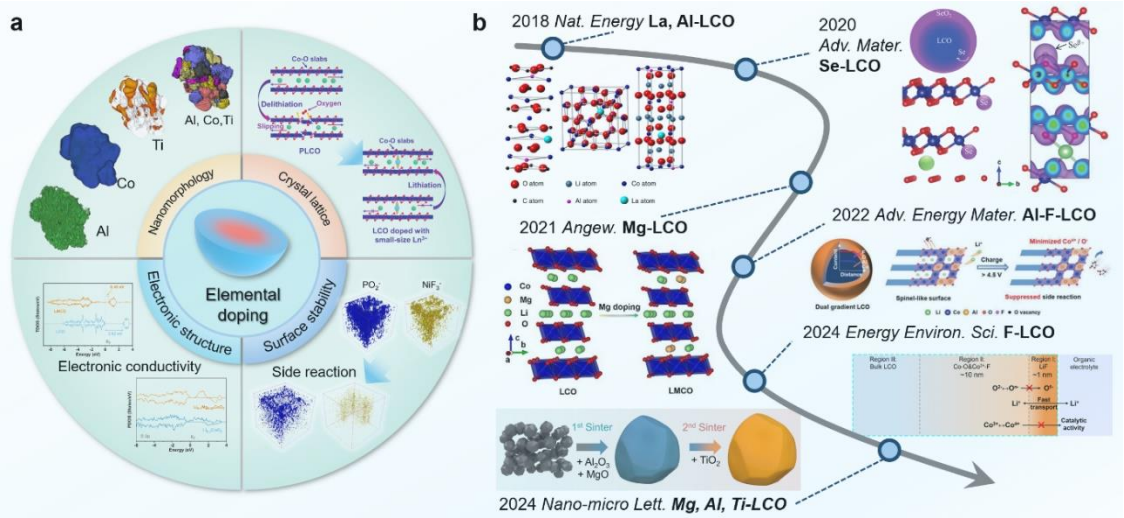

Figure 2.11 a Advantages of the elemental doping for layered TM cathode, including: nanomorphology[74], crystal lattice[75], electronic structure[76], surface stability[63]. **b** Recent research progress about elemental doping for high-voltage LCO: La, Al-LCO[81], Se-LCO[82], Mg-LCO[76], Al-F-LCO[83], F-LCO[84], and Mg, Al, Ti-LCO[85].

For LCO-based cathode materials, it is currently believed that a doping level of less than 10% is an appropriate proportion. This threshold aids in preserving the high energy density inherent to LCO while concurrently enhancing the electrochemical stability by doping. Doping with TM elements can form a solid solution system of $LiTM_xCo_{1-x}O_2$[20]. Common doping elements such as Mg, Al, Ti, Ni, Mn, Fe, Zr, La, Ce can enhance the cycling durability of LCO under high current density[86, 87]. However, when considering doping these elements, we need to consider their mutual solubility.

For example, only a small amount of Ti, Zr and Ce can be doped into the lattice on the surface of LCO, while they cannot enter the bulk structure. Their strong TM-O bonds can stabilize the lattice oxygen within the surface configuration of LCO, thereby reducing lattice oxygen oxidation reactions under high-voltage. As for elements like Al, it has a similar ionic radius to Co. Therefore, Al is well-suited as a choice for bulk doping into TM sites of LCO and has become one of the mainstream dopants[81]. Moderate doping of Al can inhibit the Co dissolution under high-voltage and improve the lattice structural stability of LCO material. **Fig. 2.11b** shows that recent research in this area has made progress, such as: La, Al-LCO[81], Se-LCO[82], Mg-LCO[76], Al-F-LCO[83], F-LCO[84] and Mg, Al, Ti-LCO[85]. Those researches confirmed that element doping can enhance the structural stability of the cathode, thus improving the cycling durability of the LCO system under high-voltage.

Taking Mg doped LCO as an example, it exhibits a series of benefits like high stability, high conductivity, and high melting point. Xie et al. have conducted in-depth studies on the mechanisms behind the performance improvement after Mg doping[88]. By replacing Co with Mg, the electrical conductivity of LCO can be enhanced, thereby improving the kinetic performance. As the Mg content increases, the interlayer spacing and conductivity of $LiCo_{1-x}Mg_xO_2$ further improve, which is believed to be the result of increased carrier concentration due to Mg doping. Additionally, Huang et al. have utilized Mg substitution for Li^+ slab as interlayer support to prevent structural collapse in highly delithiated states[76]. The stable

interlayer structure contributes to an improved Li^+ diffusion rate and inhibits the high-voltage phase transition.

In summary, trace doping is currently the mainstream doping strategy, which can enhance the cycling durability of LCO materials without altering their original system[72]. Multiple doping can combine the characteristics of different dopants to enhance the cycling durability of LCO. Therefore, appropriate multielement doping strategies have significant potential in developing high-voltage LCO-based batteries. However, the selection of doping elements, doping concentrations, and doping sites still rely on experimental findings. The specific mechanisms and their structure-activity relationship remains to be clarified. Additionally, element doping modifies the overall structure of the electrode material. To facilitate the successful doping of dopants into the internal structure of LCO, annealing temperatures above 760 ℃ and appropriate Li source supplementation are typically required. This undoubtedly adds to the challenges of low-cost large-scale production.

2.3.2 Surface coating layer

Surface modification is another commonly used and effective cathode protection strategy. As previously mentioned, volume expansion and the electrolyte decomposition reaction are significant contributors to cathode failure. Constructing a protective layer can effectively isolate the electrolyte from the unstable cathode surface, avoid the harmful side reactions on the electrode/electrolyte interface and

enable the structural stability under high-voltage.

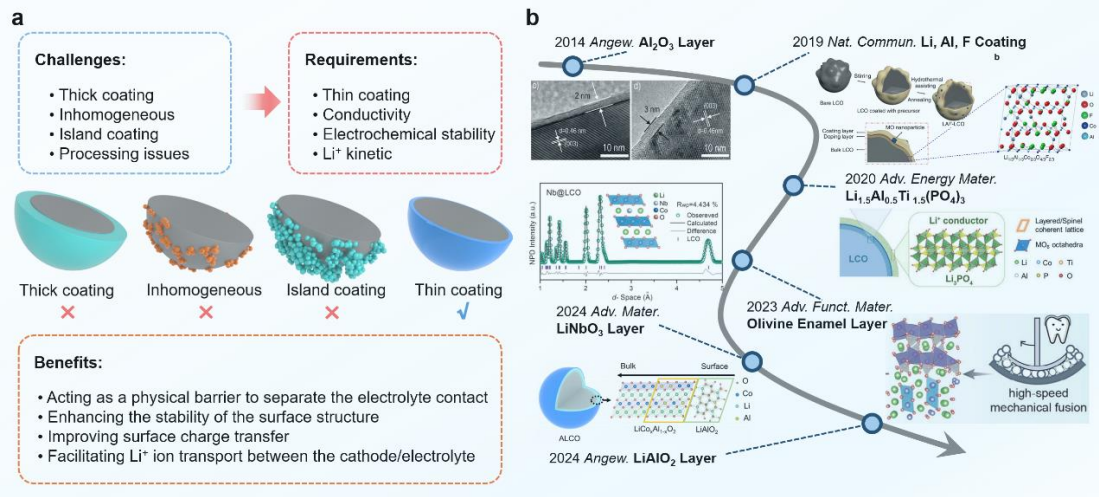

Figure 2.12 a Research challenges, updated requirements, and benefits of surface modifications for cathode materials, and corresponding morphological diagrams of thick coating, inhomogeneous, island coating and thin coating. **b** Recent research progress about surface modification: Al_2O_3[89]. Li-Al-F coating[90]. $Li_{1.5}Al_{0.5}Ti_{1.5}(PO_4)_3$[91]. Olivine Enamel layer[92]. $LiNbO_3$[93] and $LiAlO_2$ coating[94].

As shown in **Fig. 2.12a**, an appropriate cathode surface modification can provide the following benefits: (1) acting as a physical barrier to separate the direct contact between electrode and electrolyte, (2) enhancing the stability of the surface structure by alleviating the unwanted side reactions, (3) improving surface charge transfer, and (4) facilitating Li^+ ion transport of the electrode/electrolyte interface.

In previous studies, metal oxide matrixes have been widely used as coatings for LCO materials to achieve better integration. Al_2O_3, ZrO_2, $LiMn_2O_4$, TiO_2, ZnO, and other oxides have been extensively employed as coatings to protect the cathode material[95, 96].

However, the specific protective mechanisms of coatings are not yet fully understood. While coatings can serve as physical barriers to protect the cathode surface, they come at the cost of sacrificing a portion of the capacity. Under high-voltage, it is essential to maintain a delicate balance between reversible capacity and cycling durability. This balance is intricately tied to the crystal structure and thickness of the coating layer. Excessively thick amorphous coatings impede the Li^+ ions transport, increase charge transfer resistance, and result in slower Li^+ ion kinetics and reduced reversible capacity[97-100].

As shown in **Fig. 2.12b**, researchers have dedicated significant efforts to the development of effective coatings and have made considerable progress in this field. Some of the successful coating approaches include the use of Al_2O_3[89], Li-Al-F coating[90], $Li_{1.5}Al_{0.5}Ti_{1.5}(PO_4)_3$[91], Olivine Enamel layer[92], $LiNbO_3$[93], and $LiAlO_2$ coating[94]. Although metal oxides coating can offer surface protection, they often exhibit inadequate Li^+ ion conductivity, which can elevate interfacial resistance. High interfacial resistance poses certain obstacles to the overall Li^+ ion kinetics of the cathode materials. Therefore, materials with high Li^+ ion conductivity can also serve as suitable coating materials[101]. A novel $Li_{1.5}Al_{0.5}Ti_{1.5}(PO_4)_3$ surface coating was designed for LCO through *in-situ* formation[91]. The Li conductor coating in the study refers to the incorporation of Li_3PO_4 and $Li_{1.5}Al_{0.5}Ti_{1.5}(PO_4)_3$ phases in the surface modification of LCO, establishing a robust ionic transport route to bolster interfacial kinetics and enhance cycling and rate performances.

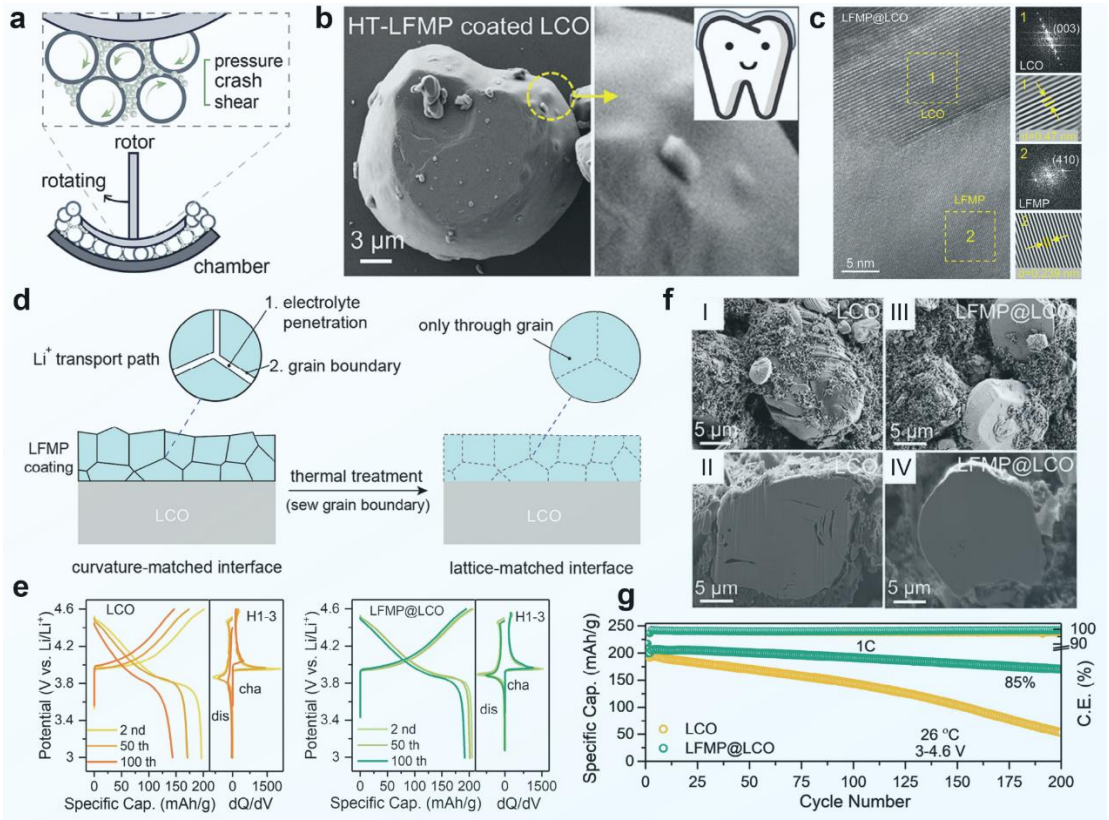

Figure 2.13 a Operational concept of coating machine. **b** SEM and **c** TEM images showcasing the continuous LFMP enamel-like layer. **d** Diagram depicting Li^+ ions transport path. **e** Typical galvanostatic charge-discharge (GCD) profiles. **f** SEM and cross-sectional images of cycled cathode. **g** Electrochemical performance[102].

Surface coating layer assumes a pivotal role in enhancing cathode performance beyond its function as a physical barrier. The interplay between the coating and the cathode surface facilitates the migration of interface electrons and ions, which is vital for improving cycling durability under high-voltage[103, 104]. As shown in **Fig. 2.13**, Yan et al. developed a novel high-speed mechanical fusion method to prepare a seamless enamel-like olivine ($LiFe_{0.4}Mn_{0.6}PO_4$, LFMP) coating on the surface of LCO (LFMP@LCO)[102]. This innovative coating strategy serves multiple functions: (1)

From the outside-in, the LFMP enamel-like layer regulates electrolyte decomposition to create a stable CEI, suppressing Co dissolution and electrolyte byproducts. (2) The robust adhesion between LCO and the LFMP, from the inside-out, stabilizes the oxygen lattice and hinders the creation of the detrimental spinel Co_3O_4 phase. Additionally, the LFMP olivine coating enhances the thermal stability of highly delithiated LCO. Consequently, the modified LCO cathode demonstrates exceptional electrochemical performance, maintaining 85% capacity after 200 cycles. This straightforward coating approach establishes a fresh technical paradigm for improving the surface stability of high-voltage LCO.

Surface modification stands out as an effective strategy for enhancing cathode performance, and appropriate coatings can enhance the electrochemical properties of high-voltage LCO to a certain degree. However, there are still some issues related to coating encapsulation that require further research. For example, the introduction of coatings using solid-state methods may lead to uneven coverage. Coating encapsulation using solution methods is only applicable to cathode materials that are stable in a water environment. Additionally, challenges such as the bonding between the coating and the cathode surface during high-temperature annealing and Li loss need to be addressed. The layer quality, crystal structure, and coating thickness require systematic research to gain a deeper understanding of their relationships.

2.3.3 Structural design

Element doping and surface modification encapsulation employ different principles to enhance the performance of cathode. To further enhance their cycling durability of cathode materials under high-voltage, researchers have attempted to use structural design for multifunction, opening a new direction in cathode material research.

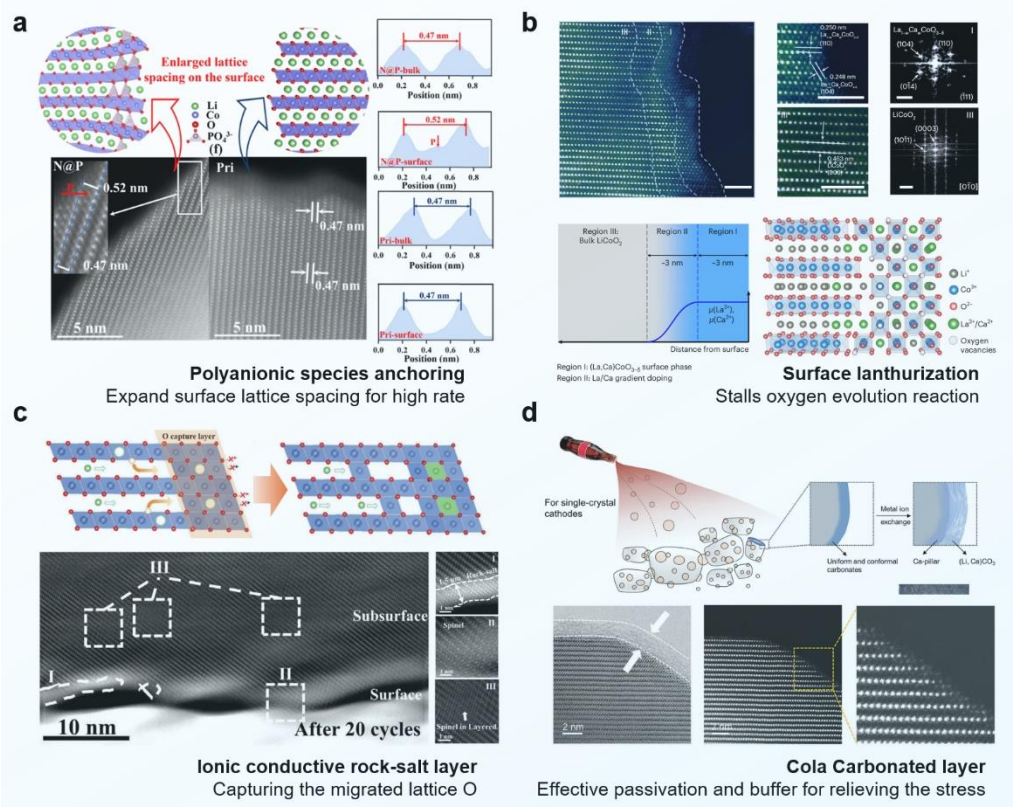

Figure 2.14 a Anchored polyanionic $(PO_4)^{3-}$ species on surface[105]. **b** Lanthurizing process to regulate the near-surface structure[50]. **c** Ionic conductive rock-salt phase layer[102]. **d** Cola carbonated layer for effective passivation[106].

For instance, polyanionic species were innovatively introduced on the surface of LCO cathode. The polyanionic species acted as "micro-funnels" to expand the lattice

spacing of surface structure by 10%, boosting Li^+ ion diffusion improve rate performance greatly, which significantly enhanced its reaction kinetics and structural stability[105] (**Fig. 2.14a**). A lanthurization process was invented to enhance the high-voltage cycling durability of LCO cathode (**Fig. 2.14b**)[50]. This innovation involves a uniform ion-exchange process that reconstructs the near-surface region, creating a strained, high-quality surface architecture that minimizes lithium vacancies and suppresses surface transformation. A novel surface rock-salt layer was introduced on LCO (RS-LCO) cathode material to enhance its structural durability at high operating voltage up to 4.65 V (**Fig. 2.14c**). The rock-salt layer effectively suppressed surface oxygen loss, side reactions, and structural degradation, while also inhibiting bulk phase separation and crack formation. This gradual phase transition from rock-salt to an ionic conductive spinel phase contributed to a capacity activation process and improved the rate capability of the RS-LCO. Liao et al. invented a highly conformal and extensible interfacial modification strategy using supersaturated CO_2 bubbles to stabilize LCO cathodes under high-voltage[106], achieving excellent capacity retention and energy density (**Fig. 2.14d**). This innovative carbonation strategy, inspired by chemistry in carbonated drinks, addresses interfacial problems in high-voltage cathodes and paves the way for future high-energy-density LIBs.

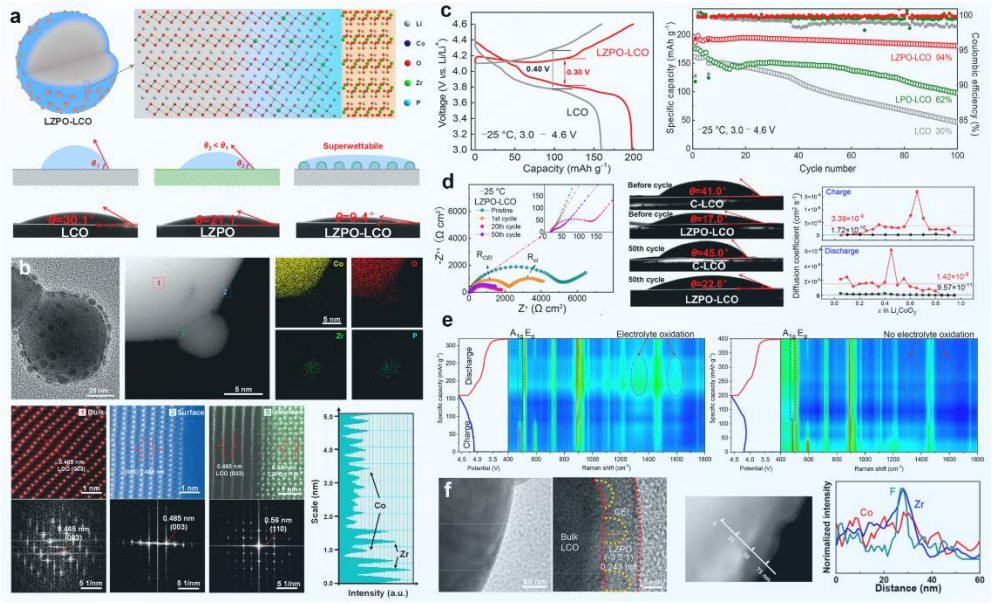

Figure 2.15 a Schematic structure and wettability. **b** Morphology characterization and element distribution of LZPO-LCO. **c** Low temperature performance. **d** Li^+ diffusion characteristics and investigation of CEI component. **e** *In-situ* Raman spectra during the initial charge-discharge cycle. **f** Surface morphology characterization after 50 cycles[107].

The structural design for near-surface region plays an importance role for multifunctional effect. For example, Dong, et al. performed surface engineering of LCO by incorporating a Zr-doped surface layer along with Li^+ conductive $Li_2Zr(PO_4)_2$ (LZPO) nanoparticles interspersed on the surface (**Fig. 2.15a**)[107]. This design aims to improve the low-temperature performance and high-voltage capability of LCO cathodes. The LZPO nanoparticle contributes to an electrolyte super-wettability on the LZPO-LCO surface, facilitating the formation of a uniform CEI with robust stability and minimal interface resistance. Even when operating at a low temperature of -25°C

and a high-voltage of 4.6 V, the LZPO-LCO composite exhibits exceptional performance, achieving an ultrahigh capacity of approximately 200 mAh g^{-1} at 0.2C and 137 mAh g^{-1} at 5C. This surface engineering strategy provides a significant improvement in the low-temperature performance, addressing the challenge of insufficient low-temperature adaptability of high-voltage cathodes. In addition, Sun et al. utilized an atomically MXenes thin layer for surface modification[108]. This multifunctional surface modification design serves to diminish the contact area between the cathode surface and organic electrolyte, inhibit structural phase transitions, and reduces Co dissolution, thereby improve the stable operation of LCO under high-voltage. Tian et al. developed an Mn/La bulk co-doping approach with a protective Li-Ti-O coating on the surface of LCO[109]. This dual-function modification led to a comprehensive enhancement in the electrochemical performance of LCO. The bulk co-doping of Mn/La enhanced the crystal structure stability of LCO and improved Li^+ ion kinetics. The Li-Ti-O coating further stabilized the surface structure, isolating it from the influence of the electrolyte.

Although the principles behind the multifunctional structural design vary, they all aim to bolster the electrochemical performance of LCO cathode and achieve better cycling durability under high-voltage. These novel structural design methods provide new possibilities for the improvement and application of cathode materials, but further research is needed to better understand their specific mechanisms and optimize their approaches.

2.3.4 Electrolyte additives

Operating LIBs under high-voltage LCO cathode can trigger instability in commercial electrolytes, which is a major challenge for realizing high-energy-density LIBs[38, 62, 110]. At voltage above 4.3 V, the commercial electrolyte, consisting of $LiPF_6$ salt and carbonate solvents, undergoes oxidative decomposition catalyzed by the LCO cathode. This triggers a vicious cycle of LCO/electrolyte interface breakdown, Co ion dissolution, and harmful HF formation, further accelerating the electrolyte degradation. To address this issue, modifying the electrolyte with minor quantities of additives has been investigated as a cost-efficient solution. Electrolyte additives can help disrupt the detrimental cycle of electrolyte degradation under high-voltage. For example, Si-containing compounds have shown promising results in inhibiting HF formation, although the underlying mechanisms are not fully understood[111]. Moreover, anhydrides have been employed to eliminate residual water in the electrolyte, a factor that can trigger the hydrolysis of $LiPF_6$ and subsequently result in HF production[112].

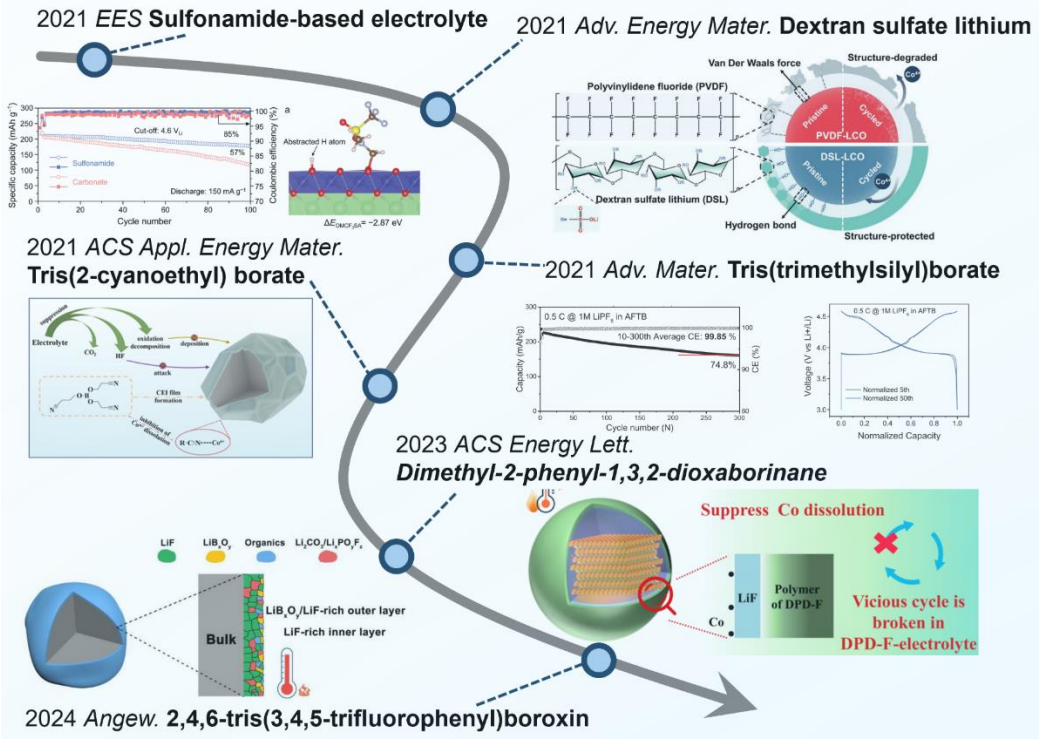

Figure 2.16 Recent research progress about electrolyte additives: Sulfonamide-based electrolyte[113]. Dextran sulfate lithium[114]. Tris(2-cyanoethyl) borate[115]. Tris(trimethylsilyl)borate[116]. Dimethyl-2-phenyl-1,3,2-dioxaborinane[62] and 2,4,6-tris(3,4,5-trifluorophenyl) boroxine[117].

Electrolyte additives play a crucial role in engineering the CEI to improve its mechanical and thermal stability[62, 115, 116]. Aiming at the problem of electrolyte oxidation, recent additives show outstanding success at the LCO under high-voltage. As shown in **Fig. 2.16**, the sulfonamide-based electrolyte that can effectively stabilize the electrode-electrolyte interfaces under high-voltage[113]. This electrolyte variant exhibited remarkable cycling performance by mitigating surface deterioration, impedance growth, and adverse side reactions on the LCO cathode, while also facilitating the operation Li metal anode. Dextran sulfate lithium (DSL) has been

employed to stabilize high-voltage LCO[114]. The DSL binder creates a homogeneous coating on the LCO surface through strong hydrogen bonding, thereby suppressing interfacial degradation. Notably, the DSL binder boosts the stability of Co-O chemical bonds, impeding the adverse phase transitions that can occur under high-voltage. Moreover, 2,4,6-tris(3,4,5-trifluorophenyl) boroxin was used to foster the creation of a LiB_xO_y-rich/LiF-rich CEI. The LiB_xO_y layer effectively maintained the integrity of the CEI, providing robust mechanical stability, while the abundant LiF enhances thermal stability and CEI uniformity. In summary, electrolyte additives play a crucial role in enhancing the thermal stability of the CEI, enabling durable high-voltage and high-temperature battery performance. These additives exhibit remarkable capabilities in suppressing electrolyte oxidation and improving the stability of the electrode-electrolyte interfaces.

As shown in **Fig. 2.17a**, a novel and facile strategy was presented to stabilize LCO cathodes under high-voltage by employing a multifunctional additive called phytate lithium (PL)[73]. The PL additive plays several critical roles: (1) PL forms a robust artificial CEI layer through strong coordination between the phosphate groups and TM ions, mitigating detrimental phase transitions and Co dissolution under high-voltage. (2) The PL effectively scavenges oxygen radicals released from the LCO lattice at high states of charge, alleviating electrolyte decomposition and interface degradation. (3) The inherent flame-retarding capability of PL enhances the thermal stability and safety of LIBs system. The utilization of PL as a modifier for the LCO

cathode has yielded remarkable results in terms of cycling performance, retaining close to 90% capacity after 200 cycles. Moreover, a pouch cell using PL-LCO as the cathode delivers impressive capacity retention of 86.5% after 100 cycles, outperforming the bare LCO counterpart. The ability of PL to effectively scavenge oxygen radicals released from the LCO structure at high SOCs, alleviating electrolyte decomposition and interface degradation.

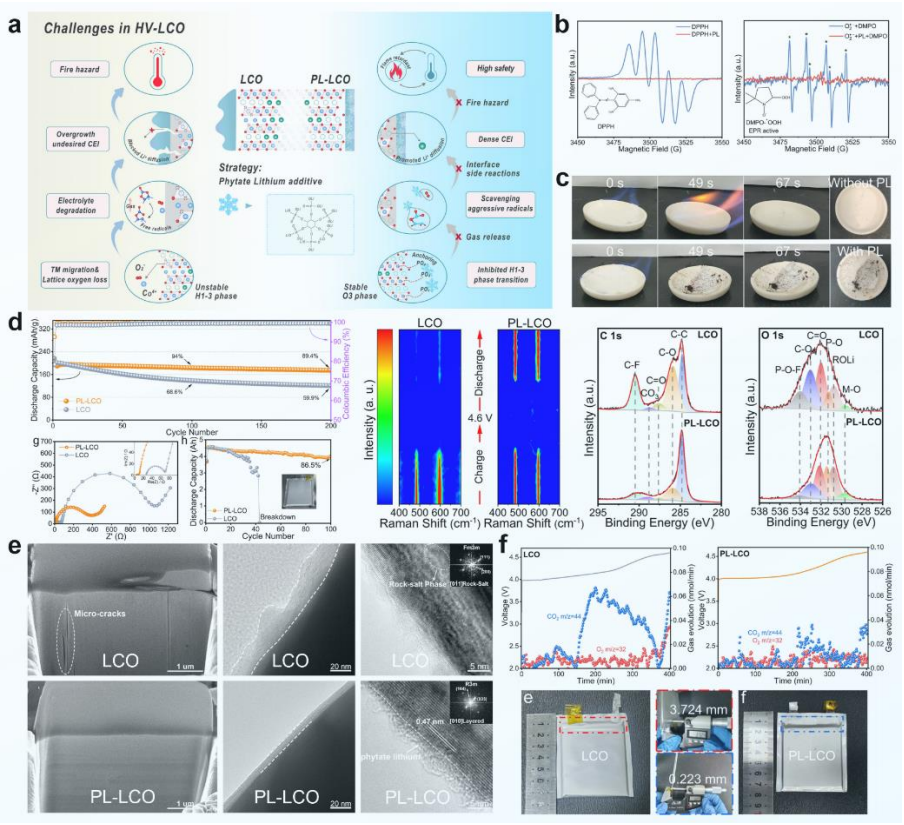

Figure 2.17 **a** Diagram depicting the multifunctional effects of PL. **b** Electron paramagnetic resonance (EPR) results indicate the annihilation capability of PL. **c** Ignition test comparison. **d** Electrochemical characterization, *in-situ* Raman and X-ray photoelectron spectroscopy (XPS). **e** DEMS profiles and **f** comparison of gas production in pouch cells[73].

As show in **Fig. 2.17d**, the *in-situ* Raman spectra showed that the modified LCO exhibited a lower proportion of the harmful H1-3 metastable phase compared to pristine LCO, indicating that PL can effectively mitigate the detrimental phase transition under high-voltage. Additionally, the gas evolution estimation test assessment illustrated the enhanced stability of the PL-modified LCO pouch cell at high temperature (45°C) and under high-voltage (4.65 V), with a capacity retention of 76% after 100 cycles, much better than the bare LCO at only 45%. In conclusion, the simple and facile addition of PL as a versatile additive in the LCO cathode slurry effectively stabilizes the LCO up to 4.6 V.

Overall, the development of effective electrolyte additives is a crucial and necessary step in realizing high-voltage LCO batteries with improved performance and safety. The ability of electrolyte additives in stabilizing the interface between the electrolyte and electrodes, as well as in mitigating the adverse impacts of high-voltage operation, makes them an indispensable part of the research on high-energy-density LIBs.

2.4 Application and challenge of high voltage LCO cathode

Single-crystal LCO, with its high tap density, is suitable to produce small-sized LIBs with high volumetric energy density. Therefore, LCO cathode materials are primarily used in LIBs for portable devices such as smartphones, smartwatches, laptops, action cameras, and portable medical devices. With hardware and software upgrades in these

portable devices, the need for LIBs with increased energy storage capacity is on the rise. Thus, improving battery performance needs to consider several aspects: reversible specific capacity, cycle life, high-rate charging, and manufacturing cost. The development of cathode materials should strike a balance between cost and performance, depending on different user requirements and application scenarios.

We have noticed that in the recent product launches by smartphone manufacturers, the two main concerns of users regarding batteries are reversible capacity and fast charging capability[118]. Reversible capacity determines the one charging use time of smartphone, while fast charging reduces the connecting time with charger. As the energy consumption of portable devices continues to increase, the previous charging speeds are no longer meeting the increased demands of users. Therefore, while achieving high energy density, the fast-charging performance of LIBs must also be considered.

Since its commercial adoption, LIBs have been driving the development of the 21st-century new energy society. Today, LIBs have become an integral part of modern smart society, enabling intelligent traffic, and connecting with the daily lives of people. LCO, favored for its high energy density and robust cycling durability, has been widely adopted as a cathode material in portable energy storage devices. These favorable characteristics attributed to its single-crystal structure and reliable safety performance. Increasing the charge cut-off voltage stands out as the simplest and most efficient method to achieve higher energy density in batteries. However, high-voltage

also presents new challenges, including decreased cycling durability and a range of safety issues. Considerable research has been conducted to understand the cathode failure mechanisms induced by high-voltage, resulting in significant advancements in our understanding of LIB operation. This has also led to the development of tailored modification strategies aimed at bolstering the cycling durability of LCO under high-voltage and prolonging its operational lifespan.

Presently, the major failure mechanisms include the following: (1) LCO with high Li^+ ion extraction experiences irreversible structural phase transitions. The voltage-induced phase transitions cause severe lattice expansion and contraction, greatly impacting the reversible capacity of the cathode material. Continuous volume changes and phase transitions lead to particle cracking and structural collapse. (2) LCO surfaces undergo Co dissolution and oxygen loss, resulting in surface structure degradation and capacity loss. The unstable surface structure can form spinel phases, releasing a significant amount of gas and posing serious safety hazards. (3) The oxidation and decomposition of the electrolyte intensify during cycling, resulting in the creation of a thicker CEI film, increased impedance, and reduced Li^+ ion kinetics. Additionally, the collapse of structures and the enlargement of grain cracks increase the contact area between the electrolyte and fresh interfaces, further degrading the surface structure.

Researchers continuously innovate and optimize battery configurations to enhance the energy density of LCO full cells. To achieve further increases in energy density,

modified cathode materials must be considered. Cathode materials hold a pivotal position in determining the overall battery energy density and represent the costliest component in the battery production chain. Increasing charging cut-off voltage is the simplest and most effective method to improve energy density of LIBs. Researchers are dedicated to maintaining good crystal structure stability under high-voltage to achieve high capacity and cycling durability in full batteries. In addition to the cathode particle modification methods mentioned earlier, such as element doping, coating encapsulation, and functional modification, there are many aspects that need to be improved for the overall battery. For example, suitable particle size distribution, appropriate roll compression force, slurry formulation, and matching structure of the cathode material. In conclusion, by striking a balance between manufacturing cost and performance improvement and optimizing the battery configuration, the energy density of full batteries can be significantly improved.

In summary, increasing the charge cut-off voltage of LCO cathodes to 4.6 V presents significant challenges due to structural phase transitions, Co ion dissolution, oxygen loss, and electrolyte degradation. Researchers are exploring various modification strategies such as foreign-ion doping, surface modification, structural design, and electrolyte additives to enhance the stability and performance of LCO cathodes under high-voltage. Further advancements in these areas are crucial to enable the safe and efficient operation of LIBs at even higher voltage.

Chapter 3 Experimental section

This chapter describes the experimental section, inducing the details of the chemicals, the synthesis method, the characterization, the electrochemical measurements, and the computational details.

3.1 Chemicals and reagents

All chemicals were used without any purity, and the related information is listed in following **Table 3.1**.

Table 3.1 The details of chemicals and reagents.

Chemicals	Purity	Company
Cobalt (II,III) oxide (Co_3O_4)	99.50%	International laboratory USA
Lithium carbonate (Li_2CO_3)	99.50%	International laboratory USA
Aluminum oxide (Al_2O_3)	99.00%	International laboratory USA
Magnesium oxide (MgO)	98.00%	International laboratory USA
Titanium (IV) oxide (TiO_2)	99.70%	Sigma-Aldrich
Lithium cobalt (III) oxide (LCO)	98.00%	International laboratory USA
Phosphoric acid (H_3PO_4)	99.50%	International laboratory USA
Triethylamine (TEA)	99.00%	International laboratory USA
Cerium (III) nitrate hexahydrate ($Ce(NO_3)_3 \cdot 6H_2O$)	99.00%	Sigma-Aldrich
Li metal (diameter:16mm; thickness:0.6 μm)	99.95%	China Energy Lithium Co., Ltd

3.2 Material synthesis

Synthesis of bare LCO, one-step Ti/Mg/Al codoped LCO, and core-shell structured LCO (chapter 3)

Bare LCO, one-step Ti /Mg/Al codoped LCO (MAT-LCO) and core-shell structured LCO (CS-LCO) were prepared by a solid-state reaction method.

For LCO, the Co_3O_4 and Li_2CO_3 were ground and sintered at 760 ℃ for 2 h and 1000 ℃ for 12 h. For MAT-LCO, the Co_3O_4, Al_2O_3, MgO, TiO_2 and Li_2CO_3 were ground and sintered at 760 ℃ for 2 h and 1000 ℃ for 12 h. For CS-LCO, the Co_3O_4, Al_2O_3, MgO, and Li_2CO_3 were ground and firstly sintered at 760 ℃ for 2 h and 1000 ℃ for 12 h to obtain AMLCO intermediate. The AMLCO powder was than mixed with TiO_2 and sintered at 900 ℃ for 10 h.

Synthesis of amorphous $AlPO_4$ coated LCO (LCO@A), and $AlPO_4$-5 zeolite coated LCO (LCO@$AlPO_4$-5) (chapter 4)

LCO@A and LCO@Z were prepared by hydrothermal method. For LCO@A, pristine LCO was mixed with pseudo-bohemite and phosphoric acid in deionized water. For LCO@Z, pristine LCO was mixed with pseudo-bohemite, phosphoric acid, and triethylamine in deionized water. Both LCO@A and LCO@Z were processed under hydrothermal condition at 155℃ for 1 h and the collected powders were annealed at 550℃ for 2 h.

Synthesis of CeO_2 and LCO@CeO_2 (chapter 5)

CeO_2 (CeO_2-500, CeO_2-700, CeO_2-850, and CeO_2-1000) and LCO@CeO_2 (Ce-500, Ce-700, Ce-850, and Ce-1000) were prepared by hydrothermal method. For CeO_2, $Ce(NO_3)_3 \cdot 6H_2O$ dissolute in deionized water. For LCO@CeO_2, bare-LCO mixed with $Ce(NO_3)_3 \cdot 6H_2O$ in deionized water. Both of CeO_2 and LCO@CeO_2 are processed with hydrothermal at 160℃ for 3 h and annealed at 500℃, 700℃, 850℃, and 1000℃ for 2 h, respectively.

3.3 Characterization methods

The morphology and phase structure of cathode materials were investigated by scanning electron microscope (SEM, MAIA3) and X-ray diffraction (XRD, Rigaku SmartLab). Cross-sectional samples were prepared by an ion milling system (IM4000plus) and the cross-sectional images were observed using FE-SEM (Regulus8100). The nanostructure of cathode materials was studied by transmission electron microscope (TEM, JEOL JEM-2100F). The fine structure for the initial and cycled electrodes (disassemble the coin-cell) were measured by postmortem electron paramagnetic resonance (EPR, Bruker EMX Plus), X-Ray photoelectron spectroscopy (XPS, Thermo Fisher Scientific Nexsa). The Ce L_3-edge X-ray absorption spectroscopy (XAS) data of electrode samples were collected at the TLS 16A beamline, NSRRC, Taiwan. The chemical composition of the cycled cathode was investigated using a TOF-SIMS equipment (IONTOF M6, Germany). A dual beam depth profiling method was used, combining a 30 keV Bi^{++} primary ion source that delivered 0.2 pA of target current over an area of 100 × 100 μm^2 for analysis, with a 1k eV Cs^+ sputter beam that delivered ≈90 nA of target current over an area of 300 × 300 μm^2 to create a sputtered crater.

3.4 Electrochemical measurement

The positive electrodes which are used in the coin-type (CR2025) cells were fabricated with 90% active material particles (cathodes), 5 wt% super P, and 5 wt% polyvinylidene fluoride (PVdF) binder. Then the above powder was dissolved in N-methyl-1,2-pyrrolidone (NMP) to obtain a homogeneous slurry.The mass loading of active oxide in the slurry was set to ~4 mg cm^{-2}. In coin-type half cells, Li metal was used as the anode. The electrolyte used in the half cells consisted of 1 M $LiPF_6$ dissolved in a mixture of ethylene carbonate (EC) and dimethyl carbonate (DMC) in a volume ratio of 1:1. The electrochemical tests were conducted at room temperature (25℃) using a LAND instrument (CT-2001 A). Galvanostatic intermittent titration technique (GITT) measurements were performed on the half cells within the voltage range of 3.0-4.6 V. A titration current of 0.3C (1C = 200 $mA{\cdot}g^{-1}$) was applied for 10 minutes, followed by a relaxation time of 1 hour to allow the system to reach the quasi-equilibrium potential. Cyclic voltammetry (CV) and electrochemical impedance spectroscopy (EIS) were conducted using a Solartron 1470E instrument (AMETEK, USA). The frequency range for EIS measurements was 10^{-2} to 10^{6} Hz. Differential electrochemical mass spectrometer (DEMS, QAS100 Li) testing was used for detecting the gas generation during charging and discharging of the anode material in a Swagelok-type cell, and the carrier gas was Argon with a flow rate of 1 mL min^{-1}.

3.5 DFT calculation

All spin-polarized density functional theory (DFT) calculations were performed by using the projector-augmented wave method in VASP code[119, 120]. Perdew-Burke-Ernzerhof (PBE) scheme of generalized gradient approximation was applied as the exchange-correlation functional[121]. The van der Waals corrections were considered by Grimme's DFT-D3 method[122]. Kinetic energy cut-off was set as 420 eV, and K-points meshes with density higher than 0.035×2π/Å were used for Brillouin zone sampling. All structures were relaxed until energy and force convergence criteria of 10^{-5} eV and 0.02 eV $Å^{-1}$ were reached, respectively. Hubbard U correction term of 3.32 eV was applied on strongly correlated cobalt atoms[123]. The adsorption energy ΔE was calculated as $\Delta E = E_{surface\text{-}ad} - E_{surface} - E_{ad}$, where $E_{surface\text{-}ad}$, $E_{surface}$, and E_{ad} represent DFT-calculated energies of surface with adsorption, clean surface, and adsorbate, respectively. Vacuum layers with a thickness of at least 15 Å were added to the slab structures to prevent spurious interactions. The climbing-image nudged elastic band (CI-NEB) method was used for calculating the diffusion barriers[124].

Chapter 4 Core-shell structured cathode by cationic heterogeneous co-doping

In Chapter 3, considering the different diffusivities of different dopant ions, we propose a simple two-step multi-element co-doping strategy to fabricate core-shell structured LCO (CS-LCO). In the current work, the high diffusivity Al^{3+}/Mg^{2+} ions occupy the core of single-crystal grain while the low diffusivity Ti^{4+} ions enrich the shell layer. *In-situ* XRD demonstrates the constrained contraction of *c*-axis lattice parameter and mitigated structural distortion. Under a high upper cut-off voltage of 4.6 V, the single-crystal CS-LCO maintains a high reversible capacity with a good retention of ~89% after 300 cycles. The proposed strategy can be extended to other pairs of low- (Zr^{4+}, Ta^{5+}, and W^{6+}, etc.) and high-diffusivity cations (Zn^{2+}, Ni^{2+}, and Fe^{3+}, etc.) for rational design of advanced layered oxide core-shell structured cathodes.

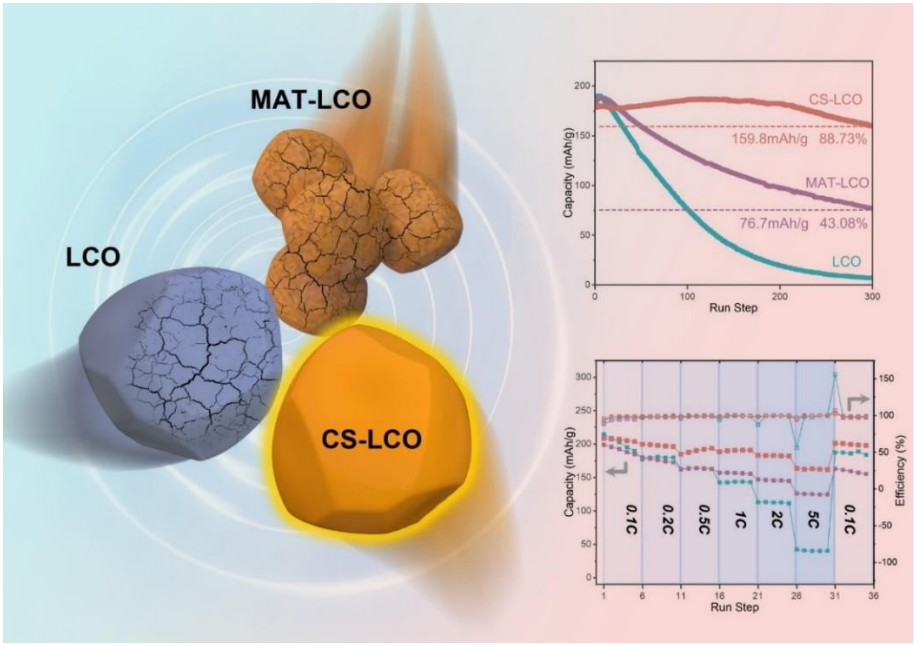

Figure 4.1 Graphic abstract of CS-LCO.

4.1 Introduction

In recent years, the promotion of the concept of carbon neutrality has led to an increasing demand for LIBs[12, 125, 126]. LIBs were first commercialized by Sony Corp. in 1991, in which layered oxide LCO was employed as insertion/extraction cathode material in LIBs. Compared with polycrystalline cathodes, single-crystal counterpart provides several advantages in practical applications[127, 128]. Single-crystal cathodes show the special monodisperse behavior and the absence of grain boundaries, and thereby avoid the unwanted microcracks that occurred in polycrystalline particles. Besides, single-crystal cathodes with lowered specific surface area and defect concentration reduce their interface side reactions and improve their structural stability. Furthermore, single crystal cathodes typically exhibit higher mechanical strength, which can contribute to an increase in packing density. This advantage is beneficial for enhancing the volumetric energy density of LIBs [128, 129]. To satisfy the increased push of smart-mobile and fast-paced society, there is a greater need for single crystal LCO processing with higher energy density and superior structural stability. To ensure structural stability, the upper cut-off voltage of LCO is normally kept no higher than 4.5 V to avoid the transformation of LCO from O3 to H1-3[41]. And the corresponding Li^+ that can be intercalated into or de-intercalated from the LCO lattice is only ~65% of the total amount of Li [130]. Indeed, increasing the upper cut-off voltage could effectively obtain the higher reversible capacity, but the highly delithiated state with higher Li^+ extraction results in a significant degradation of

cycling performance, accompanied by structural collapse, irreversible phase transition, electrolyte oxidation, lattice oxygen release, and Co dissolution[47, 131, 132].

Inactive elemental doping is commonly used to modify materials' structure and physical properties, such as band gap, lattice structure, and charge redistribution, etc. for the optimization of their electrochemical performance[81, 133]. Different doping elements (Mg, Al, Ti, Mn, Ni, Se, Zr and Sn) are often used as dopants[72, 134-138] to improve the electrochemical performance of LCO. Recent research by Huang et al. showed that the doping of Mg ions in the Li layer created the so-called pillar effect to stabilize the layered structure[136]. For multi-elements doping, a one-step co-doping strategy of ternary dopants was reported[138]. The synergistic effects of multi-element dopants stabilize the surface oxygen and promote the cycle stability of LCO at high voltage of 4.6 V. Although partial success has been achieved, the one-step co-doping strategy seems to bring some other problems. During the one-step co-doping process, several co-doped cations (heavy and/or high valence-state cation dopants Ti^{4+}, Zr^{4+}, and Y^{3+}, etc.) have been found to readily enrich on the grain surface and grain boundaries, and further induce the formation of polycrystalline particles due to the limited growth kinetics in various cathode materials[138-141]. These agglomerated polycrystalline particles possess increased grain boundaries and a larger specific surface area, which will inevitably react with electrolyte. Therefore, designing an appropriate multi-element co-doping strategy to synthesize single-crystal cathodes with high performance is still quite challenging[142-144].

The diffusivities of cations show clear dependence on cation charge and radius[139, 140, 145, 146]. In this work, considering the large variation in diffusivity of different dopant ions, we propose a novel two-step co-doping strategy to dope Ti/Mg/Al into LCO, a model layered oxide cathode material. A core-shell structured single-crystal LCO (CS-LCO) cathode material is obtained, where the high diffusivity Al^{3+}/Mg^{2+} ions occupy the core of single-crystal grains while the low diffusivity Ti^{4+} ions just enrich the shell layer of each grain. The Ti^{4+}-enriched shell layer with Co/Ti substitution and stronger Ti-O bond, reduce the number of oxygen ligand holes and enhance the oxygen stability. *In-situ* XRD reveals that the CS-LCO exhibits mitigated phase transition from O3 to H1-3, resulting in reduced contraction of *c*-axis and structural distortion. Under a high cut-off voltage of 4.6 V, the CS-LCO maintains a reversible capacity of 159.8 mAh g^{-1} with a good retention of ~89% after 300 cycles, and reaches a high specific capacity of 163.8 mAh g^{-1} at 5C. The proposed strategy can also be extended to other couples of low-diffusivity cations (Zr^{4+}, Ta^{5+}, and W^{6+}, etc.) and high-diffusivity ones (Zn^{2+}, Ni^{2+}, and Fe^{3+}, etc.) for controllable construction of single-crystal core-shell structured cathodes that improve not only the structural stability, but also the electrochemical performance of other LIB cathodes. Our work described here provides a new insight into the fabrication of single-crystal LCO with enhanced electrochemical performance *via* multi-element doping for high energy-density LIB applications.

4.2 Results and discussion

4.2.1 Cation diffusivity and co-doping strategy design

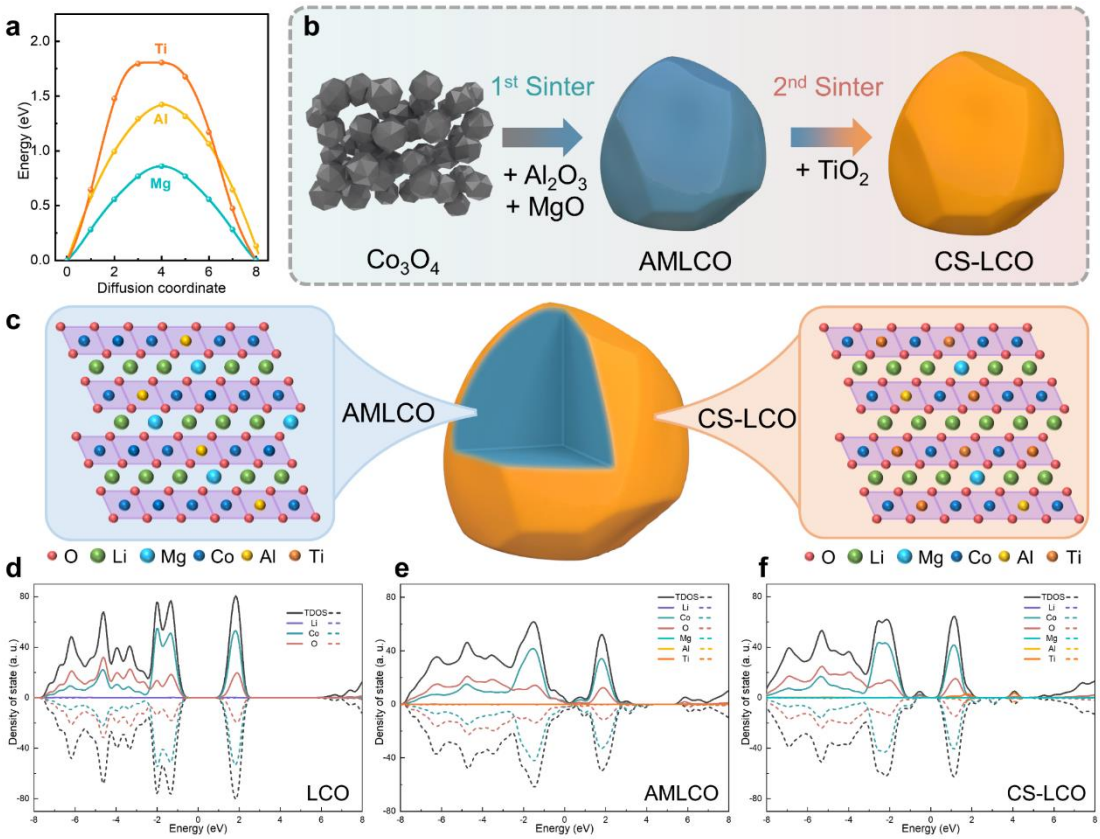

Figure 4.2 Conceptual design and preparation. **a** DFT calculation of diffusion energy barrier of Mg, Al and Ti ions along LCO interlayer. Schematic illustration of the **b** synthesis and **c** structure design of core-shell LCO. DOS of **d** LCO, **e** AMLCO and **f** CS-LCO.

For atomistic understandings, we compare the diffusion barriers of Mg, Al, and Ti ions along the interlayers using the climbing image nudged elastic band (CI-NEB) method. As shown in **Fig. 4.2a**, for Al (rAl^{3+} = 0.535 Å) and Ti (rTi^{4+} = 0.605 Å) ions diffusing along Co (rCo^{3+} = 0.545 Å) layer and Mg (rMg^{2+} = 0.72 Å) ion diffusing

along Li (rLi^+ = 0.76 Å) layer, the energy barrier follows the order of Mg (0.86 eV) < Al (1.42 eV) < Ti (1.8 eV). It is worth noting that Ti^{4+} ion exhibits the highest energy barrier among them, confirming the low diffusivity of Ti^{4+} ion in LCO. **Fig. 4.1b** schematically illustrates the design and preparation of core-shell LCO (CS-LCO) via a two-step cation co-doping method, where the low diffusivity Ti^{4+} ions and high diffusivity Al^{3+}/Mg^{2+} ions are chosen as a proof of concept. In the first sintering step, Co_3O_4 are mixed with Li_2CO_3 (Li/Co=1.1), Al_2O_3 (1 wt.%), and MgO (1 wt.%), and sintered to obtain Al^{3+}/Mg^{2+} codoped LCO (AMLCO). In the second sintering step, the AMLCO powder is further mixed with TiO_2 (1 wt.%) and sintered to obtain surface-Ti^{4+}-enriched core-shell structured LCO (CS-LCO). For comparison, one-step Ti /Mg/Al codoped LCO (MAT-LCO) is also prepared.

4.2.2 Core-shell structure characterization

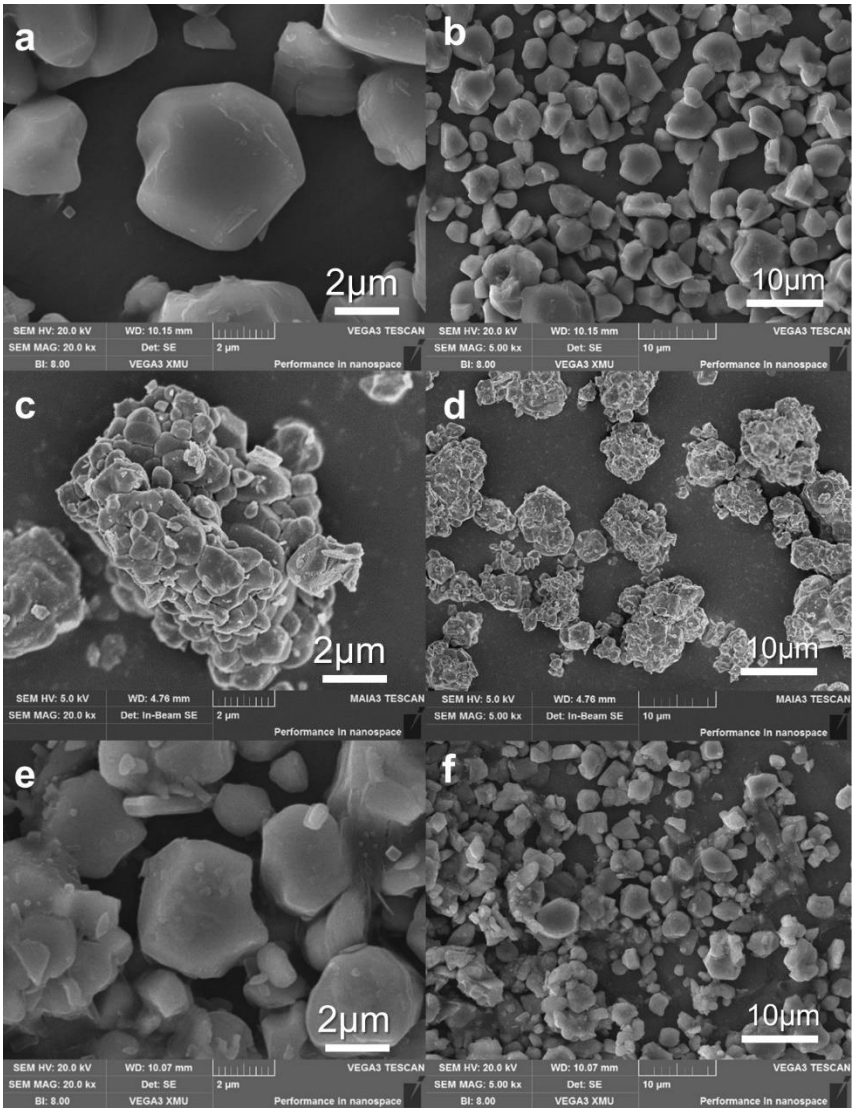

Figure 4.3 SEM image of **a-b** LCO, **c-d** MAT-LCO, and **e-f** CS-LCO.

SEM analyses are conducted to observe the distinctions of the cathode morphology,as shown in **Fig. 4.3**. The LCO and CS-LCO show micron-sized single crystallites in a size range of 2-5 μm. In contrast, MAT-LCO shows the agglomeration of primary grains with a grain size of hundreds of nanometers, which is attributed to the segregation of Ti at the grain boundaries. This segregated Ti dopant hinders the

further grain growth of LCO particles into large single-crystal grains, As shown in **Fig. 4.4**, which is consistent with previous studies[138-140].

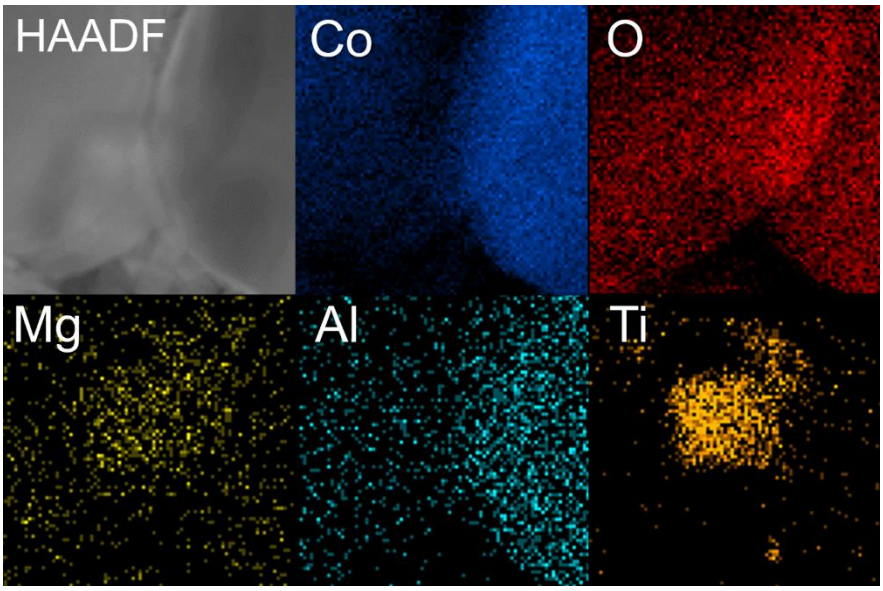

Figure 4.4 Energy dispersive spectrometer (EDS) mapping of MAT-LCO.

As shown in **Fig. 4.5**, the specific surface areas of the as-sintered LCO, CS-LCO, and MAT-LCO powders were measured by Brunauer-Emmett-Teller (BET), which are 0.359, 0.370 and 0.800 m^2 g^{-1}, respectively. For CS-LCO, the formation of large single crystalline particles with low surface area and high mechanical strength will help reduce side reactions and improve structural stability.

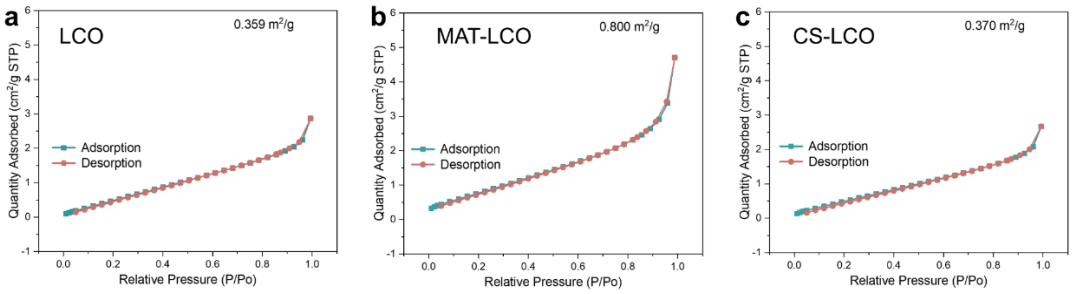

Figure 4.5 BET diagram of **a** LCO, **b** MAT-LCO, and **c** CS-LCO.

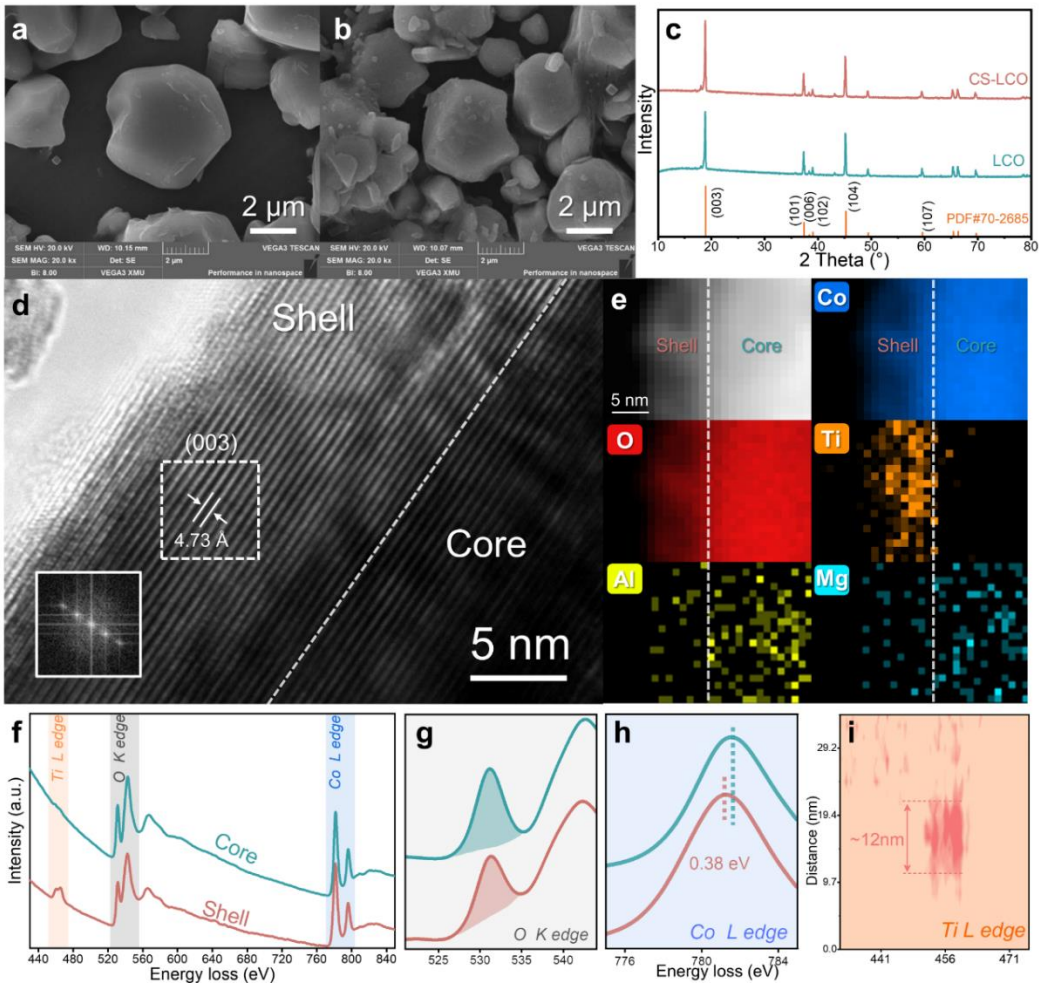

Figure 4.6 Structure characterizations. SEM image of **a** LCO and **b** CS-LCO. **c** XRD patterns. **d** HRTEM image of CS-LCO. **e** Elemental distribution. **f** EELS spectra of CS-LCO, EELS line profiling of **g** *O-K* edge and **h** *Co-L_3* edge. **i** EELS Ti L-edge intensity mapping.

XRD analysis (**Fig. 4.6c**) shows that, after co-doping, there is no detectable impurity phases in CS-LCO. All the peaks are consistent with the standard LCO, which has a typical layered α-$NaFeO_2$ structure with a space group *R-3m*[133]. The high intensity ratio of (003)/(104) peaks and clear split of (006)/(012) peaks suggest a highly ordered layered structure of CS-LCO.

The microstructural characteristics of CS-LCO are shown in **Fig. 4.6d**. After the two-step co-doping, the surface of CS-LCO remains the layered structure with the interplanar spacing of 0.473 nm. The shell layer (~12 nm in thickness) exhibits a layered structure, as demonstrated by fast Fourier transform (FFT) images. Electron energy loss spectroscopy (EELS) analysis reveals a clear difference in elemental distribution between the core and the shell regions of CS-LCO. As shown in **Fig. 4.6e**, the EELS mapping reveals a higher concentration of Ti in the shell region, while Al/Mg distribute uniformly in both the core and shell region. Above results indicate the formation of a core-shell structure.

The EELS spectra show a much higher peak intensity of Ti in the shell region than that in the core region (**Fig. 4.6f, i**). Further, the EELS spectrum mapping of Ti L-edge show that the shell layer is around 12 nm thickness. Previous research has shown that the intensity of *O-K* edge and *Co-L_3* edge are closely related to the structural stability[50]. As shown in **Fig. 4.6g-h**, the integrated area of *O-K* edge in the core is larger than that in the shell, which indicates less oxygen ligand holes and enhanced lattice oxygen stability in the shell. Moreover, the peak of *Co-L_3* edge in the shell region is 0.38 eV lower than that in the core, which could be attributed to the suppressed evolution of Co (from Co^{3+} to Co^{4+}) due to the substitution of Ti^{4+} in the shell[96, 147]. These results confirm that CS-LCO with Ti-enriched surface and Mg/Al-doped bulk is successfully prepared via the two-step cation co-doping method.

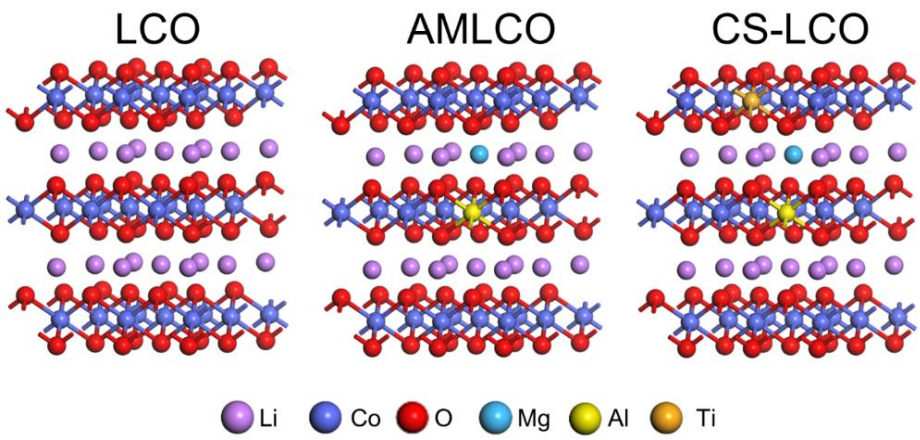

Figure 4.7 Simplified structural models.

To further clarify the effect of Ti/Mg/Al co-doping on the electronic properties and lattice stability, the electronic DOS of LCO before and after elemental doping are calculated by DFT. As shown in **Fig. 4.7a**, simplified structural models of LCO, Mg/Al-codoped LCO (AMLCO) and CS-LCO are constructed to analyze the influence of their intrinsic electronic conductivity. **Fig. 4.2d-f** illustrates that the pristine LCO exhibits semiconducting behavior with a band gap of 1.4 eV. After Mg/Al co-doping, AMLCO exhibits a metallic character with zero band gap, due to the induced orbital hybridization between Co/O and Mg/Al dopant ions near the Fermi level. The increased DOS near the Fermi level can effectively improve electrical conductivity. On the other hand, for CS-LCO, the induced Ti ion facilitates the charge balance of dopants, thereby preserving the semiconducting properties. The band gap of CS-LCO significantly reduces from 1.4 eV to 0.2 eV. These findings suggest that Ti/Mg/Al dopant ions could effectively enhance the electronic conductivity of LCO.

4.2.3 Electrochemical performance

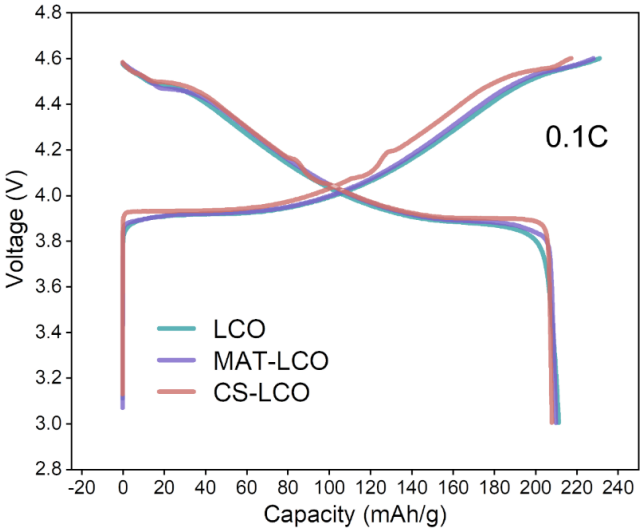

Figure 4.8 GCD profiles during the first cycle (3.0-4.6 V) at 0.1C.

The role played by the core-shell structure in stabilizing LCO cathode is evaluated by GCD profiles in half-cells within a voltage range of 3.0-4.6 V. As shown in **Fig. 4.8**, at an initial cycle of 0.1C, CS-LCO (208.6 mAh g^{-1}) and MAT-LCO (210.5 mAh g^{-1}) exhibit a lower specific capacity than LCO (211.4 mAh g^{-1}) due to the co-doping of electrochemically inactive cations, which slightly sacrifices a small amount of capacity. However, the cycling durability of these three materials shows obvious distinction.

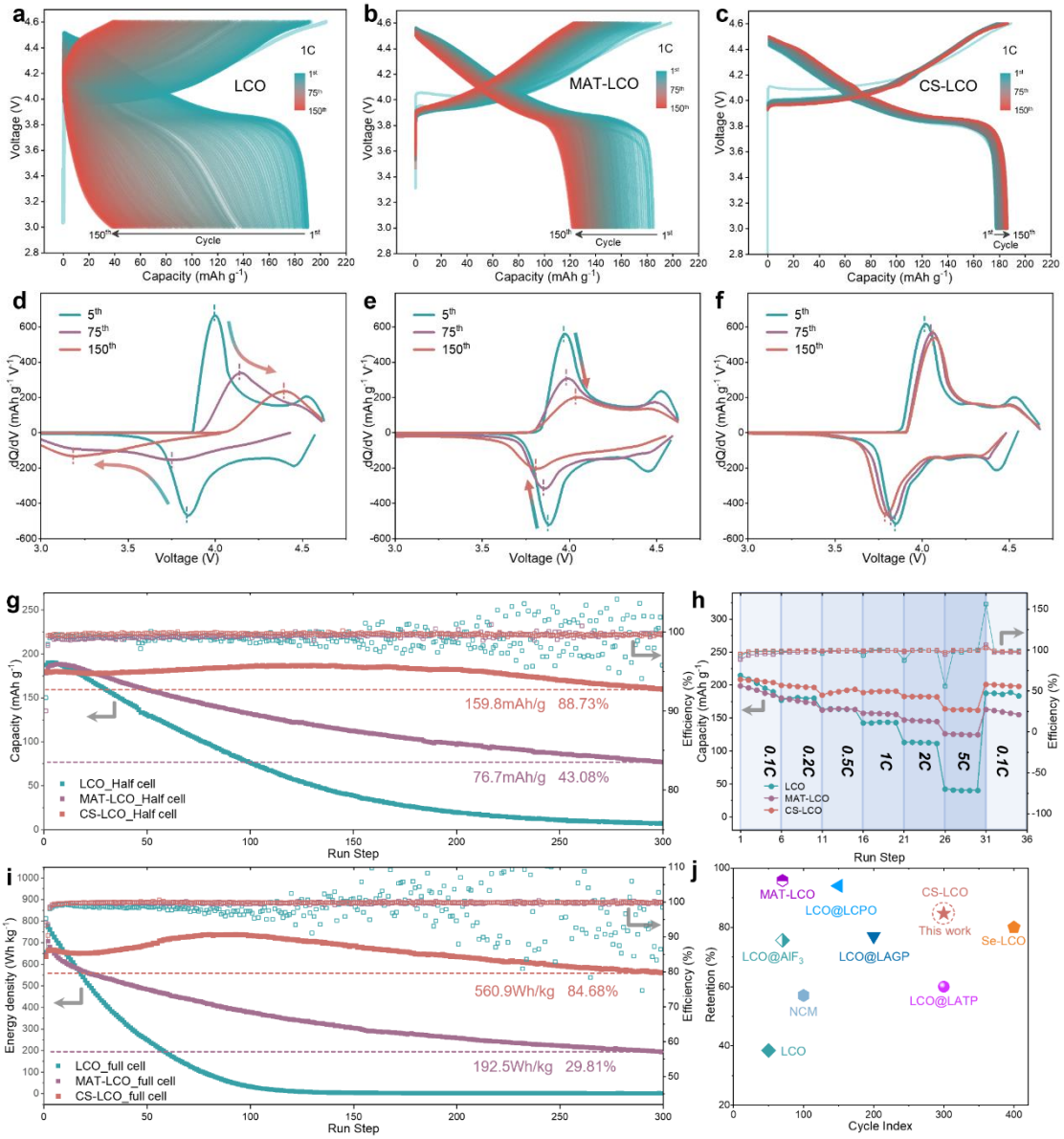

Figure 4.9 Continuous charge/discharge curves from 1st to 150th cycles of **a** LCO, **b** MAT-LCO and **c** CS-LCO at 1C under 4.6 V. Differential capacity (dQ/dV) curves at 5th, 75th and 150th cycles of **d** LCO, **e** MAT-LCO and **f** CS-LCO. **g** Cycling durability of half-cells. **h** Rate stability of half-cells. **i** Cycling durability of CS-LCO//graphite full-cells. **j** Summary of cycling lifespan of recently reported Li-ion full cells.

Fig. 4.9a-c shows the continuous charge/discharge profiles from the 1st to the 150th

cycle at 1C. The LCO displays a rapid capacity decay, resulting in a capacity of only 38.1 mAh g^{-1} after 150 cycles. In contrast, co-doping strategy is effective in improving stability, MAT-LCO exhibits a capacity of 120 mAh g^{-1}. Notably, the capacity of CS-LCO continues to increase, reaching 185.2 mAh g^{-1}.

Fig. 4.9d-f, shows the differential capacity (dQ/dV) curves measured at 5th, 75th and 150th cycles for those cathodes, respectively. For the first few cycles, all cathodes exhibit characteristic peaks at ~ 3.95, 4.21, and 4.55 V in the charge/discharge profiles. For LCO, an increased polarization and weakened characteristic peak can be observed after 150th cycles, indicating its poor structural stability under the high upper cut-off voltage of 4.6 V. Although MAT-LCO shows a little shift of the characteristic peak position, there is still a large drop in peak intensity. In contrast, the characteristic peaks of CS-LCO keep stable, indicating enhanced structural reversibility of cathode promoted by the cation co-doping strategy.

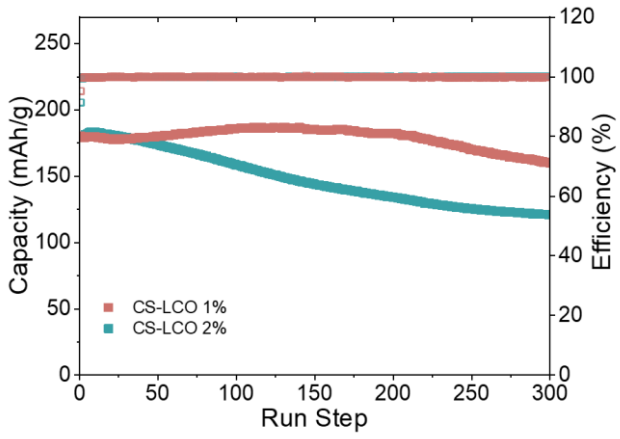

Figure 4.10 Cycling stability of CS-LCO samples (with the 1% and 2% concentration of MgO, Al_2O_3 and TiO_2 precursor) at 1C under an upper cut-off voltage of 4.6 V from 1st to 300th cycles.

Additionally, an excessively content of MgO, Al_2O_3 and TiO_2 precursor may impede Li^+ transport, leading to a cycling stability decrease after 300 cycles (1%: 88.7%, 2%: 66.7%), as shown in **Fig. 4.10**. Therefore, 1% concentration of precursor was considered the optimal doping content.

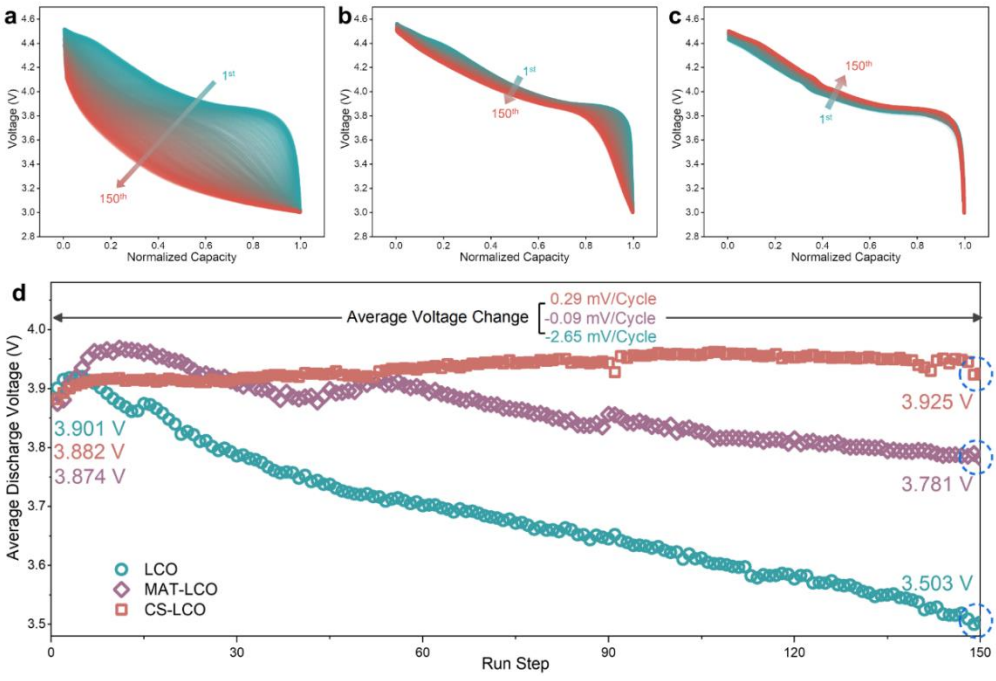

Figure 4.11 Normalized charge/discharge profiles for 150 cycles of **a** LCO, **b** MAT-LCO and **c** CS-LCO. **d** Comparison of average discharge voltage.

To further investigate the evolutions of voltage profiles, these charge/discharge curves are normalized in **Fig. 4.11a-c**. The electrochemical profiles of CS-LCO stably retain their overall shape within 150 cycles, whereas LCO suffers from dramatic voltage decay, losing its original profile. In addition, the average discharge voltage of LCO decreases from 3.901 to 3.503 V, MAT-LCO decreases from 3.874 to 3.781V, while that of CS-LCO slightly increases from 3.882 to 3.925 V (**Fig. 4.11d**). We believe that the gradually increased average voltage and reversible capacity of CS-LCO can be

ascribed to the progressive depolarization upon repeated charge/discharge cycles. The high roll strength makes low electrode porosity and inadequate infiltration for all LCO samples, indicating somewhat large electrochemical polarization. The LCO with large volume changes (**Fig. 4.14a**) and MAT-LCO with high specific surface area will result in the full infiltration of electrolyte and reduction of polarization within 10 cycles. While the weak lattice volume changes of CS-LCO (**Fig. 4.14c**) make the gradual contact between the CS-LCO and electrolyte, corresponding to the increasing average voltage and reversible capacity within 150 cycles. Even after 300 charge/discharge cycles, CS-LCO still exhibits a good capacity retention of 88.7% under 4.6 V, whereas that of LCO almost reaches zero within the same number of cycles (**Fig. 4.9g**). The rate performance (**Fig. 4.9h**) shows that the CS-LCO delivers a large capacity of 163.8 mAh g^{-1} at a high rate of 5 C, much higher than those of LCO (40 mAh g^{-1}) and MAT-LCO (125 mAh g^{-1}), suggesting its outstanding high-rate property. The CS-LCO electrode also shows reduced electrochemical polarization as the rates exceed 2 C.

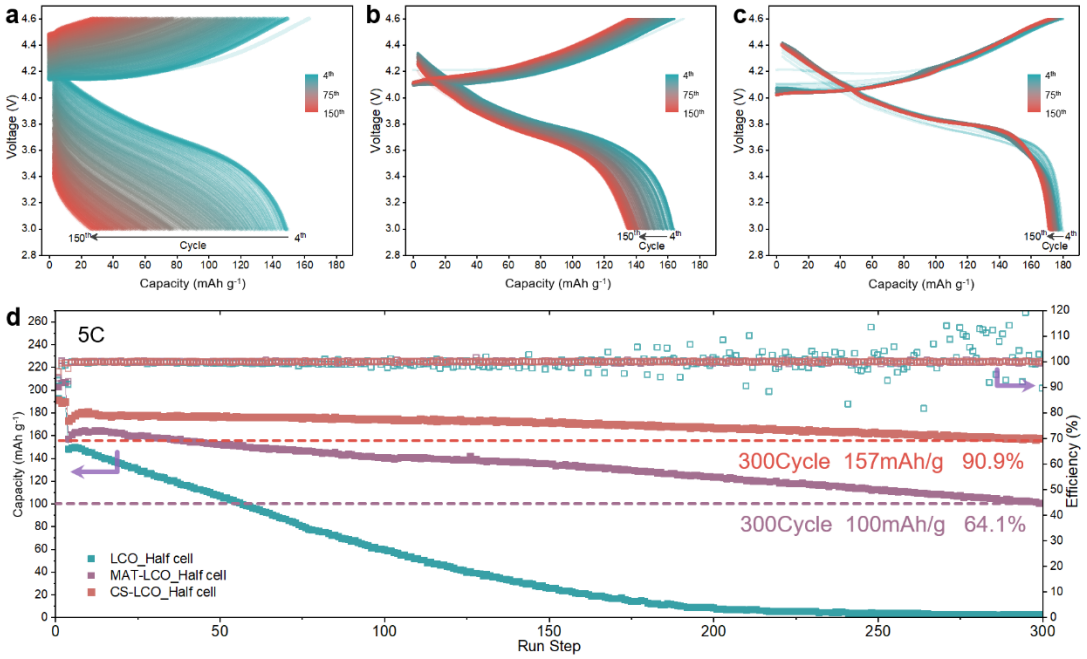

Figure 4.12 Continuous charge/discharge curves at 5C. **d** Cycling durability of half-cells, the 1st to 3rd cycles at 1C, the 4th to 300th at 5C.

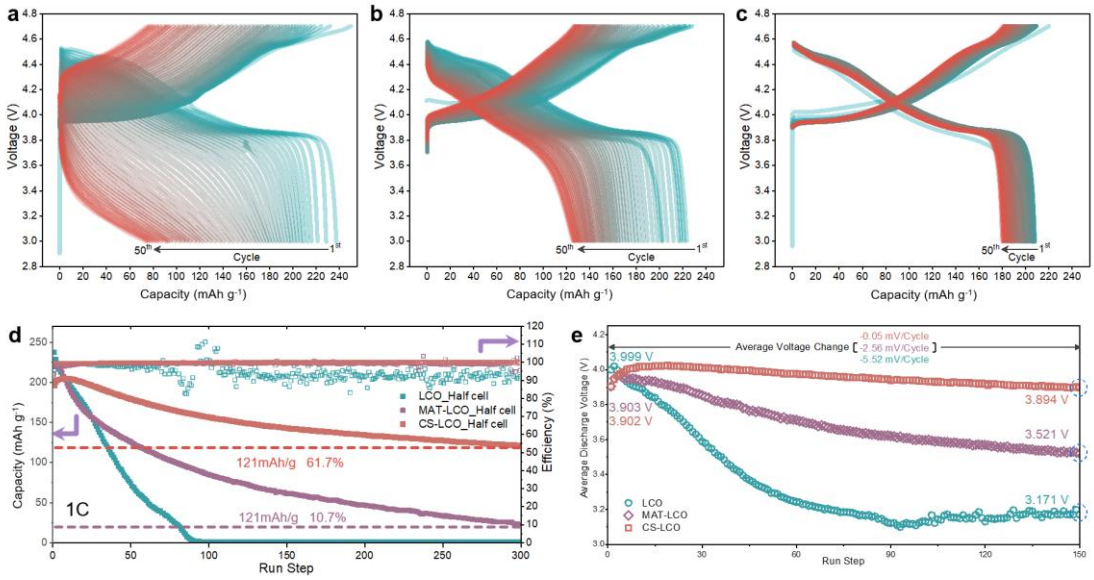

Figure 4.13 Continuous charge/discharge curves of **a** LCO, **b** MAT-LCO and **c** CS-LCO under 4.7 V. **d** Cycling durability of half-cell under 4.7 V. **e** Comparison of average discharge voltage under 4.7 V.

Moreover, the cycling durability under higher rate of 5C and higher upper cut-off

voltage of 4.7 V are measured (**Figs. 4.12-4.13**). The CS-LCO shows a capacity retention of 90.9% (157 mAh g^{-1}) under 4.6 V after 300 cycles at 5 C. And it also shows a capacity retention of 61.7% (121 mAh g^{-1}) after 300 cycles even under the higher cut-off voltage of 4.7 V. Besides, the CS-LCO//graphite full-cells exhibit exceptional long-term cycling durability, as evidenced by the capacity retention of 84.68% (569.9 Wh kg^{-1}) after 300 cycles at 1C (**Fig. 4.9i**). The comparison of reported Li-ion full cells with this work is exhibited in **Fig. 4.9j**[90, 138, 148-152], where the CS-LCO//graphite full cell reported in this work shows superior long-term cycling durability. Based on these observations, we can conclude that the core-shell structure synthesized by the co-doping strategy is effective to maintain the stability of LCO and reduce its voltage drop.

4.2.4 Mechanism of mitigating phase transition

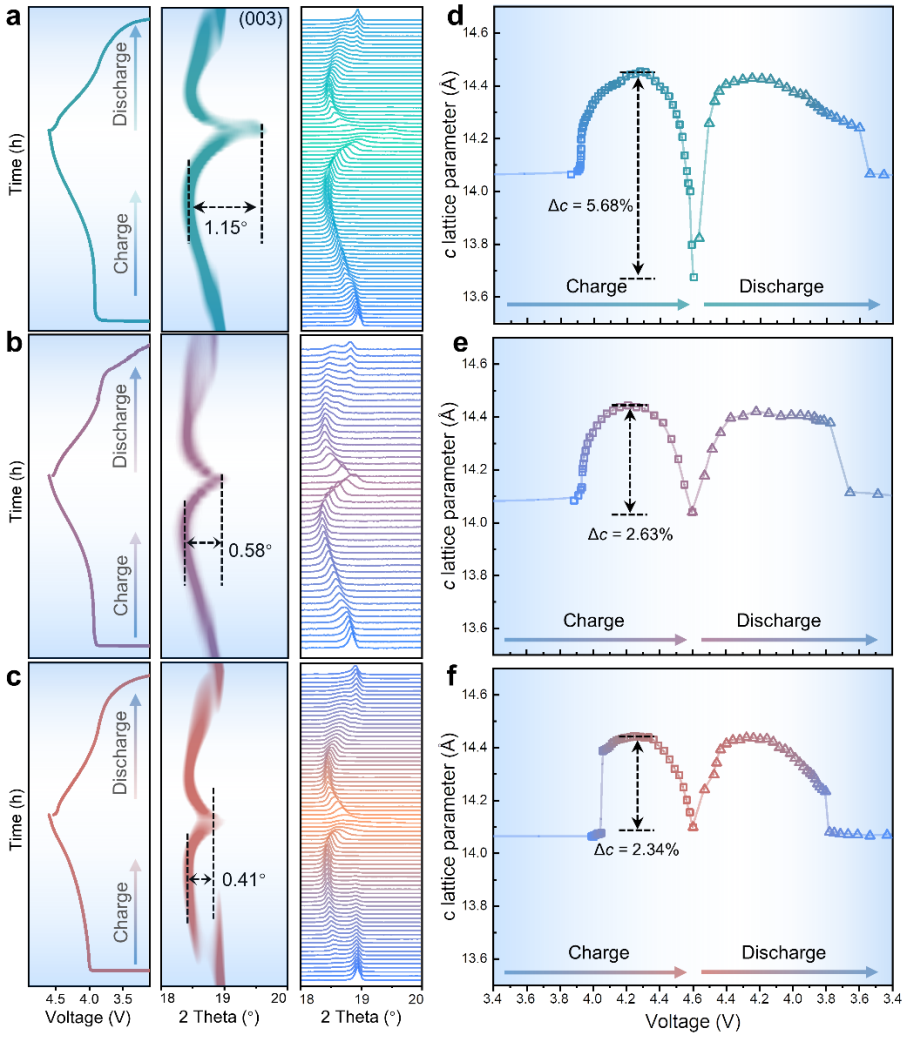

Figure 4.14 Charge/discharge curves and *in-situ* XRD results of **a** LCO, **b** MAT-LCO and **c** CS-LCO for the initial cycle. The *c* lattice evolution of **d** LCO, **e** MAT-LCO and **f** CS-LCO as a function of charge/discharge voltage.

To gain deeper insights into the structural evolutions of cathode under high voltage, *in-situ* XRD is conducted to investigate the variations in lattice parameters and phase transition behavior of LCO, MAT-LCO and CS-LCO cathodes. **Fig. 4.14a-c** shows the stacked peak profiles along with the first change-discharge cycle at 0.3C. As shown in

Fig. 4.14d-f, during charge from 3.0 to 4.2 V, phase transition from the H1 phase to the M1 phase occurs[130]. The evolution of the *c* lattice parameter, which is calculated from the (003) peak, shows similar changes for all three samples. The lattice parameter ranges from 14.06 Å to 14.43 Å. Upon charging to 4.6 V, distinct differences in the *c* lattice evolution are observed. LCO (from 14.43 Å to 13.67 Å, Δc = 5.68%) exhibits a significant contraction, whereas MAT-LCO (from 14.44 Å to 14.04 Å, Δc = 2.63%) and CS-LCO (from 14.42 Å to 14.09 Å, Δc = 2.34%) display a similar and slight contraction. Those findings suggest that pristine LCO suffers from a larger volume change (O3 to H1-3) under high voltage. As the structure transforms from O3 to H1-3, shift of the O-Co-O slabs occurs (along with Li rearrangement) and the *c*-lattice of the unit cell shrinks dramatically, resulting in internal stress accumulation and structure damage[41, 153]. In contrast, MAT-LCO and CS-LCO effectively suppress undesired lattice distortion, indicating that the layered structure is well preserved even in the highly delithiated state. Additionally, CS-LCO have a little bit higher voltage platform at the beginning of charge. As we discussed before, some Co^{3+} ions are replaced by Ti^{4+} ions, which may lead to the extraction of some Li^{+} ions for charge balance, resulting in a higher voltage platform during the charge process.

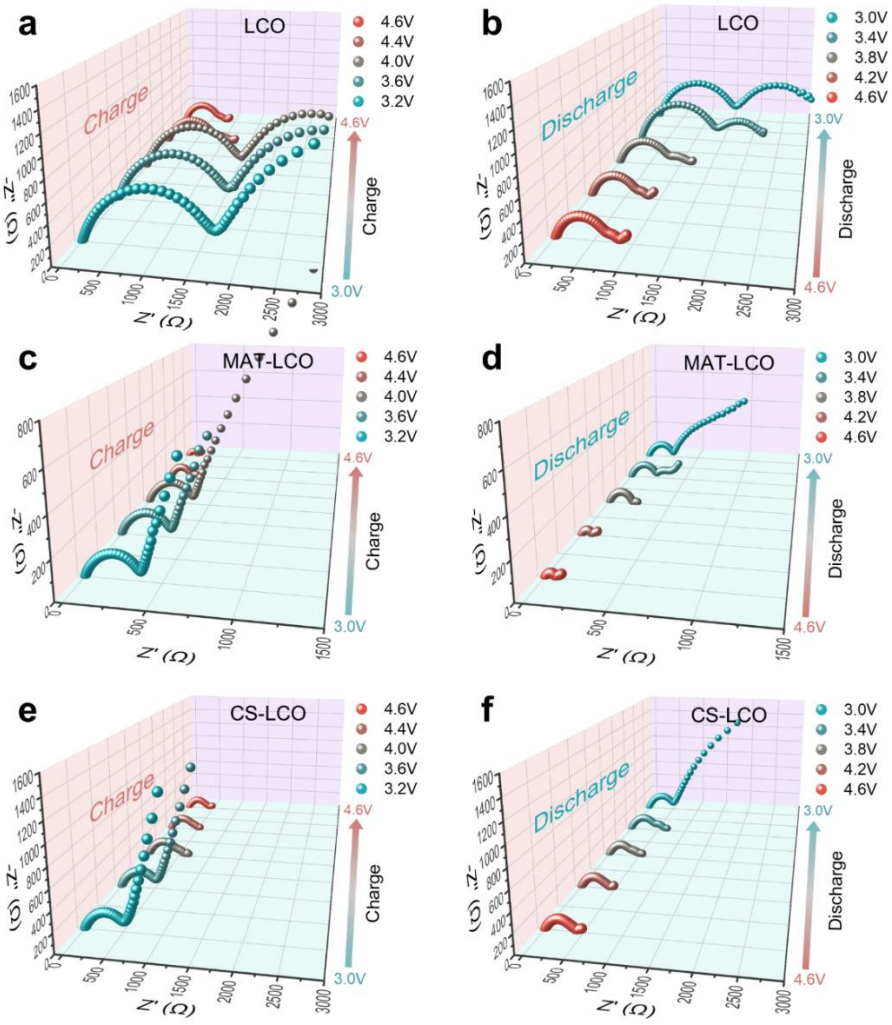

Figure 4.15 Impedance evolution during the *in-situ* charge/discharge process for **a-b** LCO, **c-d** MAT-LCO and **e-f** CS-LCO in the range of 3.0-4.6 V at 0.1 C.

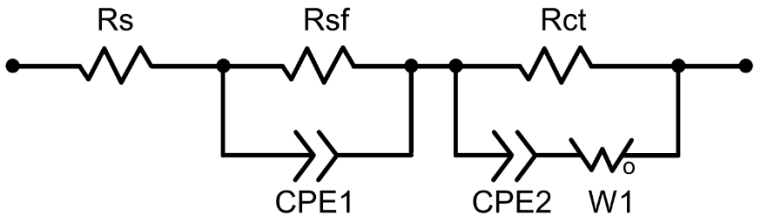

Figure 4.16 An equivalent electrical circuit that describes the impedance behavior

To further explore the changes of interfacial impedance under varied SOC, in situ electrochemical impedance spectroscopy (EIS) experiments are performed in the initial cycle (**Fig. 4.15**). **Table 4.1** shows the fitted electrochemical parameters based on the equivalent circuit shown in **Fig. 4.16**, in which R_{sf} and R_{ct} refer to the resistances of surface film and charge transfer, respectively. The R_{sf} and R_{ct} decrease gradually as the charging voltage increases from 3.2 to 4.6 V. In the subsequent discharge process, the R_{sf} and R_{ct} both increase continuously from 4.6 to 3.0 V. The CS-LCO exhibits lower electrochemical impedance than that of LCO in the initial charge/discharge process, indicating decreased charge transfer resistance and enhanced Li^+ ion diffusion during redox reactions.

Table 4.1 The simulated results from EIS spectra of LCO, MAT-LCO, and CS-LCO electrodes at various voltages during the initial charge/discharge cycle

Samples	Charge states	Simulated electrochemical parameters	
		Rsf (Ω)	*Rct* (Ω)
LCO	Charge to 3.2V	2488	1658
	Charge to 3.6V	1996	1564
	Charge to 4.0V	1761	1511
	Charge to 4.4V	424	774
	Charge to 4.6 V	329	554
	Discharge to 4.2 V	331	557
	Discharge to 3.8V	389	788
	Discharge to 3.4V	694	1437
	Discharge to 3.0V	1359	1483
MAT-LCO	Charge to 3.2V	-	364
	Charge to 3.6V	-	345
	Charge to 4.0V	-	237
	Charge to 4.4V	36	190
	Charge to 4.6 V	32	70
	Discharge to 4.2 V	41	79
	Discharge to 3.8V	37	190
	Discharge to 3.4V	167	237
	Discharge to 3.0V	706	263
CS-LCO	Charge to 3.2V	-	565
	Charge to 3.6V	-	571
	Charge to 4.0V	230	412
	Charge to 4.4V	186	318
	Charge to 4.6 V	144	314
	Discharge to 4.2 V	147	327
	Discharge to 3.8V	149	397
	Discharge to 3.4V	207	462
	Discharge to 3.0V	-	545

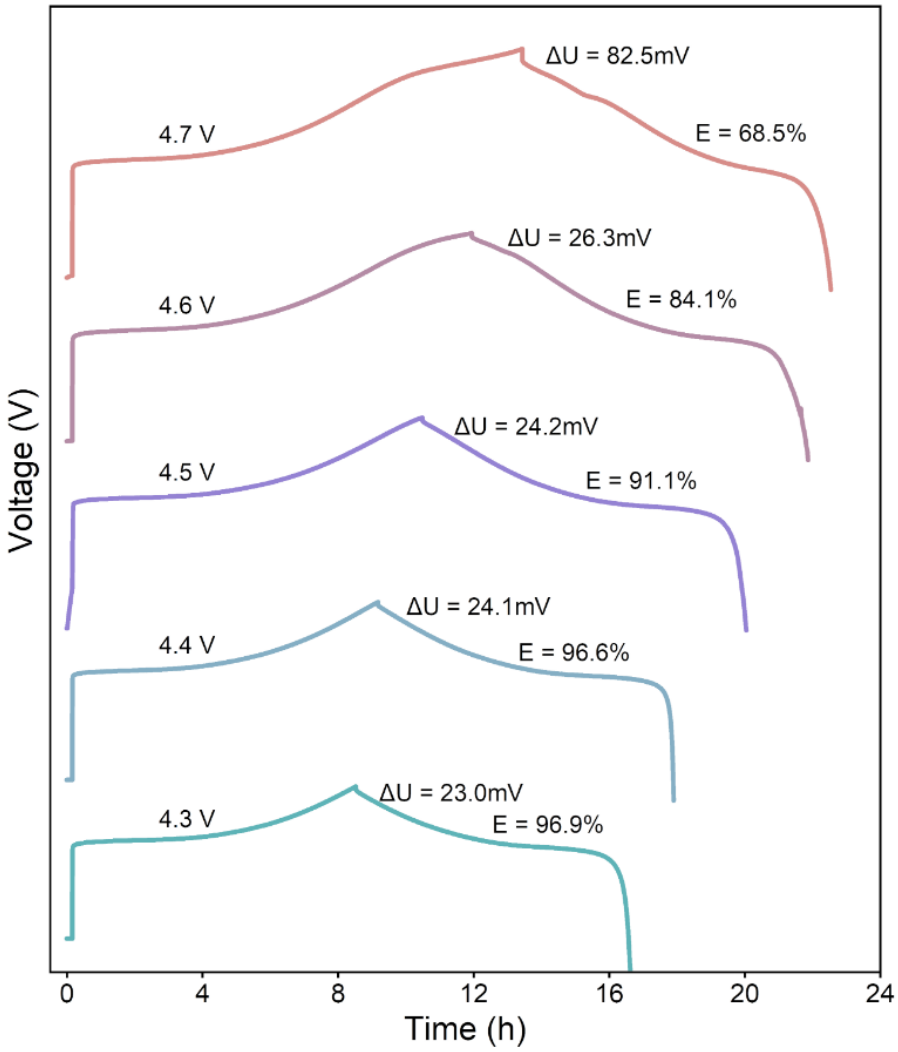

Figure 4.17 The initial charge/discharge cycle of LCO under 4.3 V - 4.7V.

In addition, as shown in **Fig. 4.17**, the polarization becomes more significant as the cut-off voltage increases, which is attributed to structural decay and electrolyte decomposition at higher voltage.

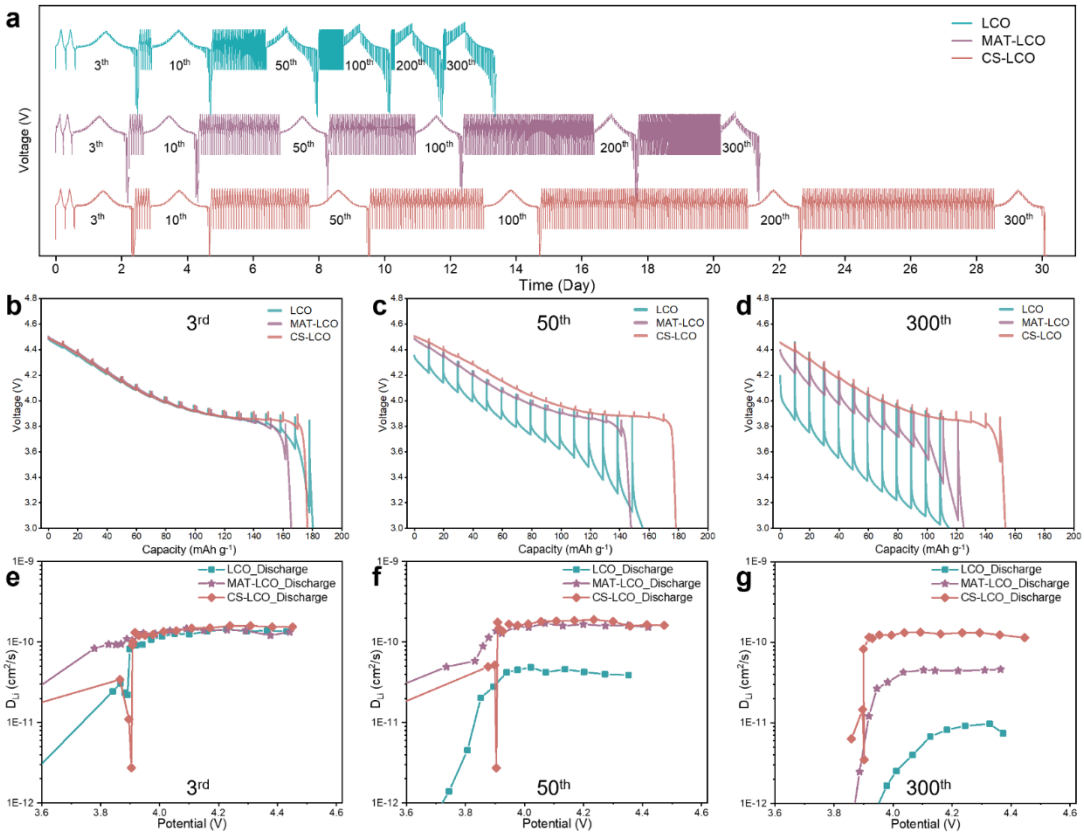

Figure 4.18 a Cycling performance and overpotential properties. The GITT curves of **b** LCO, **c** MAT-LCO and **d** CS-LCO at the 3rd, 50th, and 300th cycle. The corresponding Li^+ ion diffusion coefficients of **e** LCO, **f** MAT-LCO and **g** CS-LCO at the 3rd, 50th, and 300th cycle.

The galvanostatic intermittent titration technique (GITT) is further used to quantitatively evaluate the chemical diffusion coefficient of Li^+ ion (D_{Li+}, $cm^2\ s^{-1}$) by different methods[154-156]. GITT measurements are conducted at 0.3 C in the initial two cycle and 1C in 3rd - 300th cycles. As shown in **Fig. 4.18a-d**, CS-LCO exhibits the smallest electrode polarization during the 3rd - 300th cycle, whereas LCO and MAT-LCO exhibit rapid increase of electrode polarization since the 50th cycle. Besides, CS-

LCO takes 30 days to complete 300 cycles, which is longer than LCO (13 days) and MAT-LCO (21 days). The longer cycling time means CS-LCO has the better cycling durability.

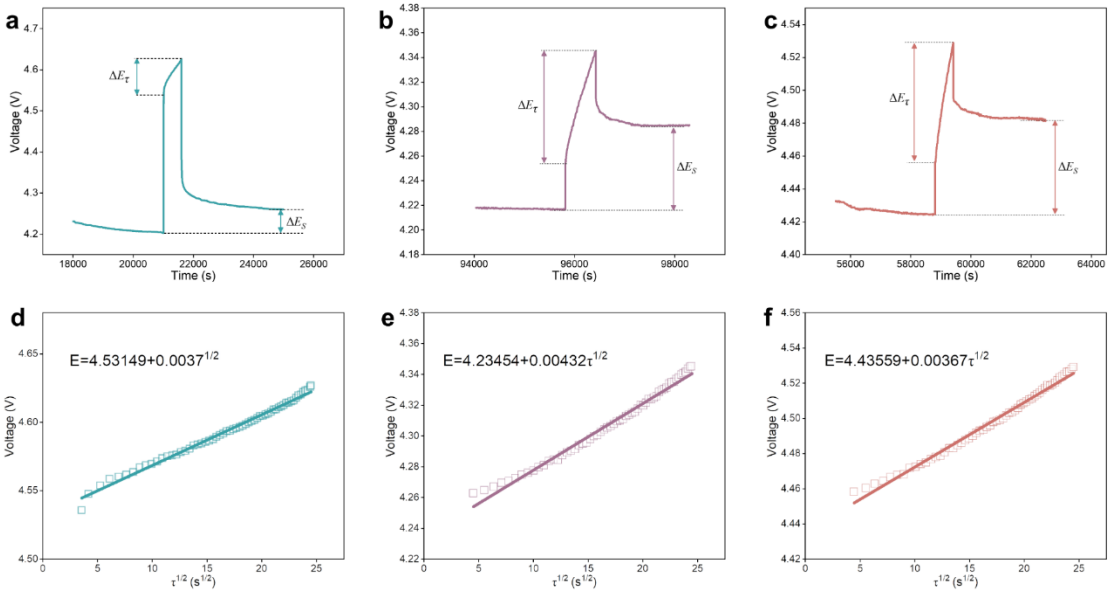

Figure 4.19 A typical time versus potential profile of **a** LCO, **b** MAT-LCO and **c** CS-LCO. A linear relationship between potential and $\tau^{1/2}$ of **d** LCO, **e** MAT-LCO and **f** CS-LCO.

The typical potential versus time profiles of LCO, MAT-LCO and CS-LCO are shown in **Fig. 4.19**. A linear relationship between potential and $\tau^{1/2}$ can be observed, and D_{Li+} can be calculated based on the Fick's second law as follows[157, 158].

$$D = \frac{4}{\pi\tau}\left(\frac{mV_M}{MA}\right)^2\left(\frac{\Delta E_S}{\Delta E_\tau}\right)^2 \quad (1)$$

where m and M indicate the mass and molar mass of the electrode material, respectively. V_M ($cm^3\ mol^{-1}$) refers to their molar volume, and A (cm^2) stands for their active area. The D_{Li+} evolution of cathodes during cycling is shown in **Fig. 4.19e-g**.

The calculated D_{Li+} values are similar for the three cathodes during the 3rd cycle, where the average D_{Li+} is around 1.4×10^{-10} cm^2 s^{-1}. The average D_{Li+} of CS-LCO has almost no change during the 50th - 300th cycle, while that of LCO drastically decreases. The GITT results confirm that the effectively co-doping strategy can maintain the stable Li^+ diffusivity. As confirmed by *in-situ* XRD, LCO undergoes a large contraction of ***c*** lattice due to the phase transition of O3 to H1-3 when charging voltage exceeds 4.5 V. This large contraction result in severe structural distortion and the formation of a thick CEI during repeated cycles, which potentially block the Li^+ diffusion[72, 144]. In contrast, cation co-doping in CS-LCO helps facilitate the (de)intercalation of Li^+ ions and prevent the structure distortion, hence maintaining a high Li^+ diffusion coefficient even after long-term cycling.

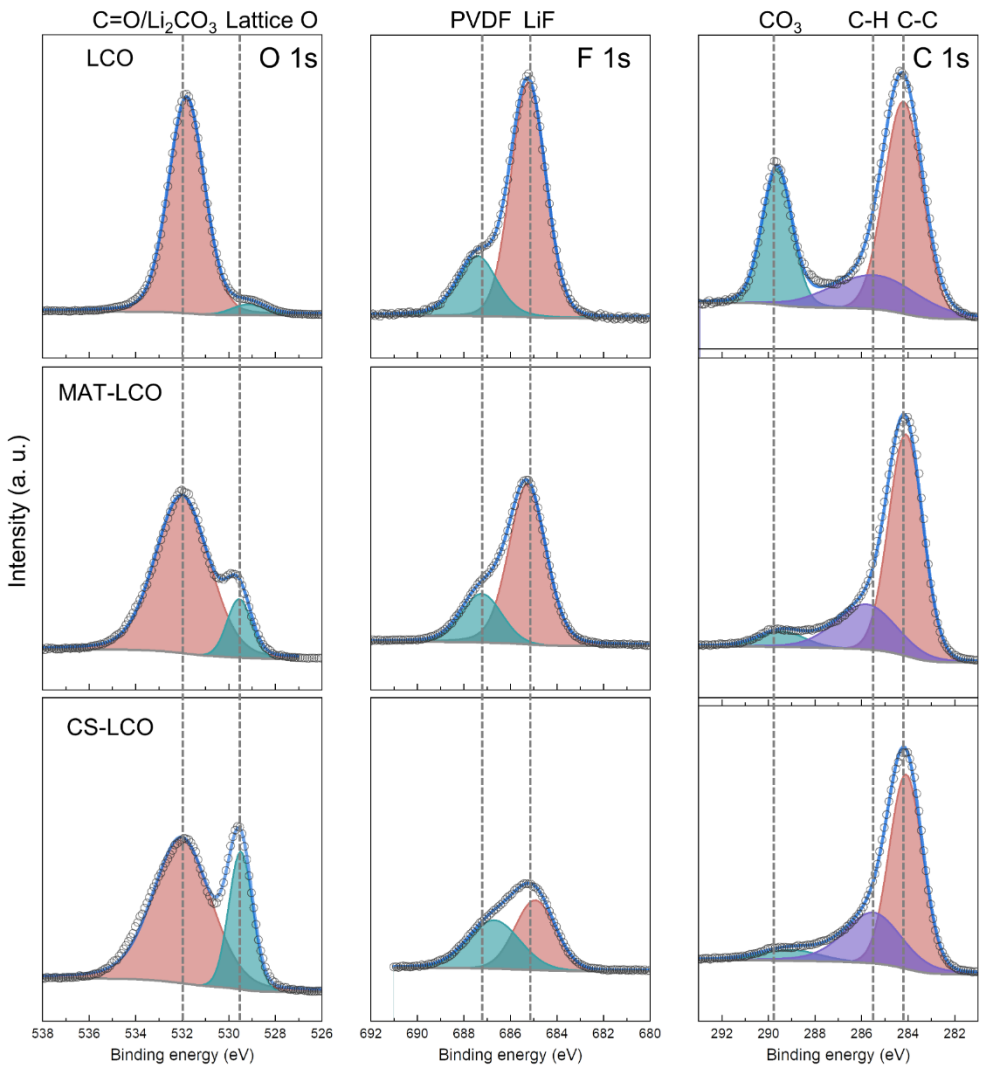

Figure 4.20 The O 1s, F 1s and C1s XPS spectra after 100 cycles.

To further examine the change of surface composition of cathode after cycling, XPS was introduced to characterize the CEI layer. In general, C=O/Li_2CO_3 (531.0 eV) and CO_3^{2-} (290.0 eV) are related to the presence of Li_2CO_3. As shown in **Fig. 4.20,** it can be found that, compared with LCO, the amount of carbonate was obviously reduced after co-doping (MAT-LCO and CS-LCO).

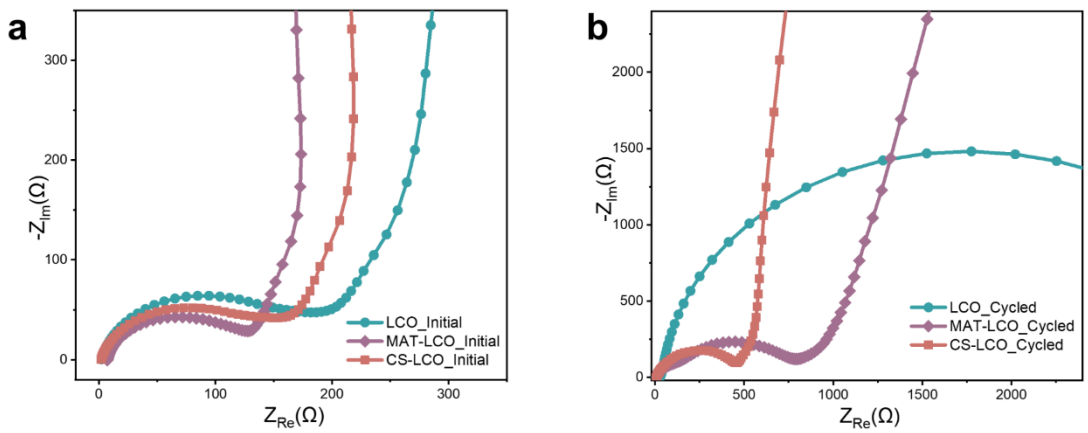

Figure 4.21 The Nyquist plots of the LCO, MAT-LCO and CS-LCO electrodes: **a** initial cycle and **b** after 100 cycles.

The presence of more carbonate on the surface always results in higher impedance, which is consistent with EIS results as shown in **Fig. 4.21**. As for F 1s, the peaks are primarily assigned to LiF (685 eV) and PVdF (687 eV). LiF is the main F-containing components in CEI due to the prevailing HF attack at cathode surface, resulting in capacity fading under high voltage[159]. The relatively low content of LiF in CS-LCO indicates a thinner CEI layer, and the reduced side reaction at cathode/electrolyte interface. As for the O 1s, the higher intensity of lattice oxygen (529.5 eV) obtained from CS-LCO confirms the suppressed lattice oxygen oxidizing ability.

4.2.5 Structural evolution after long cycling

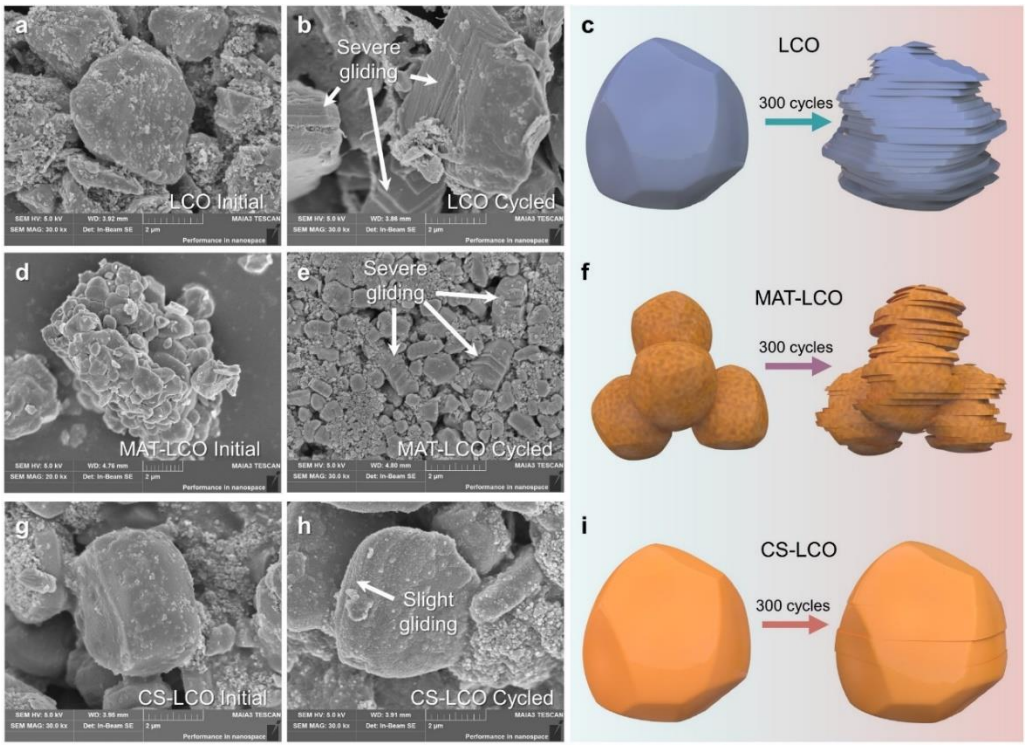

Figure 4.22 SEM images and the corresponding schematic diagrams of the initial and after 300 cycles of **a-c** LCO, **d-f** MAT-LCO and **d-i** CS-LCO cathodes

Previous studies reported the origin and evolution of gliding layers and microcracks under high voltage[160]. Charging to a high voltage, more Li^+ ions are extracted from the original structure, resulting in the slab gliding of layered structure. Typically, these gliding traces will disappear in the subsequent discharge process if the structural change is reversible. However, there are also irreversible gliding events that accumulate over long-term cycling and form microcracks, exposing fresh surfaces to the electrolyte. The penetration of the liquid electrolyte along the layered gliding increases the risk of electrolyte decomposition.

Fig. 4.21 shows the observation of lattice plane gliding at 4.6 V after 300 cycles. For LCO, the gliding traces are evident as in-plane shear along the (003) plane, vertical to the *c* axis of the layered structure, which ultimately results in the accumulation of irreversible structural deformation and the creation of significant cracks. Moreover, serve gliding is also observed in small primary particles of MAT-LCO, possibly due to the larger contact area with the electrolyte. In contrast, the entire structure of CS-LCO is well maintained after 300 cycles, showing almost reversible gliding. Notably, due to the capacity decay, LCO can only be cycled for 195 hours at 1C (relative to the theoretical capacity), whereas CS-LCO can be cycled for 825 hours, four times the cycling time of LCO (**Fig. 4.18a**). These results indicate the crucial role played by co-doping induced core-shell structure in effective suppressing irreversible gilding and maintaining structural integrity.

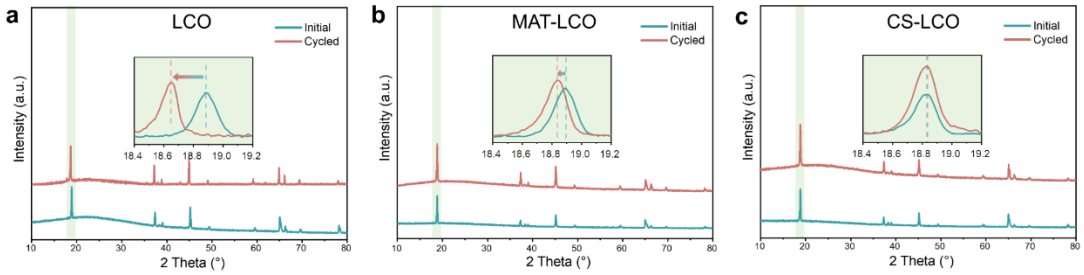

Figure 4.23 The XRD patterns of **a** LCO and **b** MAT-LCO and **c** CS-LCO cathodes before cycling and after 100 cycles

As shown in **Fig. 4.13**, LCO undergoes a significant phase transition process under 4.6 V. The accumulation of volume changes and layer gilding eventually leads to the collapse of the structure. To further illustrate the structural degradation after long-term cycling, *ex-situ* XRD is performed. The (003) peak of LCO and MAT-LCO moves to a

lower diffraction angle after 100 cycles (**Fig. 4.23**), indicating the Li^+ irreversible de-intercalation probably caused by structural transition and accumulation of SEI film during continuous cycling. In contrast, CS-LCO exhibits a weak shift of (003) peak and enhanced structural reversibility. In addition, the collapse of layered structure and the larger surface area can increase the possibility of the liquid electrolyte decomposition during long-term cycling. This could result in the larger charge transfer impedance, as shown in **Fig. 4.21b**.

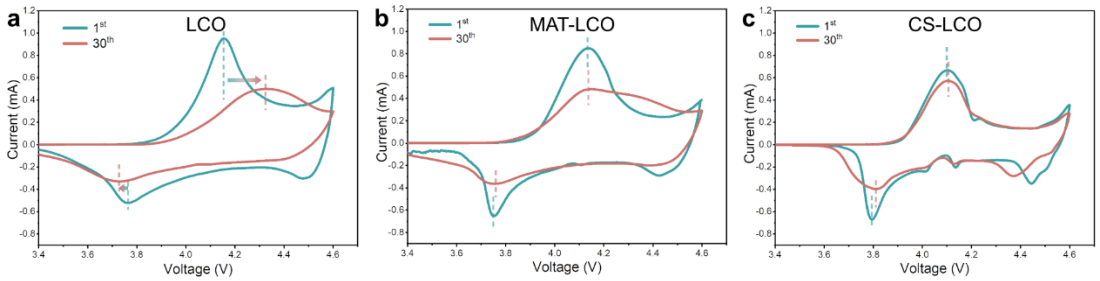

Figure 4.24 The CV curves of **a** LCO, **b** MAT-LCO and **c** CS-LCO at initial cycle and after 30 cycles at 0.1 mV s^{-1} in half-cell configuration

The redox kinetics are explored through cyclic voltammetry (CV) scanning as shown in **Fig. 4.24**. During the discharge process, the cathodic peaks at 4.45 V, 4.1V and 3.8 V relate to the phase transition of H1-3/O3, the order-disorder phase transition, and the phase transition of M2/H3, respectively[13, 90]. With increasing scanning cycles, the peaks of LCO are weakened gradually and the polarization phenomena become more pronounced. These observations suggest that the phase transitions of H1-3/O3 and H2/H1 become irreversible. Notably, the peaks of the anodic process of CS-LCO are sharper than LCO, indicating faster charge transfer kinetics. After 100 cycles, the redox peak positions and intensities of CS-LCO remain almost unchanged,

demonstrating its exceptional structural reversibility and stability during long-term cycling at high voltage.

$$V = d^3 \times \frac{\pi(2 + \cos\theta)(1 - \cos\theta)^2}{24sin^3\theta} \quad (2)$$

4.3 Conclusion

In summary, a single-crystal core-shell LCO (CS-LCO) cathode is designed and synthesized by a simple two-step co-doping strategy. This reliable co-doping strategy results in the preservation of single-crystal morphology and the suppression of phase transition under deep delithiation. In this designed core-shell structure, high-diffusivity Mg^{2+}/Al^{3+} ions are doped into the core region of single-crystal particles to optimize physical properties, such as conductivity and Li^+ ion diffusivity, while low-diffusivity Ti^{4+} ions enrich the shell layer to enhance the surface structure stability. Under a high cut-off voltage of 4.6 V, CS-LCO exhibits a stable capacity of 159.8 mAh g^{-1} (88.73% retention) at 1C after 300 cycles, and reaches a high capacity of 157 mAh g^{-1} (90.9% retention) at 5C after 300 cycles. Even at a higher cut-off voltage of 4.7 V, CS-LCO still exhibits good retention of ~61.7% at 1C after 300 cycles. These achievements may provide guidance for the rational design of core-shell structured cathodes with multiple dopants involving low-diffusivity cations (Zr^{4+}, Ta^{5+}, W^{6+}, etc.) and high-diffusivity ones (Zn^{2+}, Ni^{2+}, Fe^{3+}, etc.).

Chapter 5 Effective coating by $AlPO_4$-5 zeolite

In Chapter 5, we propose a multifunctional $AlPO_4$-5 zeolite coating with unique porous structure for developing high voltage LCO (LCO@Z). The $AlPO_4$-5 zeolite serves as a protecting layer over LCO, with good crystallinity, ordered porous channels and full surface coverage. It acts multifunctionally to remarkably alleviative phase transition via suppressing the oxygen release at high voltage, enable fast Li^+ diffusion through its nanoporous structure, accelerate the Li^+-desolvation on the cathode/electrolyte interface, and boost the redox kinetics, as supported by various *in-situ* and *ex-situ* measurements. Such zeolite coating strategy provides a new way for developing high-energy-density LIBs with great application potential.

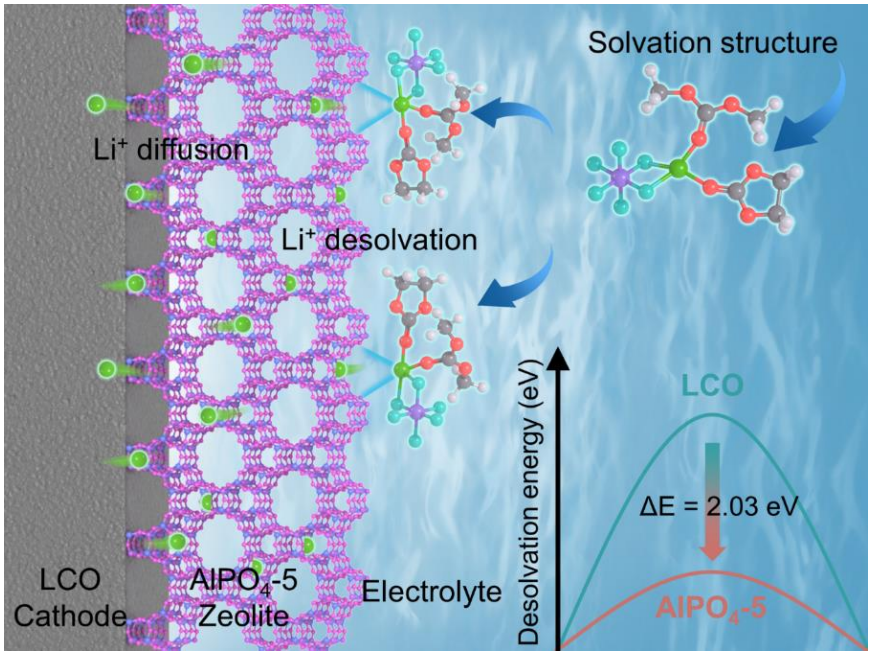

Figure 5.1 Graphic abstract of LCO@Z.

5.1 Introduction

LIBs utilizing LCO cathode and graphite anode, operating at 3.7 V, have seen widespread adoption in personal electronic equipment owing to their favorable volumetric energy density, high cyclability, and high safety. With the quickly rising demand for smart portable electronic devices, there is an urgent need for further significant improvement in the volumetric energy density of portable power source[23, 25, 161]. The cathode material is widely recognized for its pivotal influence on the energy density, cycling lifespan, and cost of LIBs. Among various cathode materials explored within the contemporary battery community, the first commercialized LCO oxide electrode with ultrahigh compaction density still dominates the market of high-volumetric-energy-density LIBs because of its numerous benefits[19, 85]. Currently, only about half of the theoretical capacity of LCO has been utilized, leaving a big room for improvement of its reversible capacity.

A simple and efficient approach to improve the energy density of a LIB involves raising the upper cut-off voltage of the cathode. Over recent years, significant endeavors have been dedicated to increase the reversible specific capacity and the energy density of corresponding LIBs. Unfortunately, numerous challenges exist for high-voltage operation of the commercial LCO cathode, including irreversible phase transitions, structural collapse, interfacial side reactions, and oxygen escape, all intertwined with the inherent high-voltage instability. These factors collectively pose negative impacts on the reversible capacity, cycling durability and safety[22, 162, 163].

Surface and/or bulk modification of LCO is necessary to make it applicable for operation at high voltage. Surface coating stands out as a promising strategy to improve the structural stability of high-voltage LCO cathode by preventing the direct interaction between cathode and electrolyte[164, 165]. An ideal coating layer should possess high Li^+ conductivity to ensure high-rate performance of the electrode while minimize electrode-electrolyte contact to reduce side reactions. Traditional coating matrixes mainly include oxides, phosphates, fluorides, and carbonaceous materials. Previous studies demonstrated that the stable phosphate-based coatings can mitigate the detrimental side reactions and enhance the electrochemical performance of cathode materials[91, 97, 144, 151, 152, 166]. However, in traditional aqueous preparation methods, aluminum salts and phosphate salts, due to their weak surface adsorption capability on the cathode material, tend to form amorphous coating in the form of non-uniform island structures with large areas of fragmented phosphate salts, and the amorphous coating itself is poor in Li^+ or electron conduction[97-100]. Therefore, it is crucial to take both the crystallinity and surface coverage of the coating layer into consideration, as excessive thickness or an amorphous structure will hinder Li^+ diffusion and partial surface coverage cannot fully protect the cathode, leading to diminished electrochemical performance[164]. Moreover, the sluggish Li^+-desolvation may also occur at the cathode/electrolyte interface upon Li^+ intercalation into the host structure during discharging process, which further hampers the redox kinetics of LIBs[167-170]. Although the traditional phosphate-based coating matrixes can enhance

cathode stability, they also create an intrinsic physical barrier that blocks the Li^+ diffusion pathways. This barrier exacerbates the already slow Li^+-desolvation process, particularly at low temperatures below 0℃. Therefore, an ideal coating should possess the following features simultaneously, (1) good crystallinity for fast Li^+ diffusion, (2) properly sized and ordered porous channels for efficient Li^+-desolvation, and (3) full surface coverage for complete electrochemical and mechanical protection of cathode.

Here, we propose a multifunctional $AlPO_4$-5 zeolite coating layer on LCO cathode. We applied triethylamine template to facilitate the full coverage of uniform crystalline phosphate-based zeolite coating on the LCO grain surface by increasing the number of nucleation sites via decreasing the surface adsorption energy. $AlPO_4$-5 zeolite possesses a unique porous structure that establishes a stable diffusion pathway for Li^+ ion transport, where the proper pore size efficiently accelerates the Li^+-desolvation process. At the same time, the zeolite coating effectively minimizes the direct contact between the electrode and the organic liquid electrolyte, thereby improving the durability of cathode. In addition, the full coverage of the highly porous coating layer acts as a robust elastic matrix to provide mechanical clamps on the cathode during charge-discharge process, thus avoiding the delamination of cathode grains during cycling. As a result, high performance LCO with long cycle life can be realized at high-voltage.

5.2 Results and discussion

5.2.1 $AlPO_4$-5 zeolite coating preparation

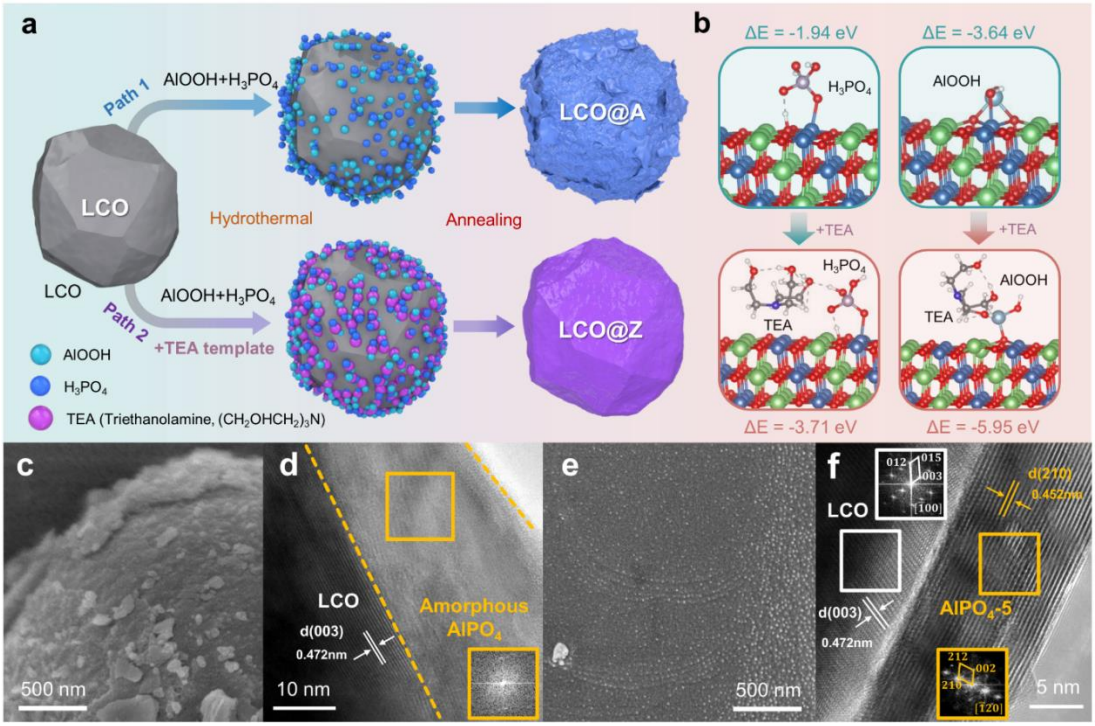

Figure 5.2 Conceptual design and preparation. **a** Schematic illustration of the synthesis design of LCO@A and LCO@Z. **b** Adsorption configurations and the corresponding adsorption energies (ΔE) of H_3PO_4 and AlOOH on LCO (upper panel) and TEA-modified LCO (lower panel). **c** SEM and **d** HRTEM images of LCO@A. **e** SEM and **f** HRTEM images of LCO@Z.

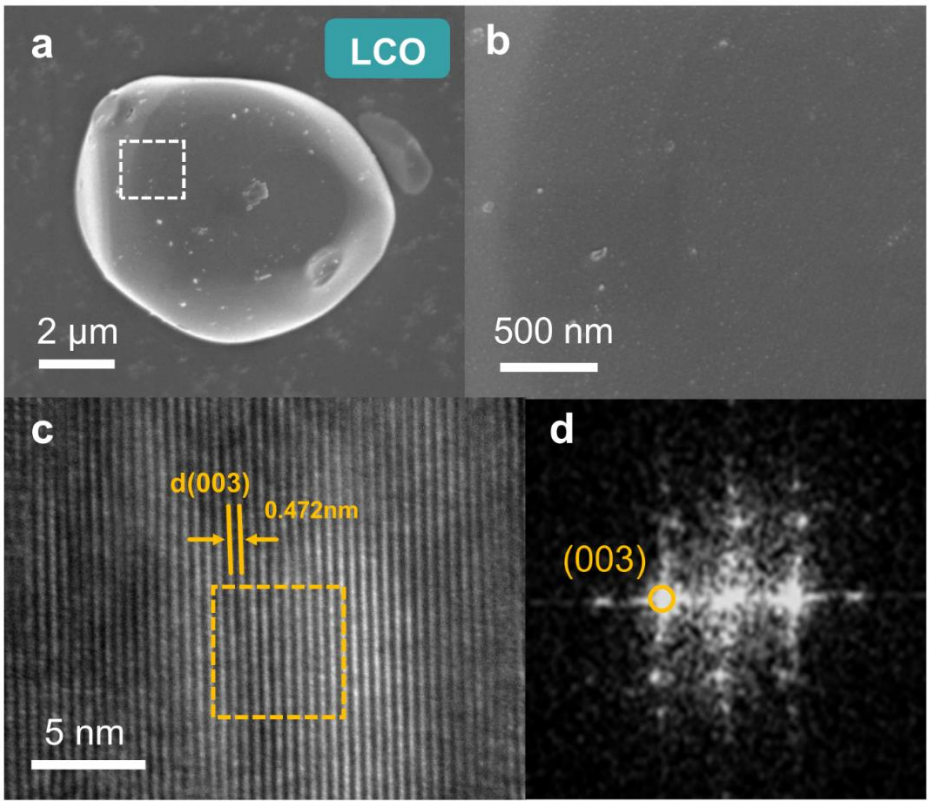

Figure 5.3 a SEM image of pristine LCO, and **b** magnified area of the white rectangle in **a**. **c** HRTEM image of pristine LCO and **d** FFT pattern of the orange rectangle in **c**.

Fig. 5.2a schematically illustrates the two different paths for $AlPO_4$ surface engineering of LCO, which are prepared with/without template agent. As shown in **Fig. 5.3**, the pristine LCO exhibits a relatively smooth surface and possesses a layered structure with a lattice spacing of 0.472 nm. In the tradition path 1 without template, amorphous and inhomogeneous $AlPO_4$ coated LCO (LCO@A) is achieved (**Figs. 5.2c, d** and **5.4**), which is like those reported phosphate-based coatings[171-173].

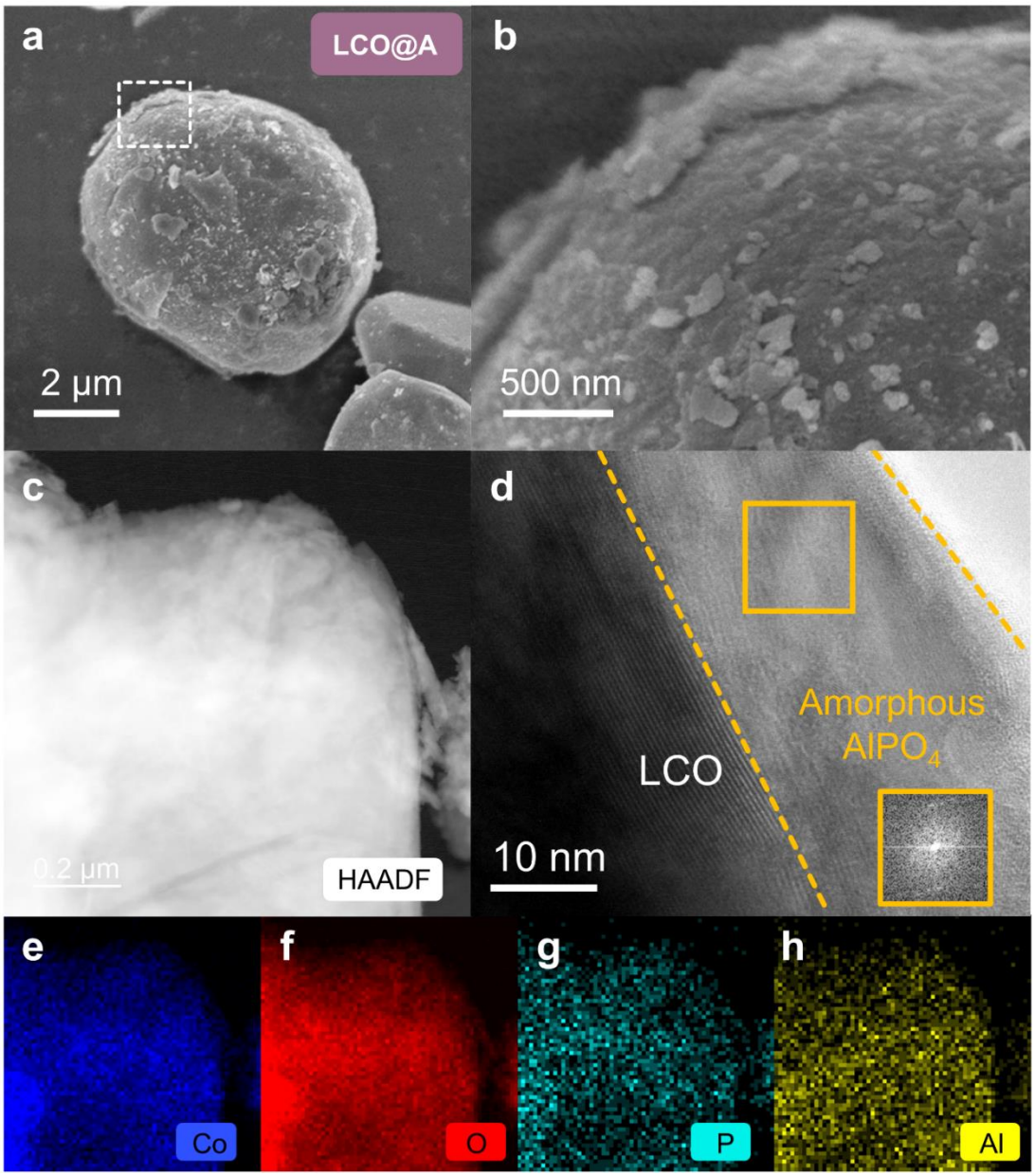

Figure 5.4 a SEM image of LCO@A, and **b** magnified area of the white rectangle in **a**. **c** HADDF and **d** HRTEM images of LCO@A and elemental distribution of **e** Co, **f** O, **g** P and **h** Al.

In the path 2 with triethylamine (TEA) template, the crystalline and homogeneous $AlPO_4$-5 zeolite fully coated LCO (LCO@Z) is successfully synthesized (**Figs. 5.2e, f** and **5.5**), where the introduction of template induces the phase transition from

amorphous to crystalline structure and the uniform formation of $AlPO_4$-5 zeolite coating layer. TEM combined with FFT images demonstrate the presence of a crystalline $AlPO_4$-5 zeolite coating layer on the surface of LCO. The coating layer exhibits a uniform thickness of approximately 10 nm.

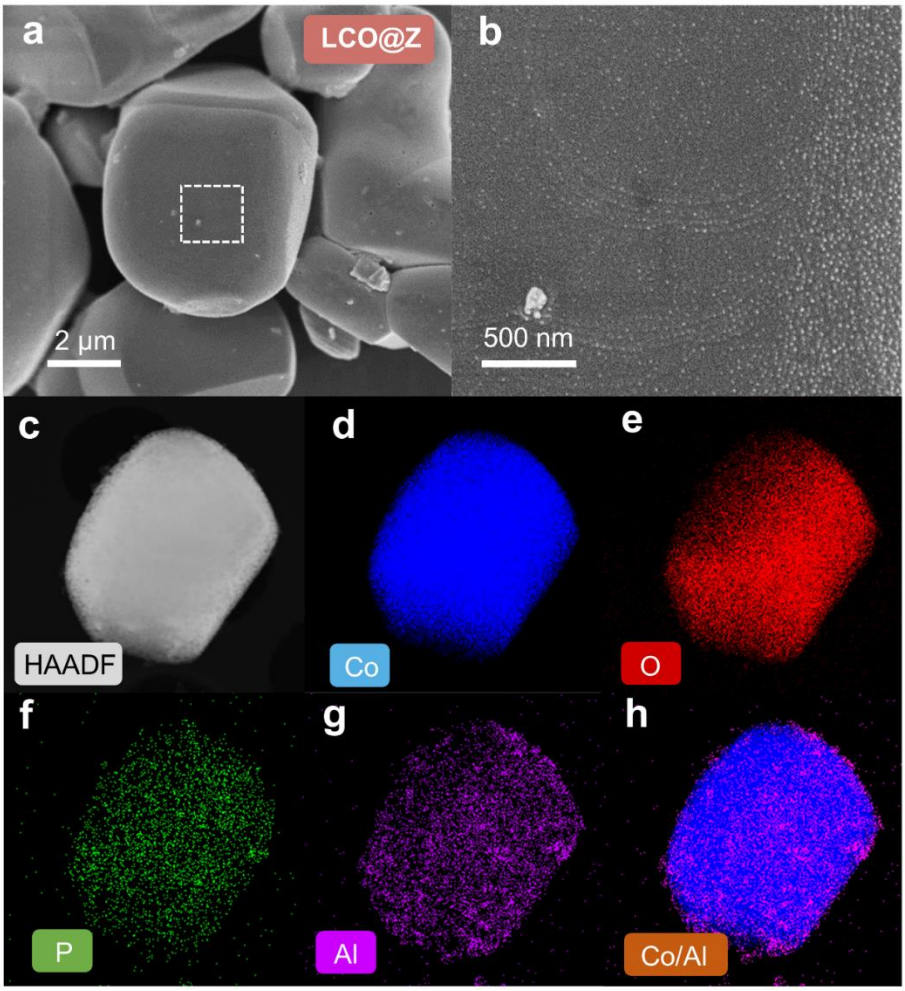

Figure 5.5 a SEM image of LCO@Z, and **b** magnified area of the white rectangle in **a**. **c** HADDF image of LCO@Z and elemental distribution of **d** Co, **e** O, **f** P, **g** Al and **h** Co/Al mixed.

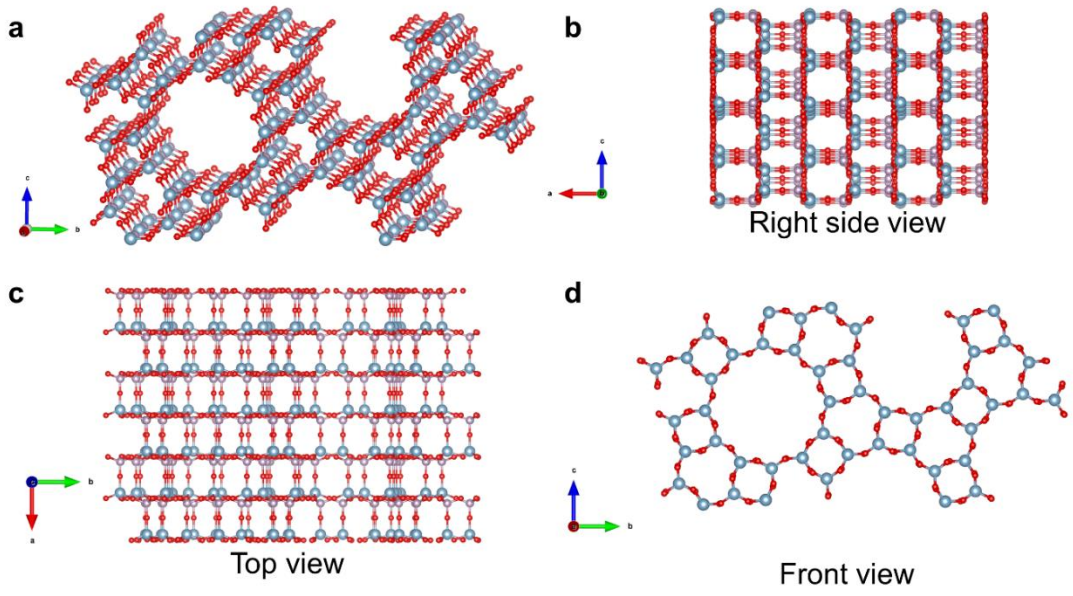

Figure 5.6 Three view of the atomic structure of the (210) slab of $AlPO_4$-5 zeolite.

The atomic structure of the (210) slab for $AlPO_4$-5 zeolite exhibits open-framework structures for Li^+ diffusion in different directions, as shown in **Fig. 5.6**. The organic structure directing agent a pivotal role in shaping the framework topology of the zeolite material[174]. In the gel, TEA acts as a structure directing agent by accepting or donating protons from the phosphoric acid (P-OH), forming hydrogen bonds with it. This interaction facilitates the incorporation of P-OH into the zeolite framework. TEA also forms stable chelation complexes with Al^{3+} ions and PO_4^{3-} ions, contributing to the formation of a stable framework structure of $AlPO_4$-5 zeolite during the hydrothermal process under high pressure[175]. The utilization of TEA as a template promotes the phase transformation of amorphous $AlPO_4$ into crystalline $AlPO_4$-5 zeolite state, as confirmed by XRD results (**Fig. 5.7**), demonstrating the important role played by TEA on the induced phase transformation of $AlPO_4$-5.

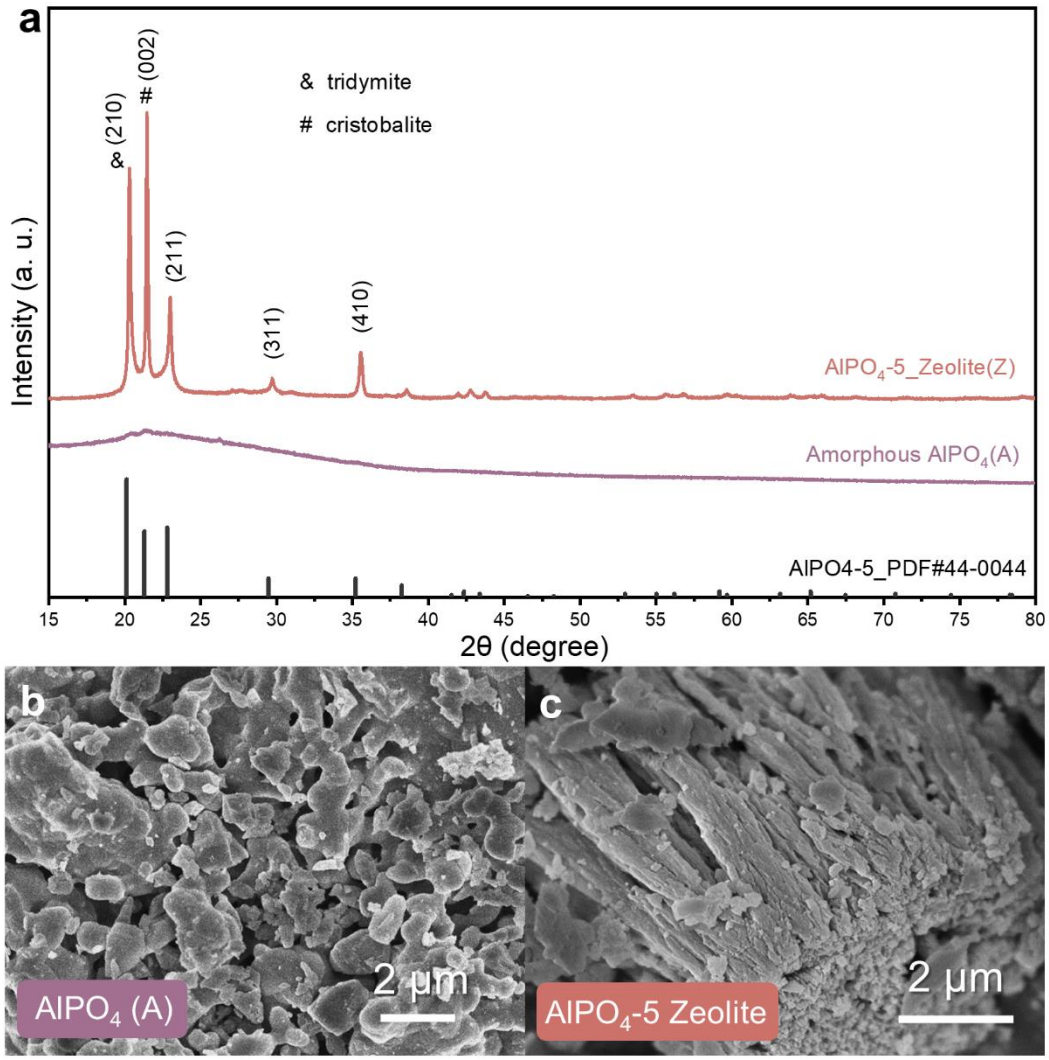

Figure 5.7 a XRD patterns of $AlPO_4$-5 zeolite and amorphous $AlPO_4$. SEM image of **b** amorphous $AlPO_4$ and **c** $AlPO_4$-5 zeolite.

Density functional theory (DFT) calculations are employed to investigate the changes of the adsorption energy between LCO surface and these reactants. From the adsorption energy (ΔE) calculations, surface-modified TEA significantly reduces the adsorption energy of both H_3PO_4 (-1.94 eV to -3.71 eV) and AlOOH (-3.64 eV to -5.95 eV) reactants on the surface of LCO (**Fig. 5.2b**). The lowered adsorption energy benefits the uniform distribution of Al and P atoms on the cathode surface, which

facilitates the homogeneous nucleation and growth of uniform $AlPO_4$-5 zeolite coating layer. Moreover, TEA as a surfactant reduces the surface tension of LCO and thereby improves the wettability of the coating, allowing for better coverage of the LCO surface by Al^{3+} and PO_4^{3-} ions[176-178].

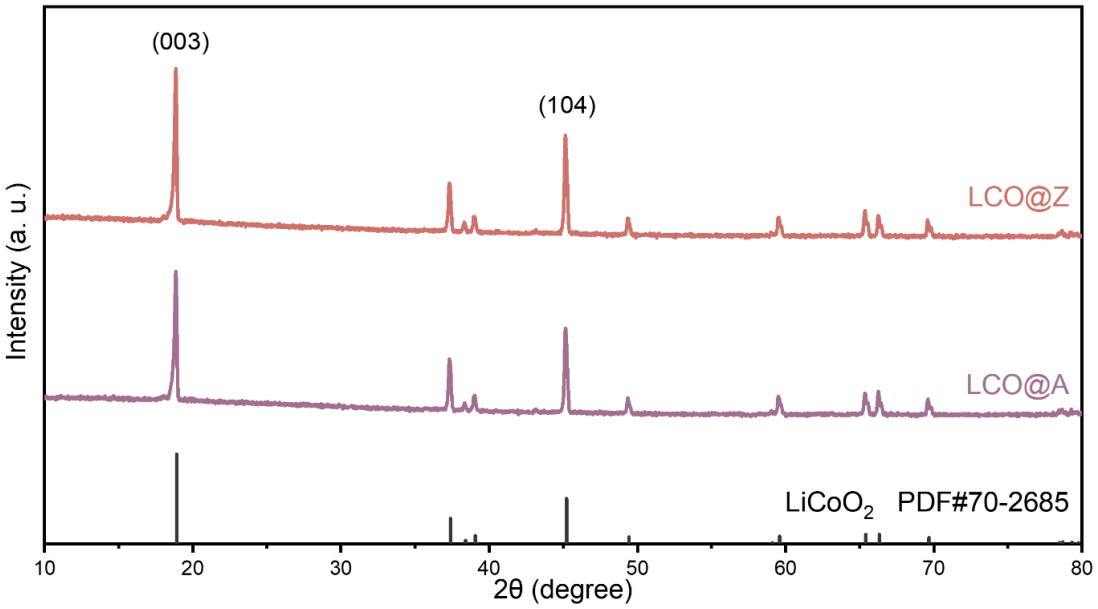

Figure 5.8 XRD patterns of as-prepared LCO@A and LCO@Z samples.

XRD patterns (**Fig. 5.8**) of LCO@A and LCO@Z samples can be indexed to a layered hexagonal α-$NaFeO_2$ phase (space group: *R-3m*)[49]. The absence of diffraction peaks related to the $AlPO_4$-5 coating layer in the XRD pattern could be due to its ultralow content. The BET results (**Fig. 5.9**) reveal an increase in specific surface area from 0.23 $m^2\ g^{-1}$ for LCO to 4.25 $m^2\ g^{-1}$ for LCO@Z after coating by $AlPO_4$-5 zeolite with a high specific surface area of 17.28 $m^2\ g^{-1}$.

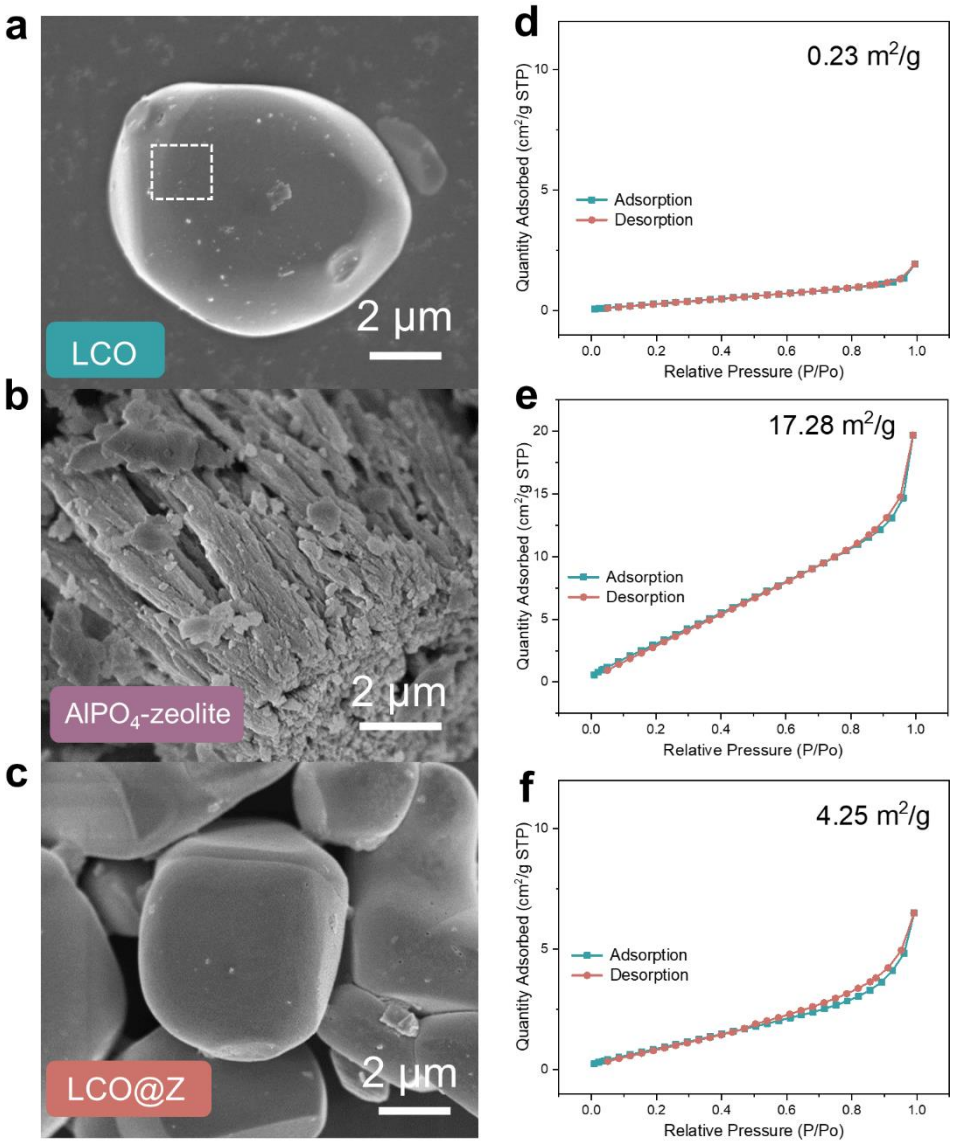

Figure 5.9 SEM images of **a** LCO, **b** $AlPO_4$-5 zeolite and **c** LCO@Z. The corresponding BET result of **d** LCO, **e** $AlPO_4$-5 zeolite and **f** LCO@Z.

5.2.2 Electrochemical performance

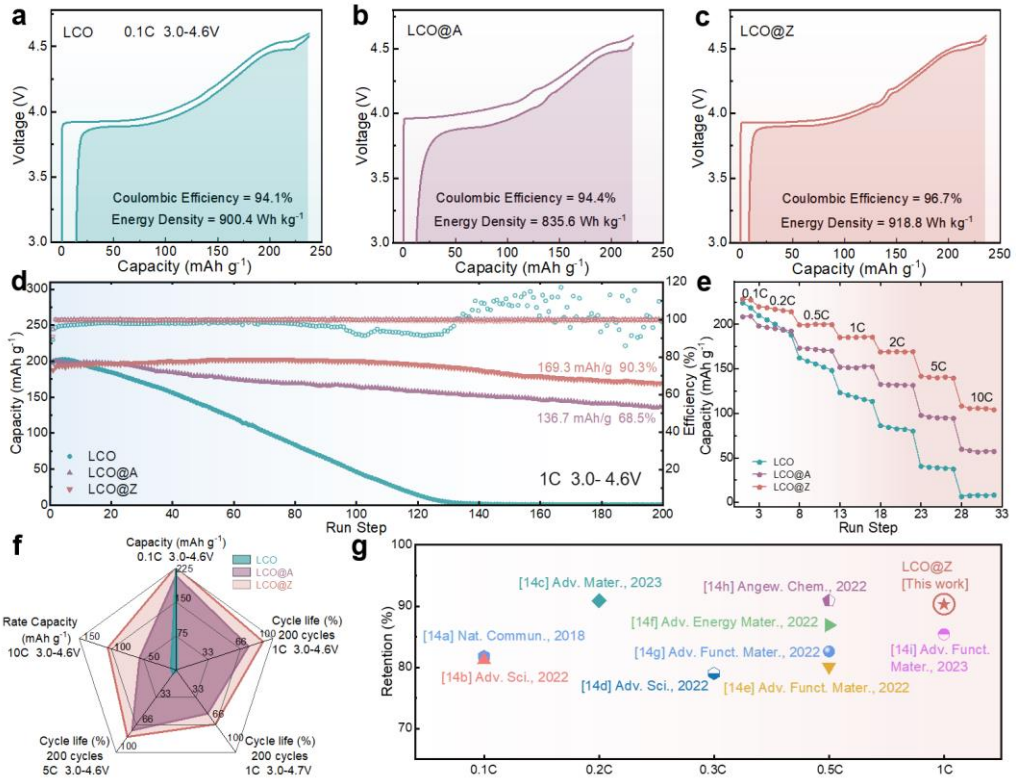

Figure 5.10 Electrochemical performance. The initial charge-discharge cycle of **a** LCO, **b** LCO@A and **c** LCO@Z at 0.1C. **d** Cycling durability at 1C under 4.6 V. **e** Rate capability. **f** Radar summary chart for comprehensive performance comparison. **g** Comparison of capacity retention of various surface-modified commercial LCO cathode after 200 cycles.

The electrochemical performances of cathodes were investigated through GCD measurements. **Fig. 5.10a-c** provides an intuitive comparison of the specific capacity and energy density of LCO, LCO@A, and LCO@Z. In the initial cycle, the LCO@Z delivers a larger specific capacity of 228.2 mAh g^{-1} with a higher initial Coulombic efficiency of 96.7% than those of LCO@A (208.4 mAh g^{-1}, 94.4%) and LCO (223.6

mAh g^{-1}, 94.1%). The $AlPO_4$-5 zeolite coating layer, acting as a distinctive elastic matrix, mitigates the unfavorable phase transitions under high-voltage for LCO@Z (confirmed by the following *in-situ* XRD analysis). This enhanced structural stability is accompanied by an improved redox reversibility and a higher Coulombic efficiency in the initial cycle of LCO@Z, resulting in a higher discharge capacity compared to the original LCO. The LCO@Z also exhibits a record high energy density of 918.8 Wh kg^{-1} (based on cathode mass only), higher than those of LCO (900.4 Wh kg^{-1}) and LCO@A (835.6 Wh kg^{-1}). Moreover, in the initial charge-discharge cycle, the uniform and crystalline $AlPO_4$-5 zeolite coating alleviates the electrochemical polarization in LCO@Z while the amorphous $AlPO_4$ coating aggravates the polarization in LCO@A.

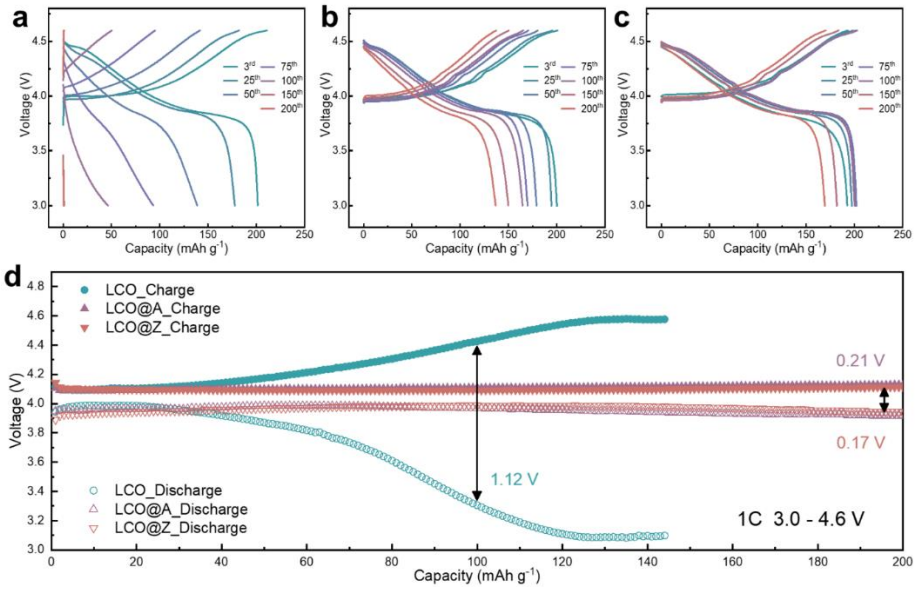

Figure 5.11 Continuous charge/discharge curves from 3rd to 200th cycles of **a** LCO, **b** LCO@A and **c** LCO@Z at 1C under 4.6 V. **d** Cycling performance of mid-point voltage.

The cycling disabilities of cathodes under high voltage of 4.6 V are measured, as shown in **Figs. 5.10d** and **5.11**. In general, the high charging voltage is accompanied by the irreversible phase transition and structural degradation of pristine LCO[18, 41, 42], leading to rapid decline of reversible capacity and almost zero capacity after 200 cycles. The cycling durability of LCO under high-voltage operation is remarkably improved by coating with the $AlPO_4$-based matrix. The LCO@Z maintains a large reversible capacity of 169.3 mAh g^{-1} with a superior capacity retention of ~90% after 200 cycles, which is better than 136.7 mAh g^{-1} and 68% of LCO@A, respectively. The capacity increase in the initial cycles can be attributed to the gradual activation process of LCO@Z cathode. As the LCO cathode particles are not perfectly monodispersed single crystals, they may contain agglomerated secondary particles with certain amount of grain boundaries within the bulk structure. During charge-discharge cycling, the anisotropic volume expansion and contraction of the single crystal primary particles gradually open up these grain boundaries, leading to a temporary increase in capacity. The uniform crystalline $AlPO_4$-5 zeolite coating also relieves the voltage decay and enhances the stability of mid-point voltage for LCO@Z in **Fig. 5.11**.

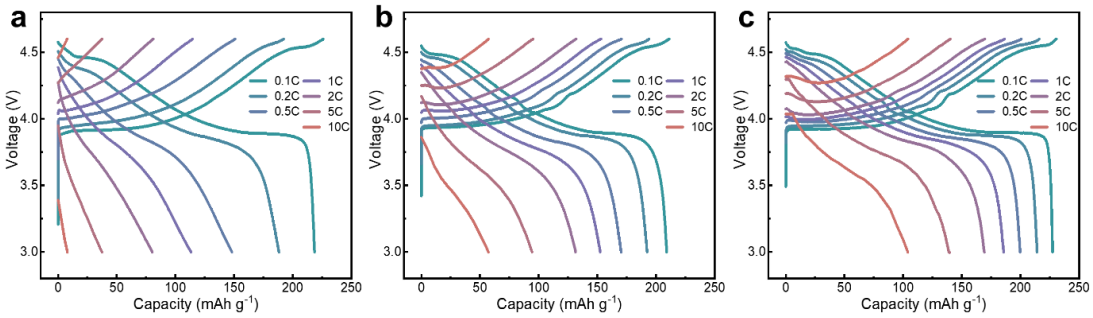

Figure 5.12 Continuous charge/discharge curves under 4.6 V from 0.1C to 10C of **a** LCO, **b** LCO@A and **c** LCO@Z.

Notably, the LCO@Z delivers higher specific capacities than those of the LCO and LCO@A at all C-rates (**Figs. 5.10e** and **5.12**), indicating enhanced rate capability. Specifically, LCO@Z still delivers a large capacity of 108.2 mAh g^{-1} even at 10C (6 min charging/discharging time), which is much higher than those of LCO@A (57.1 mAh g^{-1}) and LCO (6.3 mAh g^{-1}).

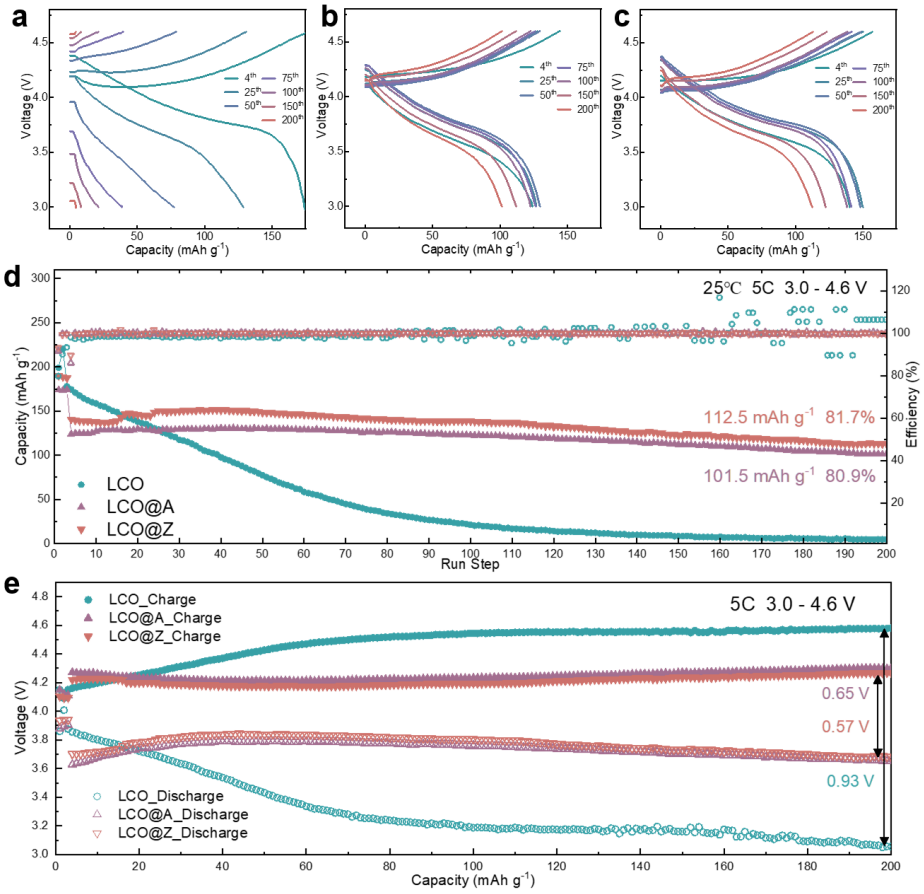

Figure 5.13 Continuous charge/discharge curves of **a** LCO, **b** LCO@A and **c** LCO@Z at 5C. **d** Cycling durability of half-cell at 5C. **e** Cycling performance of mid-point voltage at 5C.

The cycling durability of LCO, LCO@A and LCO@Z is further evaluated under a higher rate of 5C, a higher temperature of 60℃, a lower temperature of 0℃, and a higher upper cut-off voltage of 4.7 V, as shown in **Figs. 5.13-5.16**. The LCO@Z electrode exhibits a capacity retention of 81.7% (112.5 mAh g^{-1}) after 200 cycles at 5C (**Fig. 5.13**).

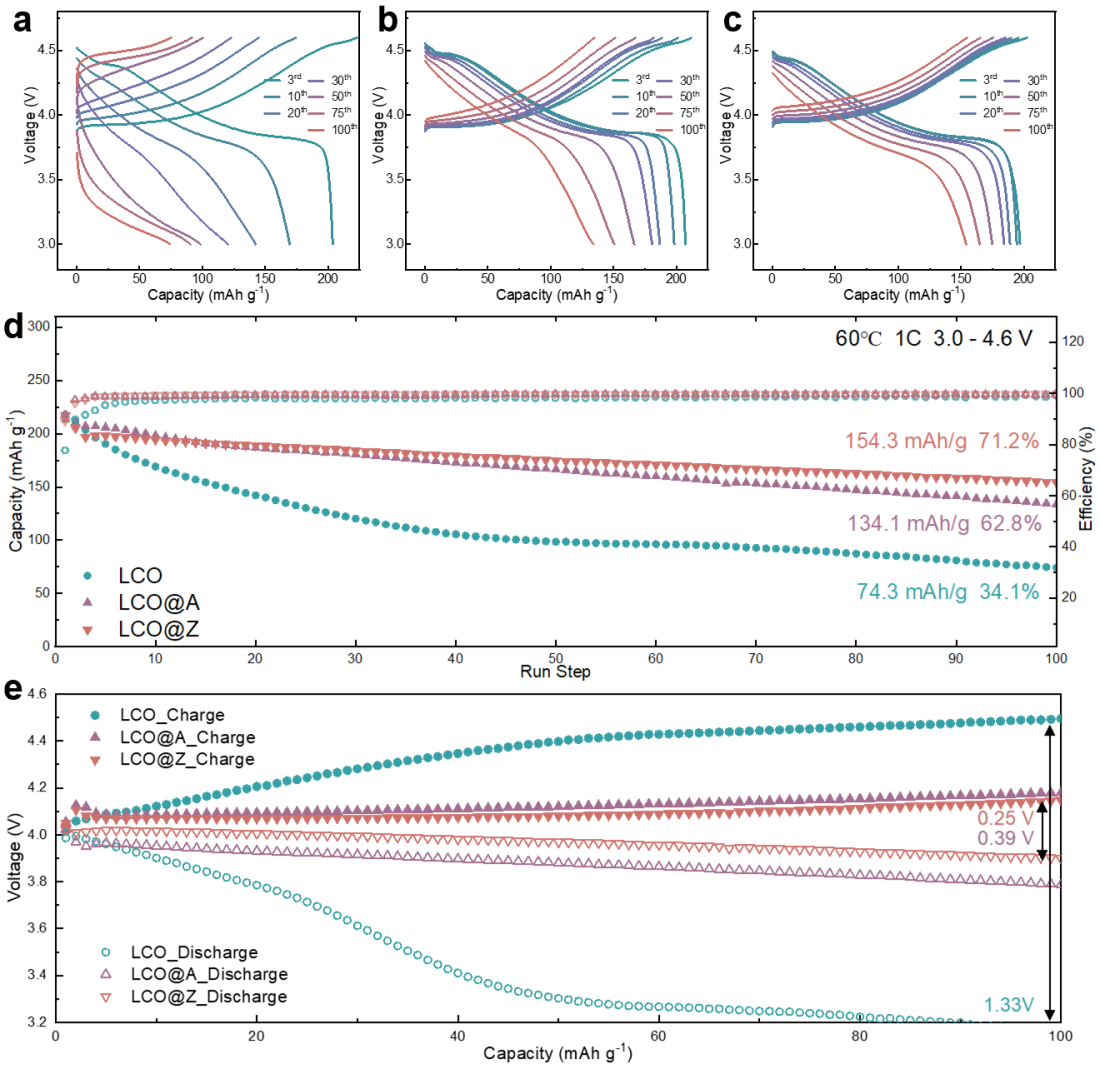

Figure 5.14 Continuous charge/discharge curves from the 3rd to the 100th cycles of **a** LCO, **b** LCO@A and **c** LCO@Z at 60℃. **d** Cycling durability of half-cell at 60℃. **e** Cycling performance of mid-point voltage at 60℃.

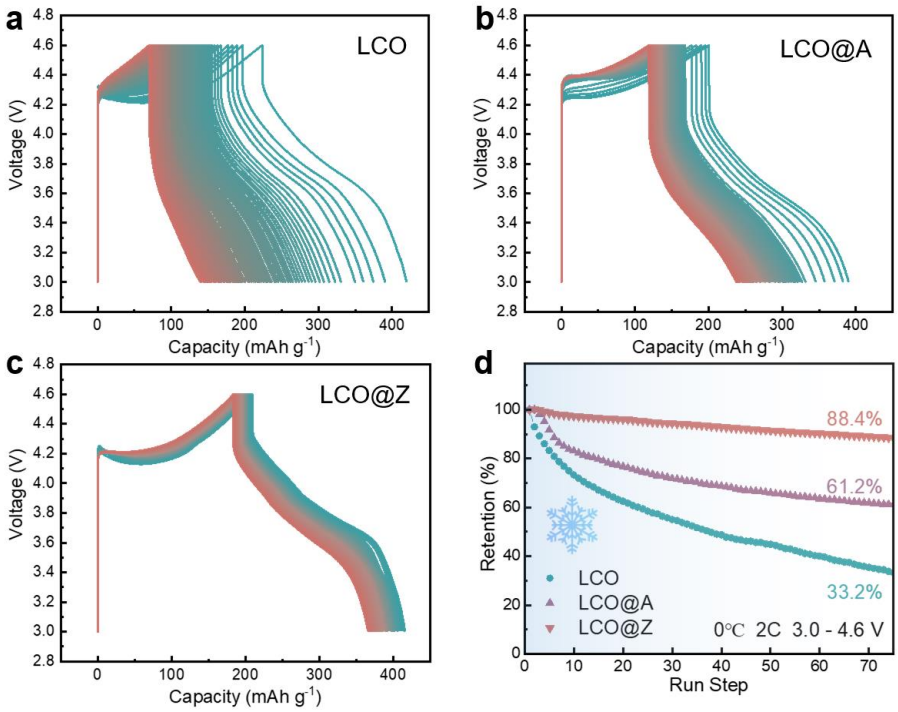

Figure 5.15 Continuous charge/discharge curves of **a** LCO, **b** LCO@A and **c** LCO@Z at 2C under 4.6 V. **d** Cycling durability of half-cells at 0℃.

Compared with LCO@A and LOC, LCO@Z also maintains an improved cycling durability under 60℃ and 0℃ (**Figs. 5.14-5.15**), indicating great application potential in wide temperature range. The LCO@Z maintains a capacity retention of 76.6% (169 mAh g^{-1}) and 65.6% (145 mAh g^{-1}) after 100 and 200 cycles, respectively, even under the higher cut-off voltage of 4.7 V, as shown in **Fig. 5.16**.

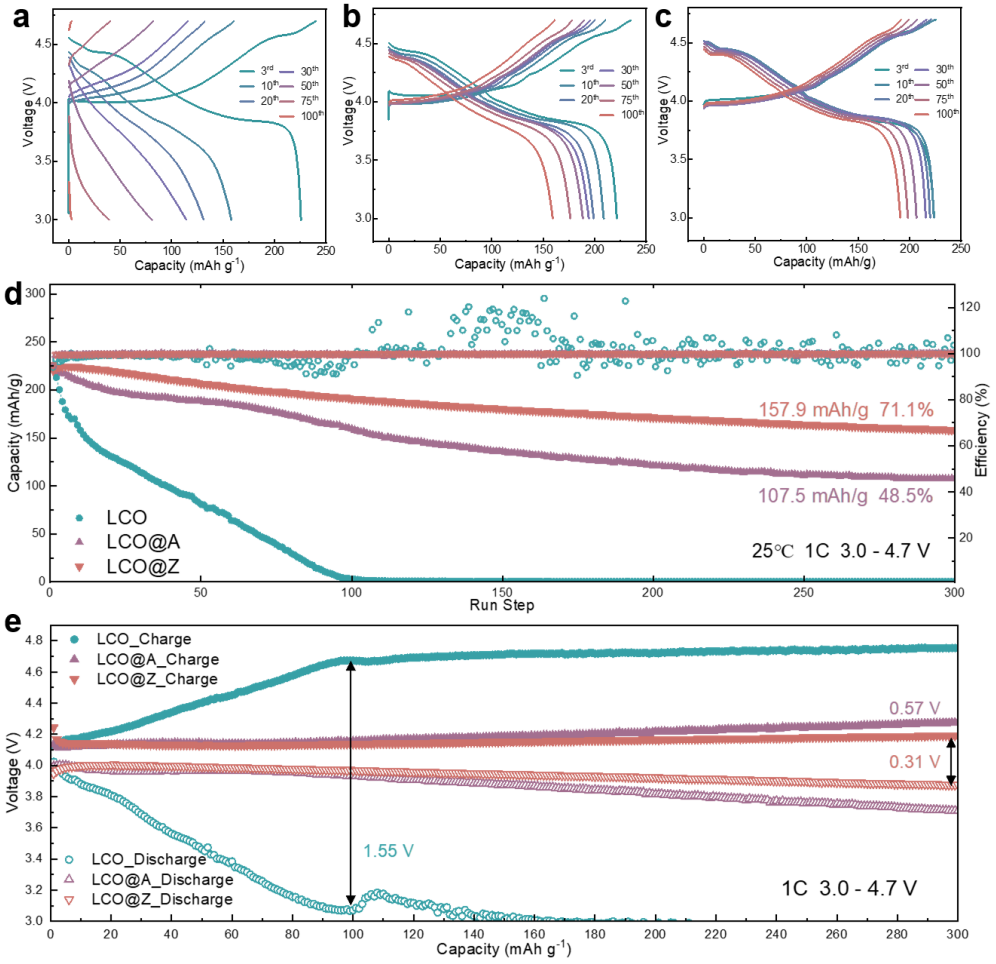

Figure 5.16 Continuous charge/discharge curves from the 3rd to the 100th cycles of **a** LCO, **b** LCO@A and **c** LCO@Z at 1C under 4.7 V. **d** Cycling durability of half-cell under 4.7 V. **e** Cycling performance of mid-point voltage under 4.7 V.

The performance comparison between pristine LCO, LCO@Z, and LCO@A is depicted in the radar chart of **Fig. 5.10f**. The LCO@Z demonstrates enhanced overall electrochemical performance including initial specific capacity, cycling durability, and rate capability. The performance of recently reported surface coated commercial LCO under high voltage is compared in **Fig. 5.10g** (detailed information listed in **Table S1**). The LCO@Z under high voltage of 4.6 V demonstrated exceptional long-term cycling

durability, which are among the great surface-modified commercial LCO cathodes reported in recent literatures[75, 83, 90, 92, 93, 179-182].

5.2.3 Li^+-desolvation and diffusion

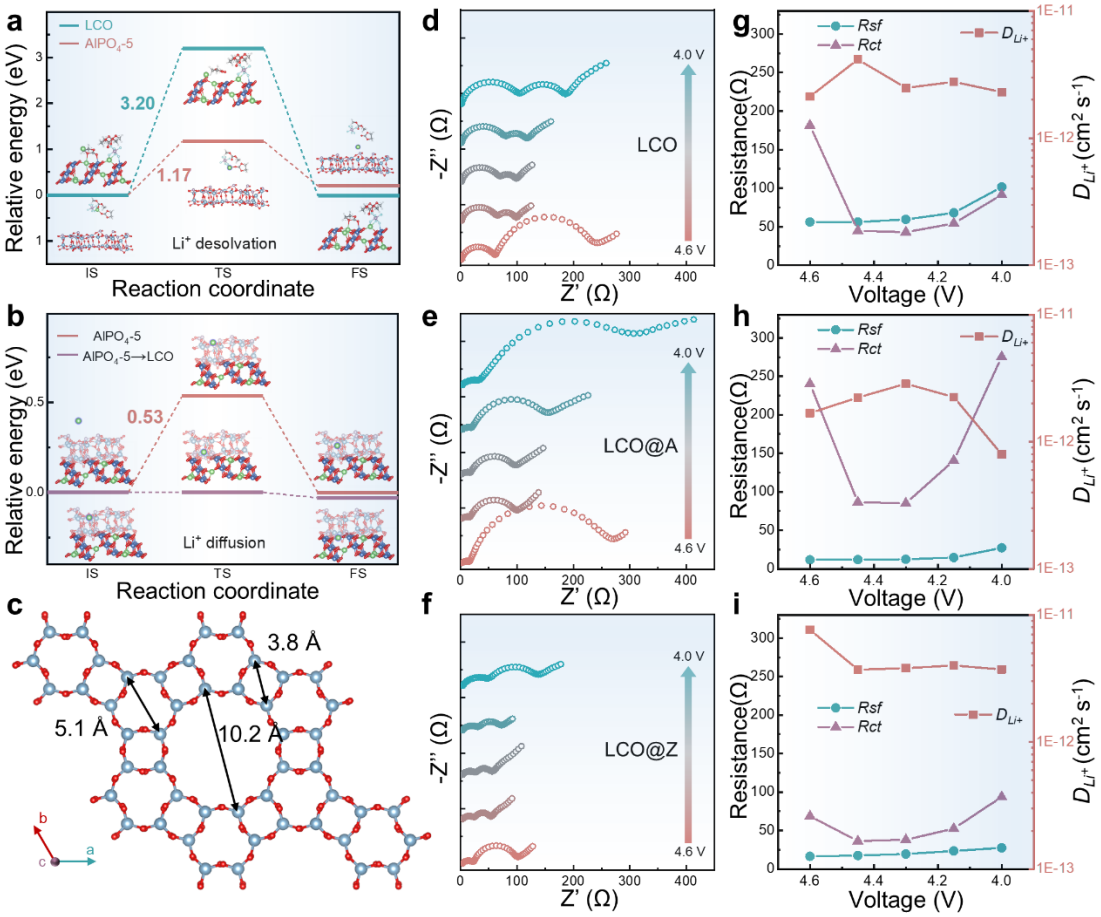

Figure 5.17 Li^+-desolvation and diffusion. **a** DFT-calculated energy barriers for the Li^+-desolvation of Li-EC-DMC-PF_6 complex on LCO and $AlPO_4$-5. **b** DFT-calculated energy barriers for the Li^+ diffusion into LCO and $AlPO_4$-5. **c** Lattice structure of $AlPO_4$-5 zeolite. *In-situ* impedance evolution during **d-f** discharge process for LCO, LCO@A and LCO@Z. The corresponding resistance and calculated Li^+ diffusion coefficient of **g** LCO, **h** LCO@A and **i** LCO@Z.

The Li^+ diffusion kinetics is closely linked to the Li^+-desolvation at the electrode/electrolyte interface, subsequently influencing the overall redox kinetics of LIBs[167-170]. To elucidate the improved redox kinetics of LCO@Z, DFT calculations are employed to analyze the energy barriers of interface Li^+-desolvation. As shown in **Fig. 5.17a**, we model the Li^+-desolvation process of the Li-EC-DMC-PF_6 complex on the surfaces of LCO and $AlPO_4$-5. DFT results show that the $AlPO_4$-5 zeolite layer lowers the Li^+-desolvation barrier from 3.20 eV (for LCO) to 1.17 eV, indicating easier Li^+-desolvation on $AlPO_4$-5 zeolite layer than on LCO. This can be partly attributed to the porous and chemically inert structure of $AlPO_4$-5 (space group *P6/mcc*, **Fig. 5.17c**). This porous structure allows for easier diffusion of the desolvated Li^+ without the creation of chemical bonds between the surface and Li^+ or solvent molecules. The desolvated Li^+ can readily diffuse through the porous structure of the $AlPO_4$-5 layer with a low energy barrier of 0.53 eV (**Fig. 5.17b**). After structure relaxation, the initial state of Li^+ in $AlPO_4$-5 will automatically transform to final state of Li^+ in LCO, indicating that the Li^+ diffusion from $AlPO_4$-5 into LCO is spontaneous (almost zero energy barrier). In contrast, LCO without an $AlPO_4$-5 zeolite layer lacks a diffusion pathway for the solvated Li^+. Additionally, Li^+-desolvation is challenging to occur on LCO due to a large energy barrier of 3.20 eV. Our calculation results indicate that Li^+-desolvation predominantly takes place on the $AlPO_4$-5 zeolite layer, facilitating the easy diffusion of desolvated Li^+ ions through the porous structure of $AlPO_4$-5 onto LCO.

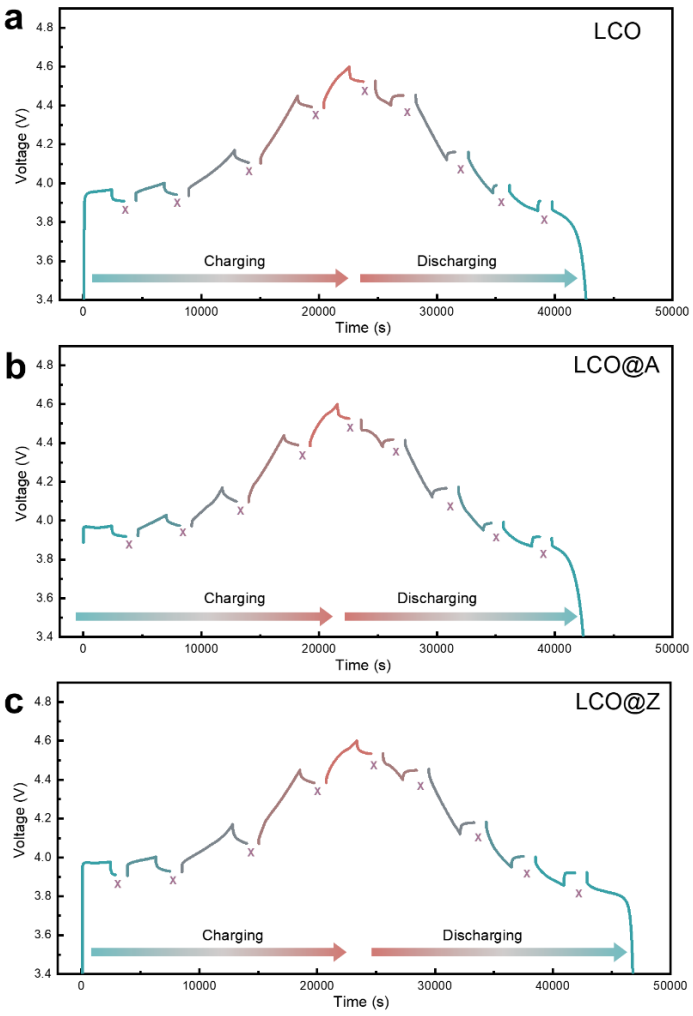

Figure 5.18 The charging and discharging curves of **a** LCO, **b** LCO@A, and **c** LCO@Z electrodes in the second cycle during *in-situ* EIS measurements.

To investigate the effects of surface engineering on overall redox kinetics of LCO, *in-situ* electrochemical impedance spectroscopy (EIS) in the discharge process of the second cycle is performed (**Fig. 5.17d-f**), and the charge/discharge curves are shown in **Fig. 5.18**. **Table S2** shows the fitted electrochemical parameters. The LCO@A and LCO@Z electrodes exhibit significantly lower R_{sf} values compared to the pristine LCO when discharging from 4.6 to 4.0 V. This reduction in R_{sf} values suggests a

decrease in the resistance of the surface film on the $AlPO_4$-coated surface during the initial cycling. The LCO@Z electrode shows lower R_{ct} values during discharge processes, especially at high voltage, than those of LCO@A and LCO. The high R_{ct} value of LCO@A electrode is probably related to the poor electronic conductivity of the amorphous $AlPO_4$ coating layer. In addition, the Li^+ diffusion coefficient (D_{Li^+}) can be calculated by the equation (1), and σ is the Warburg factor, which satisfies the following equation:

$$Z_{re} = R_{ct} + R_s + \sigma\omega^{-\frac{1}{2}} \quad (3)$$

By fitting the ($Z_{re}\ vs.\ \omega^{-\frac{1}{2}}$) plot as exhibited in **Fig. 5.19**, the σ term in equation (3) can be determined as the slope of the fitted line. In the discharge process, the D_{Li^+} at different voltages are shown in **Fig. 5.17g-i** and **Table S2**. LCO@Z shows the highest average diffusion coefficients (4.57×10^{-12} cm^2 s^{-1}), larger than those of LCO (2.76×10^{-12} cm^2 s^{-1}) and LCO@A (1.96×10^{-12} cm^2 s^{-1}). The lower R_{sf} and R_{ct} values and higher Li^+ diffusion coefficients of LCO@Z electrode demonstrate that the surface engineering with $AlPO_4$-5 zeolite effectively enhances the overall redox kinetics during discharge processes.

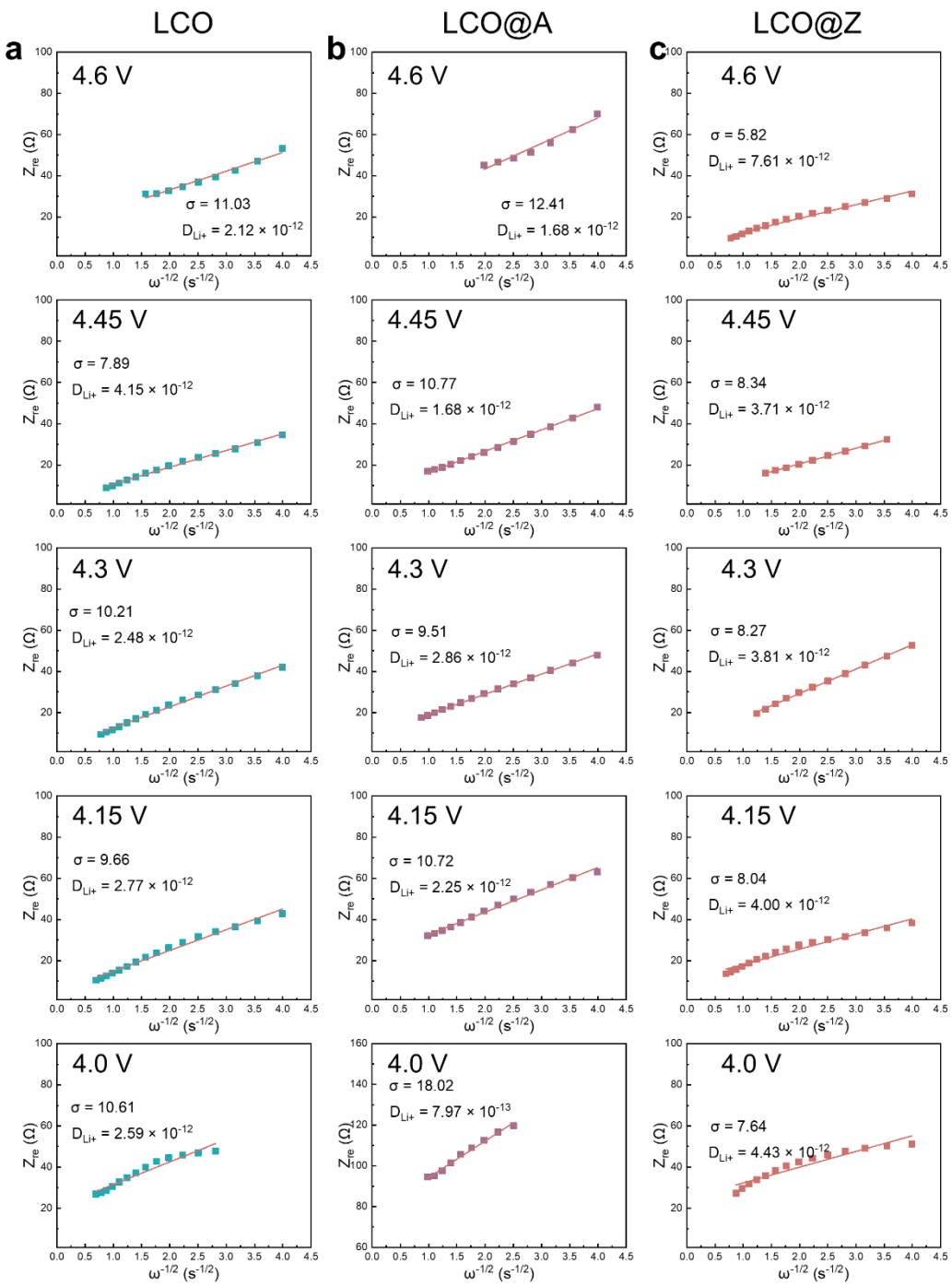

Figure 5.19 Plots of the real parts of the complex impedance versus $\omega^{-1/2}$ **a** LCO, **b** LCO@A, and **c** LCO@Z.

5.2.4 Stable lattice structure at high voltage

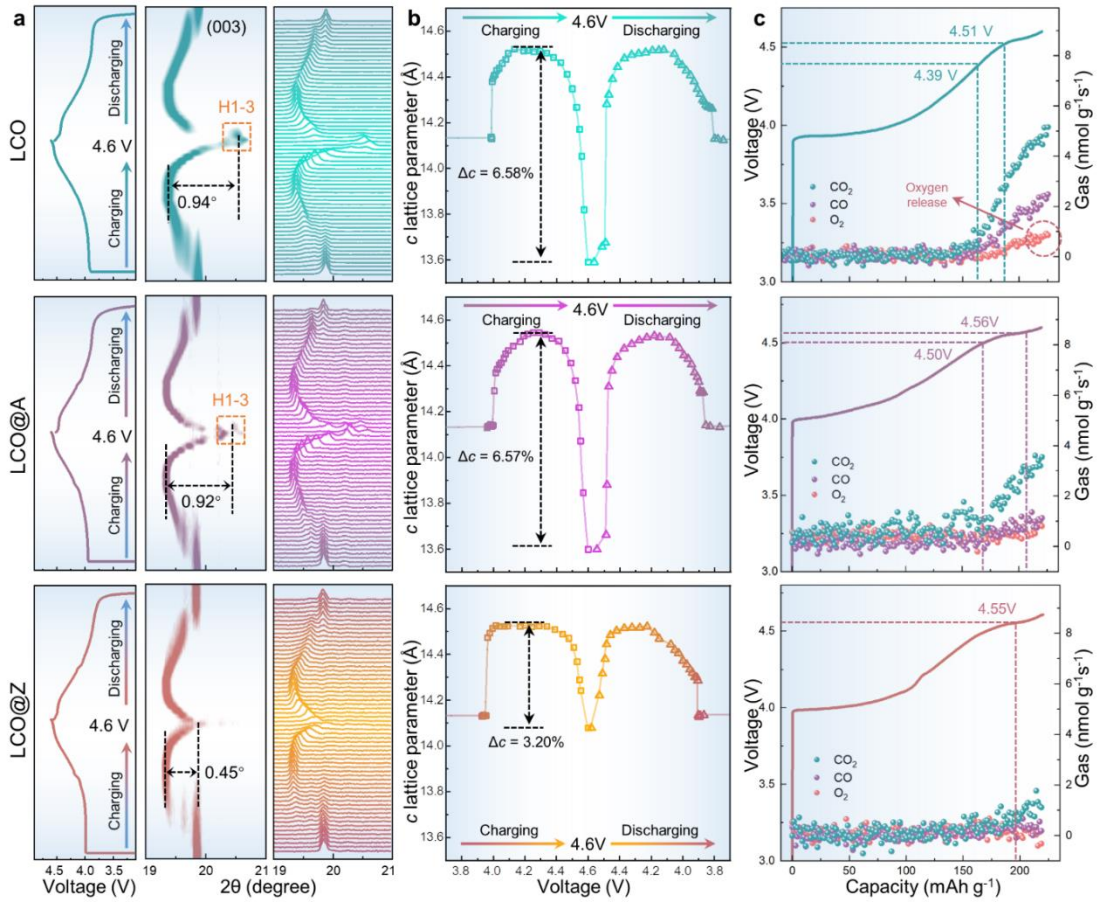

Figure 5.20 Structural evolutions under high voltage of 4.6 V. **a** Charge/discharge curves and *in-situ* XRD results. **b** The *c* lattice evolution as a function of charge/discharge voltage. **c** *In-situ* DEMS profiles performed during the initial charge process to 4.6 V at 0.2 C.

Unveiling the mechanism behind the enhanced structural stability resulting from surface $AlPO_4$-5 zeolite engineering is crucial. The phase transition from O3 to H1-3 , accompanied by notable alterations in the c-axis lattice and structural deterioration, occurs at voltage exceeding 4.5 V[18]. *In-situ* XRD measurements were performed to

investigate the phase transition behaviors of LCO, LCO@A and LCO@Z upon Li^+ de/intercalation. Although LCO, LCO@A and LCO@Z possess the same O3-type crystal structure before cycling, distinct differences in structural evolution are observed during charging and discharging, as seen in **Fig. 5.20a**. The dramatic shift of (003) diffraction peak under 4.6 V is observed in LCO and LCO@A. There is an obvious H1-3 peak appears under 4.6V. However, a relatively weak shift of the (003) diffraction peak in LCO@Z suggests the suppressed phase transition from O3 to H1-3 under 4.6 V. There is a relatively small H1-3 peak appears under 4.6V. **Fig. 5.20b** shows that the *c*-axis lattice parameter variation (Δc) is smaller for LCO@Z (3.20%) than that of pristine LCO (6.58%) and LCO@A (6.57%). These results suggest that the porous $AlPO_4$-5 zeolite as an elastic coating layer on LCO is promising in inhibiting the high-voltage phase transition and lattice shrinkage along the *c*-axis under 4.6 V.

In addition to the changes of LCO bulk structure under high voltage measured by *in-situ* XRD, the side reactions on surface are also characterized by *in-situ* DEMS (**Fig. 5.20c**). O_2 as a signature gas product indicates an irreversible oxygen evolution reaction on the particle surface[183], while carbonaceous gas is generated through the side reactions between the LCO surface and electrolyte[64, 102]. The carbonaceous gas occurs at above 4.5 V for LCO@Z and LCO@A during charging, in contrast with the 4.4 V for the pristine LCO. The gas production rates of CO_2 and CO of the pristine LCO reach 5.16 and 2.49 nmol $g^{-1}s^{-1}$, respectively, at 4.6 V (corresponding to high

state of charge), much higher than those of 3.83 and 1.09 nmol $g^{-1}s^{-1}$ for LCO@A, and 1.31 and 0.41 nmol $g^{-1}s^{-1}$ for LCO@Z, respectively. The LCO shows an onset voltage of oxygen release at ~4.5 V and a high oxygen production rate of 0.98 nmol $g^{-1}s^{-1}$ at 4.6 V. The LCO@A shows delayed onset voltage and reduced amount of oxygen production while the LCO@Z exhibits almost zero oxygen production during charging. The delayed onset voltage and reduced amount of gas production validate the effectiveness of $AlPO_4$-5 zeolite coating in inhibiting oxygen release and side reactions on the cathode surface.

5.2.5 CEI characterization after cycling

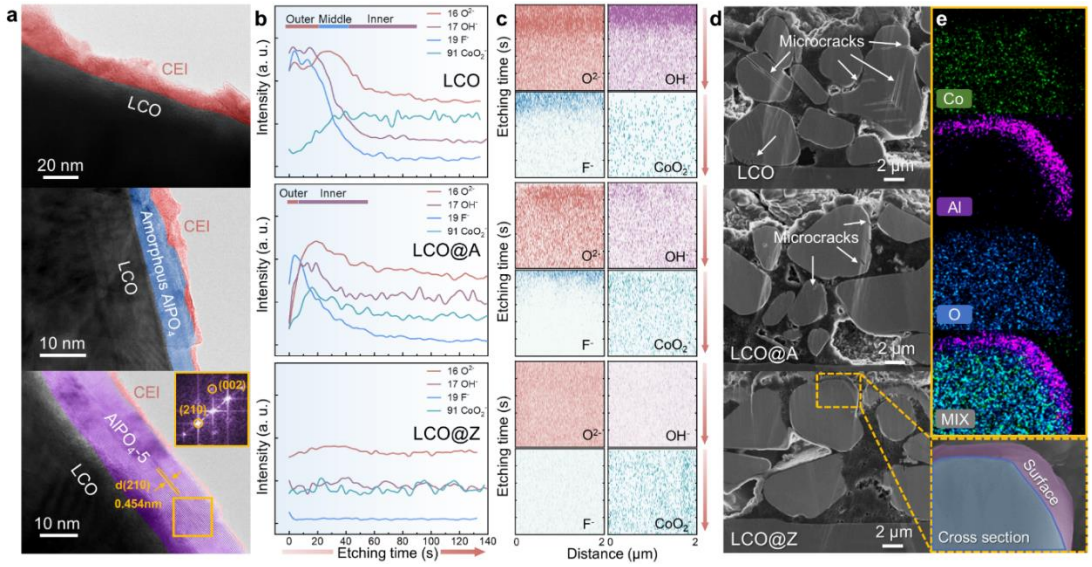

Figure 5.21 Structural evolutions during long-term cycling. **a** TEM images of surface morphology of LCO, LCO@A and LCO@Z after 200 cycles. **b** The intensity depth profiles of TOF-SIMS for O^{2-}, OH^-, F^- and CoO_2^- of LCO, LCO@A and LCO@Z, FFT pattern of the orange rectangle in LCO@Z. **c** Corresponding side section

mapping results for LCO, LCO@A and LCO@Z after 200 cycles. The mapping area is 2 × 2 μm. **d** Cross-sectional SEM images of LCO, LCO@A and LCO@Z cathodes after 200 cycles. **e** The corresponding cross-sectional EDS image of LCO@Z.

The structural evolutions after long-term cycling are also analyzed by TEM and TOF-SIMS, as shown in **Figs. 5.21** and **5.22**. The parasitic side reactions between oxidative species and organic electrolyte make the creation and accumulation of CEI on the LCO surface during repeated cycles [72, 73]. **Fig. 5.21a** illustrates TEM images of the cathodes after 200 cycles. The LCO@A and LCO@Z exhibit a thin CEI layer on the grain surface, in contrast with a thick CEI layer for LCO. Remarkably, even after long-term cycling, the $AlPO_4$-5 zeolite coating layer still maintains its original crystalline behavior on the surface of LCO@Z, as evidenced by the FFT pattern.

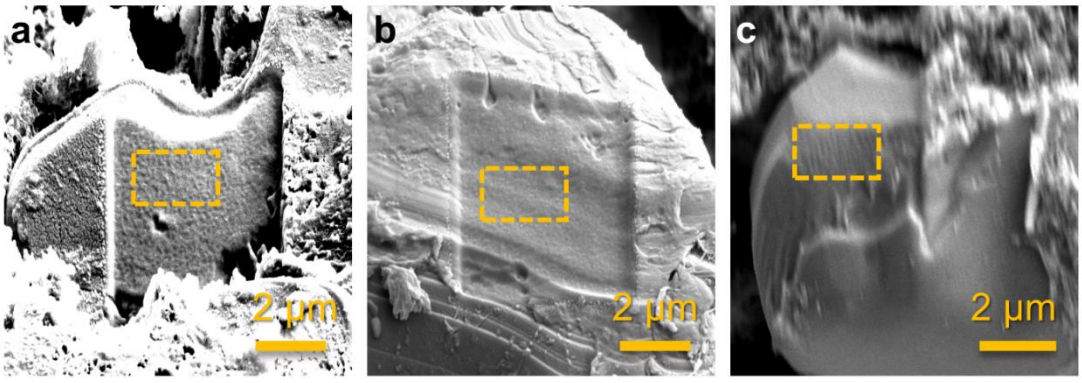

Figure 5.22 TOF-SIMS etching area of **a** LCO **b** LCO@A and **c** LCO@Z after 300 seconds.

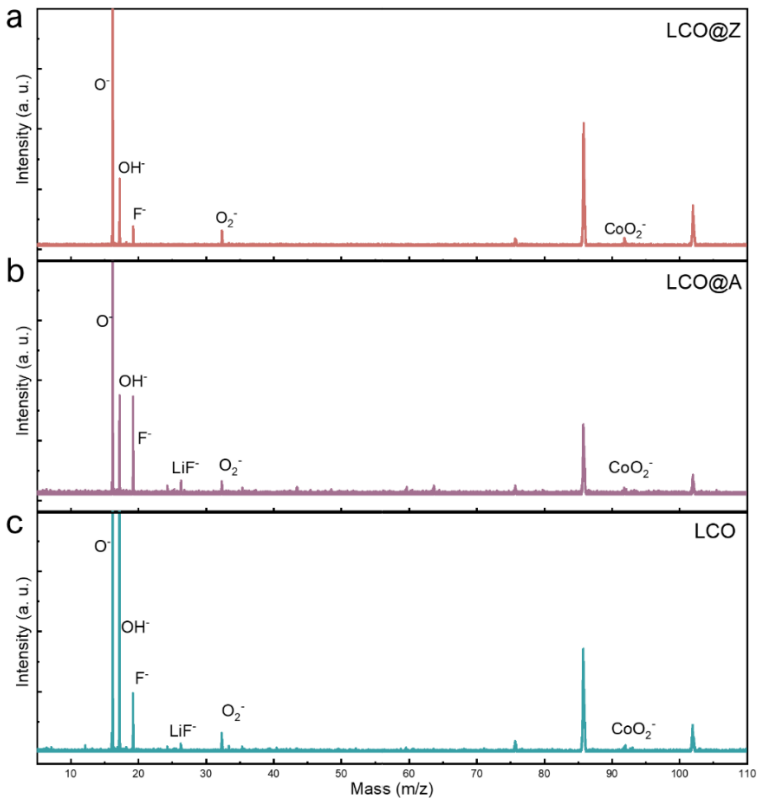

Figure 5.23 TOF-SIMS patterns for negative secondary ion mode.

The TOF-SIMS is further employed to investigate the type and distribution of CEI components. The relative intensities of negative secondary ion species are shown in **Fig. 5.20b-c**. The raw data of absolute intensities are provided in **Fig. 5.23**. A greater percentage of side reaction fragments[184] is determined from the surface of LCO, including m/z 16 [O^{2-}] and 19 [F^{-}]. LCO@Z shows relative less and homogeneous dispersion of O^{2-}, OH^{-}, F^{-} and CoO_2^{-} segments, in contrast with the O^{2-}/ OH^{-} and F^{-} enriched surface in the cycled LCO. Besides, the cycled LCO@Z exhibits a much reduced amount of C-containing species, as evidenced in **Fig. 5.24**. The decreased contents of F- and C- containing species in the cycled LCO@Z indicate a thin CEI layer and mitigated side reactions on the electrode surface. These results demonstrate

that the $AlPO_4$-5 zeolite coating serves as an effective protective layer mitigates the side reactions, leading to thin CEI layer on the LCO surface.

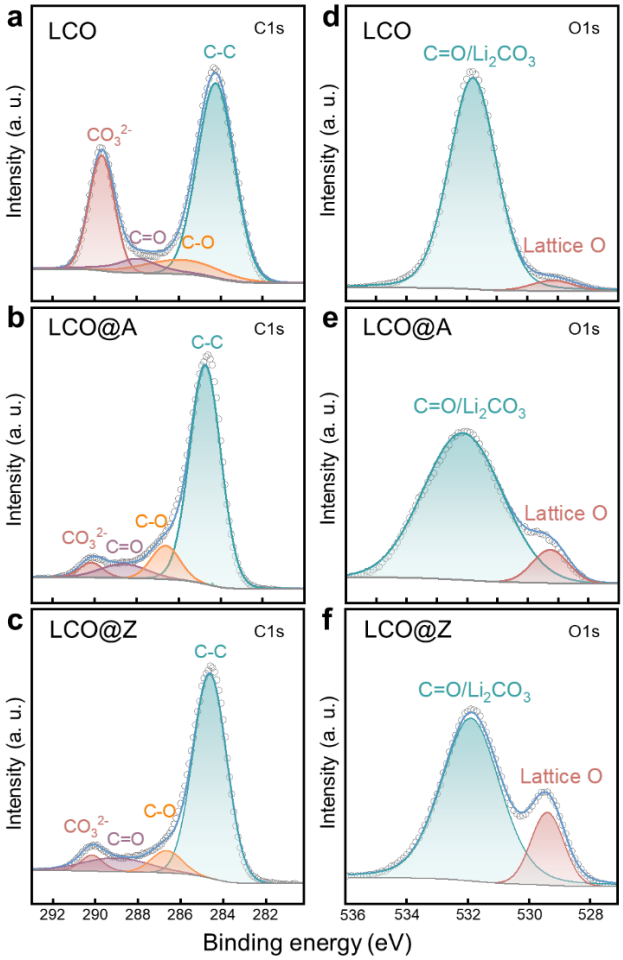

Figure 5.24 The **a-c** C1s and **d-f** O1s XPS spectra after 200 cycles.

The repeated phase transitions between O3 and H1-3 may lead to the occurrence of severe anisotropic mechanical strains in the crystal structure, resulting in microcracks within the grain[41, 150]. Cross-sectional SEM images after 200 charge-discharge cycles are shown in **Fig. 5.20d**. The cycled LCO grains exhibit severe microcracks within the bulk and surface, while the cycled LCO@A shows only some small microcracks near the surface. The cycled LCO@Z has no observable microcracks. These cracks

expose fresh LCO surfaces to electrolyte species and readily damage the grains with a substantial decrease in elastic modulus, hardness, and fracture toughness, further enhancing side reactions and creating autocatalytic scenarios[19, 185]. The EDS mapping confirms that the aluminum element still enriches on the LCO surface (**Fig. 5.20e**), indicating the good electrochemical and mechanical stability of $AlPO_4$-5 zeolite coating layer.

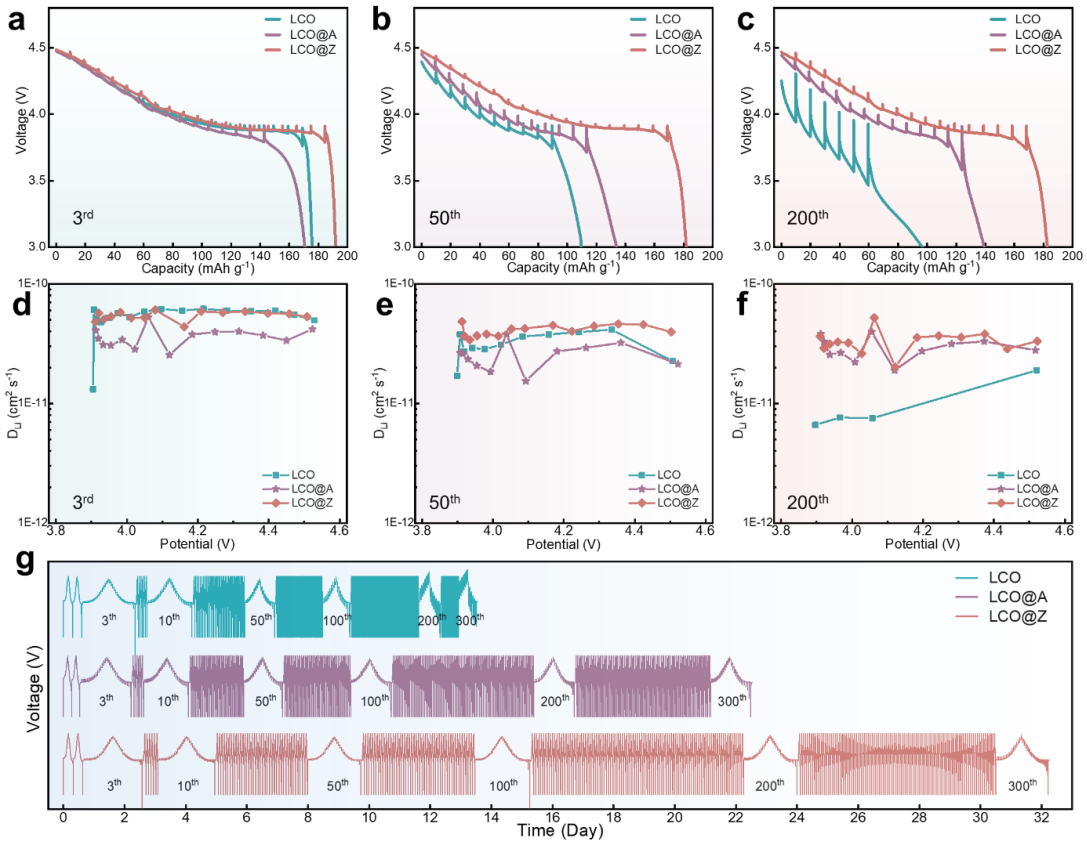

Figure 5.25 GITT curves of **a** LCO, **b** LCO@A and **c** LCO@Z. The corresponding Li^+ ion diffusion coefficients of **d** LCO, **e** LCO@A and **f** LCO@Z. **g** Cycling performance and overpotential properties.

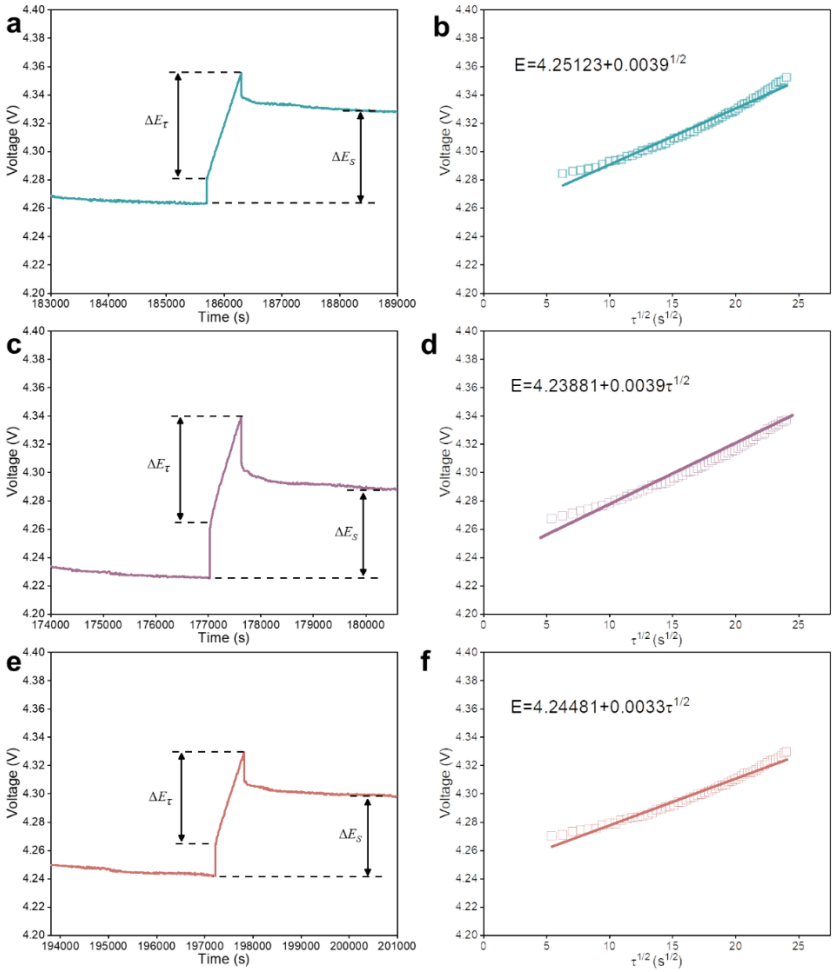

Figure 5.26 A typical voltage versus time profile of **a** LCO, **c** LCO@A and **e** LCO@Z. A linear relationship between voltage and $\tau^{1/2}$ of **b** LCO, **d** LCO@A and **f** LCO@Z.

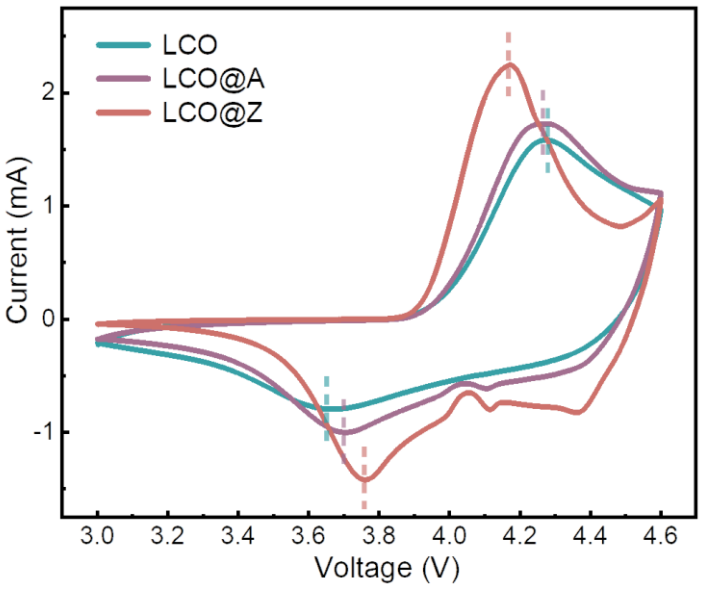

Figure 5.27 CV curve after 200 cycles.

The effect of structural evolutions of LCO within cycling on the Li^+ diffusion kinetics is further investigated by galvanostatic intermittent titration technique (GITT), as depicted in **Figs. 5.25-5.26**. These results confirm that the $AlPO_4$-5 zeolite coating maintains the stable Li^+ diffusion coefficients in the LCO@Z upon cycling, in contrast with gradually decreased Li^+ diffusion coefficients in the LCO and LCO@A. As shown in **Fig. 5.27**, the CV curve indicates the better redox reversibility and weaker electrochemical polarization of LCO@Z after 200 cycles than those of LCO and LCO@A.

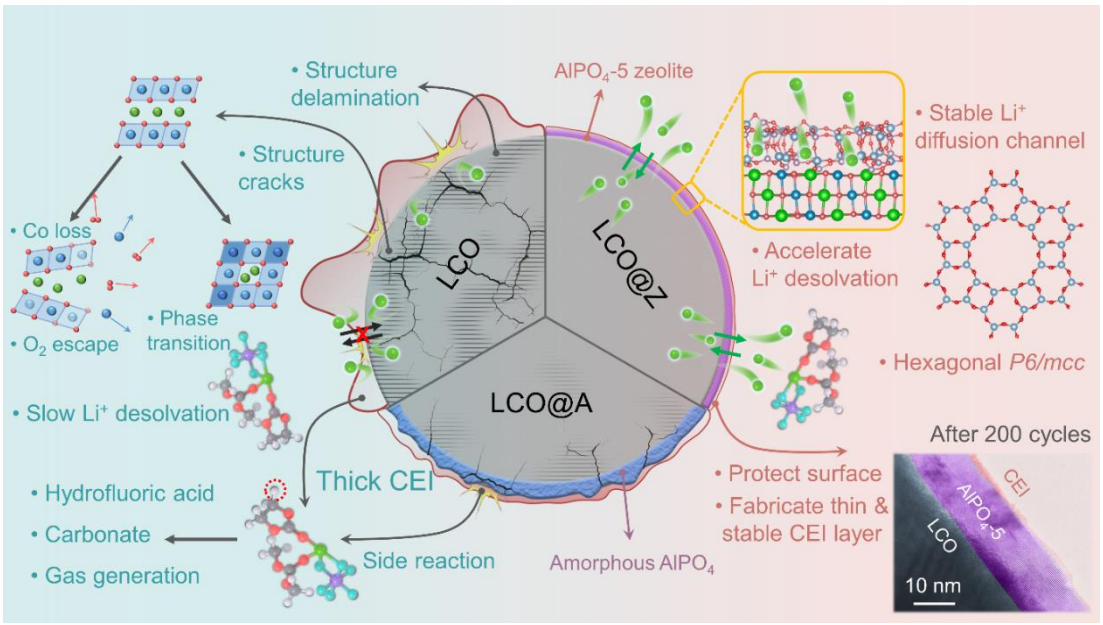

Figure 5.28 Schematic illustration of the mechanism of $AlPO_4$-5 zeolite layer in electrochemical performance enhancement.

The functional mechanism of the $AlPO_4$-5 zeolite coating in enhancing the electrochemical performance of LCO is schematically depicted in **Fig. 5.28**, and summarized as follows. (1) The electrochemically and mechanically stable $AlPO_4$-5 zeolite coating acts as a protective layer to prevent the direct contact between the organic liquid electrolyte and LCO grains, reduce the lattice oxygen loss and the side reactions on the LCO surface, and thereby relieve the surface decay and the excessive accumulation of CEI upon cycling. (2) The crystalline $AlPO_4$-5 zeolite with unique porous structure establishes a stable diffusion pathway for Li^+ ion transport, while the appropriate pore size efficiently accelerates the Li^+-desolvation process and further improves the Li^+ kinetics. (3) The full coverage of the elastic $AlPO_4$-5 zeolite coating layer on LCO effectively provides mechanical reinforcements to suppress the high-

voltage phase transition, leading to the absence of microcracks and good structural stability even under repeated high voltage cycling. As a result, a multifunctional $AlPO_4$-5 zeolite coating layer enables stable high-voltage operation of LCO cathode in high-energy LIBs.

5.3 Conclusion

The current work introduces a novel coating approach utilizing $AlPO_4$-5 zeolite, which leads to enhanced stability of the LCO cathode under 4.6 V. The improved stability observed in LCO@Z can be attributed to the multifunctional coating layer which effectively establishes fast Li^+-desolvation and diffusion pathways, mitigates irreversible phase transitions under high voltage, and protects against structure/surface degradation during long-term cycling. The well-designed surface engineering in LCO@Z successfully suppresses the high-voltage phase transition, thereby preserving the stability of the surface lattice oxygen at high voltage. Remarkably, LCO@Z exhibits an outstanding capacity retention of 90.3% after 200 cycles at 1C rate. These remarkable achievements provide a valuable insight for the rational design of advanced cathodes with zeolite-based coatings, opening new possibilities for future developments in surface engineering strategies.

Chapter 6 Multifunctional surface modification by CeO_2 nanoparticles

In Chapter 6, we propose an interspersed CeO_2 coating on LCO (LCO@CeO_2), which serves as a multifunctional protector to ensure operational stability of the electrode under 4.6 V. Specifically, CeO_2 spatially separates the LCO and electrolyte to prevent side reactions, and acts as an efficient Li^+ conductor to facilitate Li^+ de/intercalation as well as an oxygen storage material to maintain the reversibility of the lattice oxygen in LCO. This work highlights CeO_2 featured with multiple functions in protecting LCO under higher cut-off voltage and offers a practical direction for developing durable high-voltage LIBs.

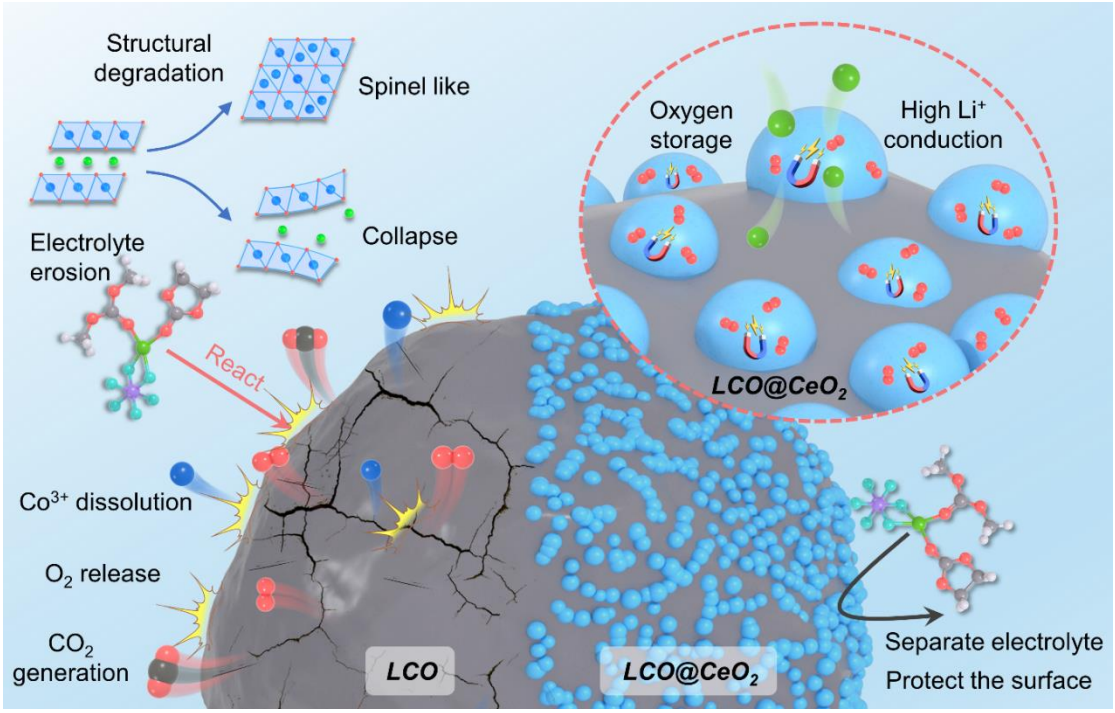

Figure 6.1 Graphic abstract of LCO@CeO_2.

6.1 Introduction

To meet the growing demands of portable smart devices, electric vehicles and grid storage, achieving high energy density is an everlasting goal in rechargeable battery development[8, 14]. In 1980, Goodenough first proposed the use of layered LCO as a reliable cathode material[186], which greatly propelled the advancement of LIBs materials and technology. LCO possesses stable charge/discharge voltage plateaus, high tap density, favorable energy density, and excellent electrochemical cycling durability, making it the predominant commercial cathode material to this day[19, 20, 74]. With the advent of the 5G era, the hardware and software functionalities of mobile devices are continuously being updated and iterated. The diverse range of advanced features has led to increased energy consumption in portable devices, necessitating the development of higher capacity rechargeable batteries. One effective method to achieve higher capacity, building upon the existing cathode, is to elevate the charge cut-off voltage, thereby extracting more Li^+ ions during the charging process.

Unfortunately, exceeding a charge cut-off voltage higher than 4.5 V results in rapid capacity decay and ultimately limits the cycle life of LCO/graphite batteries[41, 170]. The rapid capacity decay is primarily attributed to factors such as lattice oxygen loss, TM dissolution, electrolyte oxidation, and degradation of the cathode structure, leading to sluggish kinetic of Li^+ de/intercalation and loss of active lithium[42, 64, 110]. Recently, online electrochemical mass spectrometry (OEMS) has demonstrated that molecular oxygen is released from the highly delithiated cathode during the initial charging

cycles[183]. Theoretically, oxygen is released above a potential of 1.23 V vs reversible hydrogen electrode, equivalent to 4.3 V[187, 188]. For LIBs, O_2 oxidized from the lattice oxygen of the cathode is detected when the voltage exceeds 4.5 V[188, 189]. Additionally, due to the disruption of the lattice and exposure to external stimuli, the surface structure is more unstable compared to the bulk structure[187, 190], highlighting the need to consider surface structure as a primary factor in improving LIBs stability.

Common modification strategies for high voltage LIBs can be mainly classified into element doping and surface modification by inert elements. These strategies have witnessed significant research advancements in recent years. Inert element doping can benefit high voltage LIBs by stabilizing the layered structure thus ensuring stable Li^+ ion transport under high voltage[50, 85, 191]. However, external element doping partially changes the intrinsic structural performance of LCO, affecting the sliding of CoO_2 and the original redox reactions. Surface modification, which involves secondary treatment of commercial LCO cathode, has shown effective stabilization of LCO structure and improved cycle life[63, 90]. Typically, inert elements are introduced on the LCO surface as modifiers, forming a solid-solution layer. The solid-solution layer acts as a physical barrier, effectively preventing side reactions between high-valence unstable oxygen and the electrolyte under high voltage, reducing the TM dissolution, thus suppressing negative effects caused by high voltage[192, 193]. However, the introduction of inert element coatings on the surface often hinders Li^+ diffusion, and excessively thick inert coatings may lead to more capacity losses[164, 194], which are

relatively more pronounced compared to element doping strategies. Achieving a balance between stability and capacity can only be realized by controlling parameters such as the thickness and content of the surface modification layer. Up to date, developing a multifunctional coating that not only stabilizes the layered structure but also ensures fast Li^+ conductivity is full of benefits and challenges for high-voltage LIBs.

In this work, we propose a surface engineered CeO_2 coating on LCO (LCO@CeO_2), where the LCO surface was decorated with CeO_2 nanoparticles (NPs) that possess variable cationic valence and oxygen vacancy. A series of CeO_2 NPs layers with varied morphologies were fabricated on the LCO cathode at different annealing temperatures. Among them, the optimized sample with a uniformly distributed CeO_2 NPs annealed at 850 ^oC demonstrated good cycling durability and rate capacity. In addition to providing the basic functions of surface protection and insulation from the electrolyte, CeO_2 also played a crucial role in enhancing Li^+ conductivity and oxygen storage. Under high voltage, the interaction between CeO_2 and LCO established faster and easier pathways in LCO by lowering the potential of Li^+ extraction. Moreover, CeO_2 NPs acted as an oxygen storage material to store the unstable lattice oxygen of the LCO surface as reversible $(O_2)^{3-}$ species. The coupling effect of Li^+ conductivity and oxygen storage improved the stability and reversibility of the surface structure during deep delithiation, thereby improving the durability of LIBs under long-term high voltage cycling. Furthermore, the uniform loading structure of CeO_2 NPs enabled

LCO@CeO_2 to maintain a stable morphological shape even during severe volume expansion and shrinkage under high voltage. Our research reveals the multifunction played by CeO_2 NPs in surface modification strategies and demonstrates the potential of loading uniform NPs for the development of high voltage LIBs.

6.2 Results and discussion

6.2.1 Synthesis of multifunctional CeO_2 coating layer

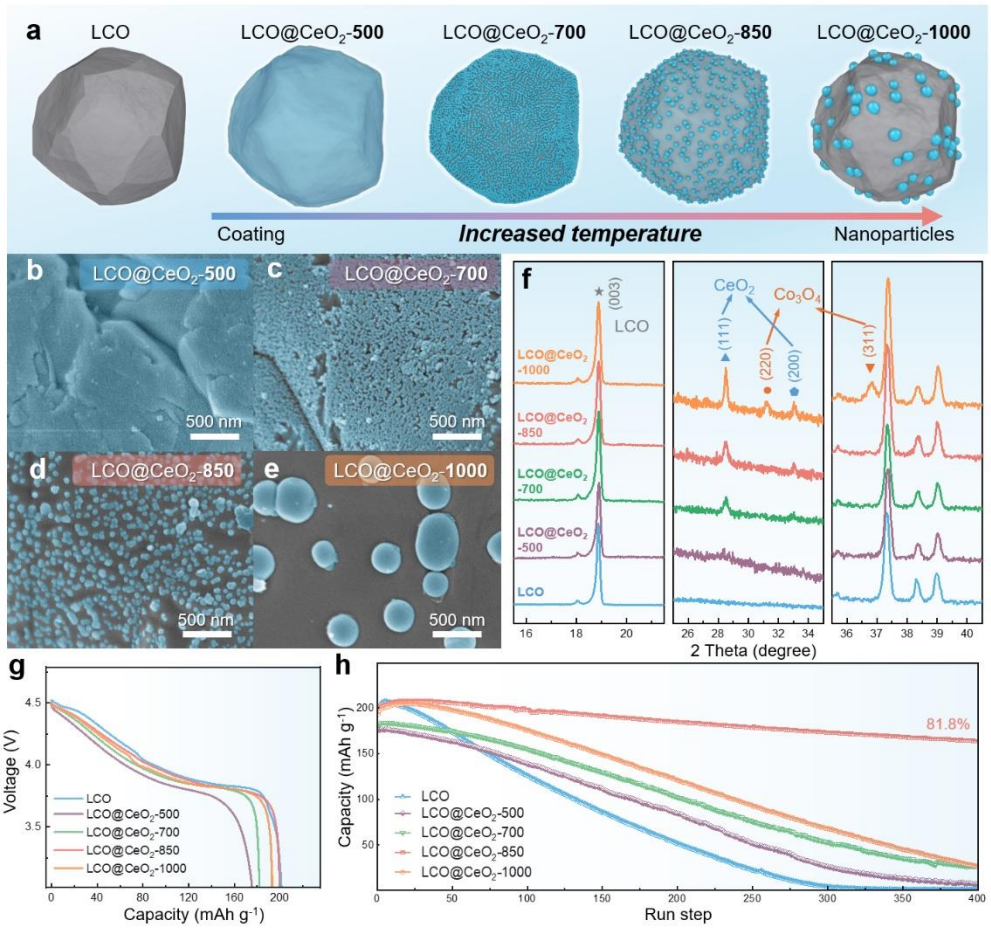

Figure 6.2 a Morphological evolution of LCO@CeO_2 under increasing temperature. SEM image of **b** LCO@CeO_2-500, **c** LCO@CeO_2-700, **d** LCO@CeO_2-850 and **e** LCO@CeO_2-1000. **f** XRD pattern of LCO@CeO_2 under increasing temperature. **g**

Initial discharge curve and **h** long-term cycling performances of LCO@CeO_2 samples at 1C under 4.6 V.

The formation of uniform CeO_2 coating on the LCO surface was achieved by a hydrothermal method, followed by high-temperature annealing. **Fig. 6.2a** schematically illustrates the morphological evolution of the LCO@CeO_2 samples annealed at different temperatures (500℃, 700℃, 850℃ and 1000℃). SEM was utilized to observe the temperature-dependent evolution of CeO_2. Upon annealing at 500 ℃ (**Fig. 6.2b**), the initially smooth surface of the bare-LCO became uniformly decorated with a rough layer. Increasing the annealing temperature to 700 ℃ (**Fig. 6.2c**) resulted in a more compact surface composed of small and homogeneously distributed CeO_2 NPs. Further elevating the temperature to 850 ℃ (**Fig. 6.2d**) led to the formation of larger grains with relatively bigger CeO_2 NPs (20-40 nm), exhibiting a massage-ball-like morphology. As the temperature further increased to above 1000 ℃ (**Fig. 6.2e**), the observed grains gradually aggregated, forming larger particles ranging from 200 to 400 nm.

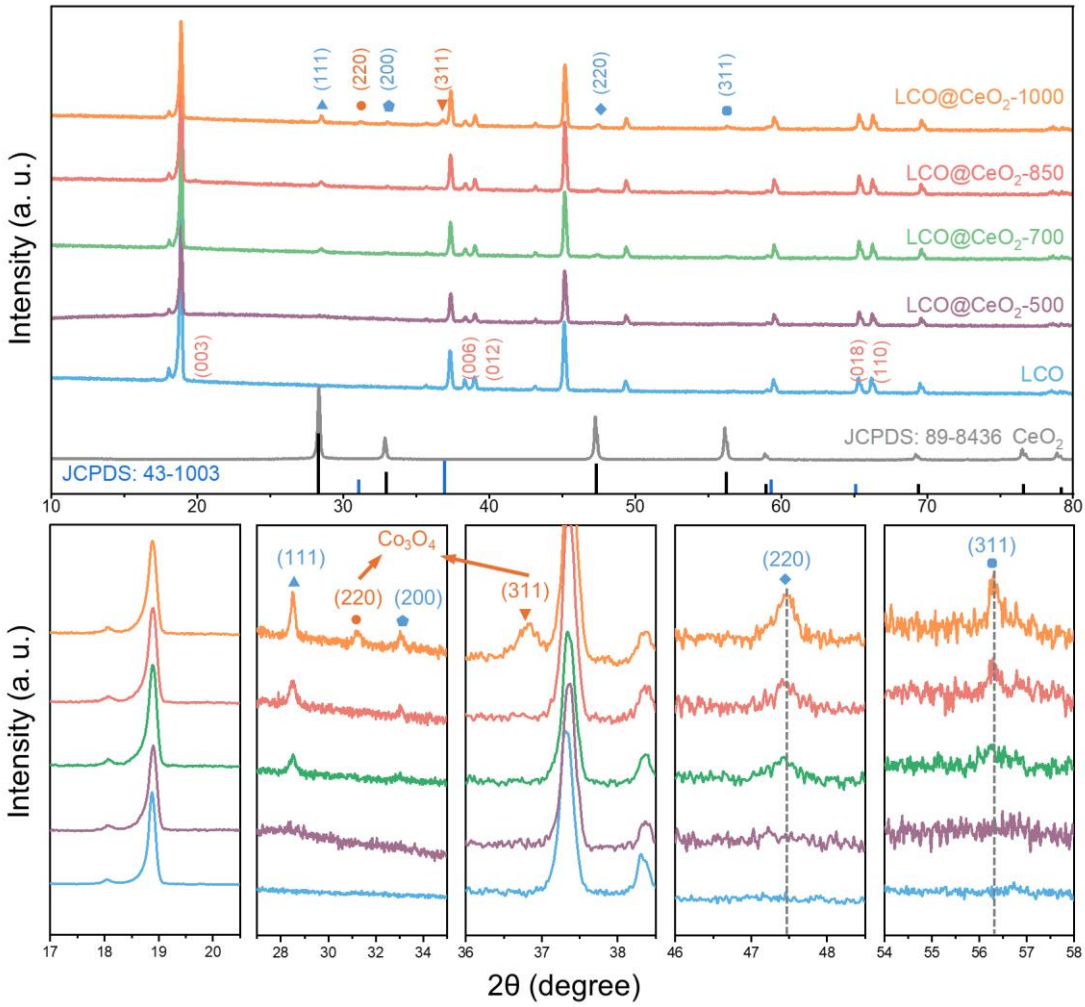

Figure 6.3 XRD patterns of LCO, LCO@CeO_2-500, LCO@CeO_2-700, LCO@CeO_2-850 and LCO@CeO_2-1000.

The XRD patterns of both bare-LCO and LCO@CeO_2 samples are shown in **Fig. 6.3**. The well-defined splitting of the (006)/(012) and (018)/(110) peaks confirm the presence of a well-ordered layer structure in all materials. Additionally, the relatively weak diffraction peaks observed at approximately 28.6°, 32.8°, 47.5°, and 56.3° correspond to the crystallographic structure of CeO_2 with a space group of *Fm-3m*. The intensities of these peaks gradually increased with higher annealing temperatures.

This increasing trend in peak intensities is like that observed in LCO@CeO_2 (**Fig. 6.2f**) and pure CeO_2 (**Fig. 6.4**) samples. Furthermore, when the annealing temperature reached 1000°C, a Co_3O_4 phase emerged, likely due to surface Li loss resulting from the higher annealing temperature[195].

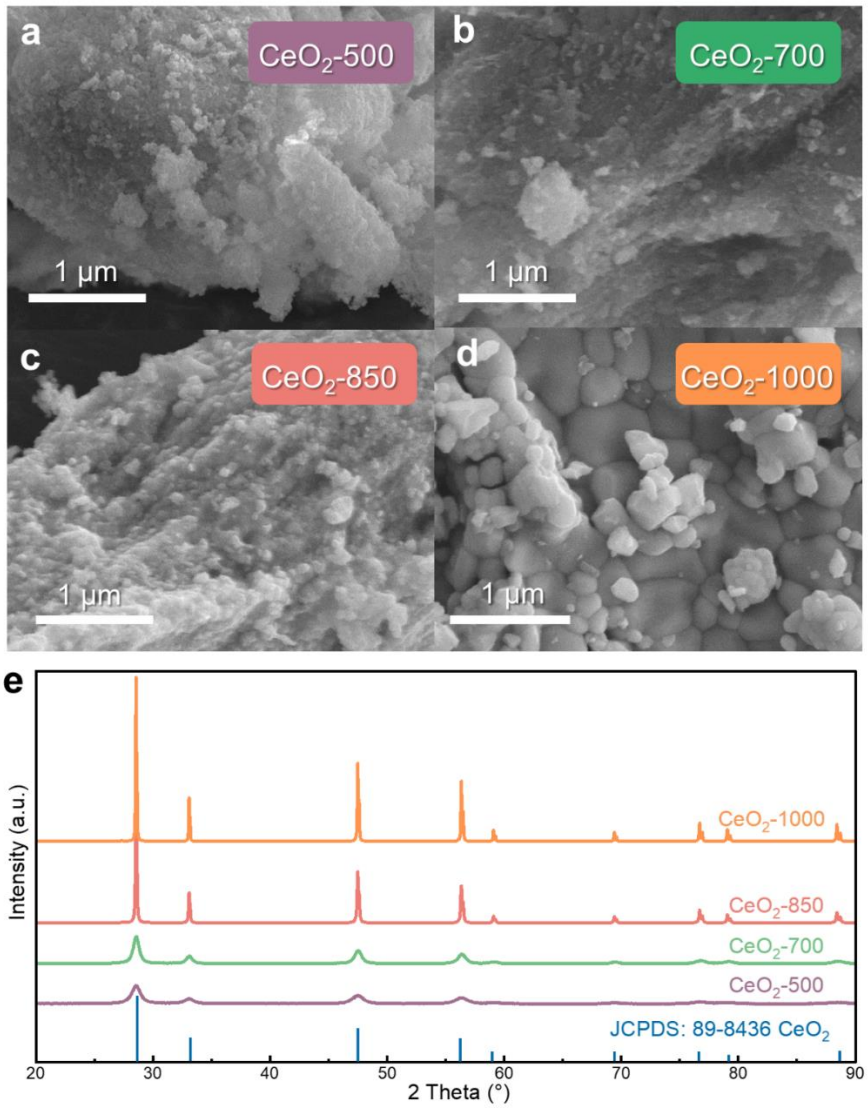

Figure 6.4 SEM images of **a** CeO_2-500, **b** CeO_2-700, **c** CeO_2-850 and **d** CeO_2-1000. **e** XRD patterns of CeO_2-500, CeO_2-700, CeO_2-850 and CeO_2-1000.

6.2.2 Structural and electrochemical properties

The preliminary electrochemical cycling performances of LCO@CeO_2 samples were investigated using GCD in Li half cells. It was observed that the CeO_2 modification resulted in a sacrifice of some capacity. This observation is consistent with the SEM images (**Fig. 6.2b-e**) and XRD patterns (**Fig. 6.3**). LCO@CeO_2-500 (175.7 mAh g^{-1}) and LCO@CeO_2-700 (182.3 mAh g^{-1}) exhibited relatively thick CeO_2 coatings with lower crystallinity, which potentially inhibited the Li^+ transport channels and consequently showed lower capacity. However, as the annealing temperature increased, LCO@CeO_2-850 (200.1 mAh g^{-1}) and LCO@CeO_2-1000 (193.5 mAh g^{-1}) only showed a slight capacity sacrifice than bare-LCO (201.4 mAh g^{-1}). This can be attributed to the larger exposed area and stronger crystalline structure of the loaded CeO_2. The cycling performances of bare-LCO and LCO@CeO_2 cathode materials are compared in **Fig. 6.2h.** The discharge capacity retention values for bare-LCO, LCO@CeO_2-500, LCO@CeO_2-700, LCO@CeO_2-850 and LCO@CeO_2-1000 are 1 mAh g^{-1} (0%), 7.6 mAh g^{-1} (4.3%), 26.4 mAh g^{-1} (14.4%), 185.2 mAh g^{-1} (81.8%) and 26.6 mAh g^{-1} (13.7%). These results clearly demonstrate the crucial role of CeO_2-850 NPs in maintaining discharge capacity and improving cycling durability.

6.2.3 Enhanced redox kinetic for high Li^+ conductivity

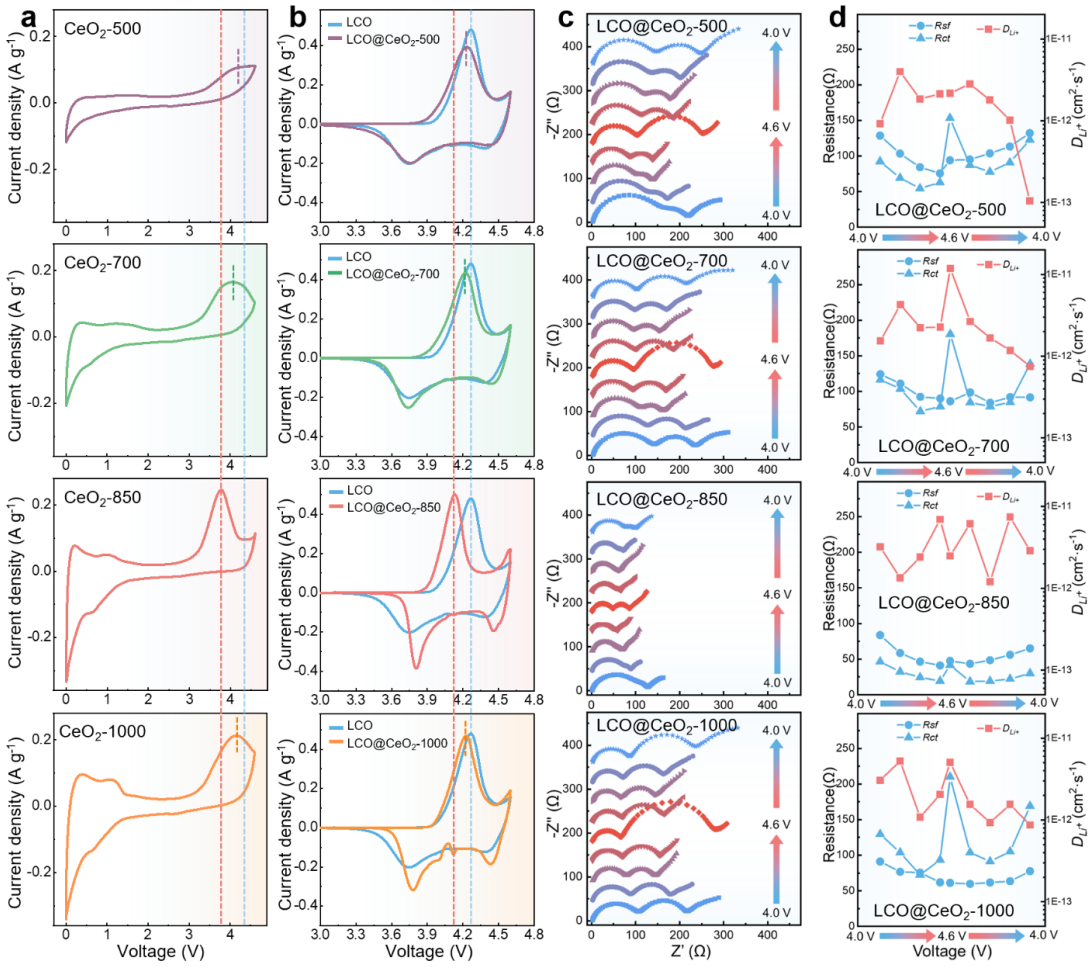

Figure 6.5 a CV curves of initial cycle at 0.1 mV s^{-1} of CeO_2-500, CeO_2-700, CeO_2-850 and CeO_2-1000. **b** CV curves of initial cycle at 0.1 mV s^{-1} of LCO@CeO_2-500, LCO@CeO_2-700, LCO@CeO_2-850 and LCO@CeO_2-1000. **c** *In-situ* EIS test and **d** calculate resistance and Li^+ diffusion coefficient of LCO@CeO_2-500, LCO@CeO_2-700, LCO@CeO_2-850 and LCO@CeO_2-1000 during the second cycle at 0.3C.

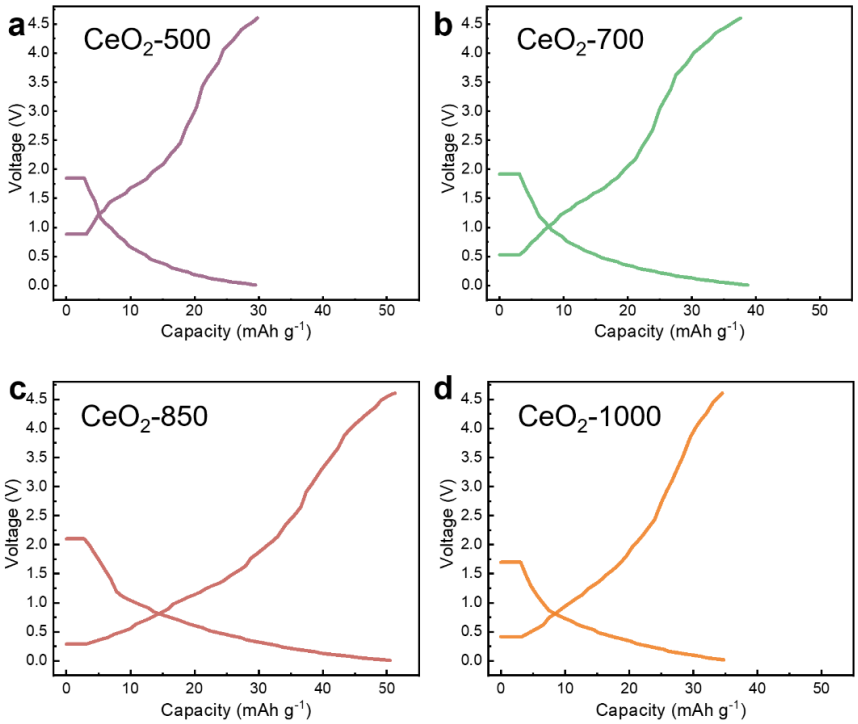

Figure 6.6 Typical GCD profiles under 0.01-4.6 V at 20C of **a** CeO_2-500, **b** CeO_2-700, **c** CeO_2-850 and **d** CeO_2-1000.

The redox peaks of pure CeO_2 NPs are dependent on their crystallinity and particle size. The SEM (**Fig. 6.4a-d**) image and XRD (**Fig. 6.4e**) results of the pure CeO_2 NPs indicate that increasing the annealing temperature results in higher crystallinity and larger particle size. At 500°C and 700°C, the XRD results showed their low crystallinity. Conversely, at 850°C and 1000°C, the crystallinity is relatively high, and the particle size gradually increases. CV (**Fig. 6.5a**) and GCD (**Fig. 6.6**) tests were conducted on the CeO_2 NPs samples. As shown in **Fig. 6.5a**, CeO_2 NP samples demonstrate relatively high oxidation potentials when they possess lower crystallinity (CeO_2-500: 4.19V, CeO_2-700: 4.04V) or larger particle size (CeO_2-1000: 4.09V). In

contrast, CeO_2-850, with higher crystallinity and smaller particle size, exhibits a significantly lower oxidation potential (3.88V).

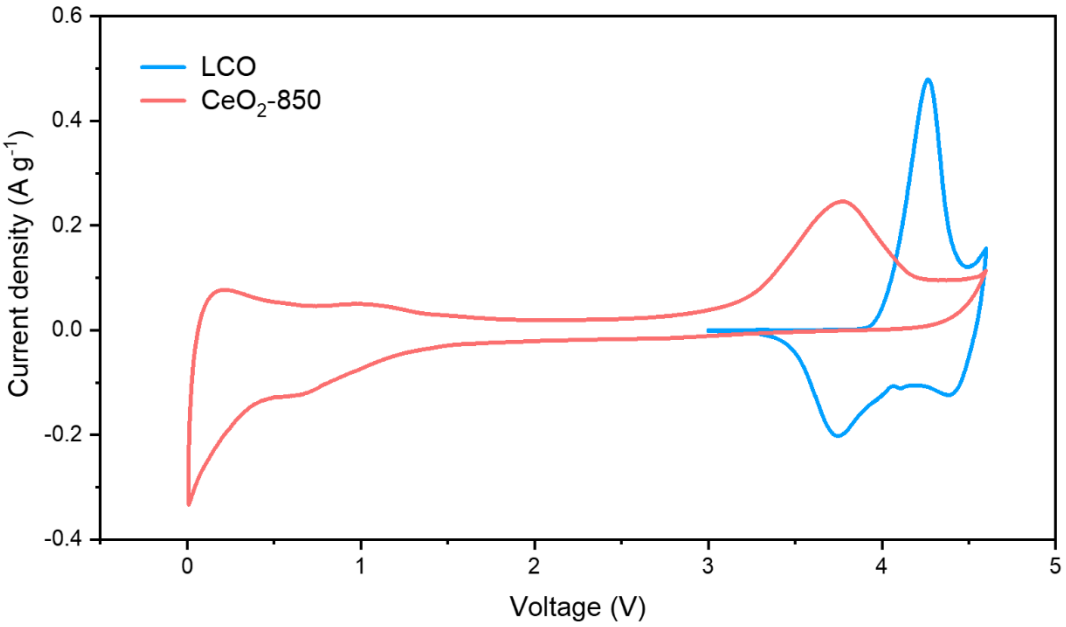

Figure 6.7 Typical CV curves of LCO and CeO_2-850.

Fig. 6.7 illustrates that the oxidation peak of CeO_2-850 is lower than bare-LCO at 4.18V. The oxidation peak of bare-LCO at approximately 4.18V corresponds to the LCO phase transition from hexagonal phase H1 to H2, where the single H2 phase represents approximately 50% Li^+ extraction[19]. As shown in **Fig. 6.2e**, LCO@CeO_2-850 exhibits a uniform distribution of small, highly crystalline CeO_2-850 NPs on LCO surface. The CV results in **Fig. 6.5b** reveal that CeO_2-850 NPs effectively reduces the oxidation peak of LCO to 4.11V. Furthermore, LCO@CeO_2-850 maintains stable redox peaks even after 30 cycles (**Fig. 6.8**).

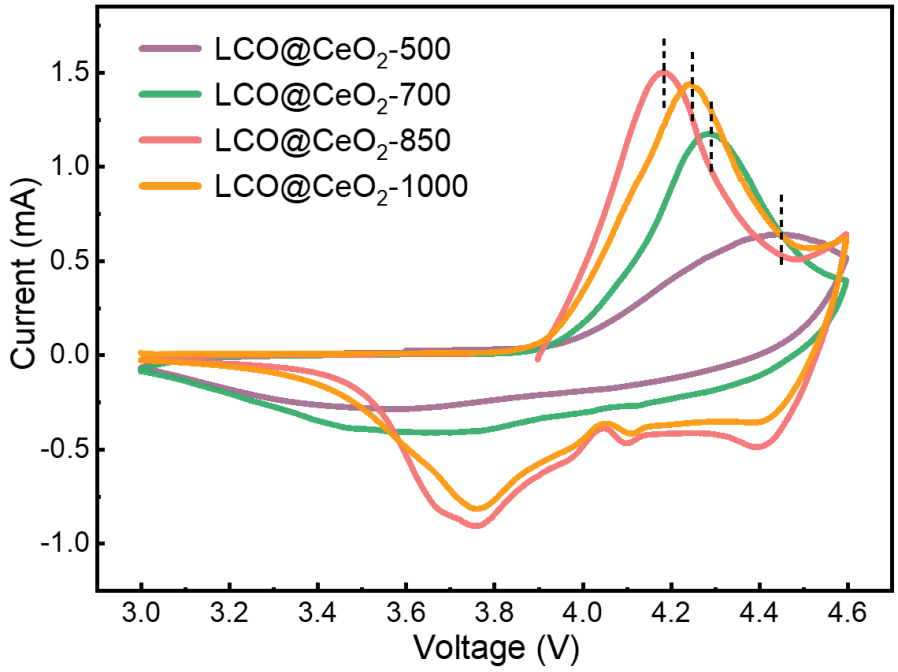

Figure 6.8 CV curves after 30 cycles at 0.1 mV s^{-1}.

The mid-point voltages of the cathodes are compared in **Fig. 6.9** to assess the reversibility of the redox reaction. For the bare-LCO cathode, the mid-point voltage difference increased significantly to 1.51V. However, for the LCO@CeO_2-500, LCO@CeO_2-700, LCO@CeO_2-850, and LCO@CeO_2-1000 samples, the mid-point voltage differences gently grew to 0.62V, 0.47V, 0.19V, and 0.27V, respectively. This lower increase in mid-point voltage differences for LCO@CeO_2 indicates that the CeO_2 modification effectively enhanced the kinetics of Li^+ de/intercalation. Additionally, the LCO@CeO_2 samples annealed at higher temperatures (≥850°C) exhibited enhanced capacity, with LCO@CeO_2-850 demonstrating the best cycling durability. The low mid-point voltage differences observed in these samples confirm that the presence of loaded CeO_2 NPs significantly improved high voltage stability.

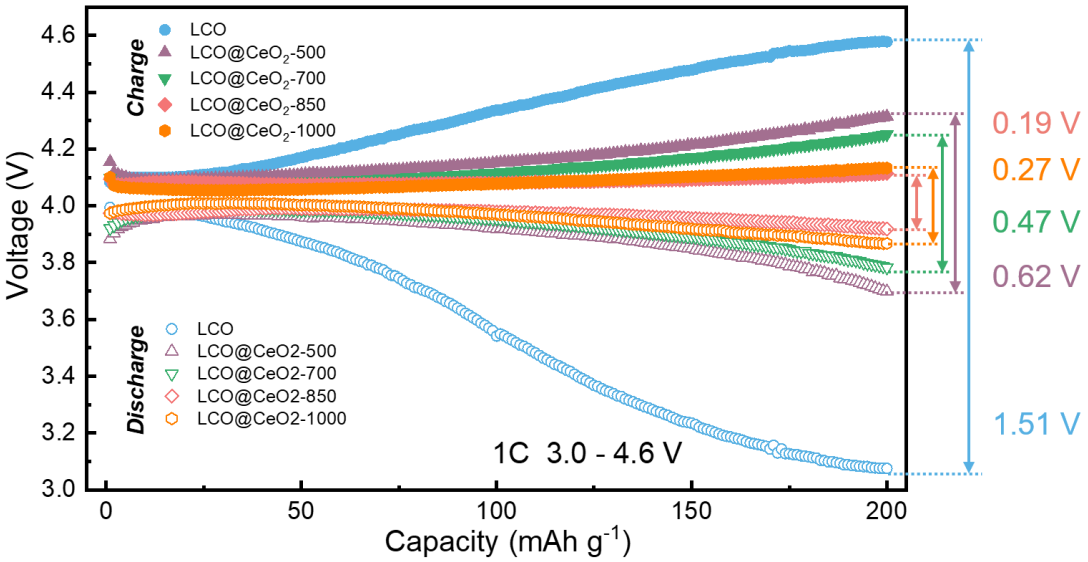

Figure 6.9 Cycling performance of mid-point voltage at 1C under 4.6 V.

By fitting the $(Z_{re} - \omega^{-\frac{1}{2}})$ plot as exhibited in **Fig. 6.10**, the σ term can be determined as the slope of the fitted line. Under the discharge process, the D_{Li^+} for different voltage are shown in **Fig. 6.5c** and **Table 6.1**.

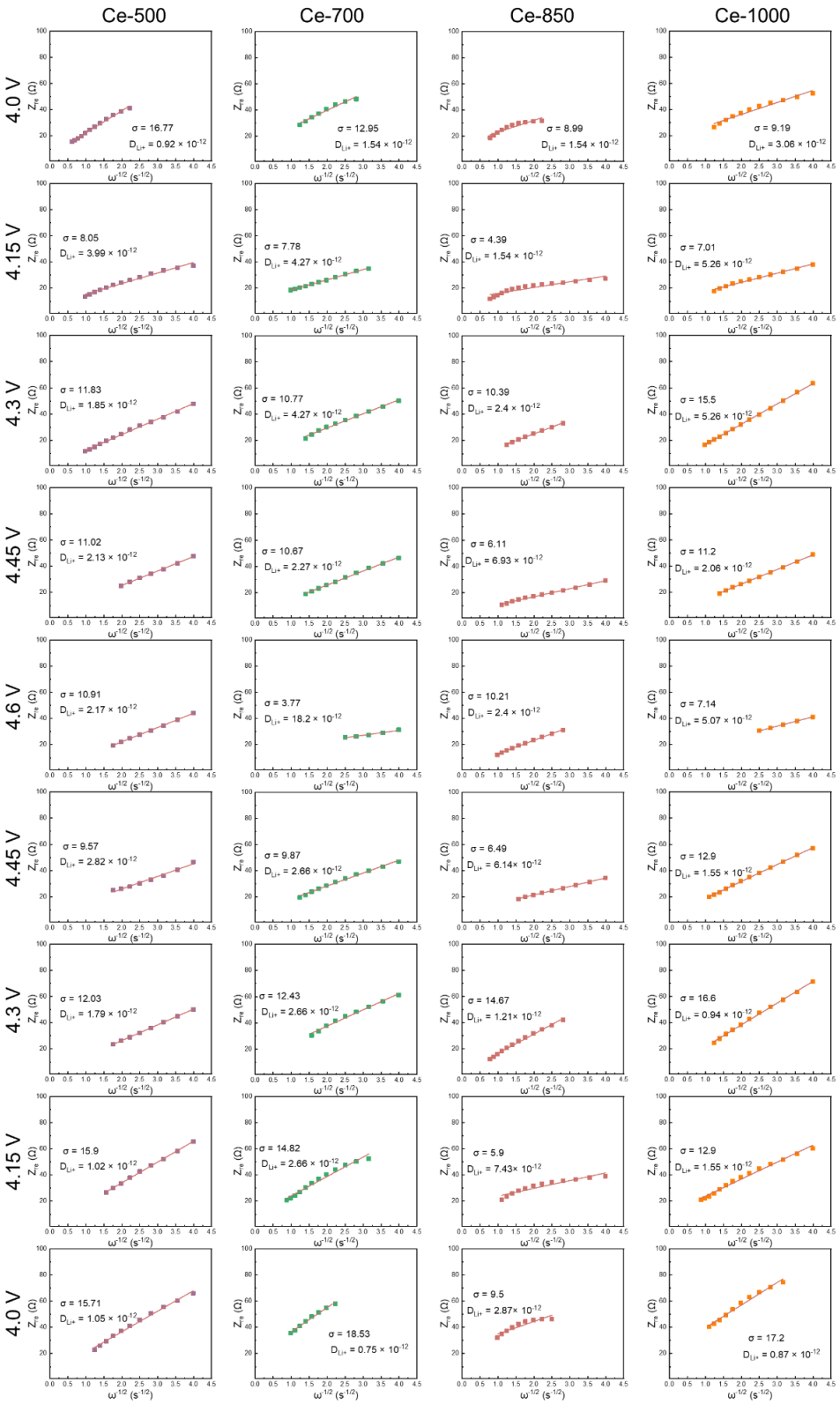

Figure 6.10 The plots of real parts of the complex impedance versus $\omega^{-1/2}$.

Table 6.1 The simulated results from EIS spectra of LCO, LCO@CeO_2-500, LCO@CeO_2-700, LCO@CeO_2-850 and LCO@CeO_2-1000 at various SOC during the second charge/discharge cycle.

Samples	**SOC**	**Simulated electrochemical parameters**			
		***Rsf* (Ω)**	***Rct* (Ω)**	**σ (Ω ·cm^2·mol$^-$**	**D_{Li+}(cm^2·s^{-1})**
LCO	Charged to 4.0V	119.3	153.7	33.04	2.37×10^{-12}
	Charged to 4.15V	102.4	114.5	10.33	2.42×10^{-12}
	Charged to 4.3 V	80.1	73.7	9.42	2.91×10^{-12}
	Charged to 4.45V	69.3	87.7	9.46	2.89×10^{-12}
	Charged to 4.6 V	73.1	182.8	11.03	2.12×10^{-12}
	Discharged to	78.3	95.8	7.89	4.15×10^{-12}
	Discharged to 4.3	81.6	73.5	10.21	2.48×10^{-12}
	Discharged to 4.15	92.5	88.3	9.66	2.77×10^{-12}
	Discharged to	99.9	184.2	10.61	2.30×10^{-12}
LCO@CeO_2-500	Charged to 4.0V	128.7	92.4	16.77	0.92×10^{-12}
	Charged to 4.15V	103.4	69.2	8.05	3.99×10^{-12}
	Charged to 4.3 V	84.3	54.5	11.83	1.85×10^{-12}
	Charged to 4.45V	75.7	62.9	11.02	2.13×10^{-12}
	Charged to 4.6 V	94.1	153.3	10.91	2.17×10^{-12}
	Discharged to	95.1	87.4	9.57	2.82×10^{-12}
	Discharged to 4.3	103.7	77.8	12.03	1.79×10^{-12}
	Discharged to 4.15	113.4	90.9	15.9	1.02×10^{-12}
	Discharged to	132.1	122.9	15.72	1.05×10^{-12}
LCO@CeO_2-700	Charged to 4.0V	124.2	116.5	12.95	1.54×10^{-12}
	Charged to 4.15V	110.9	103.6	7.78	4.27×10^{-12}
	Charged to 4.3 V	92.4	72.1	10.77	2.23×10^{-12}
	Charged to 4.45V	90.1	78.9	10.67	2.27×10^{-12}
	Charged to 4.6 V	86.2	180.6	3.77	11.82×10^{-12}

	Discharged to	98.6	84.6	9.87	2.66×10^{-12}
	Discharged to 4.3	84.1	78.9	12.43	1.67×10^{-12}
	Discharged to 4.15	92.1	84.9	14.82	1.18×10^{-12}
	Discharged to	91.6	138.7	18.53	0.75×10^{-12}
LCO@CeO_2-850	Charged to 4.0V	83.8	46.4	8.99	3.20×10^{-12}
	Charged to 4.15V	58.6	32.4	4.39	1.34×10^{-12}
	Charged to 4.3 V	46.6	24.5	10.39	2.40×10^{-12}
	Charged to 4.45V	41.2	19.4	6.11	6.93×10^{-12}
	Charged to 4.6 V	47.5	41.7	10.21	2.48×10^{-12}
	Discharged to	43.5	18.5	6.49	6.14×10^{-12}
	Discharged to 4.3	48.5	19.3	14.67	1.20×10^{-12}
	Discharged to 4.15	56.1	22.2	5.9	7.43×10^{-12}
	Discharged to	65.2	30.2	9.5	2.87×10^{-12}
LCO@CeO_2-1000	Charged to 4.0V	91.1	129.6	9.19	3.06×10^{-12}
	Charged to 4.15V	76.7	103.7	7.01	5.26×10^{-12}
	Charged to 4.3 V	75.5	72.5	15.5	1.08×10^{-12}
	Charged to 4.45V	61.9	93.5	11.2	2.06×10^{-12}
	Charged to 4.6 V	61.2	210.1	7.14	5.07×10^{-12}
	Discharged to	59.8	103.9	12.9	1.55×10^{-12}
	Discharged to 4.3	61.6	91.3	16.6	0.93×10^{-12}
	Discharged to 4.15	63.6	105.2	12.9	1.55×10^{-12}
	Discharged to	77.6	169.1	17.2	0.87×10^{-12}

To gain further insight into the enhanced kinetics induced by the loading of CeO_2 NPs, *in-situ* EIS was conducted, as shown in **Fig. 6.5c**. **Table S1** shows the fitted electrochemical parameters based on the equivalent circuit and fitting the EIS curves (**Fig. 6.10**). **Fig. 6.5d** illustrates that LCO@CeO_2-850 exhibited significantly lower resistance of charge transfer (R_{sf}) at 4.6 V and showed the highest average diffusion

kinetic among the LCO@CeO_2 samples. During long-term cycling under 4.6 V, the TEM images (**Fig. 6.11**) revealed that the pure CeO_2 crystal structure experienced lattice expansion and lattice disorder. In contrast, CeO_2 NPs, when loaded on the LCO surface, displayed regular lattice fringes, indicating their ability to serve as long-term stable Li^+ conductive pathways.

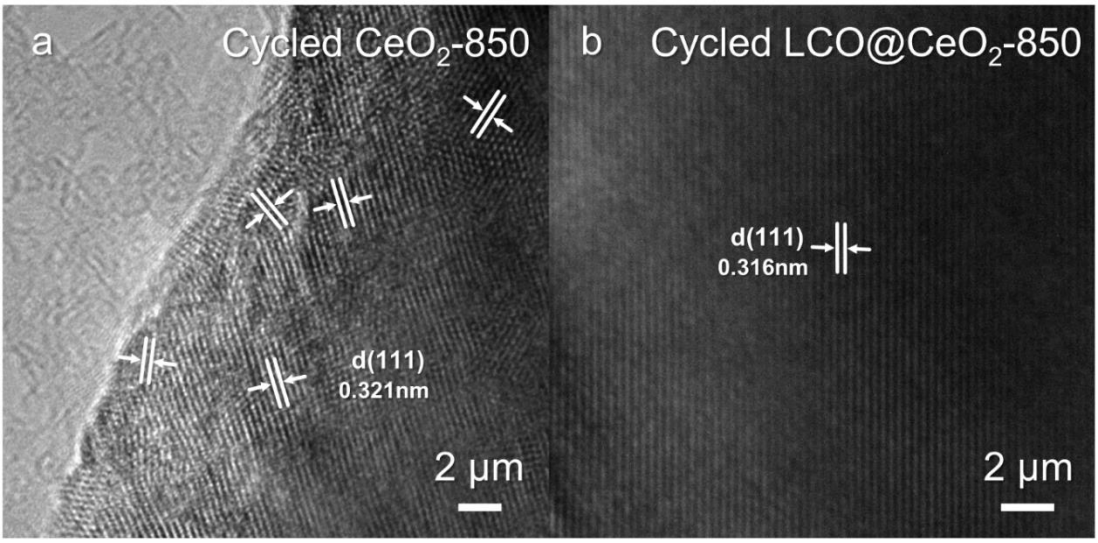

Figure 6.11 TEM image of CeO_2 nanoparticle of **a** CeO_2-850 and **b** LCO@CeO_2-850 after 200 cycles.

6.2.4 Electrochemical performance and characterization

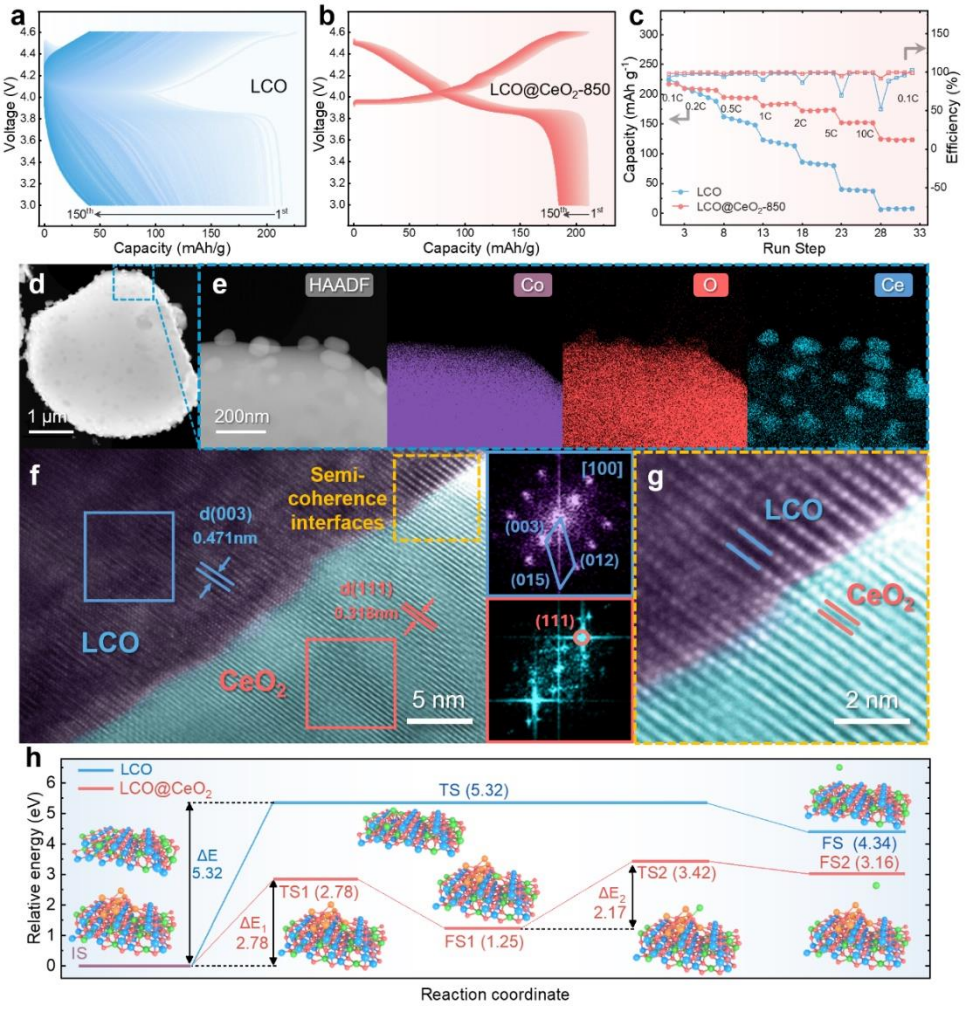

Figure 6.12 Continuous charge/discharge curves from 1st to 150th cycles of **a** LCO and **b** LCO@CeO_2-850. **c** Rate capability from 0.1C to 10C. **d** TEM image and **e** elemental distribution of LCO@CeO_2-850. **f** HRTEM image of LCO@CeO_2-850, the insets are the FFT of the rectangle. **g** Magnified area of the orange rectangle in **f**. **h** DFT-calculated energy barriers for the interface Li^+ diffusion pathway: LCO → vacuum and LCO → CeO_2 → vacuum. Color code for atoms: Li, green; Co, blue; O, red; Ce, orange.

Fig. 6.12a-b demonstrates that LCO@CeO_2-850 exhibited higher cycling durability than LCO under 4.6 V at 1C. As shown in **Fig. 6.13**, high-rate long-term cycling tests were performed on separated pure CeO_2 NPs. All CeO_2 NPs demonstrated the ability for fast charging (20 C) and maintained a high stable capacity even after 1500 cycles. The ultrahigh rate of 20C indicates the great Li conductivity of CeO_2 NPs. Among them, CeO_2@850 exhibited a wider voltage window and higher capacity, confirming the high Li^+ conductivity and structural stability of CeO_2 NPs even under high-rate conditions. This finding suggests that the optimized structure of LCO@CeO_2-850 has the potential to exhibit high-rate capability. **Fig. 6.12c** presents the rate capability of LCO and LCO@CeO_2-850, tested with cycling current densities ranging from 0.1C to 10C. At the ultrahigh rate density of 10C, bare-LCO showed almost zero capacity due to its low Li^+ conductive ability. However, due to the high Li^+ conductive pathway of CeO_2 NPs, LCO@CeO_2-850 demonstrated improved rate performance, delivering a capacity of 124.8 mAh g^{-1} at 10 C.

Fig. 6.12d shows the TEM image of morphology. As shown in **Fig. 6.12e**, EDS mapping of LCO@CeO_2-850 demonstrated that the CeO_2 NPs were uniformly distributed on the surface of LCO. Notably, the HRTEM image (**Fig. 6.12f**) provided a partial enlargement that reveals two distinct lattice fringes. These fringes corresponded to the d(003) crystal plane of the layered structure of LCO and the d(111) crystal plane of the cubic phase of CeO_2, respectively. Furthermore, the TEM magnified image (**Fig. 6.12g**) highlights the remarkable lattice matching between

CeO_2 and LCO heterostructures. This lattice matching indicates that CeO_2 grew along the (003) lattice orientation of the LCO structure, establishing a direct physical Li^+ transport channel. This channel played a pivotal role in facilitating efficient Li^+ transport within the battery system, further enhancing its overall performance.

To investigate the underlying mechanism behind the enhanced Li^+ ion conductivity of LCO@CeO_2-850 facilitated by the small-sized CeO_2-850 NPs, DFT calculations were further employed to analyze the energy barriers of interface Li^+ transport of LCO@CeO_2-850. To simulate practical conditions more accurately, a $Li_{0.5}CoO_2$ structure was used as the model system. Our design **(Fig. 6.12h)** involved two distinct pathways interface Li^+ transport: (1) LCO → vacuum and (2) LCO → CeO_2 → vacuum. Pathway (1) exhibited a relatively high energy barrier of 5.32 eV for Li^+ extraction from the LCO bulk structure. In pathway (2), the CeO_2 enabled the Li^+ deintercalation process to occur in two steps: initial capture of Li^+ ion by CeO_2 with an energy barrier of 2.78 eV, followed by its subsequent release from the CeO_2 with an energy barrier of 2.17 eV. This two-step Li^+ deintercalation process significantly reduced the high energy barrier (5.32 eV) associated with direct extraction from LCO. The calculated results demonstrate that CeO_2 establishes an effective Li^+ transport channel, facilitating the Li^+ deintercalation process at charging voltage of ~4.15V. Moreover, based on the results of CV, *in-situ* EIS, and DFT calculations, the surface modification with CeO_2 NPs was found to effectively enhance the overall redox kinetics during the charging/discharging processes.

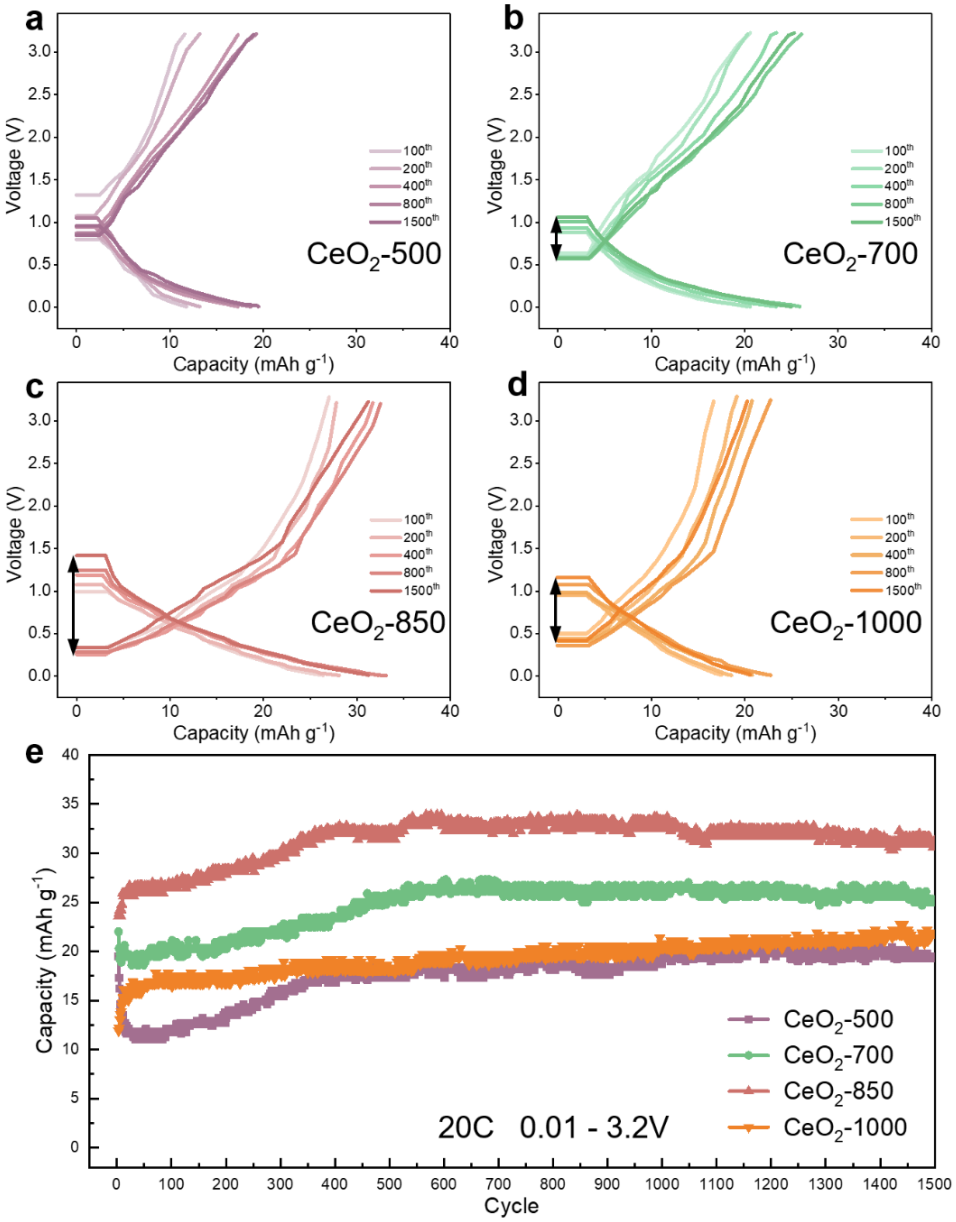

Figure 6.13 GCD profiles of **a** CeO_2-500, **b** CeO_2-700, **c** CeO_2-850 and **d** CeO_2-1000 under 4.6 V. **e** Cycling performance under 4.6 V at 20C.

6.2.5 Storage of lattice oxygen and structural reversibility

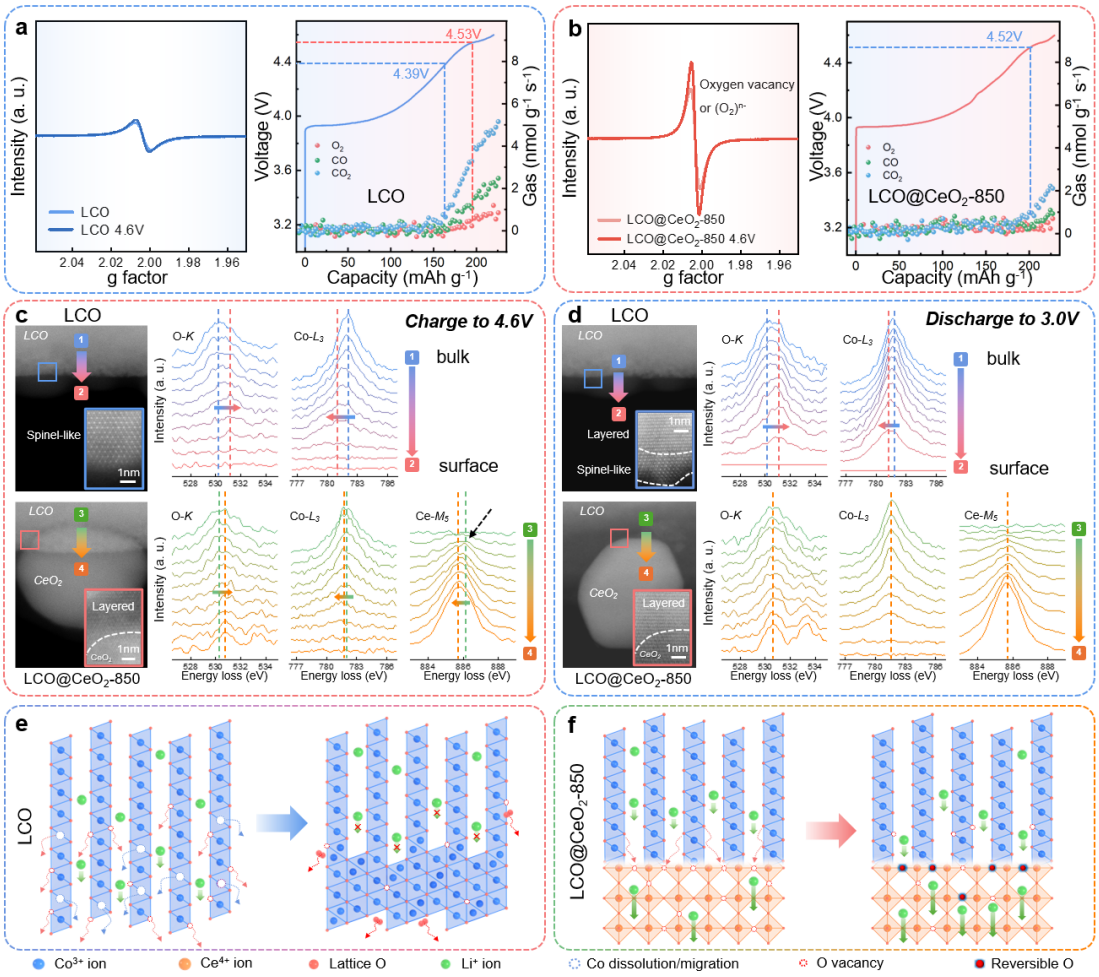

Figure 6.14 EPR spectra of pristine and fully charged state and *in-situ* DEMS collected during the initial charging to 4.6 V for **a** LCO and **b** LCO@CeO_2-850. TEM characterization of surface structure of LCO and LCO@CeO_2-850 when **c** charging to 4.6 V and **d** discharging to 3.0V, and the correlated EELS line scan of O-*K* edge, Co-L_3 edge and Ce-M_5 edge in the arrow region under the STEM-HAADF mode. Schematic diagrams of the surface structure evolution for **e** LCO and **f** LCO@CeO_2-850.

The presence of CeO_2 NPs not only facilitated the establishment of a fast Li^+

conductive pathway but also helped in storing unstable lattice oxygen to form reversible oxygen species under high voltage. EPR measurements were conducted to confirm the oxygen state and lattice oxygen migration, as shown in **Fig. 6.14a-b**. The intense sharp signal observed at an effective g-value of ~2.007 in the EPR spectra was attributed to the presence of unpaired electron resulting from the formation of oxygen vacancies or $(O_2)^{n-}$ (n = 1, 2, 3)[196, 197]. Among these species, $(O_2)^{3-}$ is often considered as a reversible oxygen species in layered metal oxide cathode[198, 199].

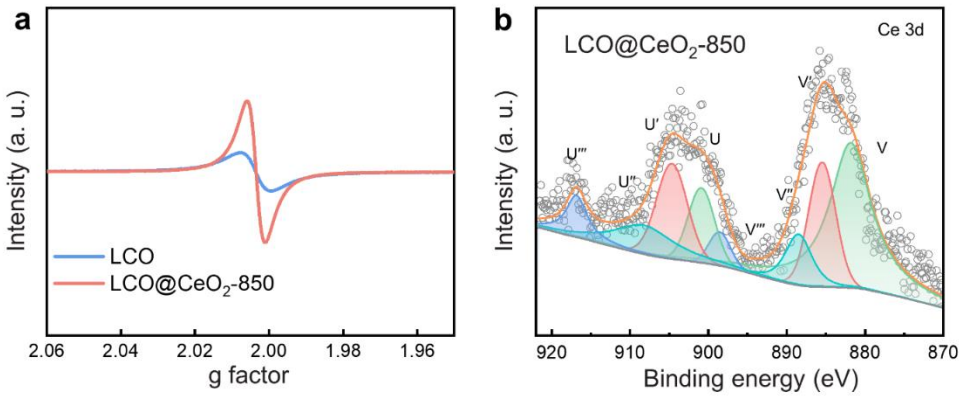

Figure 6.15 a EPR spectrum of bare-LCO and LCO@CeO_2-850. **b** Ce 3d XPS spectrum of LCO@CeO_2-850.

Fig. 6.15a demonstrates that the intensity of EPR peak of LCO@CeO_2-850 became stronger than bare-LCO, suggesting the loading CeO_2 NPs have some oxygen vacancies. This observation is consistent with the existence of the Ce^{3+} as observed in XPS at 885.1 eV and 904.0 eV (**Fig. 6.15b**). As shown in **Fig. 6.14a**, as charging to 4.6 V, the intensity of EPR peak of bare LCO slightly enhanced. *In-situ* DEMS testing revealed that a significant amount of oxygen gas started to evolve from the cathode surface above 4.53V, reaching 5.16 nmol $g^{-1}s^{-1}$ at 4.6 V. These results indicate the

instability of lattice oxygen on the cathode surface at high voltage[183], leading to the release of oxygen gas and the generation of oxygen vacancies in LCO. In the case of LCO@CeO_2-850 (**Fig. 6.14b**), almost zero oxygen generation was detected even at 4.6 V, but the intensity of EPR peak increased during charging. By combining the findings from *in-situ* DEMS and EPR testing, it can be inferred that the under high voltage condition, the unstable lattice oxygen on the LCO surface is effectively captured by CeO_2. The notable increase in the EPR peak intensity can be attributed to the deeper capture of lattice oxygen, resulting in the formation of reversible $(O_2)^{3-}$ species.

To establish a comprehensive understanding of the structure-performance relationship emerging from the CeO_2 NPs, EELS measurements were conducted to investigate the valence variation of O, Co, and Ce from the bulk to the surface lattice of bare-LCO and the LCO/CeO_2 NPs interface using the STEM-HAADF mode. For bare-LCO, charging to 4.6 V resulted in a significant reduction of TM species (Co^{3+} reduction to Co^{2+} indicated by the Co-L_3 edge in **Fig. 6.14c**) and a positive shift in near-surface lattice oxygen (observed through the pre-edge peak at ~530.5 eV of the O-*K* edge in **Fig. 6.14c**). These changes were observed in the very surface region of bare-LCO. This is mainly due to the unwanted phase transition from $LiCoO_2$ to Co_3O_4 (spinel phase) caused by deep delithiation[42, 21]. This phase transition would lead to sluggish Li^+ conductivity and the electrochemical failure[17].

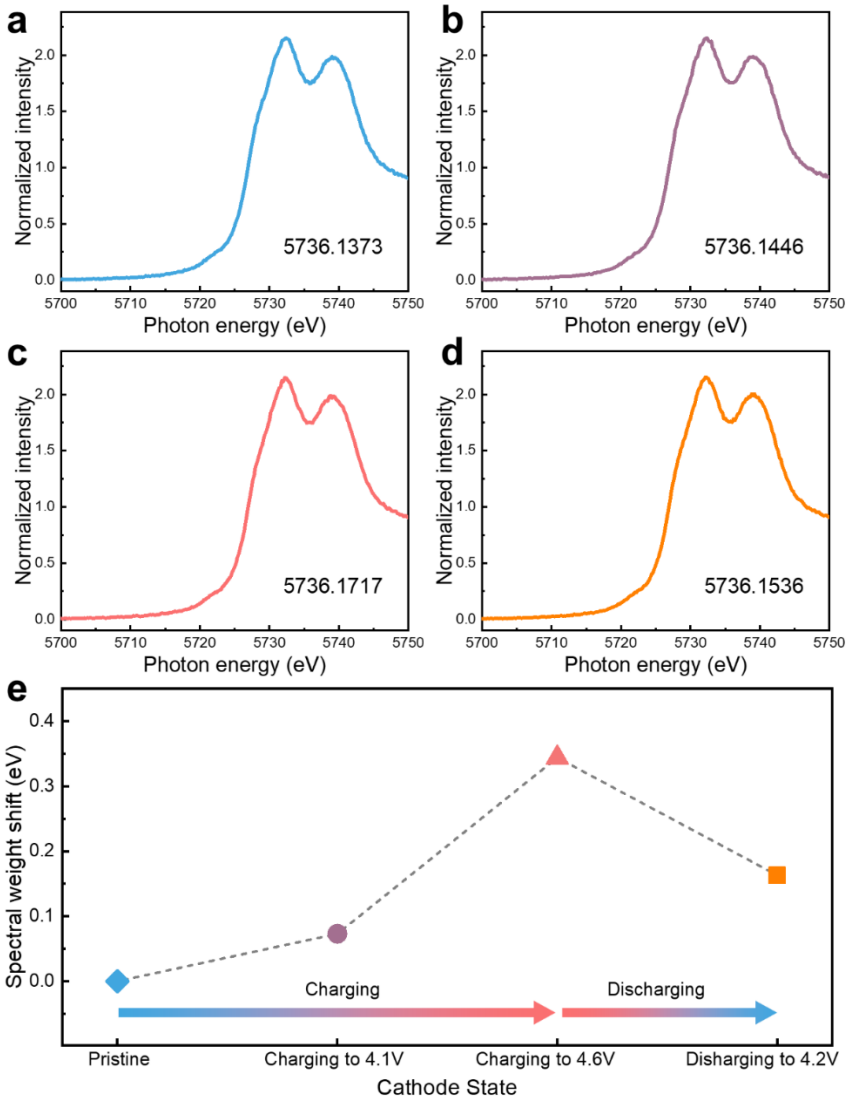

Figure 6.16 Ce L_3 edge XAS spectra of **a** pristine, **b** charging 4.1V, **c** charging 4.6 V and **d** discharging 4.2 V states of the LCO@CeO_2-850 sample. The Ce L_3 edge spectral weight shift of pristine, charging 4.1V, charging 4.6 V and discharging 4.2 V states of the LCO@CeO_2-850 sample.

In contrast, **Fig. 6.14c** demonstrates that LCO@CeO_2-850 exhibited a suppressed surface reconstruction. The scanned spectral lines of Co-L_3 edge and O-K edge showed only a minor shift relative to those in the bare LCO. At the LCO/CeO_2

interface, there was a noticeable positive shift of Ce-M_5 edge, which suggests a higher oxidation state for Ce. This positive shift (black arrow) indicates a reduction in oxygen vacancies at the interface under a high voltage of 4.6 V. The reduction in oxygen vacancies can be attributed to CeO_2 acting as an oxygen storage material, storing the unstable lattice oxygen originating from the LCO surface. Furthermore, combined with the increased intensity of the EPR peak (**Fig. 6.14b**), it can be inferred that the formation of reversible $(O_2)^{3-}$ species occurs on the CeO_2 NPs. Additionally, we investigated the change in the Ce valence state in the pristine, charging to 4.1 V, charging to 4.6 V, and discharging to 4.2 V states of the LCO@CeO_2-850 sample using Ce-L_3 edge XAS, as shown in **Fig. 6.16**. Upon charging to 4.6 V, the Ce-L_3 spectrum exhibited a positive shift of 0.344 eV in spectral weight. This positive shift in spectral weight indicates a gradual rise in the Ce valence state[200, 201], which is consistent with the valence states determined from the EELS data. The findings from both the EELS and XAS analyses align with the near-zero oxygen detection observed through in-situ DEMS at 4.6 V. This provides further evidence supporting the effectiveness of CeO_2 in capturing and stabilizing lattice oxygen from the LCO surface, thereby preventing its release and subsequent gas generation.

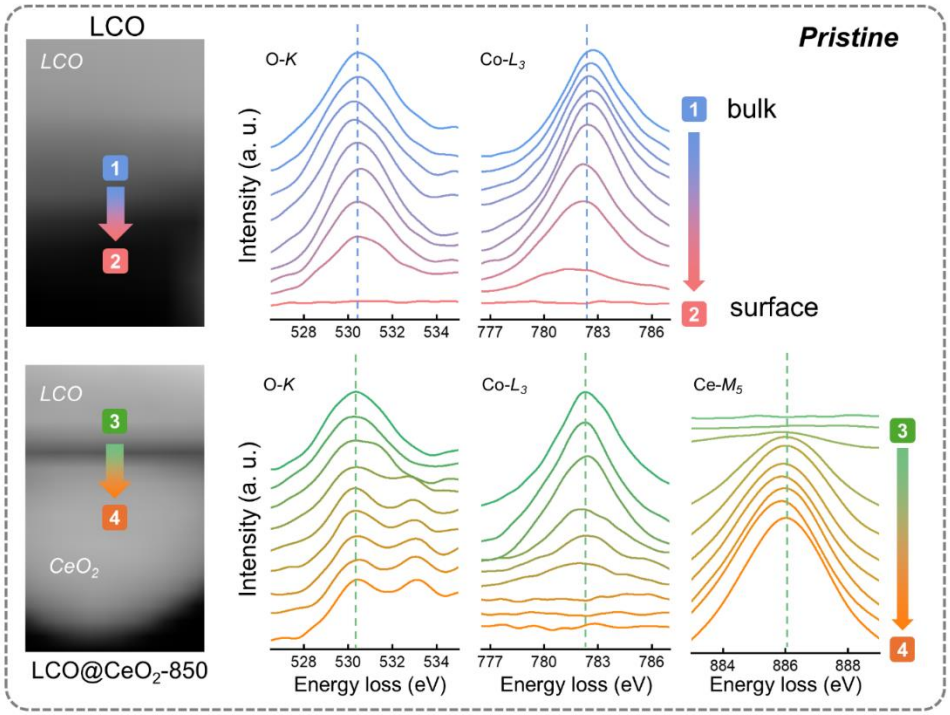

Figure 6.17 TEM characterization of surface structure of **a** bare-LCO and **b** LCO@CeO_2-850, and the correlated EELS line scan of O-*K* edge, Co-L_3 edge and Ce-M_5 edge in the arrow region under the STEM-HAADF mode.

Upon discharging to 3.0V (**Fig. 6.14d**), the surface of LCO underwent an irreversible phase transition, transforming into a spinel-like phase with a thickness of approximately 2-3 nm. In contrast, at the interface of LCO@CeO_2-850, the layered structure of LCO was retained, and the elemental composition of Co, O, and Ce remained relatively stable. As shown in **Fig. 6.17**, the EELS spectrum of the discharging 3.0 V state was similar to the pristine state of LCO@CeO_2-850. This similarity indicates that the storage and release of lattice oxygen were reversible in LCO@CeO_2-850, with CeO_2 NPs acting as an oxygen storage material for lattice oxygen and contributing to the maintenance of a stable surface structure in LCO.

Moreover, after discharge to 3.0 V, **Fig. 6.18** show that CeO_2 NPs maintained a uniform and consistent crystal structure, further demonstrating their structural stability even under the specific discharge condition. **Fig. 6.14e-f** provides a schematic diagram illustrating the migration path of lattice oxygen of bare-LCO and LCO@CeO_2-850 during the charging process. For bare-LCO, the surface lattice oxygen was oxidized to a higher valence state and migrates to the surface. When charging to 4.6 V, the escape of unstable oxygen led to a larger amount of gas generation. Additionally, the surface underwent an irreversible phase transition into a spinel-like Co_3O_4 phase[21]. In contrast, LCO@CeO_2-850, with its interspersed CeO_2 NPs, offered protective effects on the surface structure and established stable Li^+ transport channels, thereby mitigating the degradation of the cathode. The CeO_2 NPs possessed abundant oxygen vacancies and exhibited a good capacity for storing unstable lattice oxygen. The interspersed CeO_2 NPs was responsible for maintaining the reversible layered material and improving the integral stability.

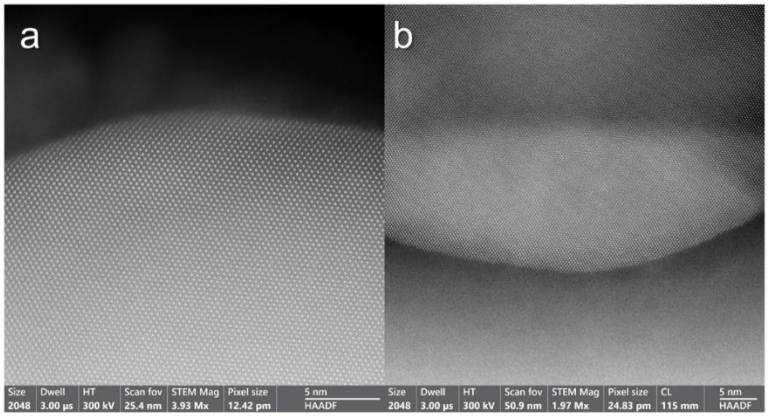

Figure 6.18 TEM image of CeO_2 nanoparticle (loading on LCO@CeO_2-850) when discharge to 3.0 V.

6.2.6 Post-cycling characterization

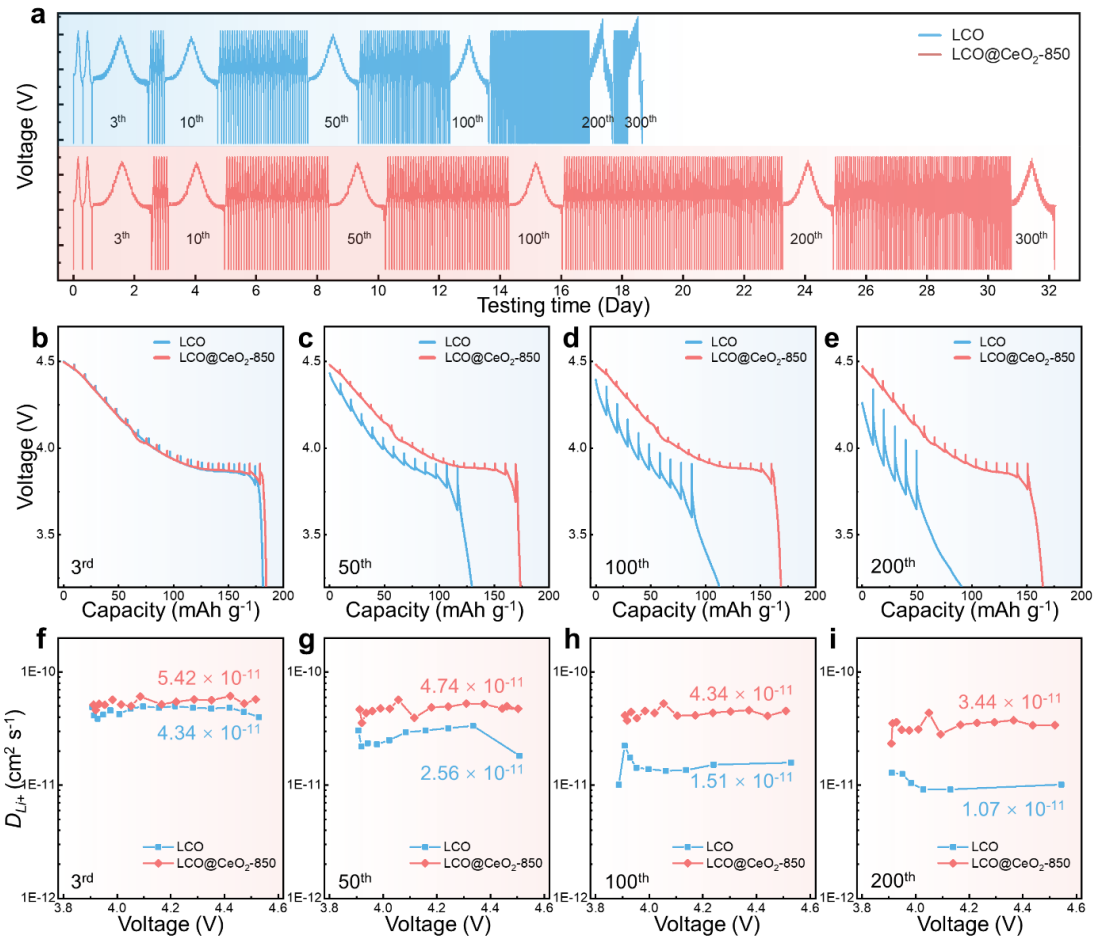

Figure 6.19 a Cycling performance and overpotential properties. The GITT curves of **b-e** LCO and LCO@CeO_2-850 at the 3rd, 50th, 100th, and 200th cycle. The corresponding Li^+ diffusion coefficients of **f-i** LCO and LCO@CeO_2-850 at the 3rd, 50th, 100th, and 200th cycle.

To investigate the influence of CeO_2 NPs on the Li^+ diffusion kinetics during long-term cycling, the GITT tests were employed. As shown in **Fig. 6.19a**, it can be observed that LCO@CeO_2-850 required 32 days to complete 300 cycles, which is longer than the 19 days required for LCO. This extended cycling time indicates that

LCO@CeO_2-850 exhibited superior cycling durability compared to LCO. **Fig. 6.19b-d** illustrates the electrode polarization and self-discharge behavior of LCO and LCO@CeO_2-850 during cycling. LCO experienced a rapid increase in electrode polarization starting from the 50th cycle.

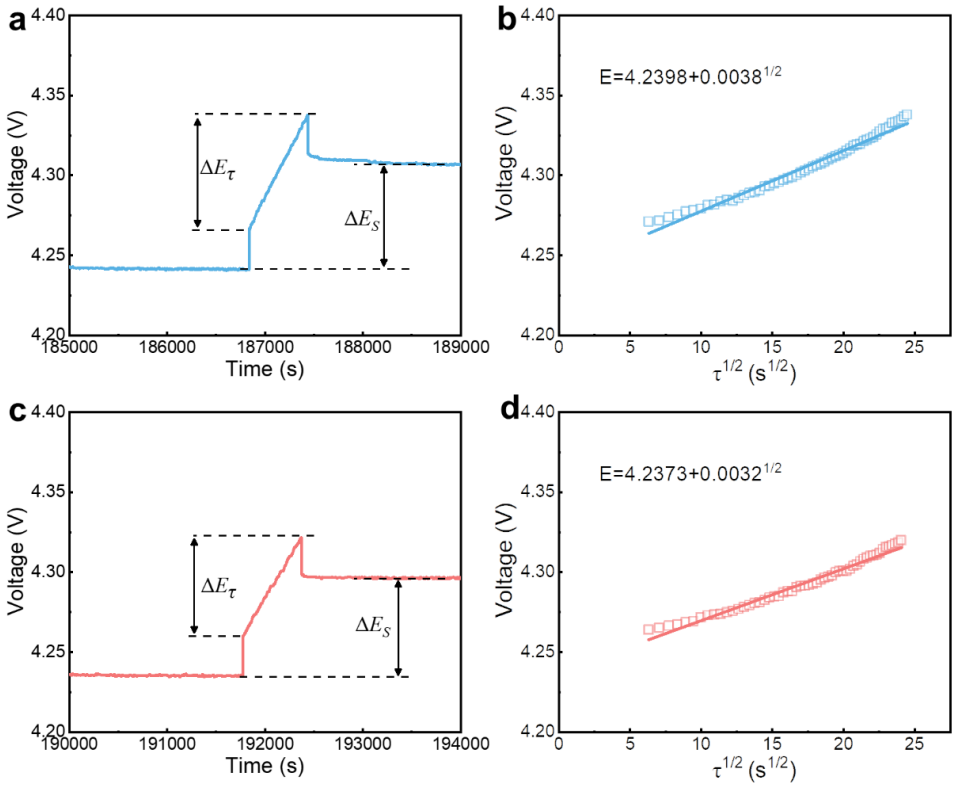

Figure 6.20 A typical time versus potential profile of **a** LCO and **c** LCO@CeO_2-850. A linear relationship between potential and $\tau^{1/2}$ of **b** LCO and **d** LCO@CeO_2-850.

The typical potential versus time profiles are shown in **Fig. 6.20**, providing further insight into their electrochemical behavior. The evolution of Li^+ diffusion coefficient (D_{Li+}) of cathodes during cycling is shown in **Fig. 6.19f-i**. During the 3rd cycle, the calculated D_{Li+} values are similar for both cathodes, indicating comparable Li^+ diffusion kinetics at the initial stage. However, as cycling progresses from the 50th to

the 200th cycle, the average D_{Li+} of LCO@CeO_2-850 remained almost unchanged, while that of LCO experienced a significant decrease. A linear relationship between potential and $\tau^{1/2}$ was observed. The GITT results provided confirmation that the effective strategy of utilizing interspersed CeO_2 NPs enhanced the Li^+ diffusion kinetics in LCO@CeO_2-850. This enhancement was evidenced by the larger and more stable Li^+ diffusion coefficients observed in LCO@CeO_2-850 (3.44×10^{-11} cm^2 s^{-1}) compared to LCO (1.07×10^{-11} cm^2 s^{-1}) after 300 cycles.

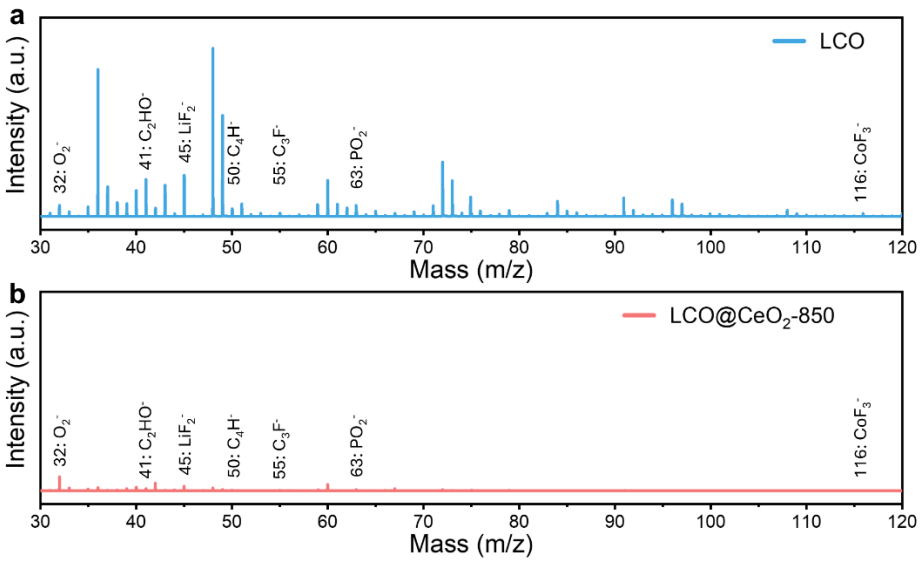

Figure 6.21 TOF-SIMS patterns for **a** LCO, **b** LCO@CeO_2-850.

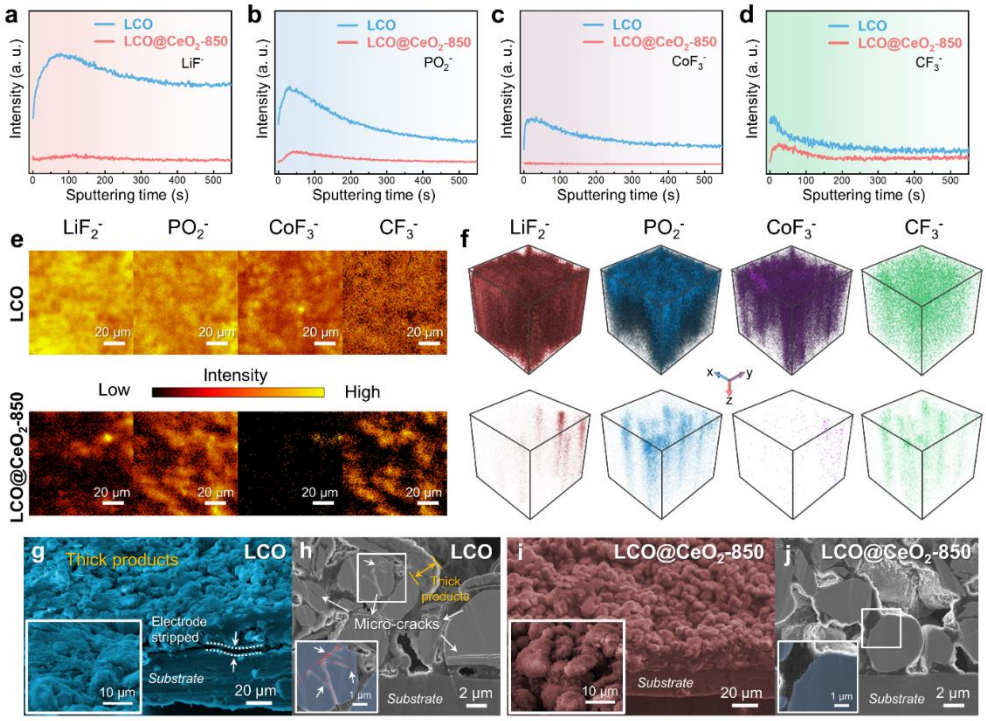

Figure 6.22 TOF-SIMS depth profiles of **a** LiF_2^-, **b** PO_2^-, **c** CoF_3^- and **d** CF_3^- for LCO and LCO@CeO_2-850 after 200 cycles. **e** Surface species distributions. **f** 3D rendering TOF-SIMS fragments. Side view and cross-sectional SEM images of **g, h** LCO and **i, j** LCO@CeO_2-850 cathodes after 200 cycles.

TOF-SIMS analysis was performed on the 200 cycled cathodes of LCO and LCO@CeO_2-850, the patterns are shown in **Fig. 6.21**. The normalized intensity analysis of select fragments (LiF_2^-, PO_2^-, CoF_3^-, CF_3^-, C_4H^- and C_2HO^-) shown in **Fig. 6.22a-d** and **6.23a, b** indicates that the CEI layer induced by surface side reactions was mitigated in the LCO@CeO_2-850 sample compared to the bare-LCO. Additionally, TOF-SIMS chemical images and 3D reconstruction (**Fig. 6.22e, f** and **6.23c, d**) demonstrated a thinner gradient concentration of interface degradation-generated species within the modified cathode.

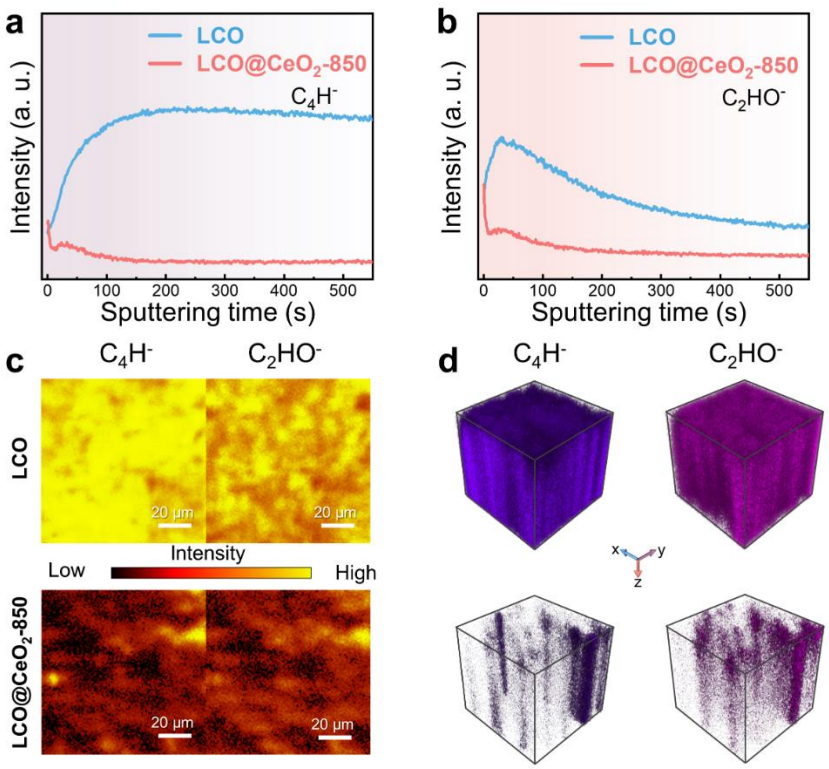

Figure 6.23 TOF-SIMS depth profiles of **a** C_4H^-, **b** C_2HO^- for LCO and LCO@CeO_2-850 after 200 cycles. **c** Surface species distributions. **d** 3D rendering TOF-SIMS fragments.

Side views of the electrode morphology after 200 cycles are presented in **Fig. 6.22g, i**. Bare-LCO electrode exhibited a thick layer of side reaction products, along with electrode stripped from the Al substrate. In contrast, the LCO@CeO_2-850 electrode displayed a distinct grain morphology and maintains excellent adhesion to the substrate. Cross-sectional SEM images of the LCO, LCO@CeO_2-500, and LCO@CeO_2-850 grains after 200 charge-discharge cycles are shown in **Figs. 6.22h, j and 6.24a, b**.

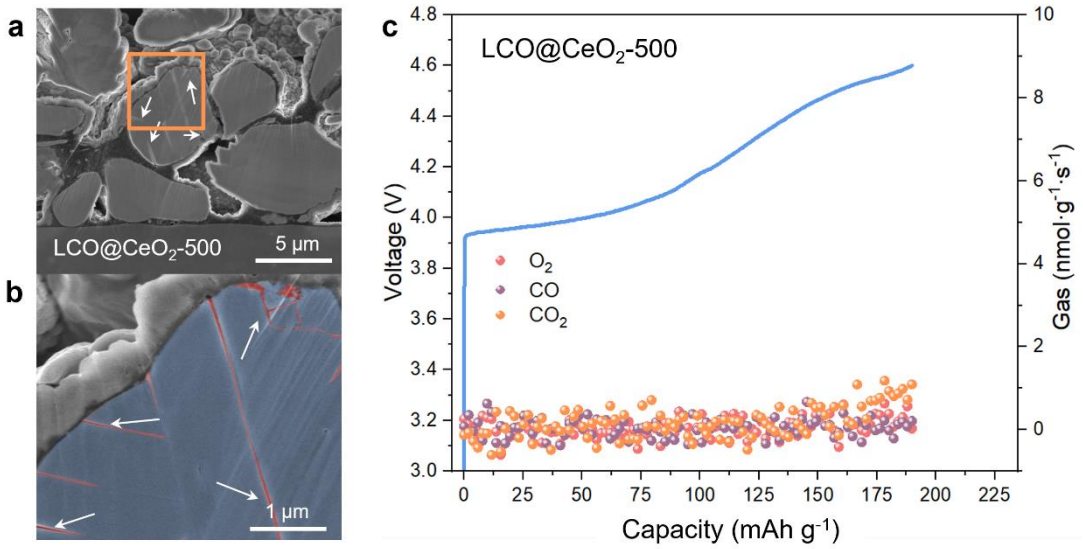

Figure 6.24 a Cross-sectional SEM images of 200 cycles LCO@CeO_2-500. **b** Magnified area of the orange rectangle in **a**. **c** *In-situ* DEMS under cut-off voltage of 4.6 V for LCO@CeO_2-500.

The cycled LCO grains exhibited severe microcracks throughout the bulk and surface. In the case of LCO@CeO_2-500, numerous microcracks were observed near the surface (**Fig. 6.24a-b**). While the thick CeO_2 coating served to prevent direct contact between the electrolyte and the LCO surface, providing cathode protection, it also suppressed the generation of gases (**Fig. 6.24c**). Additionally, the relatively rigid property of CeO_2 coating restricted the volume expansion and shrinkage of the LCO material. Consequently, incomplete capacity release and the stress accumulation at the CeO_2/LCO interface may occur, leading to the creation of microcracks near the surface region. In contrast, the interspersed CeO_2 NPs employed in LCO@CeO_2-850 enabled the normal volume expansion and shrinkage of the LCO material while offering surface protection. LCO@CeO_2-850 exhibited a relatively integral bulk

structure without observable microcracks, providing solid evidence for enhanced structure stabilities.

Differential scanning calorimetry (DSC) profiles of delithiated cathodes (**Fig. 6.25**) show that LCO@CeO_2-850 exhibited a lower exothermic peak and lower heat release intensity than bare-LCO, demonstrating that LCO@CeO_2-850 was far more stable than bare-LCO under high temperatures. This indicates that LCO@CeO_2-850 has the potential to withstand higher operating temperatures, making it suitable for high temperature environments.

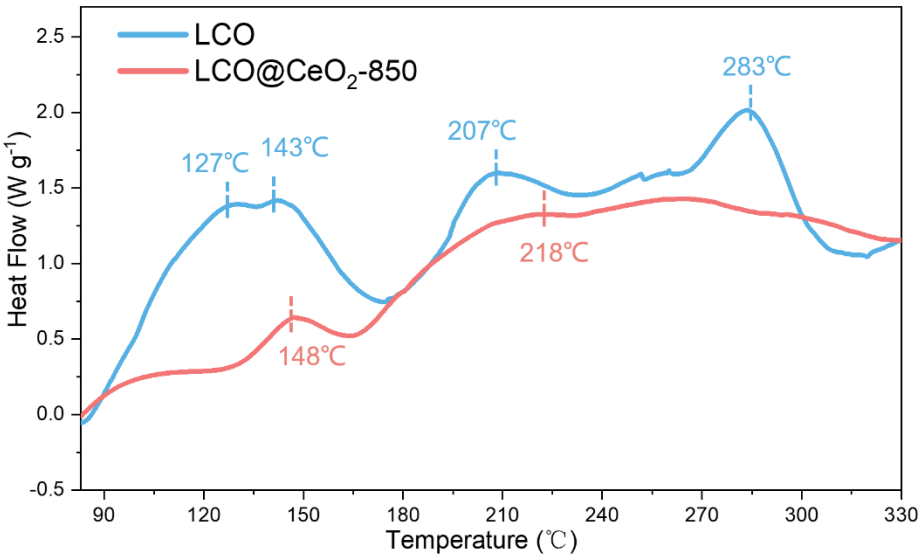

Figure 6.25 DSC tests of LCO and LCO@CeO_2-850 at first cycle charging to cut-off voltage of 4.6 V.

6.3 Conclusion

In summary, we introduced a novel coating approach employing interspersed CeO_2 layer, which resulted in a multifunction of Li^+ conductivity, suppressed lattice collapse, as well as oxygen storage in LCO cathode under 4.6 V. The enhanced stability observed in optimal LCO@CeO_2 (LCO@CeO_2-850) was attributed to the uniform distribution of small CeO_2 NPs, which effectively constructed faster and easier Li^+ conductive pathways, reduced the oxidation potential of LCO, and facilitated the kinetics of Li^+ de/intercalation. Additionally, at high voltage, CeO_2 NPs effectively stored unstable lattice oxygen as reversible oxygen species, thereby inhibiting oxygen escape from the cathode. The well-designed surface engineering in LCO@CeO_2-850 promoted the effective mitigation of structure/surface degradation during long-term cycling. Notably, LCO@CeO_2-850 demonstrated outstanding capacity retention of 88.9% after 200 cycles at a 1C rate and exhibited a high-rate capacity of 124.8 mAh g^{-1} under 10 C. These remarkable achievements provide valuable insights for the rational design of advanced cathodes with multifunctional interspersed nanoparticles structures, opening new possibilities for future developments in high-voltage batteries.

Chapter 7 Summary and future Work

7.1 Summary

In this thesis, we systematically investigate the working principles, failure mechanisms, and modification strategies of high-voltage LCO cathodes for high-performance LIBs. Achieving higher energy density in LIBs requires addressing the challenges posed by high-voltage. Therefore, a deep understanding of the working principles, failure mechanisms, and commonly employed modification strategies for cathodes is essential for the advancement of energy storage systems. In response to the growing requirements for high energy density LIBs, we designed the LCO cathode to withstand high-voltage operating conditions. Firstly, we prepare a core-shell structured single crystal co-doping LCO, based on the diffusivity of different cations. In the second work, we develop a uniform coating of $AlPO_4$-5 zeolite on the surface of LCO, enabling rapid Li^+-desolvation at the LCO-electrolyte interface. In the third work, we employ a multifunctional CeO_2 coating to modify the surface of LCO, enhancing its redox kinetics and reversible storage of lattice oxygen. The key findings of each study are highlighted below:

(1) The elemental co-doping strategy shows promising potential for long-term cycling durability. However, one-step co-doping leads to the enrichment of low-diffusivity ions at grain boundaries, reducing crystal growth kinetics and hindering single-crystal formation. To address this, we employ a two-step synthesis method to fabricate core-shell-structured single-crystal LCO, considering the diffusivity of different doping

cations. In this process, high-diffusivity Al^{3+}/Mg^{2+} ions occupy the core matrix, while low-diffusivity Ti^{4+} ions enrich the shell layer. The resulting core-shell LCO exhibits a mitigated phase transition from O3 to H1-3, leading to reduced contraction of the c-axis and structural distortion.

(2) The phosphate-based coating strategy showed significant potential for enhancing the long-term cycling durability of LIBs. However, conventional amorphous coatings could impede Li^+ diffusion, leading to sluggish Li^+ kinetics. In this study, we found that the incorporation of triethylamine as a template promotes the phase transformation of amorphous $AlPO_4$ to crystalline $AlPO_4$-5 zeolite on the surface of LCO. The $AlPO_4$-5 zeolite coating exhibited multifunctional effects, providing a stable pathway for Li^+ ion transport and accelerating the Li^+-desolvation process.

(3) Increasing the cut-off voltage in LIBs allows for additional capacity. However, it also poses a significant risk to the structural stability of the cathode. The oxidation of surface lattice oxygen in the cathode, resulting in the formation of O_2, is detected when the voltage exceeds 4.5 V. To address this challenge, we introduced a novel coating approach utilizing an interspersed CeO_2 layer. This approach offered multiple benefits, including enhanced Li^+ conductivity, suppression of lattice collapse, and oxygen storage in the LCO cathode under a high voltage of 4.6 V. The well-designed surface engineering in LCO@CeO_2-850 effectively mitigated structure/surface degradation during long-term cycling.

7.2 Future work

Among the various layered TM oxide cathodes, LCO stands out due to its stable charge/discharge voltage plateaus, high tap density, high energy density, and easy synthesis. It remains the predominant commercial cathode material to this day. However, achieving stable operation of LCO at 4.6 V demands further research and efforts. Therefore, this thesis primarily focuses on the failure mechanisms and modification strategies specifically for LCO cathodes in high-voltage LIB systems. It not only provides a comprehensive understanding of the structural aspects but also facilitates the future effective and rational development of high-voltage LCO with superior stability. Even though these achievements (clarification of failure mechanisms and performance improvement of high-voltage LCO) have been achieved in recent studies, some remaining issues still exist in high-voltage LCO-based LIB systems, as illustrated in **Fig. 7.1**. In this section, we present these remaining challenges and future perspectives in developing high-voltage LCO cathodes for advanced LIBs below.

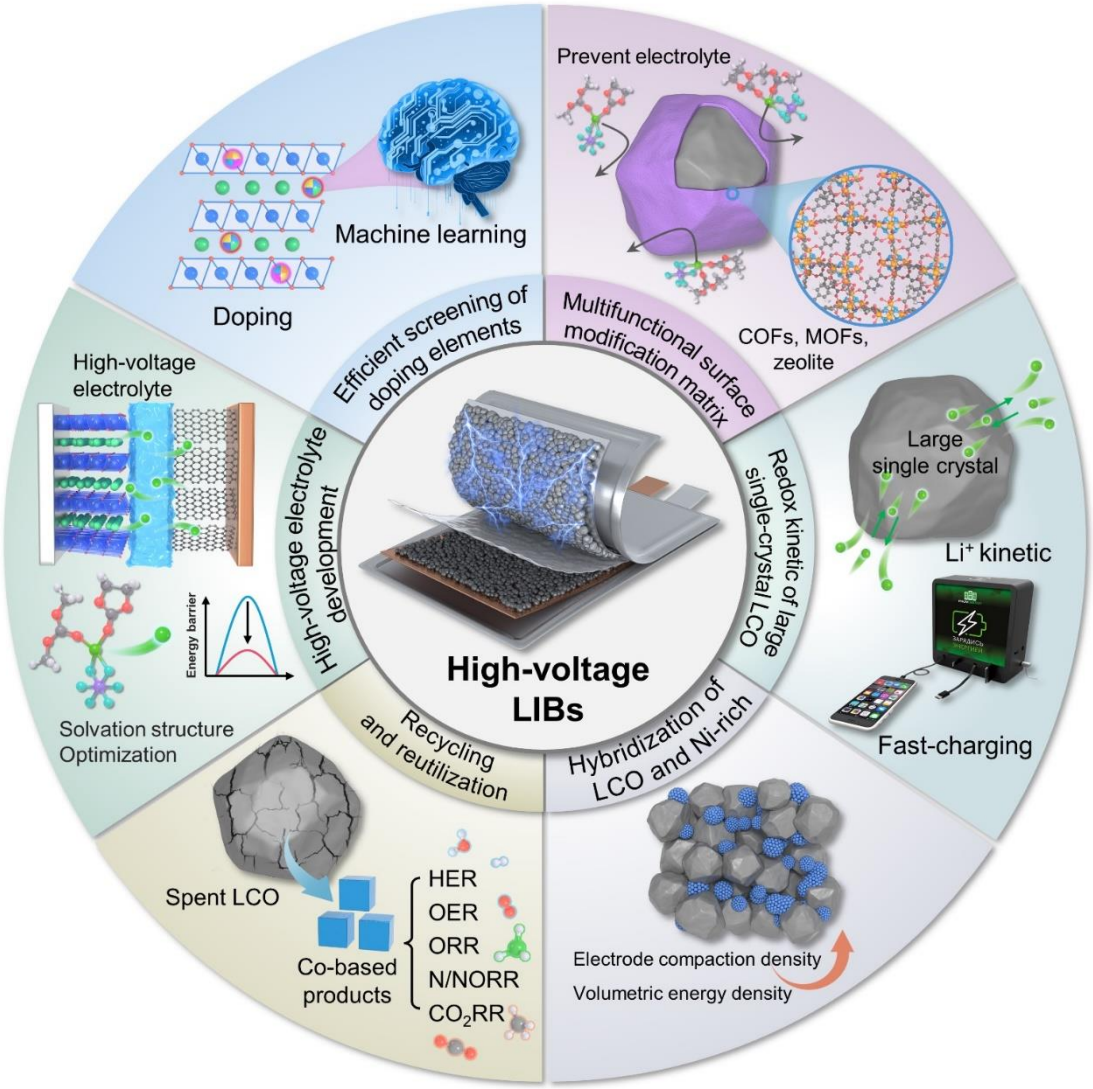

Figure 7.1 The remaining challenges of high-voltage LCO-based LIB system

(1) Efficient screening of doping elements for high-voltage LCO. Foreign-ion doping has shown great potential for enabling the stability of LCO under high-voltage. However, the type, content and combination of doping elements are still in the stage of experimental verification speculation, which is extremely time-consuming and inefficient for optimizing the doping elements. With the current blind selection of doping elements for stabilizing high-voltage LCO cathodes, there is an urgent need

for a more efficient and convenient approach. High-throughput density functional theory calculations along with machine learning could establish a database of structural properties and doping elements, and further screen the optimal doping elements by choosing the appropriate descriptor. This approach also enables efficient exploration of a vast range of combinations, prioritizing higher-order compositions and predicting material properties. Overcoming challenges such as limited diverse datasets and enhancing model interpretability will be crucial for advancing machine learning-driven research on doped LCO cathodes.

(2) Development of multifunctional surface modification matrix: The surface coatings could minimize cathode-electrolyte direct contact, stabilizing lattice oxygen, preventing TM ion dissolution, inhibiting oxidative decomposition, and thereby enabling high-voltage stability of LCO. Current coating matrixes are mainly involved oxides, phosphates, fluorides and carbonous materials, which are normally amorphous and lattice/structural mismatched with layered structure LCO. The nanocrystalline nature and emerged grain boundaries of these traditional coating matrixes probably enlarges the Li^+ transport paths, and limits Li^+ kinetics. Materials like MOFs, COFs, and zeolites with unique pore structures, excellent crystallinity and good structural compatibility offer an ideal choice as a multifunctional surface modification matrix for high-voltage cathodes. These proposed candidates as new coating matrixes on the surface of cathode will simultaneously provide physical isolation, enhance interfacial charge transfer, ensure Li^+ transport pathways, suppress TM ion dissolution, and

collect surface-unstable lattice oxygen.

(3) Necessity of high-voltage electrolyte development: Under high-voltage conditions, the interface side reactions between highly oxidized Co^{4+} and the organic electrolyte leads to electrolyte oxidation, decomposition, and degradation of the LCO surface. Besides, Co^{2+} ions dissolved into the electrolyte form the solvation sheath ($Co^{2+}(EC)_n$ or $Co^{2+}(DMC)_n$, etc.), which probably in turn accelerates the electrolyte oxidization. Considering this, there is a critical need for the development of high-voltage electrolytes to mitigate these adverse reactions and preserve electrode performance. With a thorough understanding of electrolyte consumption, future efforts should prioritize the investigation of long-lasting electrolyte formulations. This involves selecting solvents with high oxidation potential and a wide electrochemical window as alternatives to traditional commercial carbonate solvents. Promising options include sulfones, fluorinated solvents, and nitrile solvents, which have the potential to enhance high-voltage battery performance and extend its operational lifespan.

(4) Improvement of redox kinetic of large single-crystal LCO: Current studies mainly focus on enhancing the cycling durability and volumetric energy density of high-voltage LCO. The design of single crystal with a particle size exceeding 20 μm along with surface coating and element doping has shown promise for solving these issues. However, the large grain size will remarkably increase the Li^+ transport pathways, limited their reaction kinetics and high-rate capability. Nonetheless, the growing demand for fast charging rates above 2C (corresponding to charge times less than 30

minutes) in portable electronic devices necessitates improved redox kinetics in large single-crystal LCO. To tackle these challenges, there are potential strategies such as optimizing foreign-ion doping elements to enlarge the space distance of CoO_2 layer and reduce Li^+ diffusion barriers, reconstructing the cathode surface to form spinel structures with three-dimensional Li^+ transport channels, and implementing effective porous surface coating to achieve rapid Li^+ desolvation.

(5) Sustainable LCO recycling and reutilization: Co, a crucial component of LIBs, is both expensive and subject to supply chain risks due to geopolitical issues and limited abundance. Efficient recycling and reutilization of Co can address these challenges. The failure of LCO primarily involves lithium loss, structural degradation, and the accumulation of surface CEI. Re-lithiation, achieved through electrodeposition and low-temperature binary Li-containing molten salt systems, is an effective method for regenerating the spent LCO cathodes and recovering the original layered structure behavior[202-204]. Additionally, a low-temperature thermochemistry route, involving thermal reduction, can be explored for the selective recycling of Co metals from spent LCO[205]. The recycled Co-based products, i.e. spinel Co_3O_4, CoO or their derivatives, have the potential to serve as efficient electrocatalysts for applications[206, 207]. These approaches contribute to create an innovative approach within the circular economy, transforming waste into a valuable electrochemical production and conversion system.

(6) Hybridization of large-size LCO and small-size Ni-rich single crystals: Hybridizing large single crystal LCO with small Ni-rich single crystals offers a

promising strategy to improve electrode compaction density and enhance the volumetric energy density of LIBs. By filling the gaps within the large LCO crystals with small Ni-rich counterparts, this approach not only increases electrode compaction density and energy density but also reduces the cost of LIBs by utilizing lower-cost Ni resources and Ni-rich cathode materials. However, achieving an optimal balance in particle sizes and the mixing ratio of large and small crystals is crucial. This balance is necessary to simultaneously enhance compaction density and performance, but it poses a significant challenge. Future research should focus on addressing this issue to realize the full potential of this hybrid approach.

References

1. R. Istrate, V. Tulus, R. N. Grass, L. Vanbever, W. J. Stark and G. Guillen-Gosalbez, *Nat. Commun.*, 2024, **15**, 3724.
2. L. Xu, K. Feng, N. Lin, A. T. D. Perera, H. V. Poor, L. Xie, C. Ji, X. A. Sun, Q. Guo and M. O'Malley, *Nat. Rev. Electr. Eng.*, 2024, **1**, 53-66.
3. E. Aramendia, P. E. Brockway, P. G. Taylor, J. B. Norman, M. K. Heun and Z. Marshall, *Nat. Energy*, 2024, **9**, 803-819.
4. D. Larcher and J. M. Tarascon, *Nat. Chem.*, 2015, **7**, 19-29.
5. E. Fan, L. Li, Z. Wang, J. Lin, Y. Huang, Y. Yao, R. Chen and F. Wu, *Chem. Rev.*, 2020, **120**, 7020-7063.
6. D. L. Ramada, J. de Vries, J. Vollenbroek, N. Noor, O. Ter Beek, S. M. Mihaila, F. Wieringa, R. Masereeuw, K. Gerritsen and D. Stamatialis, *Nat. Rev. Nephrol.*, 2023, **19**, 481-490.
7. M. T. F. Rodrigues, G. Babu, H. Gullapalli, K. Kalaga, F. N. Sayed, K. Kato, J. Joyner and P. M. Ajayan, *Nat. Energy*, 2017, **2**, 17108.
8. J. Xie and Y. C. Lu, *Nat. Commun.*, 2020, **11**, 2499.
9. L. A. Ellingsen, C. R. Hung, G. Majeau-Bettez, B. Singh, Z. Chen, M. S. Whittingham and A. H. Stromman, *Nat. Nanotechnol.*, 2016, **11**, 1039-1051.
10. H. Li, L. Wang, Y. Song, Z. Zhang, A. Du, Y. Tang, J. Wang and X. He, *Adv. Mater.*, 2024, **36**, e2312292.
11. J. Y. Liao, Q. Hu, X. R. Sheng, Z. Z. Zhang, Y. F. Xu, X. Y. Mo and X. S. Zhou, *ACS Mater. Lett.*, 2022, **4**, 1653-1659.
12. J. B. Goodenough and Y. Kim, *Chem. Mater.*, 2010, **22**, 587-603.
13. L. Wang, B. Chen, J. Ma, G. Cui and L. Chen, *Chem. Soc. Rev.*, 2018, **47**, 6505-6602.
14. C. Y. Wang, T. Liu, X. G. Yang, S. Ge, N. V. Stanley, E. S. Rountree, Y. Leng and B. D. McCarthy, *Nature*, 2022, **611**, 485-490.
15. J. Wang, Q. Zhang, J. Sheng, Z. Liang, J. Ma, Y. Chen, G. Zhou and H. M. Cheng, *Natl. Sci. Rev.*, 2022, **9**, nwac097.
16. Y. Y. Jiang, C. D. Qin, P. F. Yan and M. L. Sui, *J. Mater. Chem. A*, 2019, **7**, 20824-20831.
17. D. Eum, S. O. Park, H. Y. Jang, Y. Jeon, J. H. Song, S. Han, K. Kim and K. Kang, *Nat. Mater.*, 2024, **23**, 1093-1099.
18. G. G. Amatucci, J. M. Tarascon and L. C. Klein, *J. Electrochem. Soc.*, 2019,

143, 1114-1123.

19. C. Lin, J. Li, Z. W. Yin, W. Huang, Q. Zhao, Q. Weng, Q. Liu, J. Sun, G. Chen and F. Pan, *Adv. Mater.*, 2024, **36**, e2307404.
20. Q. Wang, Z. Yao, J. Wang, H. Guo, C. Li, D. Zhou, X. Bai, H. Li, B. Li, M. Wagemaker and C. Zhao, *Nature*, 2024, **629**, 341-347.
21. S. Li, Y. Sun, A. Gao, Q. Zhang, X. Lu and X. Lu, *Proc. Natl. Acad. Sci.*, 2022, **119**, e2120060119.
22. J. X. Wang, K. Jia, J. Ma, Z. Liang, Z. F. Zhuang, Y. Zhao, B. H. Li, G. M. Zhou and H. M. Cheng, *Nat. Sustain.*, 2023, **6**, 797-805.
23. H. W. Ji, J. P. Wu, Z. J. Cai, J. Liu, D. H. Kwon, H. Kim, A. Urban, J. K. Papp, E. Foley, Y. S. Tian, M. Balasubramanian, H. Kim, R. J. Clément, B. D. McCloskey, W. L. Yang and G. Ceder, *Nat. Energy*, 2020, **5**, 213-221.
24. H. M. Wang, S. S. Chen, C. L. Fu, Y. Ding, G. R. Liu, Y. L. Cao and Z. X. Chen, *ACS Mater. Lett.*, 2021, **3**, 956-977.
25. W. D. Li, E. M. Erickson and A. Manthiram, *Nat. Energy*, 2020, **5**, 26-34.
26. A. K. Padhi, K. S. Nanjundaswamy and J. B. Goodenough, *J. Electrochem. Soc.*, 1997, **144**, 1188-1194.
27. M. M. Thackeray, P. J. Johnson, L. A. Depicciotto, P. G. Bruce and J. B. Goodenough, *Mater. Res. Bull.*, 1984, **19**, 179-187.
28. R. Qian, Y. Liu, T. Cheng, P. Li, R. Chen, Y. Lyu and B. Guo, *ACS Appl. Mater. Interfaces*, 2020, **12**, 13813-13823.
29. R. H. Wang, X. Y. Dai, Z. F. Qian, Y. L. Sun, S. T. Fan, K. Y. Xiong, H. Zhang and F. X. Wu, *ACS Mater. Lett.*, 2020, **2**, 280-290.
30. I. Martens, N. Vostrov, M. Mirolo, M. Colalongo, P. Kús, M. I. Richard, L. Z. Wang, X. B. Zhu, T. U. Schülli and J. Drnec, *ACS Mater. Lett.*, 2022, **4**, 2528-2536.
31. M. Bianchini, M. Roca-Ayats, P. Hartmann, T. Brezesinski and J. Janek, *Angew. Chem., Int. Ed.*, 2019, **58**, 10434-10458.
32. J. M. Zheng, S. J. Myeong, W. R. Cho, P. F. Yan, J. Xiao, C. M. Wang, J. Cho and J. G. Zhang, *Adv. Energy Mater.*, 2017, **7**, 1601284.
33. J. H. Yang, H. Kim and G. Ceder, *Molecules*, 2021, **26**, 3173.
34. W. E. Gent, G. M. Busse and K. Z. House, *Nat. Energy*, 2022, **7**, 1132-1143.
35. Q. Chang, Y. X. A. Ng, D. H. Yang, J. H. Chen, T. Liang, S. Chen, X. Y. Zhang, Z. H. Ou, J. Kim, E. H. Ang, H. F. Xiang and X. H. Song, *ACS Mater. Lett.*, 2023, **5**, 1506-1526.

36. Y. Bi, J. Tao, Y. Wu, L. Li, Y. Xu, E. Hu, B. Wu, J. Hu, C. Wang, J. G. Zhang, Y. Qi and J. Xiao, *Science*, 2020, **370**, 1313-1317.

37. M. Sathiya, J. B. Leriche, E. Salager, D. Gourier, J. M. Tarascon and H. Vezin, *Nat. Commun.*, 2015, **6**, 6276.

38. Y. R. Zhang, Y. Katayama, R. Tatara, L. Giordano, Y. Yu, D. Fraggedakis, J. G. W. Sun, F. Maglia, R. Jung, M. Z. Bazant and Y. Shao-Horn, *Energy Environ. Sci.*, 2020, **13**, 183-199.

39. J. Molenda, A. Stoklosa and T. Bak, *Solid State Ionics*, 1989, **36**, 53-58.

40. L. Sun, Z. Zhang, X. Hu, H. Tian, Y. Zhang and X. Yang, *J. Electrochem. Soc.*, 2019, **166**, A1793-A1798.

41. Z. H. Chen and J. R. Dahn, *Electrochim. Acta*, 2004, **49**, 1079-1090.

42. J. Li, C. Lin, M. Weng, Y. Qiu, P. Chen, K. Yang, W. Huang, Y. Hong, J. Li, M. Zhang, C. Dong, W. Zhao, Z. Xu, X. Wang, K. Xu, J. Sun and F. Pan, *Nat. Nanotechnol.*, 2021, **16**, 599-605.

43. H. Xia, L. Lu, Y. S. Meng and G. Ceder, *J. Electrochem. Soc.*, 2007, **154**, A337-A342.

44. Z. Zhou, C. Cazorla, B. Gao, H. D. Luong, T. Momma and Y. Tateyama, *ACS Appl. Mater. Interfaces*, 2023, **15**, 53614-53622.

45. S. Li, K. Li, J. Zheng, Q. Zhang, B. Wei and X. Lu, *J.Phys. Chem. Lett.*, 2019, **10**, 7537-7546.

46. W. Huang, T. Liu, L. Yu, J. Wang, T. Zhou, J. Liu, T. Li, R. Amine, X. Xiao, M. Ge, L. Ma, S. N. Ehrlich, M. V. Holt, J. Wen and K. Amine, *Science*, 2024, **384**, 912-919.

47. G. G. Amatucci, J. M. Tarascon and L. C. Klein, *Solid State Ionics*, 1996, **83**, 167-173.

48. P. Byeon, H. Bin Bae, H. S. Chung, S. G. Lee, J. G. Kim, H. J. Lee, J. W. Choi and S. Y. Chung, *Adv. Funct. Mater.*, 2018, **28**, 1804564.

49. J. Chen, H. Chen, S. Zhang, A. Dai, T. Li, Y. Mei, L. Ni, X. Gao, W. Deng, L. Yu, G. Zou, H. Hou, M. Dahbi, W. Xu, J. Wen, J. Alami, T. Liu, K. Amine and X. Ji, *Adv. Mater.*, 2022, **34**, e2204845.

50. M. Z. Cai, Y. H. Dong, M. Xie, W. J. Dong, C. L. Dong, P. Dai, H. Zhang, X. Wang, X. Z. Sun, S. N. Zhang, M. Yoon, H. W. Xu, Y. S. Ge, J. Li and F. Q. Huang, *Nat. Energy*, 2023, **8**, 159-168.

51. E. Y. Hu, Q. H. Li, X. L. Wang, F. Q. Meng, J. Liu, J. N. Zhang, K. Page, W. Q. Xu, L. Gu, R. J. Xiao, H. Li, X. J. Huang, L. Q. Chen, W. L. Yang, X. Q. Yu and X. Q. Yang, *Joule*, 2021, **5**, 720-736.

52. S. Sharifi-Asl, J. Lu, K. Amine and R. Shahbazian-Yassar, *Adv. Energy Mater.*, 2019, **9**, 1900551.

53. X. B. Jia, J. Wang, Y. F. Liu, Y. F. Zhu, J. Y. Li, Y. J. Li, S. L. Chou and Y. Xiao, *Adv. Mater.*, 2024, **36**, e2307938.

54. Y. H. Zhou, H. F. Cui, B. Qiu, Y. H. Xia, C. Yin, L. Y. Wan, Z. P. Shi and Z. P. Liu, *ACS Mater. Lett.*, 2021, **3**, 433-441.

55. W. M. Seong, K. Yoon, M. H. Lee, S. K. Jung and K. Kang, *Nano Lett.*, 2019, **19**, 29-37.

56. Z. Wu, G. Zeng, J. Yin, C.-L. Chiang, Q. Zhang, B. Zhang, J. Chen, Y. Yan, Y. Tang, H. Zhang, S. Zhou, Q. Wang, X. Kuai, Y.-G. Lin, L. Gu, Y. Qiao and S.-G. Sun, *ACS Energy Lett.*, 2023, **8**, 4806-4817.

57. W.-S. Yoon, K.-B. Kim, M.-G. Kim, M.-K. Lee, H.-J. Shin, J.-M. Lee, J.-S. Lee and C.-H. Yo, *J. Phys. Chem. B.*, 2002, **106**, 2526-2532.

58. X. Ren, X. Zhang, Z. Shadike, L. Zou, H. Jia, X. Cao, M. H. Engelhard, B. E. Matthews, C. Wang, B. W. Arey, X. Q. Yang, J. Liu, J. G. Zhang and W. Xu, *Adv. Mater.*, 2020, **32**, e2004898.

59. B. Hu, F. S. Geng, M. Shen, C. Zhao, Q. Qiu, Y. Lin, C. X. Chen, W. Wen, S. Zheng, X. S. Hu, C. Li and B. W. Hu, *J. Power Sources*, 2021, **516**, 230661.

60. J. Oh, S. Y. Lee, H. Kim, J. Ryu, B. Gil, J. Lee and M. Kim, *Adv. Sci.*, 2022, **9**, e2203639.

61. Y. Q. Liao, H. Y. Zhang, Y. F. Peng, Y. G. Hu, J. D. Liang, Z. L. Gong, Y. M. Wei and Y. Yang, *Adv. Energy Mater.*, 2024, **14**, 2304295.

62. Z. Y. Sun, F. K. Li, J. Y. Ding, Z. Y. Lin, M. Q. Xu, M. Zhu and J. Liu, *ACS Energy Lett.*, 2023, **8**, 2478-2487.

63. Z. Dai, Z. Li, R. Chen, F. Wu and L. Li, *Nat. Commun.*, 2023, **14**, 8087.

64. B. L. D. Rinkel, D. S. Hall, I. Temprano and C. P. Grey, *J. Am. Chem. Soc.*, 2020, **142**, 15058-15074.

65. H. Zeng, J. Chen, C. Wang, J. Qi, Z. Liu, M. Li, L. Gu, J. Wang, E. Hong, Y. Zhang, J. Xu and C. Yang, *ACS Mater. Lett.*, 2024, **6**, 2295-2303.

66. H. Adenusi, G. A. Chass, S. Passerini, K. V. Tian and G. H. Chen, *Adv. Energy Mater.*, 2023, **13**, 2203307.

67. S. K. Heiskanen, J. Kim and B. L. Lucht, *Joule*, 2019, **3**, 2322-2333.

68. B. W. Xiao and X. L. Sun, *Adv. Energy Mater.*, 2018, **8**, 1802057.

69. Y. Zhou, M. Su, X. Yu, Y. Zhang, J. G. Wang, X. Ren, R. Cao, W. Xu, D. R. Baer, Y. Du, O. Borodin, Y. Wang, X. L. Wang, K. Xu, Z. Xu, C. Wang and Z. Zhu, *Nat. Nanotechnol.*, 2020, **15**, 224-230.

70. Q. J. Sun, Z. Cao, Z. Ma, J. L. Zhang, W. Wahyudi, T. Cai, H. R. Cheng, Q. Li, H. Kim, E. R. Xie, L. Cavallo, Y. K. Sun and J. Ming, *ACS Mater. Lett.*, 2022, **4**, 2233-2243.

71. P. Peljo and H. H. Girault, *Energy Environ. Sci.*, 2018, **11**, 2306-2309.

72. L. Wang, J. Ma, C. Wang, X. Yu, R. Liu, F. Jiang, X. Sun, A. Du, X. Zhou and G. Cui, *Adv. Sci.*, 2019, **6**, 1900355.

73. F. C. Zhang, N. Qin, Y. Z. Li, H. Guo, Q. M. Gan, C. Zeng, Z. Q. Li, Z. Y. Wang, R. Wang, G. Y. Liu, S. Gu, H. Huang, Z. L. Yang, J. Wang, Y. H. Deng and Z. G. Lu, *Energy Environ. Sci.*, 2023, **16**, 4345-4355.

74. J.-N. Zhang, Q. Li, C. Ouyang, X. Yu, M. Ge, X. Huang, E. Hu, C. Ma, S. Li, R. Xiao, W. Yang, Y. Chu, Y. Liu, H. Yu, X.-Q. Yang, X. Huang, L. Chen and H. Li, *Nat. Energy*, 2019, **4**, 594-603.

75. J. Xia, N. Zhang, Y. Yang, X. Chen, X. Wang, F. Pan and J. Yao, *Adv. Funct. Mater.*, 2022, **33**, 2212869.

76. Y. Huang, Y. Zhu, H. Fu, M. Ou, C. Hu, S. Yu, Z. Hu, C. T. Chen, G. Jiang, H. Gu, H. Lin, W. Luo and Y. Huang, *Angew. Chem., Int. Ed.*, 2021, **60**, 4682-4688.

77. C. Delmas and S. I, *Solid State Ionics*, 1992, **53**, 370-375.

78. R. Alcántara, P. Lavela, P. L. Relaño, J. L. Tirado, E. Zhecheva and R. Stoyanova, *Inorg. Chem.*, 1998, **37**, 264-269.

79. C. Delmas, I. Saadoune and A. Rougier, *J. Power Sources*, 1993, **44**, 595-602.

80. W. Cho, S. Myeong, N. Kim, S. Lee, Y. Kim, M. Kim, S. J. Kang, N. Park, P. Oh and J. Cho, *Adv. Mater.*, 2017, **29**, 1605578.

81. Q. Liu, X. Su, D. Lei, Y. Qin, J. G. Wen, F. M. Guo, Y. M. A. Wu, Y. C. Rong, R. H. Kou, X. H. Xiao, F. Aguesse, J. Bareño, Y. Ren, W. Q. Lu and Y. X. Li, *Nat. Energy*, 2018, **3**, 936-943.

82. Z. Zhu, H. Wang, Y. Li, R. Gao, X. Xiao, Q. Yu, C. Wang, I. Waluyo, J. Ding, A. Hunt and J. Li, *Adv. Mater.*, 2020, **32**, e2005182.

83. W. Huang, Q. Zhao, M. Zhang, S. Xu, H. Xue, C. Zhu, J. Fang, W. Zhao, G. Ren, R. Qin, Q. Zhao, H. Chen and F. Pan, *Adv. Energy Mater.*, 2022, **12**, 2200813.

84. Z. Bi, Z. Yi, L. Zhang, G. Wang, A. Zhang, S. Liao, Q. Zhao, Z. Peng, L. Song, Y. Wang, Z. Zhao, S. Wei, W. Zhao, X. Shi, M. Li, N. Ta, J. Mi, S. Li, P. Das, Y. Cui, C. Chen, F. Pan and Z.-S. Wu, *Energy Environ. Sci.*, 2024, **17**, 2765-2775.

85. Z. Lin, K. Fan, T. Liu, Z. Xu, G. Chen, H. Zhang, H. Li, X. Guo, X. Zhang, Y. Zhu, P. Hou and H. Huang, *Nano-Micro Lett.*, 2023, **16**, 48.

86. J. Feng, C. Wang, H. Lei, S. Liu, J. Liu, Y. Han, J. Zhang and W. Li, *J. Energy Chem.*, 2023, **85**, 324-334.

87. Y. Liu, Z. Yang, J. Zhong, J. Li, R. Li, Y. Yu and F. Kang, *ACS Nano*, 2019, **13**, 11891-11900.

88. Q. Xie, W. D. Li and A. Manthiram, *Chem. Mater.*, 2019, **31**, 938-946.

89. W. Zhang, Z. X. Chi, W. X. Mao, R. W. Lv, A. M. Cao and L. J. Wan, *Angew. Chem., Int. Ed.*, 2014, **53**, 12776-12780.

90. J. Qian, L. Liu, J. Yang, S. Li, X. Wang, H. L. Zhuang and Y. Lu, *Nat. Commun.*, 2018, **9**, 4918.

91. Y. Wang, Q. Zhang, Z. C. Xue, L. Yang, J. Wang, F. Meng, Q. Li, H. Pan, J. N. Zhang, Z. Jiang, W. Yang, X. Yu, L. Gu and H. Li, *Adv. Energy Mater.*, 2020, **10**, 2001413.

92. Y. Yan, S. Zhou, Y. Zheng, H. Zhang, J. Chen, G. Zeng, B. Zhang, Y. Tang, Q. Zheng, C. Wang, C. W. Wang, H. G. Liao, I. Manke, X. Kuai, K. Dong, Y. Sun, Y. Qiao and S. G. Sun, *Adv. Funct. Mater.*, 2023, **34**, 2310799.

93. Y. Yan, Q. Fang, X. Kuai, S. Zhou, J. Chen, H. Zhang, X. Wu, G. Zeng, Z. Wu, B. Zhang, Y. Tang, Q. Zheng, H. G. Liao, K. Dong, I. Manke, X. Wang, Y. Qiao and S. G. Sun, *Adv. Mater.*, 2024, **36**, e2308656.

94. J. Yao, Y. Li, T. Xiong, Y. Fan, L. Zhao, X. Cheng, Y. Tian, L. Li, Y. Li, W. Zhang, P. Yu, P. Guo, Z. Yang, J. Peng, L. Xue, J. Wang, Z. Li, M. Xie, H. Liu and S. Dou, *Angew. Chem., Int. Ed.*, 2024, **63**, e202407898.

95. T. Cheng, Z. T. Ma, R. C. Qian, Y. T. Wang, Q. Cheng, Y. C. Lyu, A. M. Nie and B. K. Guo, *Adv. Funct. Mater.*, 2021, **31**, 2001974.

96. C. W. Wang, Y. Zhou, J. H. You, J. D. Chen, Z. Zhang, S. J. Zhang, C. G. Shi, W. D. Zhang, M. H. Zou, Y. Yu, J. T. Li, L. Y. Zeng, L. Huang and S. G. Sun, *ACS Appl. Energy Mater.*, 2020, **3**, 2593-2603.

97. F. Wu, X. Zhang, T. Zhao, L. Li, M. Xie and R. Chen, *ACS Appl. Mater. Interfaces*, 2015, **7**, 3773-3781.

98. J. Song, Y. Wang, Z. Feng, X. Zhang, K. Wang, H. Gu and J. Xie, *ACS Appl. Mater. Interfaces*, 2018, **10**, 27326-27332.

99. G. Nava, J. Schwan, M. G. Boebinger, M. T. McDowell and L. Mangolini, *Nano Lett.*, 2019, **19**, 7236-7245.

100. Y. Zhang, Y. Pei, W. Liu, S. Zhang, J. J. Xie, J. Xia, S. Nie, L. Liu and X. Y. Wang, *Chem. Eng. J.*, 2020, **382**, 122697.

101. A. Yano, K. Hikima, J. Hata, K. Suzuki, M. Hirayama and R. Kanno, *J. Electrochem. Soc.*, 2018, **165**, A3221-A3229.

102. W. Ding, H. Ren, Z. Li, M. Shang, Y. Song, W. Zhao, L. Chang, T. Pang, S. Xu, H. Yi, L. Zhou, H. Lin, Q. Zhao and F. Pan, *Adv. Energy Mater.*, 2024, **14**, 2303926.

103. J.-H. Shim, K.-S. Lee, A. Missyul, J. Lee, B. Linn, E. C. Lee and S. Lee, *Chem. Mater.*, 2015, **27**, 3273-3279.

104. R. Gu, Z. Ma, T. Cheng, Y. Lyu, A. Nie and B. Guo, *ACS Appl. Mater. Interfaces*, 2018, **10**, 31271-31279.

105. W. Zheng, G. Liang, H. Guo, J. Li, J. Zou, J. A. Yuwono, H. Shu, S. Zhang, V. K. Peterson, B. Johannessen, L. Thomsen, W. Hu and Z. Guo, *Energy Environ. Sci.*, 2024, **17**, 4147-4156.

106. H. Liao, M. Cai, W. Ma, Y. Cao, S. Zhao, Y. Dong and F. Huang, *Adv. Mater.*, 2024, **36**, e2402739.

107. W. J. Dong, B. Ye, M. Z. Cai, Y. Z. Bai, M. Xie, X. Z. Sun, Z. R. Lv and F. Q. Huang, *ACS Energy Lett.*, 2023, **8**, 881-888.

108. C. Sun, B. Zhao, J. Mao, K. H. Dai, Z. y. Wang, L. b. Tang, H. z. Chen, X. h. Zhang and J. c. Zheng, *Adv. Funct. Mater.*, 2023, **33**, 2300589.

109. T. Tian, T. W. Zhang, Y. C. Yin, Y. H. Tan, Y. H. Song, L. L. Lu and H. B. Yao, *Nano Lett.*, 2020, **20**, 677-685.

110. Z. Bai, Z. Ying, F. Zhang, W. Wang, Z. Huang, T. Yang, W. Li, W. Dong, J. Yan, C. Lin, L. Hu, T. Liu, Z. Lin, T. Li, C. Sun, L. Li, Y. Wang, Q. Kong, S. Gu, H. Shen, S. Hao, X. Chen, L. Y. Frank Lam, X. Hu, H. Huang, X.-L. Wang, F. Xie, G. Chen, Q. Liu and Y. Ren, *ACS Energy Lett.*, 2024, **9**, 2717-2726.

111. K. Kim, D. Hwang, S. Kim, S. O. Park, H. Cha, Y. S. Lee, J. Cho, S. K. Kwak and N. S. Choi, *Adv. Energy Mater.*, 2020, **10**, 2000012.

112. A. Fu, C. J. Xu, J. D. Lin, Y. Su, H. T. Zhang, D. Y. Wu, X. Z. Zhang, M. Xia, Z. R. Zhang, J. M. Zheng and Y. Yang, *J. Mater. Chem. A*, 2023, **11**, 3703-3716.

113. Z. Zhang, F. Y. Liu, Z. Y. Huang, J. H. Gu, Y. Song, J. Q. Zheng, M. Y. Yi, Q. Y. Mao, M. H. Bai, X. M. Fan, B. Hong, Z. A. Zhang and Y. Q. Lai, *ACS Appl. Energy Mater.*, 2021, **4**, 12954-12964.

114. H. Huang, Z. Q. Li, S. Gu, J. C. Bian, Y. Z. Li, J. J. Chen, K. M. Liao, Q. M. Gan, Y. F. Wang, S. S. Wu, Z. Y. Wang, W. Luo, R. Hao, Z. Q. Wang, G. Y. Wang and Z. G. Lu, *Adv. Energy Mater.*, 2021, **11**, 2101864.

115. J. Zhang, P. F. Wang, P. Bai, H. Wan, S. Liu, S. Hou, X. Pu, J. Xia, W. Zhang, Z. Wang, B. Nan, X. Zhang, J. Xu and C. Wang, *Adv. Mater.*, 2022, **34**, e2108353.

116. W. J. Xue, R. Gao, Z. Shi, X. H. Xiao, W. X. Zhang, Y. R. Zhang, Y. G. Zhu, I.

Waluyo, Y. Li, M. R. Hill, Z. Zhu, S. Li, O. Kuznetsov, Y. M. Zhang, W. K. Lee, A. Hunt, A. Harutyunyan, Y. Shao-Horn, J. A. Johnson and J. Li, *Energy Environ. Sci.*, 2021, **14**, 6030-6040.

117. D. Wu, C. Zhu, H. Wang, J. Huang, G. Jiang, Y. Yang, G. Yang, D. Tang and J. Ma, *Angew. Chem., Int. Ed.*, 2024, **63**, e202315608.

118. S. Xu, B. Peng, X. Pang and F. Huang, *ACS Mater. Lett.*, 2022, **4**, 2195-2209.

119. G. Kresse and J. Furthmüller, *Phys. Rev. B*, 1996, **54**, 11169.

120. G. Kresse and D. Joubert, *Phys. Rev. B*, 1999, **59**, 1758.

121. J. P. Perdew, K. Burke and M. Ernzerhof, *Phys. Rev. Lett.*, 1996, **77**, 3865.

122. S. Grimme, J. Antony, S. Ehrlich and H. Krieg, *J. Chem. Phys.*, 2010, **132**, 154104.

123. A. Jain, S. P. Ong, G. Hautier, W. Chen, W. D. Richards, S. Dacek, S. Cholia, D. Gunter, D. Skinner, G. Ceder and K. A. Persson, *APL Mater.*, 2013, **1**, 011002.

124. G. Henkelman, B. P. Uberuaga and H. Jónsson, *J. Chem. Phys.*, 2000, **113**, 9901-9904.

125. K. Zhao, Y. Wang, L. Han, Y. Wang, X. Luo, Z. Zhang and Y. Yang, *Nano-Micro Lett.*, 2019, **11**, 19.

126. J. Xu, *Nano-Micro Lett.*, 2022, **14**, 166.

127. Y. Liu, T. Zeng, G. Li, T. Wan, M. Li, X. Zhang, M. Li, M. Su, A. Dou, W. Zeng, Y. Zhou, R. Guo and D. Chu, *Energy Storage Mater.*, 2022, **52**, 534-546.

128. H. Zhu, Y. Tang, K. M. Wiaderek, O. J. Borkiewicz, Y. Ren, J. Zhang, J. Ren, L. Fan, C. C. Li, D. Li, X.-L. Wang and Q. Liu, *Nano Lett.*, 2021, **21**, 9997-10005.

129. Z. Zhong, L. Chen, S. Huang, W. Shang, L. Kong, M. Sun, L. Chen and W. Ren, *J. Mater. Sci.*, 2020, **55**, 2913-2922.

130. G. G. Amatucci, J. M. Tarascon and L. C. Klein, *J. Electrochem. Soc.*, 1996, **143**, 1114-1123.

131. Y. Lyu, X. Wu, K. Wang, Z. Feng, T. Cheng, Y. Liu, M. Wang, R. Chen, L. Xu, J. Zhou, Y. Lu and B. Guo, *Adv. Energy Mater.*, 2021, **11**, 2000982.

132. D. Takamatsu, Y. Koyama, Y. Orikasa, S. Mori, T. Nakatsutsumi, T. Hirano, H. Tanida, H. Arai, Y. Uchimoto and Z. Ogumi, *Angew. Chem., Int. Ed.*, 2012, **51**, 11597-11601.

133. W. Kong, J. Zhang, D. Wong, W. Yang, J. Yang, C. Schulz and X. Liu, *Angew. Chem. Int. Ed.*, 2021, **133**, 27308-27318.

134. J. Ahn, J. Kang, M. K. Cho, H. Park, W. Ko, Y. Lee, H. S. Kim, Y. H. Jung, T. Y. Jeon, H. Kim, W. H. Ryu, J. Hong and J. Kim, *Adv. Energy Mater.*, 2021, **11**, 2102311.

135. M. Wang, X. Feng, H. Xiang, Y. Feng, C. Qin, P. Yan and Y. Yu, *Small Methods*, 2019, **3**, 1900355.

136. Y. Huang, Y. Zhu, H. Fu, M. Ou, C. Hu, S. Yu, Z. Hu, C. T. Chen, G. Jiang, H. Gu, H. Lin, W. Luo and Y. Huang, *Angew. Chem., Int. Ed.*, 2021, **60**, 4682-4688.

137. A. Liu, J. Li, R. Shunmugasundaram and J. R. Dahn, *J. Electrochem. Soc.*, 2017, **164**, A1655-A1664.

138. J. N. Zhang, Q. Li, C. Ouyang, X. Yu, M. Ge, X. Huang, E. Hu, C. Ma, S. Li, R. Xiao, W. Yang, Y. Chu, Y. Liu, H. Yu, X. Q. Yang, X. Huang, L. Chen and H. Li, *Nat. Energy*, 2019, **4**, 594-603.

139. Y. Hong, X. Huang, C. Wei, J. Wang, J. Zhang, H. Yan, Y. S. Chu, P. Pianetta, R. Xiao, X. Yu, Y. Liu and H. Li, *Chem*, 2020, **6**, 2759-2769.

140. M. Hirooka, T. Sekiya, Y. Omomo, M. Yamada, H. Katayama, T. Okumura, Y. Yamada and K. Ariyoshi, *J. Power Sources*, 2020, **463**, 228127.

141. H. Ronduda, M. Zybert, A. Szczęsna, T. Trzeciak, A. Ostrowski, P. Wieciński, W. Wieczorek, W. Raróg-Pilecka and M. Marcinek, *Solid State Ionics*, 2020, **355**, 115426.

142. J. Xiang, Y. Wei, Y. Zhong, Y. Yang, H. Cheng, L. Yuan, H. Xu and Y. Huang, *Adv. Mater.*, 2022, **34**, 2200912.

143. J. Langdon and A. Manthiram, *Energy Storage Mater.*, 2021, **37**, 143-160.

144. C. Yang, X. Liao, X. Zhou, C. Sun, R. Qu, J. Han, Y. Zhao, L. Wang, Y. You and J. Lu, *Adv. Mater.*, 2023, **35**, e2210966.

145. S. Kim, S. Choi, K. Lee, G. J. Yang, S. S. Lee and Y. Kim, *Phys. Chem. Chem. Phys.*, 2017, **19**, 4104-4113.

146. S. Song, Y. Li, K. Yang, Z. Chen, J. Liu, R. Qi, Z. Li, C. Zuo, W. Zhao, N. Yang, M. Zhang and F. Pan, *J. Mater. Chem. A*, 2021, **9**, 5702-5710.

147. Y. Wang, Q. Zhang, Z. C. Xue, L. Yang, J. Wang, F. Meng, Q. Li, H. Pan, J. N. Zhang, Z. Jiang, W. Yang, X. Yu, L. Gu and H. Li, *Adv. Energy Mater.*, 2020, **10**.

148. Z. Li, A. Li, H. Zhang, F. Ning, W. Li, A. Zangiabadi, Q. Cheng, J. J. Borovilas, Y. Chen, H. Zhang, X. Xiao, C. Ouyang, X. Huang, W.-K. Lee, M. Ge, Y. S. Chu, X. Chuan and Y. Yang, *Energy Storage Mater.*, 2020, **29**, 71-77.

149. J. H. Shim, J. M. Han, J. H. Lee and S. Lee, *ACS Appl. Mater. Interfaces*, 2016, **8**, 12205-12210.

150. Z. Zhu, H. Wang, Y. Li, R. Gao, X. Xiao, Q. Yu, C. Wang, I. Waluyo, J. Ding, A. Hunt and J. Li, *Adv. Mater.*, 2020, **32**, 2005182.

151. Z. Feng, R. Rajagopalan, D. Sun, Y. Tang and H. Wang, *Chem. Eng. J.*, 2020, **382**, 122959.

152. X. R. Yang, C. W. Wang, P. F. Yan, T. P. Jiao, J. L. Hao, Y. Y. Jiang, F. C. Ren, W. G. Zhang, J. M. Zheng, Y. Cheng, X. S. Wang, W. Yang, J. P. Zhu, S. Y. Pan, M. Lin, L. Y. Zeng, Z. L. Gong, J. T. Li and Y. Yang, *Adv. Energy Mater.*, 2022, **12**, 2200197.

153. W. Zheng, Q. Liu, Z. Wang, Z. Wu, S. Gu, L. Cao, K. Zhang, J. Fransaer and Z. Lu, *Energy Storage Mater.*, 2020, **28**, 300-306.

154. Y. Lai, H. Xie, P. Li, B. Li, A. Zhao, L. Luo, Z. Jiang, Y. Fang, S. Chen, X. Ai, D. Xia and Y. Cao, *Adv. Mater.*, 2022, **34**, 2206039.

155. H. Wang, Z. Cui, S.-A. He, J. Zhu, W. Luo, Q. Liu and R. Zou, *Nano-Micro Lett.*, 2022, **14**, 189.

156. Q. Ding, W. Zheng, A. Zhao, Y. Zhao, K. Chen, X. Zhou, H. Zhang, Q. Li, X. Ai, H. Yang, Y. Fang and Y. Cao, *Adv. Energy Mater.*, 2023, **13**, 2203802.

157. H.-G. Jung, J. Hassoun, J.-B. Park, Y.-K. Sun and B. Scrosati, *Nat. Chem.*, 2012, **4**, 579-585.

158. F. Li, K. Fan, Y. Tian, P. Hou, H. Zhang, Y. Sun, J. Huang, X. Xu and H. Huang, *J. Mater. Chem. A*, 2022, **10**, 16420-16429.

159. Y. C. Lu, A. N. Mansour, N. Yabuuchi and Y. Shao-Horn, *Chem. Mater.*, 2009, **21**, 4408-4424.

160. Y. Bi, J. Tao, Y. Wu, L. Li, Y. Xu, E. Hu, B. Wu, J. Hu, C. Wang, J.-G. Zhang, Y. Qi and J. Xiao, *Science*, 2020, **370**, 1313-1317.

161. C.-Y. Wang, T. Liu, X.-G. Yang, S. Ge, N. V. Stanley, E. S. Rountree, Y. Leng and B. D. McCarthy, *Nature*, 2022, **611**, 485-490.

162. P. Xiao, Y. Zhao, Z. Piao, B. Li, G. Zhou and H.-M. Cheng, *Energy Environ. Sci.*, 2022, **15**, 2435-2444.

163. T. Zhu, G. Liu, D. Chen, J. Chen, P. Qi, J. Sun, X. Gu and S. Zhang, *Energy Storage Mater.*, 2022, **50**, 495-504.

164. U. Nisar, N. Muralidharan, R. Essehli, R. Amin and I. Belharouak, *Energy Storage Mater.*, 2021, **38**, 309-328.

165. S. Kalluri, M. Yoon, M. Jo, S. Park, S. Myeong, J. Kim, S. X. Dou, Z. Guo and J. Cho, *Adv. Energy Mater.*, 2017, **7**, 1601507.

166. Q. Hu, Y. F. He, D. S. Ren, Y. Z. Song, Y. Z. Wu, H. M. Liang, J. H. Gao, G. Xu, J. Y. Cai, T. Y. Li, H. Xu, L. Wang, Z. H. Chen and X. M. He, *Nano*

Energy, 2022, **96**, 107123.

167. Y. Chen, Q. He, Y. Zhao, W. Zhou, P. Xiao, P. Gao, N. Tavajohi, J. Tu, B. Li, X. He, L. Xing, X. Fan and J. Liu, *Nat. Commun.*, 2023, **14**, 8326.

168. Z. Chang, H. Yang, Y. Qiao, X. Zhu, P. He and H. Zhou, *Adv. Mater.*, 2022, **34**, 2201339.

169. X. Zhou, Y. Huang, B. Wen, Z. Yang, Z. Hao, L. Li, S.-L. Chou and F. Li, *Proc. Natl. Acad. Sci.*, 2024, **121**, e2316914121.

170. Z. Sun, J. Zhao, M. Zhu and J. Liu, *Adv. Energy Mater.*, 2023, **14**, 2303498.

171. X. Wang, Q. Wu, S. Y. Li, Z. M. Tong, D. Wang, H. L. L. Zhuang, X. Y. Wang and Y. Y. Lu, *Energy Storage Mater.*, 2021, **37**, 67-76.

172. F. L. Yang, W. Zhang, Z. X. Chi, F. Q. Cheng, J. T. Chen, A. M. Cao and L. J. Wan, *Chem. Commun.*, 2015, **51**, 2943-2945.

173. B. Kim, J. G. Lee, M. Choi, J. Cho and B. Park, *J. Power Sources*, 2004, **126**, 190-192.

174. M. Moliner, F. Rey and A. Corma, *Angew. Chem., Int. Ed.*, 2013, **52**, 13880-13889.

175. Z. Li and Y.-W. Yang, *Adv. Mater.*, 2022, **34**, 2107401.

176. B. You, Z. Wang, F. Shen, Y. Chang, W. Peng, X. Li, H. Guo, Q. Hu, C. Deng, S. Yang, G. Yan and J. Wang, *Small Methods*, 2021, **5**, 2100234.

177. S. Ding, L. Chen, J. Liao, Q. Huo, Q. Wang, G. Tian and W. Yin, *Small*, 2023, **19**, 2300341.

178. G. Dantelle, S. Beauquis, R. Le Dantec, V. Monnier, C. Galez and Y. Mugnier, *Small*, 2022, **18**, 2200992.

179. S. Mao, Z. Shen, W. Zhang, Q. Wu, Z. Wang and Y. Lu, *Adv. Sci.*, 2022, **9**, e2104841.

180. T. Fan, Y. Wang, V. K. Harika, A. Nimkar, K. Wang, X. Liu, M. Wang, L. Xu, Y. Elias, H. Sclar, M. S. Chae, Y. Min, Y. Lu, N. Shpigel and D. Aurbach, *Adv. Sci.*, 2022, **9**, e2202627.

181. T. Fan, W. Kai, V. K. Harika, C. Liu, A. Nimkar, N. Leifer, S. Maiti, J. Grinblat, M. N. Tsubery, X. Liu, M. Wang, L. Xu, Y. Lu, Y. Min, N. Shpigel and D. Aurbach, *Adv. Funct. Mater.*, 2022, **32**, 2204972.

182. J. Liu, J. Wang, Y. Ni, J. Liu, Y. Zhang, Y. Lu, Z. Yan, K. Zhang, Q. Zhao, F. Cheng and J. Chen, *Angew. Chem., Int. Ed.*, 2022, **61**, e202207000.

183. J. Wandt, A. T. S. Freiberg, A. Ogrodnik and H. A. Gasteiger, *Mater. Today*, 2018, **21**, 825-833.

184. S. Zhao and F. Huang, *ACS Nano*, 2024, **18**, 1733-1743.

185. J. G. Swallow, W. H. Woodford, F. P. McGrogan, N. Ferralis, Y.-M. Chiang and K. J. Van Vliet, *J. Electrochem. Soc.*, 2014, **161**, F3084.

186. K. Mizushima, P. C. Jones, P. J. Wiseman and J. B. Goodenough, *Mater. Res. Bull.*, 1980, **15**, 783-789.

187. Y. Fan, E. Olsson, G. Liang, Z. Wang, A. M. D'Angelo, B. Johannessen, L. Thomsen, B. Cowie, J. Li, F. Zhang, Y. Zhao, W. K. Pang, Q. Cai and Z. Guo, *Angew. Chem., Int. Ed.*, 2023, **62**, e202213806.

188. A. Grimaud, W. T. Hong, Y. Shao-Horn and J. M. Tarascon, *Nat. Mater.*, 2016, **15**, 121-126.

189. R. A. House, U. Maitra, L. Jin, J. G. Lozano, J. W. Somerville, N. H. Rees, A. J. Naylor, L. C. Duda, F. Massel, A. V. Chadwick, S. Ramos, D. M. Pickup, D. E. McNally, X. Lu, T. Schmitt, M. R. Roberts and P. G. Bruce, *Chem. Mater.*, 2019, **31**, 3293-3300.

190. J. Peng, Y. Li, Z. Chen, G. Liang, S. Hu, T. Zhou, F. Zheng, Q. Pan, H. Wang, Q. Li, J. Liu and Z. Guo, *ACS Nano*, 2021, **15**, 11607-11618.

191. X. Ou, T. Liu, W. Zhong, X. Fan, X. Guo, X. Huang, L. Cao, J. Hu, B. Zhang, Y. S. Chu, G. Hu, Z. Lin, M. Dahbi, J. Alami, K. Amine, C. Yang and J. Lu, *Nat. Commun.*, 2022, **13**, 2319.

192. C. Zhao, C. Wang, X. Liu, I. Hwang, T. Li, X. Zhou, J. Diao, J. Deng, Y. Qin, Z. Yang, G. Wang, W. Xu, C. Sun, L. Wu, W. Cha, I. Robinson, R. Harder, Y. Jiang, T. Bicer, J.-T. Li, W. Lu, L. Li, Y. Liu, S.-G. Sun, G.-L. Xu and K. Amine, *Nat. Energy*, 2024, **9**, 345-356.

193. Z. Hao, H. Sun, Y. Ni, G. Yang, Z. Yang, Z. Hao, R. Wang, P. Yang, Y. Lu, Q. Zhao, W. Xie, Z. Yan, W. Zhang and J. Chen, *Adv. Mater.*, 2024, **36**, e2307617.

194. J. M. Kim, X. H. Zhang, J. G. Zhang, A. Manthiram, Y. S. Meng and W. Xu, *Mater. Today*, 2021, **46**, 155-182.

195. D. Guan, C. Shi, H. Xu, Y. Gu, J. Zhong, Y. Sha, Z. Hu, M. Ni and Z. Shao, *J. Energy Chem.*, 2023, **82**, 572-580.

196. F. Geng, B. Hu, C. Li, C. Zhao, O. Lafon, J. Trébosc, J.-P. Amoureux, M. Shen and B. Hu, *J. Mater. Chem. A*, 2020, **8**, 16515-16526.

197. C. Zhao, C. Li, H. Liu, Q. Qiu, F. Geng, M. Shen, W. Tong, J. Li and B. Hu, *J. Am. Chem. Soc.*, 2021, **143**, 18652-18664.

198. Q. Shen, Y. Liu, X. Zhao, J. Jin, X. Song, Y. Wang, X. Qu and L. Jiao, *Adv. Energy Mater.*, 2023, **13**, 2203216.

199. H. Lu, S. Chu, J. Tian, Q. Wang, C. Sheng, C. Cheng, R. Liu, A. M. D'Angelo, W. K. Pang, L. Zhang, H. Zhou and S. Guo, *Adv. Funct. Mater.*, 2024, **34**,

2305470.

200. Z. Wang, Z. Luo, H. Xu, T. Zhu, D. Guan, Z. Lin, T.-S. Chan, Y.-C. Huang, Z. Hu, S. P. Jiang and Z. Shao, *Adv. Funct. Mater.*, 2024, **34**, 2402716.

201. D. Guan, G. Ryu, Z. Hu, J. Zhou, C.-L. Dong, Y.-C. Huang, K. Zhang, Y. Zhong, A. C. Komarek, M. Zhu, X. Wu, C.-W. Pao, C.-K. Chang, H.-J. Lin, C.-T. Chen, W. Zhou and Z. Shao, *Nat. Commun.*, 2020, **11**, 3376.

202. L. Li, X. X. Zhang, M. Li, R. J. Chen, F. Wu, K. Amine and J. Lu, *Electrochem. Energy Rev.*, 2018, **1**, 461-482.

203. H. Lei, Z. H. Zeng, J. X. Li, X. W. Cui, B. Wang, Y. K. Shi, W. Sun, X. B. Ji, Y. Yang and P. Ge, *Adv. Funct. Mater.*, 2024, **34**, 2402325.

204. G. Ji, D. Tang, J. Wang, Z. Liang, H. Ji, J. Ma, Z. Zhuang, S. Liu, G. Zhou and H. M. Cheng, *Nat. Commun.*, 2024, **15**, 4086.

205. X. P. Chen, Y. Wang, S. Z. Li, Y. Z. Jiang, Y. Cao and X. Ma, *Chem. Eng. J.*, 2022, **434**, 134542.

206. S. A. Mirshokraee, M. Muhyuddin, R. Morina, L. Poggini, E. Berretti, M. Bellini, A. Lavacchi, C. Ferrara and C. Santoro, *J. Power Sources*, 2023, **557**, 232571.

207. H. Y. Zhu, S. M. Chen, X. M. Yao, K. Yang, W. G. Zhao, T. W. Chen, L. Y. Yang and F. Pan, *Adv. Funct. Mater.*, 2024, **34**, 2401470.